

2007

Ultra-wideband electronics, design methods, algorithms, and systems for dielectric spectroscopy of isolated B16 tumor cells in liquid medium

Erick N. Maxwell
University of South Florida

Follow this and additional works at: <http://scholarcommons.usf.edu/etd>



Part of the [American Studies Commons](#)

Scholar Commons Citation

Maxwell, Erick N., "Ultra-wideband electronics, design methods, algorithms, and systems for dielectric spectroscopy of isolated B16 tumor cells in liquid medium" (2007). *Graduate Theses and Dissertations*.
<http://scholarcommons.usf.edu/etd/2280>

This Dissertation is brought to you for free and open access by the Graduate School at Scholar Commons. It has been accepted for inclusion in Graduate Theses and Dissertations by an authorized administrator of Scholar Commons. For more information, please contact scholarcommons@usf.edu.

Ultra-Wideband Electronics, Design Methods, Algorithms, and Systems for Dielectric
Spectroscopy of Isolated B16 Tumor Cells in Liquid Medium

by

Erick N. Maxwell

A dissertation submitted in partial fulfillment
of the requirements for the degree of
Doctor of Philosophy
Department of Electrical Engineering
College of Engineering
University of South Florida

Major Professor: Thomas Weller, Ph.D.
Kenneth A. Buckle, Ph.D., P.E.
Arthur David Snider, Ph.D., P.E.
Dennis K. Killinger, Ph.D.

Date of Approval:
October 29, 2007

Keywords: UWB, ITC, pulse generator, genetic algorithm, time-domain reflectometry

© Copyright 2007, Erick N. Maxwell

Dedication

To my wife, son, and parents for their support and encouragement.

Acknowledgements

This Ph.D. degree was a journey that would have been impossible without God. First, I would like to thank God for giving me the opportunity, strength, endurance, and hope to complete this degree. During this journey, several others made significant contributions toward degree completion and professional development. I would like to acknowledge Dr. Thomas Weller and Dr. Jeffrey Harrow for providing guidance for this research and devoting countless hours in support of this effort. I would like to acknowledge my mentor at Merck Pharmaceuticals, Dr. Thomas Fare, for his guidance and giving me a vision for the technology developed during this dissertation. I would also like to acknowledge Dr. Mark Jaroszeski for allowing me use of his cell culture laboratory as well as Jose Rey, who dedicated many hours to culture cancer cells for me.

I would also like to acknowledge Bernard Batson who worked to ensure that I had the financial resources, networking opportunities, and career guidance to sustain this pursuit. Finally, I would like to acknowledge those who contributed financial support including the Florida Education Fund, SKINS/IGERT (National Science Foundation), Institute on Black Life, USF Engineering, United Negro College Fund-Merck Pharmaceuticals, and Harris Corp. Finally, I would like to acknowledge my wife Jamie Maxwell and friends Ed and Joan Jean-Pierre for helping me review this manuscript.

Table of Contents

List of Tables	v
List of Figures	vii
List of Symbols	xiii
ABSTRACT	xvii
Chapter 1 Introduction	1
1.1 Background and motivation	1
1.2 Statement of the research problem	4
1.3 Contribution of the dissertation	5
1.4 Materials and methods overview	6
1.5 Overview of chapters	9
1.6 Summary	11
Chapter 2 Literature Review on Characterizing and Quantifying Cell Suspensions	12
2.1 Background	12
2.2 Review of characterizing cell suspensions	18
2.3 Review of time-domain dielectric spectroscopy	21
2.4 Review of dielectric measurement methods	25
2.5 Summary	27
Chapter 3 Novel Circuits for Ultra-Wideband/RF-Microwave Pulse Generation	28
3.1 Background	28
3.2 Step recovery diode	30
3.2.1 Basic principles of SRD operation	31
3.2.2 SRD device modeling	33
3.3 Novel circuits for UWB pulse shaping	37
3.3.1 Theory for UWB coupled-line coupler differentiator	38
3.3.2 Theory for UWB Schottky detector differentiator	43
3.3.3 Implementation of a practical UWB differentiator	49
3.4 Novel circuits for UWB pulse generation	54
3.4.1 Tunable pulse-duration UWB generator	55
3.4.1.1 Validation of new design approach	56
3.4.1.2 Circuit design and description	61

3.4.1.3 Fabrication and measurement	65
3.5 Summary	70
Chapter 4 Dielectric Properties of Lossy Liquids From Transmission-Reflection Measurements	72
4.1 Background	72
4.2 Theory	75
4.3 General solution to Nicholson-Ross-Weir method	79
4.4 Coaxial-line test fixture construction	82
4.5 The utility of Teflon for PTFE core	85
4.6 Frequency-domain simulation and measurement	86
4.6.1 Simulation results and analysis	86
4.6.2 Measurement system and procedures	92
4.6.3 Measurement results and analysis	95
4.7 Measurement uncertainty and error	97
4.8 Summary	98
Chapter 5 A Genetic Algorithm Approach to the Electromagnetic Characterization of Materials in a Coaxial Fixture	99
5.1 Background and motivation	99
5.2 Overview of genetic algorithms	101
5.3 Genetic-based approach for parametric extraction	102
5.4 Calculated S-parameters for comparison in GA objective function	109
5.5 Performance results for the genetic algorithm	111
5.5.1 Measurement procedure	111
5.5.2 Algorithm convergence using traceable standards	111
5.6 Error and uncertainty	114
5.7 Summary	120
Chapter 6 Ultra-Wideband/RF-Microwave Measurement System	121
6.1 Background	121
6.2 Theory for time-domain reflectometry	123
6.2.1 Resolving the propagation times and coefficients	127
6.2.2 Isolation and clear-time considerations	129
6.3 System-level architecture of the UWB measurement system	130
6.4 Calibration and validation of UWB measurement system	132
6.4.1 Measurement procedures	132
6.4.2 UWB measurement system calibration	133
6.4.3 UWB measurement system validation	133
6.5 Measurement uncertainty and error	138
6.6 Summary	139
Chapter 7 An Investigation of Isolated B16-F10 Tumor Cells in Liquid Medium	140
7.1 Background	140
7.2 Materials and methods	141

7.3	Approach to evaluating statistical uncertainty	145
7.4	Approach and methodology	147
7.5	Results and analysis for frequency-domain measurement	149
7.5.1	Frequency-domain data analysis using the GA	149
7.5.2	Uncertainty analysis of GA performance	152
7.5.3	Frequency-domain data analysis using Nicholson-Ross-Weir	154
7.5.4	Uncertainty analysis of NRW performance	155
7.5.5	Discussion of frequency-domain measurement	157
7.6	Results and analysis for time-domain measurement	158
7.6.1	Time-domain data analysis using the GA technique	158
7.6.2	Uncertainty analysis of GA performance	166
7.6.3	Time-domain data analysis using NRW technique	166
7.6.4	Uncertainty analysis of NRW performance	169
7.6.5	Discussion of time-domain measurement	170
7.7	Summary	172
Chapter 8	Summary and Future Recommendations	173
	References	177
	Appendices	190
Appendix A:	Quantitative description for Gaussian pulse	191
A.1	Methodology	191
A.2	Standard deviation rise time	192
A.3	Formulation of Gaussian pulse based on 10-90% rise time	195
A.4	Mathematical approach to identifying points for axis shifting	196
A.5	A starting point for periodic signal evaluation	199
A.6	Results and discussion	201
Appendix B:	MATLAB code for Courtney and Motil technique	205
B.1	Data pre-processing	205
B.2	Data post-processing	209
B.3	Summary	213
Appendix C:	C++ code for genetic algorithm	214
C.1	Measurement data acquisition	214
C.2	S-parameters of fixture	217
C.3	Dielectric properties of specimen	219
C.4	S-parameter comparison	220
C.5	NRW estimation	222
C.6	Parametric determination	227
C.7	Summary	231

Appendix D: Evolutionary development of the UWB VERC circuits	232
D.1 2 nd generation of UWB VERC circuit	232
D.2 3 rd generation of UWB VERC circuit	236
D.3 Summary	236
About the Author	End Page

List of Tables

Table 2.1: Dielectric mechanisms versus dispersion type.	15
Table 2.2: Formalism of dielectric relaxation.	16
Table 2.3: Comparison of methods for dielectric spectroscopy.	26
Table 3.1: A p-n junction diode model and MMD-841 parameters.	34
Table 4.1: Half-wavelength resonance frequency ($f_{r1/2}$) and percentage error for measurement of ϵ_r in fixture with a continuous and corrected step-discontinuity interface.	92
Table 4.2: NIST approximations of the Debye model parameters for ethanol, methanol and de-ionized water at 27°C.	94
Table 5.1: Genetic representation for genome construction in permittivity extraction GA.	104
Table 5.2: Parameter set for genetic algorithm performance.	105
Table 5.3: GA uncertainty ($u_i(\bar{x})$) and sample size (n) required for measurement of air, ethanol, methanol and de-ionized water at a 90% confidence level.	118
Table 5.4: A comparison of GA uncertainty in measurement of de-ionized water using two methods for comparing the difference in the measured and computed S-parameter values.	120
Table 7.1: Extracted GA parameters for frequency-domain measurement data (test-set #3).	152
Table 7.2: Type-A evaluation on a 90% confidence interval of frequency-domain GA test-set #3.	153
Table 7.3: Type-A evaluation at a 90% confidence level for frequency-domain NRW data population.	156

Table 7.4: One-tail paired t-test at a 90% confidence level for frequency-domain NRW data population.	156
Table 7.5: Computed time intervals for test-set #2 of B16 cell suspensions.	161
Table 7.6: Extracted GA parameters for time-domain measurement data (test-set #2).	166
Table 7.7: Type-A evaluation on a 90% confidence interval of time-domain test-set #2.	167
Table 7.8: Type-A evaluation at a 90% confidence level for time-domain NRW data population.	169
Table 7.9: One-tail paired t-test at a 90% confidence level for time-domain NRW data population.	170

List of Figures

Figure 1.1: System-level block diagram of the time-domain dielectric spectroscopy system.	8
Figure 2.1: Dielectric constant decreasing with frequency.	15
Figure 2.2: Complex plane plot for four relaxation types: (A) Debye, (B) Cole-Cole, (C) Davidson-Cole, and (D) Havriliak-Negami.	17
Figure 2.3: Confocal microscopy of B16-F10 tumor cells incubated with the following fluorescein: (A) free fluorescein, (B) fluorescein encapsulated unilamellar liposomes, and (C) hyaluronan-liposomes.	19
Figure 2.4: (A) Single-shell dielectric model for biological particle and (B) schematic diagram of frequency dependence.	20
Figure 2.5: Diagram of a Gaussian pulse and its (A) 1 st – 3 rd and (B) 4 th – 6 th derivatives.	23
Figure 2.6: Diagram of a Gaussian pulse and the spectrum associated with its (A) 1 st – 3 rd and (B) 4 th – 6 th derivatives.	24
Figure 2.7: 3-dimensional view of spectrum for derivative 1-6.	25
Figure 3.1: Gaussian derived waveforms with a 250 <i>psec</i> duration.	29
Figure 3.2: Parts of SRD operation, including (A) p-n junction diode diagram, (B) doping profile, (C) reverse forward bias representation, and (D) potential at the diode junction.	31
Figure 3.3: Simulated I-V characteristics of a step recovery diode.	33
Figure 3.4: Simulated and measured SRD output for a simple series and shunt configuration.	35
Figure 3.5: Simulation of forward and reverse biased diodes in a shunt configuration.	36

Figure 3.6: Comparison of simulated and measured data for simple double-shunt circuits.	37
Figure 3.7: A single section microstrip coupled-line coupler (A) schematic and (B) lumped element equivalent circuit of a lossy transmission line coupler.	39
Figure 3.8: A single section microstrip coupled-line coupler (A) ADS schematic block, (B) variable rise time input at V_{in} , and (C) output waveform at V_{out} .	42
Figure 3.9: A Schottky detector diode differentiator (A) schematic and (B) lumped element equivalent circuit.	45
Figure 3.10: A Schottky detector diode differentiator (A) ADS schematic block, (B) V_x square wave response, and (C) V_{out} output waveform.	48
Figure 3.11: Schematic block of the designed MCS ³ P.	49
Figure 3.12: Time-domain (A,C,E,G) and frequency-domain (B,D,F,H) responses of multi-port circuit for simultaneous shaping of sub-nanosecond UWB pulses.	50
Figure 3.13: Component layout for the MCS ³ P with SMA connectors attached.	52
Figure 3.14: Measured and simulated waveforms responses for (A) edge compression sub-circuit, (B) coupled-line coupler differentiator sub-circuit, and (C) Schottky detector differentiator sub-circuit.	54
Figure 3.15: SRDs in a series (A) and shunt (B) configuration with power supply.	57
Figure 3.16: ADS simulations showing voltage waveforms generated using a $1.0 V_{pp}$ and $20 V_{pp}$ 14 MHz sources for a series (A) and shunt (B) connected SRD.	58
Figure 3.17: Schematic of the variable edge-rate compressor.	59
Figure 3.18: ADS simulation (A) and measurement (B) results of the variable edge-rate compression approach, for 1, 2, 5, 10 and 20 pF capacitance values.	60
Figure 3.19: Schematic of a tunable UWB generator.	62

Figure 3.20: Photo of the single-stage tunable UWB pulse generator consisting of a variable edge-rate compressor, amplifier, pulse forming network and RF/microwave differentiator, from left to right.	64
Figure 3.21: Simulated and measured Gaussian waveforms at 1, 2, 5, 10 and 20 pF capacitance, with (A) simulated and (B) measured Gaussian pulse at the output of pulse shaper, over capacitance.	66
Figure 3.22: Simulated and measured monocycle waveforms at 1, 2, 5, 10 and 20 pF capacitance with (A) simulated and (B) measured monocycle pulses resulting from 2 nd derivative of pulse forming output.	67
Figure 3.23: Shaped spectrum with FCC mask for medical imaging and normalized frequency response of waveforms generated using 1 and 10 pF capacitance with (A) Gaussian and (B) monocycle responses.	69
Figure 4.1: Calibration reference-plane and sample interface of coaxial fixture with a relative complex permittivity (ϵ_{r2}) and permeability (μ_{r2}) of specimen so that $\epsilon_{r2} = \epsilon_2' - j\epsilon_2''$ and $\mu_{r2} = \mu_2' - j\mu_2''$.	80
Figure 4.2: Coaxial transmission line fixture for dielectric measurements of lossy liquids, whereby the sample holder is constructed from a semi-rigid coaxial line with fluid inlet and pressure relief.	83
Figure 4.3: ADS schematic block of a coaxial fixture for computing the complex relative permittivity from S-parameter simulation data.	87
Figure 4.4: A simulated comparison of the de-embedded S-parameters for an unaltered holder with a 5.31 to 6.35 mm diameter, where (A) is phase and magnitude of S_{11} and (B) S_{21} (TL5/TL6 de-embedded).	88
Figure 4.5: A simulation of the real and imaginary part of ϵ_r for a specimen holder that transitions smoothly (continuous) at PTFE-specimen interface.	89
Figure 4.6: A simulated comparison of the error associated with the real part of ϵ_r , for a continuous specimen holder against ones with a discontinuity at the PTFE-specimen (PTFE-S) interface.	91
Figure 4.7: Experimental setup for dielectric characterization using transmission-reflection techniques.	93

Figure 4.8: Permittivity measurement comparison of the corrected Nicholson-Ross-Weir (NRW) algorithm to NIST Debye dispersion data for (A) air, (B) methanol, (C) ethanol and (D) DI-water.	95
Figure 4.9: Percentage error for dilute substances using NRW algorithm.	96
Figure 5.1: Evolutionary process of a genetic algorithm.	102
Figure 5.2: Flow chart for the GA, which demonstrates the components of the objective function.	106
Figure 5.3: Flow chart of the genetic algorithm for permittivity determination.	108
Figure 5.4: Measured versus calculated S-parameters for ethanol comparing (A) reflection and (B) transmission coefficients of 2 nd GA stage, and (C) reflection and (D) transmission coefficients of 3 rd stage at 27°C.	112
Figure 5.5: Measured versus computed S-parameters from 3 rd GA stage for measurements of S11-S21 in (A-B) air, (C-D) ethanol, (E-F) methanol and (G-H) de-ionized water at 27°C.	113
Figure 5.6: The complex permittivity and loss tangent for a stage 4 solution in the genetic algorithm for (A) air and (B) ethanol, at 27°C.	115
Figure 5.7: The complex permittivity and loss tangent for a stage 4 solution in the genetic algorithm for (A) methanol and (B) de-ionized water, at 27°C.	116
Figure 5.8: The uncertainty for various methods of representing the error associated with the fit between measured and computed S-parameters.	119
Figure 6.1: Diagrams for (A) time-domain reflectometry system configuration and (B) classical lumped element equivalent model for a transmission line.	123
Figure 6.2: Bounce diagram for the time-domain waveform for the incident signal in the fixture.	125
Figure 6.3: Complex ultra-wideband/RF-microwave measurement system for time-domain extraction of dielectric properties of materials.	131
Figure 6.4: Contextual view of measured waveforms at (A) port 1 and (B) port 2 of the oscilloscope.	134

Figure 6.5: Isolation waveforms for the (A) incident, (B) interface 1-2 reflected, (C) interface 2-3 reflected and (D) transmitted signals using the data acquisition and analysis algorithm.	135
Figure 6.6: Computed S-parameters (A) S_{11} and (B) S_{21} from time-domain waveforms.	136
Figure 6.7: The resulting real parts of the complex relative permittivity, obtained using NRW technique.	137
Figure 7.1: Flow chart of the process for preparing a cultured B16-F10 tumor cell for counting and measurement.	142
Figure 7.2: Process flow for preparation and measurement of B16-F10 tumor cell suspension.	144
Figure 7.3: Flow for time- and frequency-domain electromagnetic characterization of B16 suspension.	148
Figure 7.4: A comparison of the VNA measured and GA computed results for S_{11} and S_{21} of the 3 rd frequency-domain test, for (A)-(B) 3 M, (C)-(D) 2 and, (E)-(F) 1 M <i>cells/mL</i> , (G)-(H) McCoy's medium.	150
Figure 7.5: GA produced complex permittivity for B16 cell suspension for frequency-domain measurement data (test-set #3).	151
Figure 7.6: The real part of the NRW complex permittivity for frequency-domain test-set #3.	154
Figure 7.7: The NRW static permittivity for test population of B16 suspensions in frequency-domain.	155
Figure 7.8: A contextual view of two-port time-domain measurement of (A) waveforms transmitted and reflected from specimen interface for B16 suspension test #2 with (B) zoom on through transmission.	159
Figure 7.9: Pre-processing for converting time-domain data to S-parameters in B16 test-set #2, where (A) is waveform launched down fixture, (B) reflected from 1 st and (C) 2 nd interfaces, and (D) transmitted through.	160
Figure 7.10: Computed S-parameters (A) S_{11} and (B) S_{21} associated with a conversion of time-domain measurement data for the test #2 of B16 cell suspensions.	162

Figure 7.11: A comparison of measured and computed results for S_{11} and S_{21} of the 3 rd test, for (A-B) 3 M <i>cells/mL</i> , (C-D) 2 M <i>cells/mL</i> , (E-F) 1 M <i>cells/mL</i> , (G-H) McCoy's 5A medium.	164
Figure 7.12: Complex permittivity for B16 cell suspension using the GA on test-set #2.	165
Figure 7.13: The real part of the NRW complex permittivity in the time-domain.	168
Figure 7.14: The NRW static permittivity for the population of tests of B16 suspensions in the time-domain.	169
Figure A.1: Imprecise rise time for (A) Gaussian of a normalized 1.0 <i>nsec</i> pulse and (B) normalized spectrum with imprecise interpretation for F_{Knee} using a 1.0 <i>nsec</i> Gaussian pulse.	194
Figure A.2: Normalized spectrum with F_{Knee} for (A) a 1.0 <i>nsec</i> 10-90% rise time and (B) normalized spectrum with F_{Knee} for 1.0 <i>nsec</i> pulse width using 10-90% rise time interpretation.	198
Figure A.3: Normalized periodic (A) 1.0 <i>nsec</i> pulse and (B) normalized spectrum for pulse train with a 1.0 <i>nsec</i> pulse width.	202
Figure D.1: A DC biased UWB VERC circuit (A) diagram and (B) ADS schematic.	233
Figure D.2: Fabricated circuit for a DC biased UWB VERC on FR4 at (A) bird's eye view and (B) zoomed view.	234
Figure D.3: DC biased UWB VERC circuit (A) simulated and (B) measured results.	235
Figure D.4: A fixed pulse UWB VERC circuit (A) diagram and (B) ADS schematic.	237
Figure D.5: Fabricated circuit for a fixed pulse UWB VERC on FR4 at (A) bird's eye view and (B) zoomed view.	238
Figure D.6: Fixed pulse UWB VERC circuit (A) simulated and (B) measured results.	239

List of Symbols

α	(Alpha) Cole-Cole distribution parameter in dielectric model	[-]
a	Radius of inner conductor of coax	[m]
A	Ampere	[A]
β	(Beta) Havrilak-Negami distribution parameter in dielectric model	[-]
β_1	Phase of complex propagation constant in fixture regions 1 and 3	[Np/m]
β_2	Phase of complex propagation constant in fixture regions 2	[Np/m]
b	Radius of outer conductor of coax	[m]
\vec{B}	Magnetic flux density	[W/m^2]
c_0	Speed of light	[m/s]
dB	Decibels = $10 \log (P_2/P_1)$ or $20 \log (V_2/V_1)$	[dB]
\vec{D}	Electric flux density	[C/m^2]
$\vec{E}, \vec{E}_n, \vec{E}_t$	Electric field intensity, (n-normal and t-tangential components)	[V/m^2]
E_{nTEM}^+, E_{nTEM}^-	Reverse/forward normal parts of TEM electric field intensity	[V/m^2]
E_{nTE}^+, E_{nTE}^-	Reverse/forward normal parts of TE electric field intensity	[V/m^2]
E_{nTM}^+, E_{nTM}^-	Reverse/forward normal parts of TM electric field intensity	[V/m^2]
E_{tTE}	Tangential parts of TE electric field intensity	[V/m^2]

E_{iTEM}, E_{iTM}	Tangential parts of TM and TEM electric field intensity	$[V/m^2]$
E_I, E_{II}, E_{III}	Normalized electric fields in regions I, II and III of coax fixture	$[V/m^2]$
ε	Complex valued dispersive absolute dielectric permittivity	$[F/m]$
$\varepsilon_r, \varepsilon_{r1}, \varepsilon_{c2}$	Relative dielectric permittivity (r1-regions 1&3, c2-regions 2)	[-]
$\varepsilon', \varepsilon_2'$	Real part of complex relative dielectric permittivity (2-region 2)	[-]
$\varepsilon'', \varepsilon_2''$	Imaginary part of complex rel. dielectric permittivity (2-region 2)	[-]
ε_0	Absolute dielectric permittivity	$[F/m]$
ε_∞	Infinite frequency limit of complex valued dielectric permittivity	[-]
f	Frequency	$[Hz]$
f_x	Time-domain Gaussian probability density function	[-]
F_{knee}	Knee frequency at 3 dB below peak amplitude of spectrum	[-]
F_x	Frequency-domain Gaussian probability density function	[-]
γ_n, γ_2	Complex valued propagation constant (n-normal, 2-region 2)	$[1/m]$
$\vec{H}, \vec{H}_n, \vec{H}_t$	Magnetic field intensity (n-normal and t-tangential components)	$[A/m]$
\vec{J}_c	Current density due to conduction	$[A/m^2]$
\vec{J}_i	Current density due to impressed source	$[A/m^2]$
L_1, L_3	Length of coax for regions 1 and 3 of the experimental fixture	$[m]$
L_2	Length of sample in experimental fixture	$[m]$
Γ_{12}	Reflection coefficient	[-]

m_x	Statistical mean	[-]
$m_{4\sigma}$	Time shift of four standard deviations	[s]
λ_{nc}	Cut-off wavelength for mode n	[m]
\vec{M}_t	Tangential component of magnetization	[Vs/ m ²]
Ω	(Omega) Unit for ohmic resistance	[Ω]
\vec{r}_t	Transverse vector	[-]
σ_x	(Sigma) Statistical variance	[-]
σ_0	DC conductivity	[mhos/m]
S_{11}	Scatter reflection parameter	[-]
S_{21}	Scatter transmission parameter	[-]
sr	Slew-rate	[V/s]
τ	Pulse rise time	[s]
τ_r	Relaxation time	[s]
τ_1	Propagation time from port 1 to sample face of fixture	[s]
$\tau_{10-90}, \tau_{20-80}$	10-90 and 20-80 rise times	[s]
τ_2	Transmission time through the material in fixture	[s]
τ_3	Propagation time from sample face to port 2 of fixture	[s]
τ_4	Propagation time from port 1 to port 2 of fixture	[s]
$\tau_{\Delta V}$	Rise time associated with full-width-half-maximum measurement	[s]
τ_σ	Standard deviation rise time	[s]

$t_x, t_{10\%}, t_{90\%}$	Time of rise to x, 10% and 90% voltage levels	[s]
T_{PFWHM}	Pulse-duration measured from full-width-half-maximum	[s]
T_{12}, T_{21}	Transmission coefficient measured at ports 1 and 2	[-]
μ	Complex valued dispersive absolute dielectric permeability	[H/m]
$\mu_r, \mu_{r1}, \mu_{c2}$	Relative dielectric permeability (r1-regions 1&3, c2-regions 2)	[-]
μ', μ'_2	Real part of complex relative dielectric permeability (2-region 2)	[-]
μ'', μ''_2	Imaginary part of complex rel. dielectric permeability (2-region 2)	[-]
μ_0	Absolute dielectric permeability	[H/m]
V	Volts	[V]
V_{PP}	Peak to peak voltage	[V]
j	Sqrt (-1)	[-]
ω	Angular frequency	[rad/s]
Z_{nTE}, Z_{nTM}	Intrinsic impedance normal to propagation for modes TE and TM	[Ω]
Z_0	Characteristic impedance	[Ω]

Ultra-Wideband Electronics, Design Methods, Algorithms, and Systems for Dielectric Spectroscopy of Isolated B16 Tumor Cells in Liquid Medium

Erick N. Maxwell

ABSTRACT

Quantifying and characterizing isolated tumor cells (ITCs) is of interest in surgical pathology and cytology for its potential to provide data for cancer staging, classification, and treatment. Although the independent prognostic significance of circulating ITCs has not been proven, their presence is gaining clinical relevance as an indicator. However, researchers have not established an optimal method for detecting ITCs. Consequently, this Ph.D. dissertation is concerned with the development and evaluation of dielectric spectroscopy as a low-cost method for cell characterization and quantification. In support of this goal, ultra-wideband (UWB), microwave pulse generator circuits, coaxial transmission line fixtures, permittivity extraction algorithms, and dielectric spectroscopy measurement systems were developed for evaluating the capacity to quantify B16-F10 tumor cells in suspension.

First, this research addressed challenges in developing tunable UWB circuits for pulse generation. In time-domain dielectric spectroscopy, a tunable UWB pulse generator facilitates exploration of microscopic dielectric mechanisms, which contribute to dispersion characteristics. Conventional approaches to tunable pulse generator design

have resulted in complex circuit topologies and unsymmetrical waveform morphologies. In this research, a new design approach for low-complexity, tunable, sub-nanosecond and UWB pulse generator was developed. This approach was applied to the development of a novel generator that produces symmetrical waveforms (patent pending 60/597,746).

Next, this research addressed problems with transmission-reflection (T/R) measurement of cell suspensions. In T/R measurement, coaxial transmission line fixtures have historically required an elaborate sample holder for containing liquids, resulting in high cost and complexity. Furthermore, the algorithms used to extract T/R dielectric properties have suffered from myriad problems including local minima and half-wavelength resonance. In this dissertation, a simple coaxial transmission line fixture for holding liquids by dispensing with the air-core assumption inherent in previous designs was developed (patent pending 60/916,042). In addition, a genetic algorithm was applied towards extracting dielectric properties from measurement data to circumvent problems of local minima and half wavelength resonance.

Finally, in this research the capacity for using dielectric properties to quantify isolated B16-F10 tumor cells in McCoy's liquid medium was investigated. In so doing, the utility of the Maxwell-Wagner mixture formula for cell quantification was demonstrated by measuring distinct dielectric properties for differing volumes of cell suspensions using frequency- and time-domain dielectric spectroscopy.

Chapter 1

Introduction

Presented in this chapter is background information and the motivation for this dissertation research. Overviews of the research problem, dissertation contributions, materials and methods as well as dissertation chapters are also presented.

1.1 Background and motivation

Detecting, quantifying and characterizing isolated tumor cells (ITCs) is of interest in surgical pathology and cytology for its potential to provide data for cancer staging, classification and treatment [1-3]. ITCs are individual tumor cells that spread to the lymph nodes or general circulation, which includes blood, bone marrow, and other distant sites. In literature, the terms disseminated and circulating tumor cells are synonymous to ITCs. Many researchers believe that the spread of ITCs is one of the mechanisms involved in the formation of tumors in distant sites [4, 5]. Among these researchers is Uchikura, Takajo, and Nakajo, who reported on a connection between circulating tumors in the blood and the formation of hematogenous metastasis [6]. However, Hermanek, Hutter, Sobin and others reported that ITCs are detected in approximately 15% of sentinel lymph nodes in which no metastasis is found [7]. As such, the independent prognostic significance of circulating ITCs has not been proven. Consequently, the tumor-lymph

node-metastasis (TNM) classification system—the most widely used means for classifying the spread of malignant tumors—does not assign clinical significance to the occurrence of ITCs [8, 9].

Although the TNM system does not regard ITCs as positive for disease, detecting, quantifying, and characterizing them is an integral part of the metastatic work-up for cancer patients [10]. The Pathology Associates of Lexington, Pennsylvania stated the following: “Regardless of the lack of any current consensus as to the significance of isolated tumor cells and clusters $< 0.2 \text{ mm}$ in greatest dimension (ITCs), excellence in surgical pathology practice requires that a staging lymph node exam actually be truly negative when diagnosed as negative. Equally important is the discovery of malignant cells in a node, be they individually dispersed lobular carcinoma cells or other malignant cells” [11, 12]. Consequently, Hermanek noted that the presence of ITCs is gaining clinical relevance as a prognostic indicator and attention as a selection criteria for more aggressive treatment options (adjuvant treatment) as well as surrogate markers for monitoring the efficiency of adjuvant therapy.

Traditionally, pathologists have used hematoxylin and eosin (H&E)-stained sections from each dissected lymph node to diagnose disease. In H&E-staining, a single section evaluates less than 1% of the lymph node, thus it is not used exclusively for diagnosing disease [13]. Pathologists frequently follow the H&E-staining with immunohistochemistry (IHC)-stained sections, which is more sensitive and capable of detecting ITCs. However, Weaver, Krag, Manna and others showed that an optimal

method for detecting single tumor cells or small cluster of tumor cells has not been established. In their research, these authors asserted that, “automated computer-assisted detection of candidate tumor cells may have the potential to significantly assist the pathologist” [14]. Mesker, Torrenga, Sloos and others demonstrated this potential by showing that supervised automated microscopy is more sensitive for detecting IHC-stained micrometastasis and ITCs [15]. The authors confirmed that automation improves the reproducibility of diagnosing micrometastases and ITCs by reducing the amount of human involvement in the process.

H&E-stained, IHC-stained, and computer-assisted detection are considered morphologic methods because they require preparation of the dissections onto slides for histological examination using a microscope. Nonmorphologic methods do not require microscopic examination of stained slides and rely on biochemical and genetic information for detection [16]. Lee, Moon, Park and others demonstrated a nonmorphologic method called imprint cytology for assessing lymph nodes status. They demonstrated that this technology could be useful if the sensitivity and specificity was improved [17]. Flow cytometry is another nonmorphologic method that has emerged as a useful application in clinical pathology [18]. This is used for quantifying and characterizing cells in suspension. In flow cytometry, single particles are suspended in a stream of liquid and interrogated using a laser-based coherent light source. This interrogation results in data upon which multivariate techniques are applied to characterize large numbers of particles in a short period of time [19]. Flow cytometers range in price from \$50,000.00 to \$500,000.00, which is a limiting factor for many

academic institutions [20]. As such, researchers have explored other techniques for characterizing cells, including dielectric spectroscopy. Paraskevas, Vassiliou and Dervos noted that dielectric spectroscopy provides a high-sensitivity low-cost diagnostic tool for characterizing oil-based emulsions [21]. Consequently, this dissertation applies a nonmorphologic method based on dielectric spectroscopy for cell characterization and quantification.

1.2 Statement of the research problem

Dielectric spectroscopy measures the dielectric properties of a medium by capturing polarization effects at the system, molecular, atomic and sub-atomic levels. Researchers have reported on the capacity of dielectric spectroscopy for characterizing tumor cell suspensions, but not for cell quantification [22-24]. Maxwell and Wagner confirmed the possibility of using dielectric spectroscopy for quantifying blood cells by relating the dielectric properties of individual cells to its volume fraction in a mixture. Consequently, this research adds to the body of knowledge on dielectric spectroscopy by relating cell quantity to the dielectric properties of a heterogeneous mixture of cells and medium to obtain the complex relative permittivity. The most frequently used method for measuring these properties, for liquid samples, involves use of an open-ended coaxial probe [25]. Two-port methods based on a coaxial transmission line offer an advantage over the open-ended probe by providing a measure of the complex relative permittivity as well as permeability. However, such transmission line methods are problematic for cell suspensions because they are not suitable for holding liquid samples, which has led to

increased fixture complexity and cost [26]. Other problems exist for dielectric spectroscopy in the time-domain. Time-domain dielectric spectroscopy (TDDS) provides the best resolution of the structural and dynamic properties of cell suspensions [27]. Tunable Gaussian pulses (also known as ultra-wideband waveforms) facilitate access to this resolution by controlling the spectral content of the waveform. However, the availability of simple, low-cost circuits for generating sub-nanosecond tunable pulses is limited [28].

1.3 Contribution of the dissertation

This research applies frequency- and time-domain dielectric spectroscopy to a study of isolated tumor cells suspended in medium. It provides an answer to the question: To what extent are different volumes of cancer cells electrically distinctive? In so doing, this dissertation demonstrates that the complex relative permittivity of a mixture of tumor cells in medium is sufficient for quantifying cells. It also presents circuits for pulse generation, a coaxial transmission line fixture for holding small liquid samples, and a multi-parametric genetic algorithm for permittivity determination. Consequently, this dissertation contributes:

- Novel circuits for tunable pulse generation (ultra-wideband generators) by proposing a new approach to generator design,
- A low-cost method for transmission-reflection (T/R) measurements that is based on the construction of a test fixture from a semi-rigid coaxial

transmission line with a Teflon-PolyTetraFlouroEthylene (PTFE) core, which eliminates the need for waveguide walls for holding the sample,

- A genetic algorithm (GA) approach for permittivity extraction which circumvents the problem of half-wavelength resonance in the Nicholson-Ross-Weir (NRW) technique and extends Oswald's approach, and
- An investigation of the capacity for dielectric spectroscopy to quantify isolated B16-F10 tumor cells in McCoy's liquid medium.

1.4 Materials and methods overview

The materials and methods used to develop the ultra-wideband (UWB) generators include the following: Agilent's Advanced Design System (ADS) for circuit design and simulation, LPFK's Protomat 6000 for board fabrication, and Hewlett Packard's (now Agilent) HP 54750A digitizing oscilloscope with a 20 GHz plug-in for circuit testing. The UWB generator was developed with a Metelics SMMD-0841 step recovery diode and an Agilent HSMS-2862 Schottky detector diode. These diodes were modeled for simulation with a "p-n junction diode model" and "di_hp_HSMS2862_2000301" from the Agilent high frequency diode library. Following simulation, the circuit was fabricated onto a 2.54 mm thick Rogers Corporation circuit board material (TMM4), comprised of an FR4 substrate that was laminated with ½ oz copper cladding on both sides. Finally, an Agilent 33120A 15 MHz function/arbitrary waveform generator was used to supply the input for the UWB generator for verification testing.

Many of the above materials and methods were applied in the development and verification of the coaxial transmission line fixture that was used in the T/R measurement systems for frequency-domain dielectric spectroscopy (FDDS) and time-domain TDDS. The coaxial transmission line fixture was designed and simulated using ADS and constructed by the University of South Florida machine shop. The fixture was then calibrated and verified in a FDDS system, which consisted of an HP 8573D vector network analyzer (VNA) and personal computer (PC) for waveform capture and processing, respectively. The standards used in this calibration included 200 proof ethyl alcohol (also known as ethanol – No. 64-17-5) and methyl alcohol (methanol – No. 67-56-1) from Fischer Scientific. De-ionized water (DI-water) from the USF clean room facility was also used to verify the calibration. Verification and calibration data was obtained from the VNA in the form of scattering parameters (S-parameters). This data was transferred to a PC and processed by algorithms for permittivity determination. These algorithms were written using C++ and executed using Microsoft Visual C++ 2005 express edition.

The TDDS system was also calibrated and verified using all of the above materials and methods, except for a VNA. Instead, a 20 GHz digitizing oscilloscope, consisting of a mainframe and sampling head, was used with a coaxial transmission line fixture, UWB pulse generator, waveform generator, and PC (see Figure 1.1 below). In this configuration, a UWB signal was generated then sent through a coaxial transmission line fixture where the T/R waves were passed through a sampling head and digitized. These digitized waveforms were stored onto a PC for processing using code written with

Mathwork's MATLAB 7.1, which converted time-domain data to the frequency-domain. Next, this frequency-domain data was processed using a GA written with Microsoft's Visual C++, which extracted the dielectric parameters.

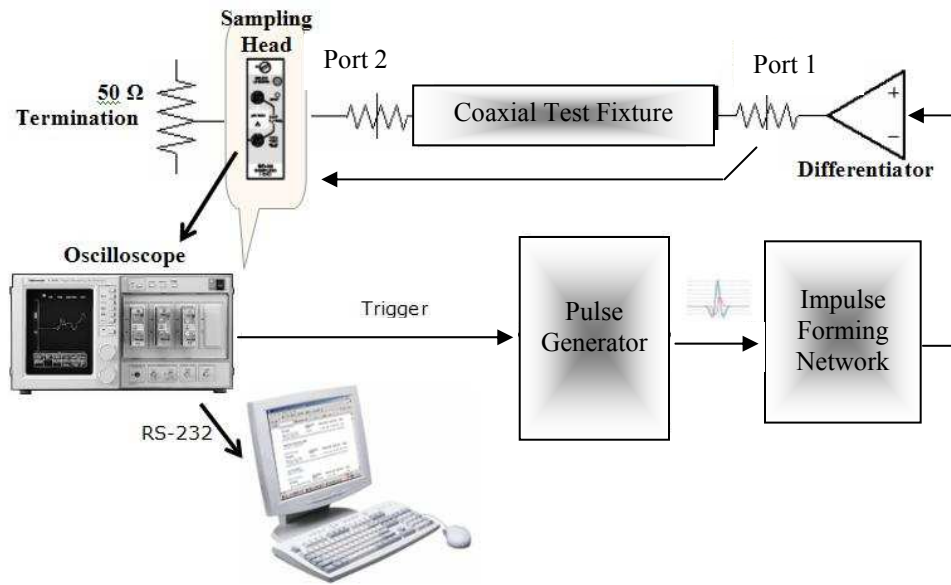


Figure 1.1: System-level block diagram of the time-domain dielectric spectroscopy system.

The materials and methods used to characterize the B16-F10 cell suspension included culturing B16-F10 cancer cells in the USF cell culture laboratory. The B16 cells in culture required one week for growth and included protocols that were jointly established by the local lab and American Type Culture Collection (ATCC). Tumor cell suspensions consisting of McCoy's 5A liquid medium with volumes of 1.0, 2.0, and 3.0 million cells per milliliter ($M \text{ cells/mL}$) were tested using the FDDS and TDDS systems. Aseptic techniques were applied in handling the cell suspensions, which included an

ethanol wash of the coaxial test fixture and the use of latex gloves and sterile pipettes. Labnet pipette controller (P200) and a low speed shaker (S2030-LS) were also used for transferring the suspensions to the fixture and maintaining the cells in suspension, respectively.

1.5 Overview of chapters

This dissertation is arranged in eight chapters. Chapter 2 presents a review of dielectric spectroscopy and its application towards characterizing and quantifying cell suspensions. It includes a background on frequency dispersion in dielectric materials as well as literature reviews on dielectric characterization of cell suspensions, time-domain dielectric spectroscopy, and methods for measuring dielectric properties of materials.

In Chapter 3, a new design approach to pulse generation is presented. This approach is described as a variable edge-rate compression (VERC) approach to tunable UWB generator design. It entails tuning prior to Gaussian pulse formation and provides advantages of a broader tuning range, improved tuning sensitivity and increased design simplicity over conventional approaches. The VERC approach was validated, in this chapter, through the modeling and simulation of various circuits for pulse generation.

Chapter 4 is devoted to the development of a new coaxial-line test fixture, which provides a simpler construction by dispensing with the conventional air-core assumption. In support of a non-air-core assumption, this chapter provides a general solution to the NRW algorithm for permittivity determination. Methods for diluting the effects of half-

wavelength resonance—a problem that is characteristic of the NRW algorithm—are also presented. These methods are applied towards frequency-domain validation of the fixture using ethanol, methanol, and de-ionized water.

In Chapter 5, a GA for the electromagnetic characterization of materials is presented. This algorithm offers a means to circumvent the problems of half-wavelength resonance in the NRW technique and local minima in iterative techniques. In this chapter, background information of permittivity models is provided. Also, the GA is applied to measurement of traceable materials, including ethanol, methanol, and de-ionized water. This chapter concludes with an evaluation of error and uncertainty.

A time-domain validation of the coaxial-line fixture is provided in Chapter 6. This study begins with a presentation of time-domain reflectometry theory, which includes an analysis for transforming the time-domain measurements to S-parameters. In this chapter, theory is applied to the extraction of dielectric properties for ethanol, methanol, and de-ionized water. The results are compared with the data obtained in the frequency-domain analysis as well as with National Institute of Standards and Technology (NIST) data for assessing the efficacy of the UWB time-domain measurement system.

Chapter 7 presents a study of the UWB electrical properties for different volumes of cancer cells suspended in McCoy's medium. It presents data from TDDS and FDDS. This chapter also contains a comparison of the time- and frequency-domain results. Last, conclusions are drawn and future work is recommended in Chapter 8.

1.6 Summary

Research has shown that the efficacy of classifying cancer by histological type or primary site rather than by molecular composition is fundamentally flawed [29].

Although the prognostic significance of isolated tumor cells is uncertain, the need to characterize and quantify isolated tumor cells will increase with its clinical relevance. A low-cost method based on dielectric spectroscopy enables broad access to this capability, which could speed up assessment of its relevance through research and experimentation.

Chapter 2

Literature Review on Characterizing and Quantifying Cell Suspensions

Presented in this chapter is a review of dielectric spectroscopy and its application towards characterizing and quantifying cell suspensions. It includes a background on frequency dispersion in dielectric materials as well as literature reviews on characterizing cell suspensions, time-domain dielectric spectroscopy, and methods for measuring dielectric properties. The circuits, fixtures, and algorithms that comprise the dielectric spectroscopy systems are reviewed in later chapters.

2.1 Background

A material is a dielectric if it stores and dissipates energy with application and removal of an electric field. Upon application of a field, the material's storage capacity increases when charges that appear on the electrode surfaces neutralize those bound in the material. Consequently, the material interacts with an externally applied electric field. The term permittivity, which describes this interaction, is one of several dielectric properties. Dielectric spectroscopy measures the dielectric properties of a medium, including complex relative permittivity and/or permeability, as a function of frequency. These properties result from the displacement of electrons, molecules, or groups thereof

in the dielectric material. Polarization density (\vec{P}) describes this electric field displacement (\vec{D}) by the following constitutive relation:

$$\vec{D} = \epsilon_0 \vec{E} + \vec{P} = (1 + \chi_e) \epsilon_0 \vec{E} = \epsilon \vec{E} \quad , \quad (2.1)$$

where \vec{E} is the electric field intensity of the material, χ_e electric susceptibility, ϵ electric permittivity, and ϵ_0 permittivity of free space [30]. The relationship in (2.1) is considered along with the Kramers-Kronig relations to describe the frequency dispersion characteristics for complex permittivity and permeability [31]. In their relations, Kramers and Kronig provided a set of mathematical properties that connect the real and imaginary parts for any complex analytic function. These properties are associated with a system response (or response function) which results from application of an oscillatory force in a physical system. They include the observation that the system response is not instantaneous so that at high frequencies it does not have enough time to react before the force changes direction. As a result, the response function diminishes with an increase in frequency. Consequently, a complex system response to an applied force is compatible with the Kramers-Kronig relations, which includes dielectric spectroscopy.

In dielectric spectroscopy, the complex relative permittivity is synonymous to the response function of the physical system described above using the Kramers-Kronig relations. Complex relative permittivity (ϵ_r) is defined as:

$$\epsilon_r = \epsilon_r' - j\epsilon_r'' = \epsilon_r' - j \left(\epsilon_{rd}'' + \frac{\sigma - \sigma_0}{\epsilon_0 \omega} \right) \quad , \quad (2.2)$$

where ϵ_r' and ϵ_r'' are the real and imaginary parts of ϵ_r , σ ac conductivity, σ_0 dc conductivity, ω angular frequency ($\omega = 2\pi f$, f is frequency), and $j = \sqrt{-1}$ [32]. The real part of the complex permittivity captures how energy from an external electric field is stored in the material and the imaginary part captures how energy is dissipated. The imaginary part (ϵ_r'' , loss tangent) of the complex permittivity also comprises a measure of dielectric loss (ϵ_{rd}'') and conductivity over frequency. The term dielectric relaxation (or dielectric dispersion) describes the phase delay between the application of an external electric field and orientation of an electric dipole moment.

Peter Debye recognized that this phase delay produces a permittivity that decreases from a static value (ϵ_l) at low frequencies to a smaller limiting value (ϵ_h) at higher frequencies [33]. He derived an expression that is compatible with the Kramers-Kronig relations in which the constants ϵ_l and ϵ_h are called relaxation parameters. This expression is of the following form:

$$\epsilon_r = \epsilon_h + \frac{\epsilon_l - \epsilon_h}{1 - (j\omega\tau)} \quad , \quad (2.3)$$

where the relaxation time ($\tau = (2\pi f_0)^{-1}$, f_0 the characteristic frequency) is the amount of time required for the material to revert to a random state after removal of the external electric field. The difference between these relaxation parameters ($\Delta\epsilon = \epsilon_l - \epsilon_h$) is called the relaxation intensity (or relaxation magnitude). Debye attributed the occurrence

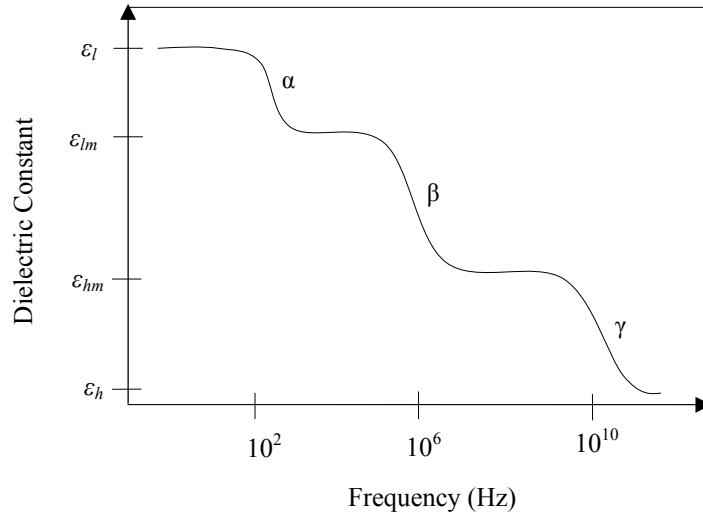


Figure 2.1: Dielectric constant decreasing with frequency.

of material relaxation to dipole polarization, in general. Later, Schwan recognized that the relaxation intensity in heterogeneous systems occurs in three distinct steps (see Figure 2.1 above), at low, radio-frequency and microwave frequencies [34]. He called these changes in intensity α , β , and γ dispersions (see Table 2.1) and related γ dispersion to the

Table 2.1: Dielectric mechanisms versus dispersion type.

Dielectric Mechanism	Dispersion Type	Resonance Frequency	Level	Applied E-Field
Electronic Polarization	-	Visible (PHz)	Sub-Atomic	- Displacement of nucleus or orbiting electrons
Atomic Polarization	-	Infrared (THz)	Atom	- Stretching of adjacent positive /negative ions
Orientation Polarization	γ	Microwave (GHz)	Molecules	- Orientation of permanent dipole moment
Interfacial Polarization	β	Radio Frequency (MHz)	Cells	- Storage of charges between cell & medium
Schwan Polarization	α	Low Frequency (Hz-kHz)	Suspension	- Counterion atmosphere around charged particle

Table 2.2: Formalism of dielectric relaxation.

Formalism	Complex permittivity	Real and imaginary parts
Debye (semicircular arc rule)	$\varepsilon_r = \varepsilon_h + \frac{\Delta\varepsilon}{1 + j\omega\tau}$	$\varepsilon_r' = \varepsilon_h + \frac{\Delta\varepsilon}{1 + (\omega\tau)^2}$ $\varepsilon_r'' = \frac{\Delta\varepsilon\omega\tau}{1 + (\omega\tau)^2}$
Cole-Cole (circular arc rule)	$\varepsilon_r = \varepsilon_h + \frac{\Delta\varepsilon}{1 + (j\omega\tau)^{1-\alpha}}$ $(0 < \alpha < 1)$	$\varepsilon_r' = \varepsilon_h + \frac{\Delta\varepsilon [1 + (\omega\tau)^{1-\alpha} \cos\{\pi(1-\alpha)/2\}]}{1 + 2(\omega\tau)^{1-\alpha} \cos\{\pi(1-\alpha)/2\} + (\omega\tau)^{2(1-\alpha)}}$ $\varepsilon_r'' = \frac{\Delta\varepsilon(\omega\tau)^{1-\alpha} \sin\{\pi(1-\alpha)/2\}}{1 + 2(\omega\tau)^{1-\alpha} \cos\{\pi(1-\alpha)/2\} + (\omega\tau)^{2(1-\alpha)}}$
Davidson-Cole (skewed arc rule)	$\varepsilon_r = \varepsilon_h + \frac{\Delta\varepsilon}{1 + (j\omega\tau)^\beta}$ $(0 < \beta < 1)$	$\varepsilon_r' = \varepsilon_h + \Delta\varepsilon \cos(\beta\theta) \cos^\beta(\theta)$ $\varepsilon_r'' = \Delta\varepsilon \sin(\beta\theta) \cos^\beta(\theta)$ $\theta = \tan^{-1}(\omega\tau)$
Havrilak-Negami	$\varepsilon_r = \varepsilon_h + \frac{\Delta\varepsilon}{[1 + (j\omega\tau)^{1-\alpha}]^\beta}$ $(0 < \alpha < 1, 0 < \beta < 1)$	$\varepsilon_r' = \varepsilon_h + r^{-\beta/2} \Delta\varepsilon \cos(\beta\theta)$ $\varepsilon_r'' = r^{-\beta/2} \Delta\varepsilon \sin(\beta\theta)$ $r = [1 + (\omega\tau)^{1-\alpha} \sin(\alpha\pi/2)]^2 + [(\omega\tau)^{1-\alpha} \cos(\alpha\pi/2)]^2$ $\theta = \tan^{-1} \left(\frac{(\omega\tau)^{1-\alpha} \cos(\alpha\pi/2)}{1 + (\omega\tau)^{1-\alpha} \sin(\alpha\pi/2)} \right)$

dielectric mechanism called orientation polarization. Schwan acknowledged that dispersion parameters were due to mechanisms more specific than dipole polarization. As a result, he related α -dispersion to a low-frequency dispersion mechanism caused by the counterion atmosphere surrounding the charged particle surface. Later, Maxwell and Wagner related β dispersion to a mechanism called interfacial polarization in biological materials, whereby the cell membranes interact with the medium in which they are suspended following application of an electric field [35-37].

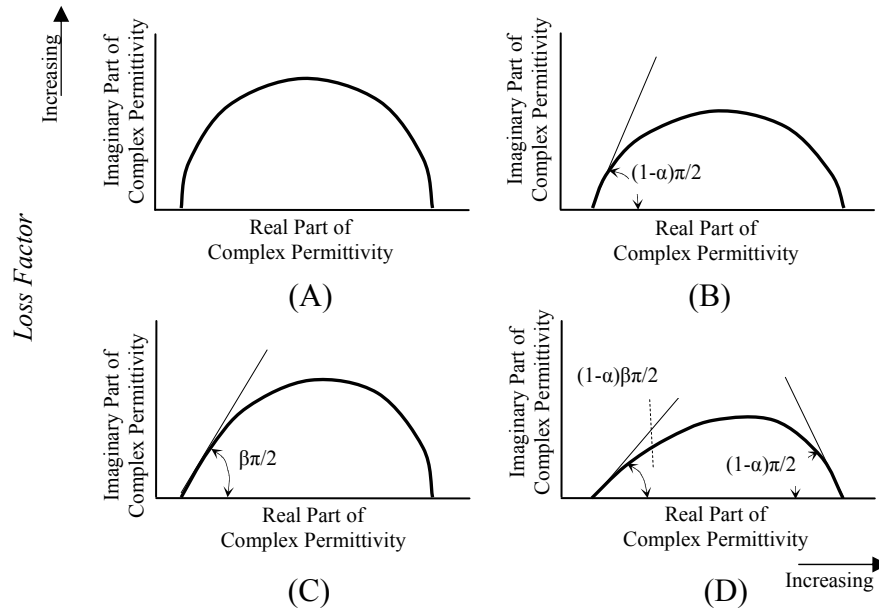


Figure 2.2: Complex plane plot for four relaxation types: (A) Debye, (B) Cole-Cole, (C) Davidson-Cole, and (D) Havriliak-Negami.

Kenneth and Robert Cole recognized that the Debye formalism in (2.3) does not support the possibility for multiple dispersion mechanisms and proposed a modification (see Table 2.2) which better approximates the permittivity under non-ideal conditions

[38]. The Cole brothers introduced a complex plane plot in which the loss factor (ϵ_r'') is plotted against the real part (ϵ_r') of the relative complex permittivity to produce a graph that permits verification of the presence of multiple relaxation frequencies. In this complex plane plot, a semicircle indicates the existence of only a single relaxation time (Debye type relaxation) (see Figure 2.2A-D). If this complex plane plot deviates from a semicircle then multiple relaxation times exist. Several authors provided formalisms to capture this deviation including, Davidson and Cole [39], Havrilač and Negami [40] and so forth, see Table 2.2 for the most heavily referenced equations.

2.2 Review of characterizing cell suspensions

The formalisms for dielectric relaxation provide a means to extract the dielectric properties of materials by recognizing various characteristic polarization mechanisms. The mechanisms relate to the physical structure of the medium. They have been applied to understanding the dispersion in cell suspensions. Cell suspensions are heterogeneous systems that have interfaces where materials of different electrical properties contact each other. Although the characteristic polarization for heterogeneous systems is interfacial polarization, which demonstrates β dispersion, dielectric relaxation mechanisms involving the intracellular structure exist for a cell suspension [41]. These mechanisms include atomic, electronic, and orientation polarization. Dielectric mechanisms at the atomic and sub-atomic levels are a function of the physical structure of the cell as opposed to a system-level interaction between the cell membrane and suspension. Asami

noted that these microscopic mechanisms may be ignored because they are not dominant in heterogeneous mixtures consisting of cells.

In this research, the heterogeneous system consists of B16-F10 tumor cells (see Chapter 7, section 2 for more detail description) suspended in McCoy's 5A medium.

B16-F10 mice tumor cells are generally round in shape with a single cell membrane and

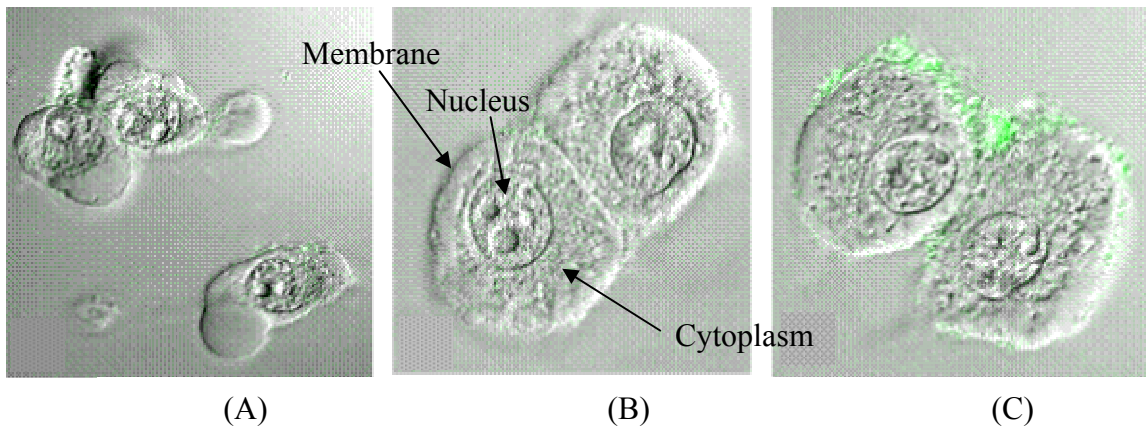


Figure 2.3: Confocal microscopy of B16-F10 tumor cells incubated with the following fluorescein: (A) free fluorescein, (B) fluorescein encapsulated unilamellar liposomes, and (C) hyaluronan-liposomes. Courtesy of Rimona Margalit, Department of Biochemistry, Tel Aviv University, Israel.

cytoplasm (see Figure 2.4A-C). These cells measure between 6.4-12.8 μm in diameter with a cytoplasm that is 1/3 the diameter of the membrane. Based on the microscopic structure of the B16-F10 tumor cells, it is reasonable to anticipate molecular, atomic, and sub-atomic dielectric mechanisms. However, if these mechanisms are ignored the cell suspension may be considered as a composite material in which a single shell model that consists of cytoplasm and a cell membrane is appropriate (see Figure 2.4A) [42, 43]. Irimajiri, Hanai and Inouye demonstrated that every shelled particle interface in the

suspension gives rise to a single Debye-type dispersion [44]. As such, a suspended single shell model results in two relaxation processes that correspond to the cytoplasm-cell membrane and cell membrane-suspending medium interfaces (see Figure 2.4B). The following equation for dielectric permittivity is explicitly represented by the following cell model:

$$\epsilon_r = \epsilon_h + \frac{\epsilon_m - \epsilon_h}{1 - (j\omega\tau_Q)} + \frac{\epsilon_l - \epsilon_m}{1 - (j\omega\tau_P)}, \quad (2.4)$$

where τ_Q and τ_P ($f_{Q,P} = 1/2\pi\tau_{Q,P}$) are the relaxation times. However, Pauly and Schwan showed that for biological cells these two dispersions degenerate to a single dispersion process [45]. As a result, the Cole-Cole model of Table 2.2 is appropriate for describing dielectric dispersion for a cell suspension.

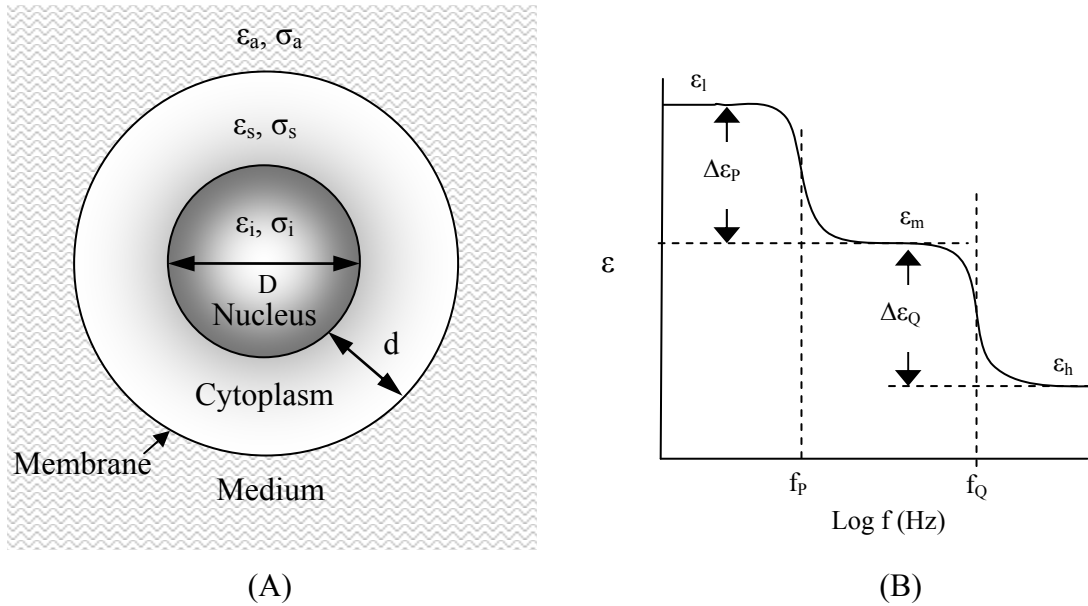


Figure 2.4: (A) Single-shell dielectric model for biological particle and (B) schematic diagram of frequency dependence.

Researchers have proposed several other theoretical models to describe the dielectric behavior of cell suspensions [46]. The Maxwell-Wagner formula is the best-known formula for describing the dielectric behavior of mixtures because it provides a means to extract properties of individual cells from measurement of the cell suspension [47]. Maxwell proposed the 1st derivation of a mixture formula for spherical particles and later Wagner extended it, which became known as the Maxwell-Wagner mixture formula. The Maxwell-Wagner mixture formula is defined as:

$$\epsilon_{mix} = \epsilon_a \frac{(2\epsilon_a + \epsilon_c) - 2p(\epsilon_a - \epsilon_c)}{(2\epsilon_a + \epsilon_c) + p(\epsilon_a - \epsilon_c)}, \quad (2.5)$$

where permittivity associated with the heterogeneous cell suspension (ϵ_{mix}) is a function of the permittivity of the medium (ϵ_a) and cell (ϵ_c) as well as a function of the volume fraction (p) that the cells occupy in the medium [48]. Although, this dissertation research is not concerned with the electrical properties of the individual cells, the Maxwell-Wagner formalism is important because it demonstrates that the permittivity of a mixture changes with the volume fraction of cells in the suspension [49]. As a result, cell quantification may be related through the volume fraction of cells in the mixtures by measurement of the permittivity.

2.3 Review of time-domain dielectric spectroscopy

Automated techniques for measuring the dielectric properties of materials may be divided into time- and frequency-domain techniques. Frequency-domain techniques are preferred to time-domain techniques because they present a simple closed-form solution

for measuring dielectric properties. Bonet, Ginzburg, and others were the first to apply time-domain dielectric spectroscopy to the measurement of cell suspensions [50]. These authors noted that a time-domain dielectric spectroscopic method is advantageous to a frequency-domain method because a single measurement is sufficient to give information over a wide frequency spectrum. To accomplish this, a fast-edge signal is launched down a low-loss transmission line that contains a dielectric medium. The reflected voltage that returns from the sample is used along with the transmitted signal to compute the permittivity, following application of a Fourier transform.

Historically, time-domain techniques have been challenged with the complications of relating measurement with the actual dielectric parameters, due to the need to apply iterative computational techniques and Fourier transforms for analysis on a large number of points [51, 52]. However, it has been shown that time-domain dielectric spectroscopy provides new information on the structural and dynamic properties of heterogeneous systems, which may be inaccessible using frequency-domain techniques [53]. This new information is made possible by the additional spectral content that is associated with the rise time of the applied signal [54]. Deng, Schoenbach and others showed the importance of pulse-duration for this applied signal by recognizing an increasing probability for the electric field to interact with intracellular substructures when the electric pulse-duration is reduced to sub-microsecond range [55].

These pulses may be described by any non-damped waveforms including: Gaussian, Rayleigh, Laplacian, and modified Hermitian monocycle [56]. Because of its

smooth and continuous roll-off, the Gaussian waveforms have gained the most attention for use in time-domain systems [57]. An equation by Karl F. Gauss describes these zero-mean waveforms, represented by:

$$G(x) = \frac{1}{\sqrt{2\pi\sigma^2}} e^{-\frac{x^2}{2\sigma^2}}, \quad (2.6)$$

where σ is standard deviation and x is the random variate. In this expression, the standard deviation reduces the amplitude as well as rounds the intensity of the peak, which decreases spectrum flatness. Consequently, the following modification to (2.6) above is often preferred:

$$y_{g1}(t) = K_1 e^{-\frac{t^2}{\tau_f^2}}, \quad (2.7)$$

where K_1 is a constant amplitude, and τ_f is the time-scaling factor which represents the temporal width of the pulse. The non-sinusoidal nature of the waveform above provides an opportunity to construct alternative waveforms through the application of filtering

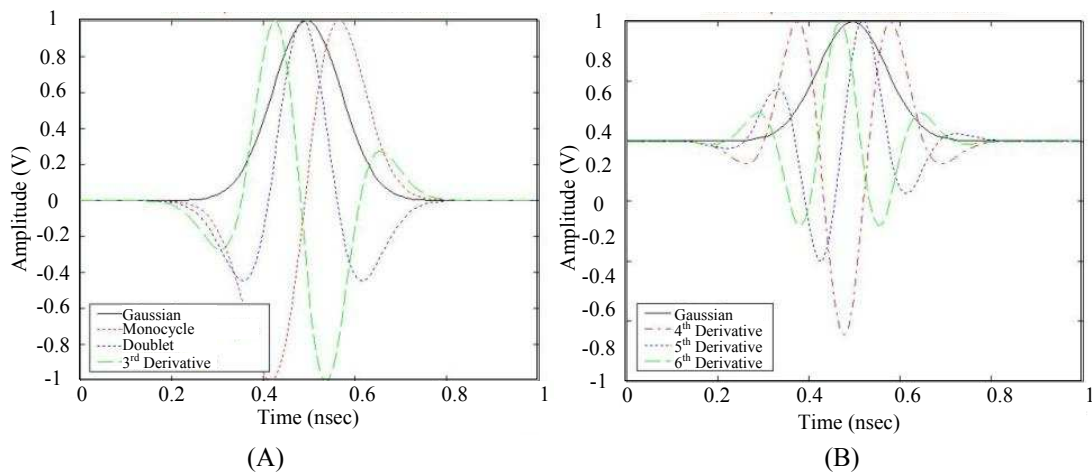


Figure 2.5: Diagram of a Gaussian pulse and its (A) 1st – 3rd and (B) 4th – 6th derivatives. Note: The number of zero crossings increases with each derivative.

techniques. Filtering acts in a manner of taking the derivative of (2.7). The 1st and 2nd Gaussian derivatives (see Figure 2.5 above), also known as a monocycle and doublet, have found common use in time-domain systems and are expressed in the equations below:

$$y_{g2}(t) = K_2 \frac{-2t}{\tau^2} e^{-\left(\frac{t}{\tau}\right)^2}, \text{ and} \quad (2.8)$$

$$y_{g3}(t) = K_3 \frac{-2t}{\tau} \left(1 - \frac{2t^2}{\tau^2}\right) e^{-\frac{t^2}{\tau^2}}, \quad (2.9)$$

where t is time, and K_2 and K_3 are constants. The spectral content associated with these pulses is non-symmetric, so that the peak frequency increases with successive pulse derivatives (see Figure 2.6). Approximately 90% of the spectral energy in a Gaussian based time-domain system lies between its 3 dB band edges about this peak frequency. A

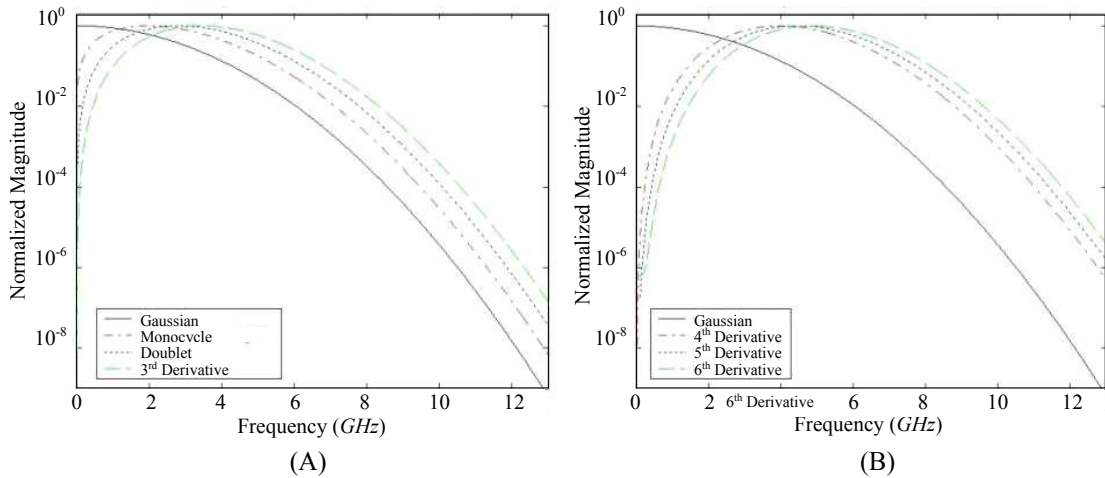


Figure 2.6: Diagram of a Gaussian pulse and the spectrum associated with its (A) 1st – 3rd and (B) 4th – 6th derivatives.

3-dimensional view of the spectrum for six Gaussian derivatives (Figure 2.7) confirms a shift in center frequency with increasing derivative as well as changes in the overall

shape of the spectrum, accompanied by a decrease in magnitude. Consequently, exploration of the varied levels of dielectric mechanisms (atomic and sub-atomic) may be facilitated by modifying the shape and duration of the Gaussian pulse, in TDDS.

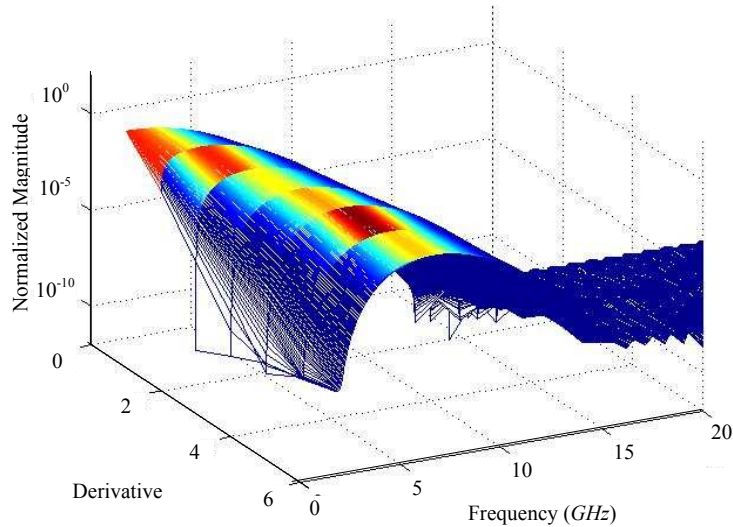


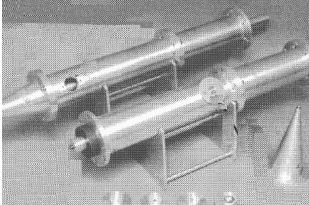




Figure 2.7: 3-dimensional view of spectrum for derivative 1-6.

2.4 Review of dielectric measurement methods

Dielectric spectroscopy may be accomplished with several fixture types. The fixture type dictates the analysis required for permittivity extraction, thus are described as methods. Coaxial probe methods are most heavily utilized in biomaterials measurement because they are nondestructive, convenient, and easy to use [58, 59]. However, these methods provide only a measure for electric permittivity and assume a value of free space for the magnetic permeability. Although this approximation may be suitable for non-magnetic materials, measurement of magnetic permeability is gaining importance in

Table 2.3: Comparison of methods for dielectric spectroscopy. Note: The probe kits shown are developed by Agilent Technologies and Farr Research.

Method	Parameter	Frequency (typical)	Comments
<p>Parallel Plate</p> 	ϵ_r only	< 30 MHz	<p>Sample: flat, disk-shaped sample</p> <p>Ideal use: thin sheets, films</p> <p>Benefits: inexpensive, simple analysis</p> <p>Limits: low frequency</p>
<p>Coaxial Probe</p> 	ϵ_r only	200 MHz to 20 GHz	<p>Sample: solids must have flat surface</p> <p>Ideal use: liquids, semi-solids</p> <p>Benefits: convenient, easy use, nondestructive</p> <p>Limits: low-loss resolution</p>
<p>Transmission Line*</p> 	ϵ_r and u_r	500 MHz to 20 GHz	<p>Sample: brick, toroid shaped sample</p> <p>Ideal use: solids, semi-solids</p> <p>Benefits: simple fixture with solids</p> <p>Limits: liquid/gas containment, destructive, low-loss resolution</p>
<p>Cavity</p> 	ϵ_r and u_r	500 MHz to 110 GHz	<p>Sample: brick, toroid shaped sample</p> <p>Ideal use: solids, semisolids</p> <p>Benefits: very accurate, nondestructive, sensitive to low-loss tangents</p> <p>Limits: complex to analyze, precisely known sample shape</p>
<p>Free Space</p> 	ϵ_r and u_r	2 GHz to 110 GHz	<p>Sample: flat parallel faced sample</p> <p>Ideal use: solids, semisolids</p> <p>Benefits: no fixture required, nondestructive</p> <p>Limits: large sample required (must be 3x beam width)</p>

biomaterials research, with the introduction of nanoparticles. Safarik and Safarikova summarized methodologies for employing small magnetic particles towards the isolation and purification of target proteins and peptides [60]. Sillerud, Popa and Coutias conjugated magnetic nanoparticles with antibodies which target lung tumors [61]. Although this dissertation research does not apply nanoparticles or magnetic fields in the characterization and quantification of cells, the capability to measure both permittivity and permeability is considered important in the selection of methods for dielectric spectroscopy. Of the methods available for dielectric spectroscopy, transmission line methods provide a means to measure both electric permittivity and magnetic permeability of a small sample (see Table 2.3). However, transmission line methods have traditionally required a sample holder, for containing liquids, which increases fixture cost and complexity [62]. Furthermore, the sample lengths associated with transmission line fixtures have been several inches, i.e. Folgero demonstrated a transmission line method using a 7.5-inch sample holder with a PTFE Teflon interface [63].

2.5 Summary

Quantifying and characterizing isolated tumor cells in dissected tissue is important in surgical pathology and cytology. However, the tools are expensive. Dielectric spectroscopy offers the possibility to reduce cost, but the ability to relate permittivity to cell count, as predicted by the Maxwell-Wagner mixture equations, must be assessed. Even so, quantifying cell suspensions using a transmission line method requires improvements in fixture design, algorithms, and pulse shaping.

Chapter 3

Novel Circuits for Ultra-Wideband/RF-Microwave Pulse Generation

Presented in this chapter are novel circuits for UWB pulse generation and formation. First, this chapter provides background and theory for the application of Gaussian waveforms to generator design. Next, step recovery diode theory of operation and simulation model are presented. The following section presents application of the ADS simulation model and step recovery diode to the development of a novel pulse shaping circuit that contains a coupled-line coupler and Schottky detector differentiator. This chapter concludes with a presentation of methods and circuits for developing novel UWB pulse generators with a tunable duration, followed by a design.

3.1 Background

The Federal Communication Commission (FCC) defines ultra-wideband (UWB) as an intentional radiator with an instantaneous 10 dB-fractional and total bandwidth of at least 0.2 and 500 MHz, respectively [64]. This bandwidth is achieved primarily by radiating ultra-short pulses that are derived from a basic Gaussian shape, which typically includes the monocycle, doublet, and 3rd derivative types (see Figure 3.1). The bandwidth for UWB systems is not symmetric (see Chapter 2, Figure 2.7). As a result, it

requires definition of the frequencies at the upper (f_H) and lower (f_L) band edges, which are 10 *dB* below the highest radiated emission, as described in the equation

$$BW_{fractional} = \frac{2 \cdot (f_H - f_L)}{(f_H + f_L)}. \quad (3.1)$$

UWB is not to be confused with narrowband, wideband, ultra-broadband, or super-wideband, hereafter referred to collectively as conventional systems. The primary difference between UWB and conventional systems is in the waveform shape. Sinusoidal waveforms are used in conventional systems whereas non-sinusoidal waveforms are used

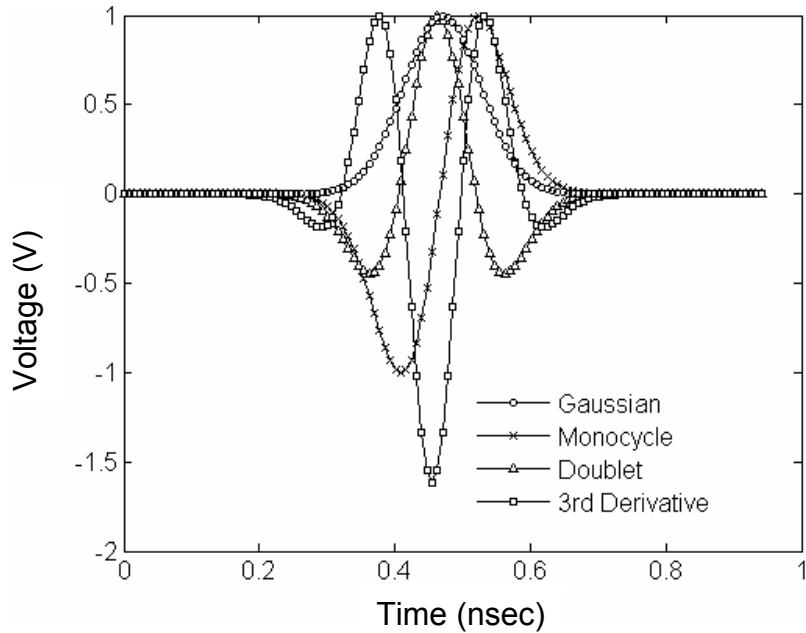


Figure 3.1: Gaussian derived waveforms with a 250 *psec* duration.

in UWB systems. The sinusoidal waveforms of a conventional system maintain their shape over time and space but an UWB waveform may produce a change upon transmission, reflection and reception. “From the conventional perspective, these changes would be looked upon as distortions –distortions, which would require additional

complexity in the receiver if it were to collect all of the available energy; but ... these distortions may be valuable for target identification [65].” Implicitly this means that tools commonly used in conventional waveform synthesis may be unsuitable for UWB waveforms, which originate from Gaussian and Gaussian derived waveforms.

Besides bandwidth, UWB technology offers the possibility of improvement over conventional systems in the areas of target response, clutter suppression, propagation, and target identification [66]. Consequently, UWB radio-frequency (RF)/microwave techniques have been applied to impulse radio, cardiovascular and respiratory monitoring, and other sensing applications [67]. In this research, UWB is of interest for applications in time-domain dielectric spectroscopy (TDDS) [68]. Solid-state UWB pulse generators provide the stimulus, which makes TDDS possible. Typically, step recovery diodes (SRDs) are used in these generators to achieve the fast switching needed for classifying the technology as UWB. Since these diodes are also applied in this research, the SRD principles of operation and modeling are presented below.

3.2 Step recovery diode

The step recovery diode (SRD) is a fundamental building block in low-cost solid-state UWB pulse generator design. Basic operational principles are presented in this section to aid in presentations of the ADS simulation model parameter for the diode and UWB pulse generator circuits in this dissertation. These principles are not covered in exhaustive detail. For more details, please refer to Sedra and Smiths’ text, “Microelectronic Circuits” [69].

3.2.1 Basic principles of SRD operation

A step recovery diode (SRD) is a p-n junction diode (see Figure 3.2A) that stores electric charge during forward conduction (or forward conduction state) and rapidly removes these charges during reverse conduction (or reverse cut-off state). The time

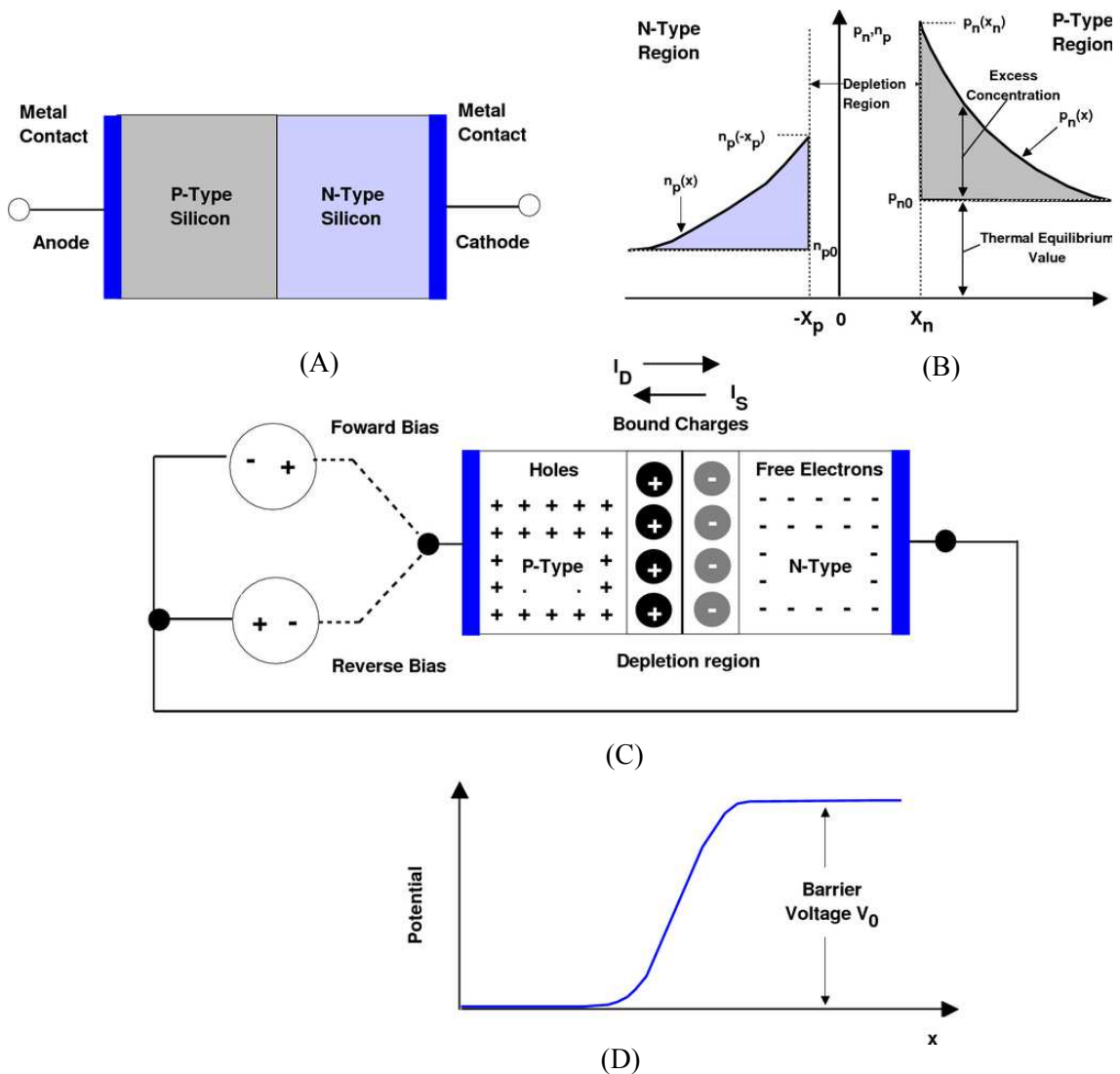


Figure 3.2: Parts of SRD operation, including (A) p-n junction diode diagram, (B) doping profile, (C) reverse forward bias representation, and (D) potential at the diode junction.

associated with the transition between forward and reverse conduction states can be less than 60 picoseconds for commercially available SRDs. Step recovery diodes are also called snap-off, charge-storage, and memory varactor diodes. Boff, Moll and Shen noted that this fast transitioning edge occurs in a p-n junction diode (see Figure 3.2B) that is doped with linearly or exponentially graded impurity [70]. If excited with a field in the reverse direction (or reverse biased), so that the positive and negative terminals of the supply connect to the negatively-charged n-type and positively-charged p-type diode materials (see Figure 3.2C), electrons and holes are drawn away from the material which widens the carrier depletion region. As the reverse bias amplitude is increased, this depletion region widens even more, which increases the junction capacitance as well as the charge stored in the depletion region. If the voltage is continually increased, the junction breaks down, after which current begins to flow through the diode (see Figure 3.2D).

When the junction is excited with a field in forward direction (forward biased) so that the positive and negative terminals of the supply connect to the p-type and n-type materials of the diode, electrons and holes are repelled in the material. This has an effect of decreasing the depletion region width until the diode conducts current (see Figure 3.3). Unlike the reverse biased condition, the amount of voltage amplitude required for full conduction in forward bias is much smaller. If a charge exists in the depletion region, it is swept from the diode when placed in forward bias. As a result, the step recovery diode operates similarly to a simple p-n junction diode, with a distinguishing feature being the graded junction, which gives rise to a fast switching action.

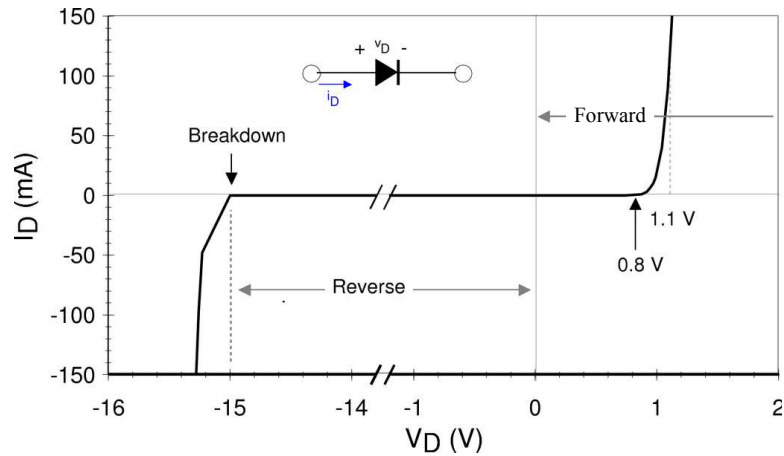


Figure 3.3: Simulated I-V characteristics of a step recovery diode.

3.2.2 SRD device modeling

Since the SRD is simply a p-n junction diode with a fast switching time, the parameters of an ADS basic p-n junction diode model was modified to obtain an SRD model. This diode model consisted of the default parameters in Table 3.1 below. SPICE model parameters for a SRD in the MMD-840 series, obtained from Aeroflex Metelics Corporation, were used as initial values in converting the basic p-n junction diode model. Primarily, four parameters distinguished a p-n junction diode model from a SRD model, which includes the mean transit time (τ_T), emission coefficient (N), zero bias junction capacitance (Cj0), and grading coefficient (M). The mean transit time is also called the switching time of the diode. It describes the time required for building up and removing charge from the depletion region. The emission coefficient is also called the diode ideality factor. It indicates the electromagnetic power output per unit time and is affected by the fabrication process and materials used. This value ranges from 1 to 2 where 1

represents an ideal p-n junction diode. The zero bias junction capacitance is used to describe the linear capacitance that exists between the p-type and n-type material, before the application of a bias. This capacitance affects the charging and discharging characteristics of the diode. The grading coefficient describes the slope associated with the impurities introduced at the diode junction. A value of 1/3 indicates a linearly graded junction where as 1/2 indicates an abrupt junction.

Table 3.1: A p-n junction diode model and MMD-841 parameters.

Name	Description	Unit	P-N Junction Diode Model Default	MMD-840 SPICE Model Parameters	MMD-841 Device Model Parameters
Is	Saturation current (with N, determines diode dc characteristics)	A	10^{-14}	50×10^{-14}	82×10^{-13}
Rs	Ohmic resistance	Ohm	0.0	0.22	0.22
N	Emission coefficient (with Is, determines diode dc characteristics)		1.0	1.3	1.8
τ_T	Transit-time	nsec	0.0	10	10
Cj0	Zero-bias junction capacitance	pF	0.0	0.545	0.545
Cj6	Sidewall zero-bias capacitance	pF	$.9 \times 10^{-12}$	0.3	0.4
Vj	Junction potential	V	1.0	0.5	0.5
M	Grading coefficient	-	0.5	0.235	0.235
XTI	Saturation-current temperature exponent (with Eg, helps define the dependence of Is on temperature)	-	3.0	3.0	3.0
EG	Energy gap (with Xti, helps define the dependence of Is on temperature)	eV	1.11	1.12	1.12
BV	Reverse break down voltage	V	∞	15	15
IBV	Current at reverse break down voltage	A	.001	10^{-6}	10^{-6}

The MMD-840 spice model parameters were tuned for fit with an ADS MMD-841 diode by comparing simulated and measured data. Measurement data was obtained from two simple circuits fabricated onto an FR4 substrate. These circuits consisted of SRD in series and shunt configurations with respect to a $50\ \Omega$ load (see Figure 3.4). An arbitrary waveform generator was used to apply a $10\ V$, $14\ MHz$ sinusoidal input via SMA edge mount connectors on the circuit. The circuits produced output waveforms which were morphologically similar those in the simulation. However, the measured waveform in the series configuration was slightly degraded by reflections due to parasitics associated with the SMA interconnects and inductive ground. The agreement between simulated and measurement data was deemed acceptable for a design model.

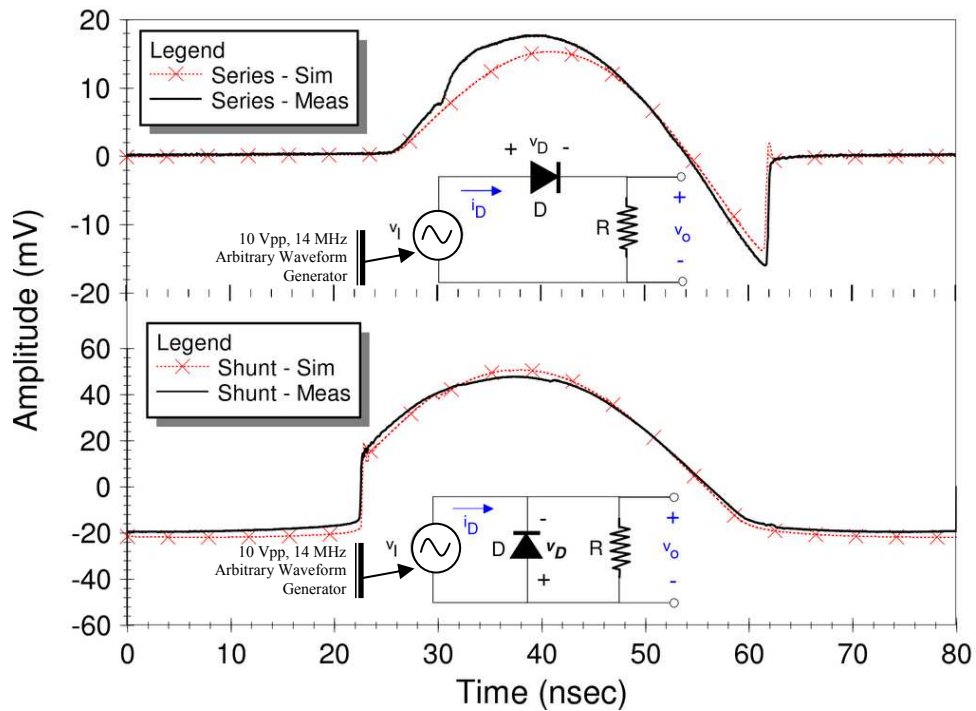


Figure 3.4: Simulated and measured SRD output for a simple series and shunt configuration.

The negative voltage in the shunt configuration showed a voltage rail that was approximately flat. As a result, a double-shunt configuration was explored for generating a square wave response. In a double-shunt configuration, two diodes acts on the falling and rising edges of the source, respectively (see Figure 3.5). In an ADS simulation, the circuit produced a waveform that can be approximated to a square wave. The simple

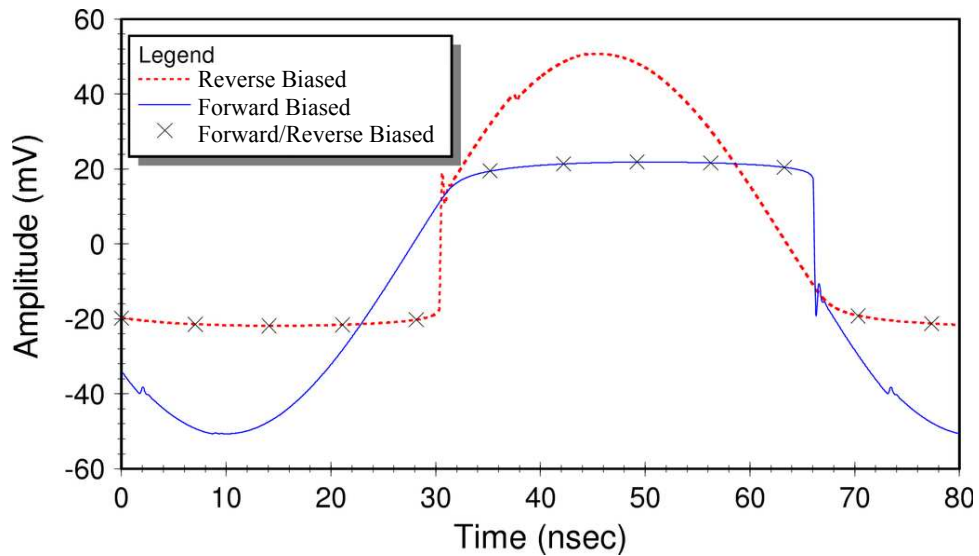


Figure 3.5: Simulation of forward and reverse biased diodes in a shunt configuration.

ADS circuit configuration was fabricated onto an FR4 board for verification and measurement. Good agreement between simulated and measured waveforms was observed (see Figure 3.6). As a result, the SRD modeled in ADS demonstrated good agreement between measured and simulated data for three simple circuit topologies. This model and diode were applied to all circuits requiring an SRD in this dissertation research.

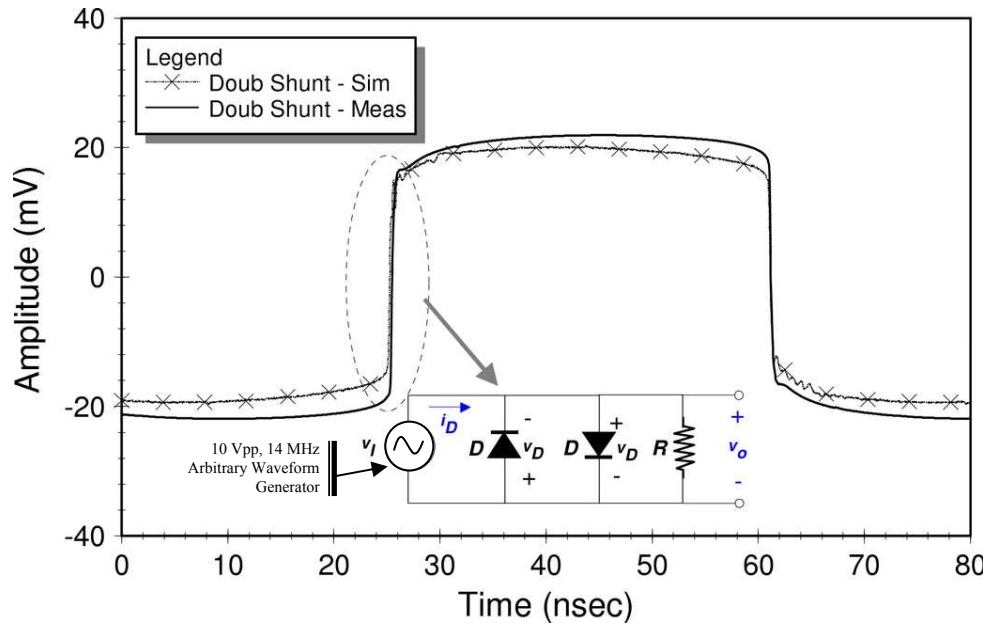


Figure 3.6: Comparison of simulated and measured data for simple double-shunt circuits.

3.3 Novel circuits for UWB pulse shaping

Ultra-wideband waveform pulse formation (or pulse shaping) is critical to the performance of a UWB system. Pulse formation is used in communication and radar systems to optimize the spectrum for meeting the U.S. Federal Communication Commission's (FCC) emission requirements [71]. UWB pulse shaping has been implemented with GaAs MESFETs, non-linear transmission lines, short-circuit stub transmission lines and resistive-reactive circuits [72-74]. In these applications, the waveform response to circuit reactance is fundamental to pulse formation. As such, the reactive elements form a simple resistor-capacitor (RC) or resistor-inductor (RL)

network. In an RC network, waveform differentiation occurs in a process of charging and discharging the circuit capacitance [75]. The capacitor builds up charge in accordance with the RC time constant (τ_{RC} , where $\tau_{RC} = R \cdot C$), which defines the time required for a signal to rise to 63.2% of its full value. When used in conjunction with a 50 ohm load, the RC time constant requires less than a 20 pF capacitance (C) for shaping sub-nanosecond pulses. In this research, a coupled-line coupler and Schottky detector diode are considered for UWB signal differentiation because the mutual and junction capacitances are small enough to accommodate shaping of sub-nanosecond pulses within an RC configuration.

3.3.1 Theory for UWB coupled-line coupler differentiator

The basis for UWB coupled-line differentiation originates from a combination of theories for analyzing crosstalk in multi-conductor transmission lines and transients in resistor-capacitor (RC) networks [76, 77]. Typically, crosstalk is treated as unwanted distortion or switching noise that result from lossy multiconductor transmission lines. It is often discouraged in time-domain applications by increasing the distance between conductors, adding capacitance (decoupling capacitance) at the end of transmission lines, and limiting the number and length of parallel traces. However, transients are desirable in UWB coupled-line differentiation.

A microstrip parallel coupled-line (or edge coupled) structure may be applied as an UWB differentiator by using the mutual capacitance that exists between the two conductors in an RC network. The amount of capacitance is a function of the distance

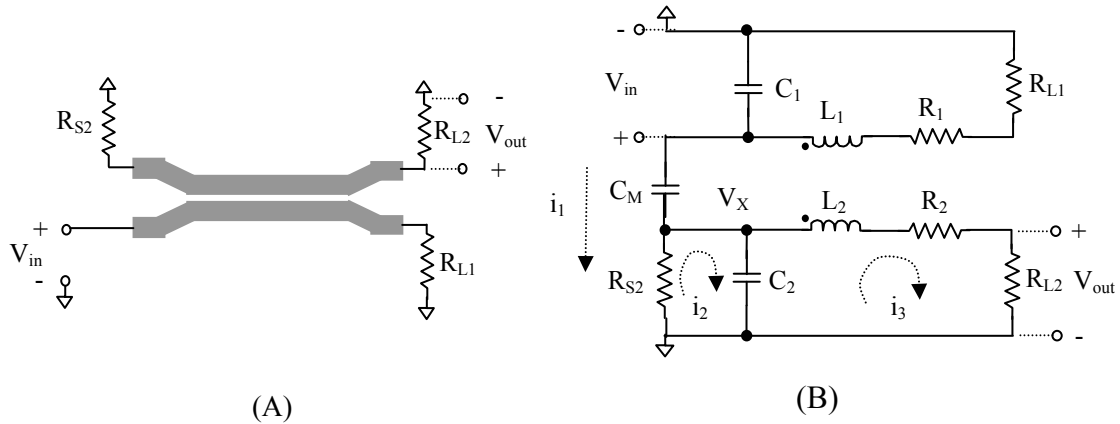


Figure 3.7: A single section microstrip coupled-line coupler (A) schematic and (B) lumped element equivalent circuit of a lossy transmission line coupler.

between the conductors, which can be adjusted to be small enough to support sub-nanosecond transients. Application of Kirchoff's current law (KCL) to a lumped element equivalent circuit of a coupled-line coupler, demonstrates its potential as a differentiator (see Figure 3.7). This potential is seen by relating the output voltage (V_{out}) to the input voltage (V_{in}). This relationship can be determined by applying KCL to the output in loop 3 (i_3), which produces the following relationship:

$$V_{out} = i_3 \cdot R_{L2} , \quad (3.2)$$

where R_{L2} is the resistive load over which the output is measured. The above equation

can be expanded by relating i_3 to i_2 of loop 2 in an evaluation of the current through the C_2 capacitor. This relationship is represented by the following equation:

$$i_3 = i_2 - i_{C_2} = i_2 - C_2 \cdot \frac{dV_{C_2}}{dt} , \quad (3.3)$$

where i_{C_2} is the current through capacitor C_2 and V_{C_2} is the voltage across that capacitor. Similarly, i_2 relates to i_1 of loop 1 by evaluating the current through resistor R_{S2} and capacitor C_M , which yields the following relations:

$$i_2 = i_1 - i_{R_{S2}} = i_1 - \frac{V_X}{R_{S2}} \quad \text{and} \quad (3.4)$$

$$i_1 = C_M \cdot \frac{dV_{C_M}}{dt} , \quad (3.5)$$

where $i_{R_{S2}}$, V_{C_M} , and V_X are the current through the R_{S2} resistor, voltage across the C_M capacitor and nodal voltage, respectively. Application of (3.2)-(3.4) to (3.1) gives rise to a relationship for the output voltage that includes the coupling capacitance, which takes the following form:

$$V_{out} = \left(C_M \cdot \frac{dV_{C_M}}{dt} - \frac{V_X}{R_{S2}} - C_2 \cdot \frac{dV_{C_2}}{dt} \right) \cdot R_{L2} . \quad (3.6)$$

The nodal voltage V_X and capacitor voltage V_{C_2} may be related to the input voltage by recognizing that $V_{C_2} = V_X$ and $V_X = V_{in} - V_{C_M}$, so that (3.5) may be represented in terms of the input voltage, as shown by the following expression:

$$V_{out} = \left[C_M \cdot \frac{dV_{C_M}}{dt} - \frac{V_{in} - V_{C_M}}{R_{S2}} - C_2 \cdot \frac{d(V_{in} - V_{C_M})}{dt} \right] \cdot R_{L2} . \quad (3.7)$$

If proportionality is assumed for the input and coupled voltages so that $V_{C_M} = K \cdot V_{in}$, where K is a constant, then the output may be related primarily in terms of the voltage across the mutual capacitance. As a result, equation (3.6) takes on the form:

$$V_{out} = \left\{ [C_M - C_2 \cdot (K - 1)] \cdot \frac{dV_{in}}{dt} - \underbrace{\frac{V_{in} (K - 1)}{R_{S2}}}_{\text{Not differentiated}} \right\} \cdot R_{L2} . \quad (3.8)$$

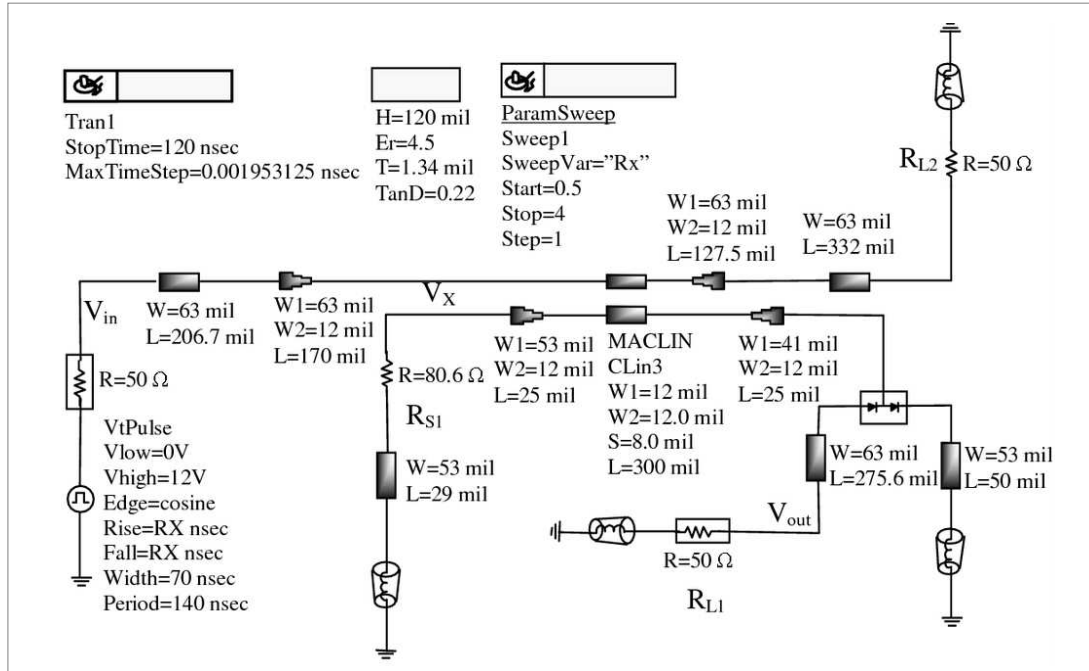
Equation (3.7) demonstrates that the output voltage is formed by differentiating the voltage at the input of the coupled-line coupler. In addition, this equation shows a second term that is not differentiated, which conditionally dominates expression. This condition is illuminated in the consideration that parasitic capacitance in the line is very small, the term $C_M - C_2 \cdot (K - 1)$ of (3.7) is less than the $(K - 1) / R_{S2}$ term. As a result, the derivative term only dominates under the condition that the rate of change in the input signal follows the relationship:

$$\frac{dV_{in}}{dt} \gg V_{in} , \quad (3.9)$$

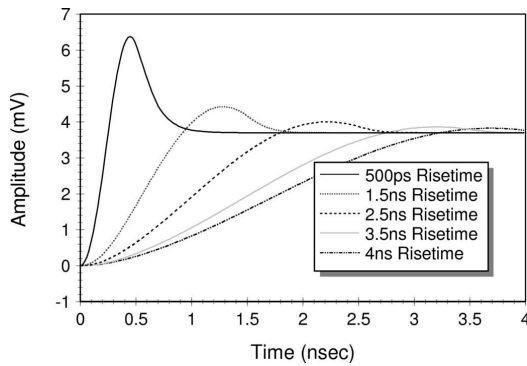
which is true for signals with a very sharp rise time. Thus, the coupled-line coupler acts as a differentiator for UWB signals.

The above conditional derivative was verified by capturing a coupled-line circuit in Agilent ADS 2004A and performing a transient/convolution simulation (see Figure 3.8A). The input port to this line was excited with a square wave with a variable rise time (see Figure 3.8B). The coupled-line coupler responded to this stimulus by

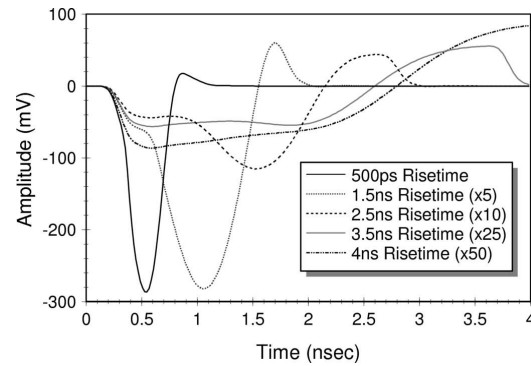
producing positive and negative amplitude Gaussian pulses from the falling and rising edges of the square wave. The positive amplitude Gaussian was filtered using a Schottky



(A)



(B)



(C)

Figure 3.8: A single section microstrip coupled-line coupler (A) ADS schematic block, (B) variable rise time input at V_{in} , and (C) output waveform at V_{out} .

detector diode and the negative pulse was measured across the load at the circuit output. After simulating over a 140-144 *nsec* time period, the circuit output showed waveform differentiation for fast rise square waves. As the rise time of the input signal increased, the circuit response became less like a derivative and more like a square wave (see Figure 3.8C). Therefore, the simulation provided confirmation of the differentiated waveform in (3.8) for fast rise signals as well as the dominance of the non-differentiated part of the equation as rise time increased. As a result, we conclude that the coupled-line coupler differentiation is rooted in the construction of an RC network using the junction and parasitic capacitances in the coupled-line structure.

3.3.2 Theory for UWB Schottky detector differentiator

Since capacitance contributes to waveform differentiation in coupled-line differentiation, we also consider the use of a Schottky detector diode for differentiation. A Schottky diode is advantageous for its low forward voltage (typically 0.3 volts) and very fast switching action. These diodes are used in switch mode power converters, discharge protection circuits and other applications requiring fast picosecond switching. Moreover, Schottky diodes are used in the development of UWB circuits [78-80]. The fast switching time in the Schottky diode is made possible by the metal-semiconductor junction that comprises its physical structure, which promotes fast injection of majority carriers into the conduction band. Schottky diodes are the fundamental component of detector diodes, which are diodes that recover baseband information from a modulated wave. As a result, the diode is applied in this work as a Schottky detector differentiator

as well as an envelope detector for smoothing high frequency oscillations in the UWB waveforms.

A Schottky detector differentiator is based on configuring an RC network from the capacitance that exists at the diode junction. In classical device physics, a steady state diode is viewed as a short or open circuit, as a function of whether it is in forward or reverse bias [81]. In reality, a junction capacitance (depletion capacitance) is formed as the voltage across the p-n junction changes to the reverse direction and a diffusion capacitance is formed in the forward direction [82]. The depletion capacitance (C_j) relates to charge storage in the diode and is expressed as

$$C_j = \frac{C_{j0}}{(1 + V_R/V_0)^m} = \frac{A\sqrt{(\epsilon_S q/2)} \cdot [N_A N_D / (N_A + N_D)] \cdot (1/V_0)}{(1 + V_R/V_0)^m}, \quad (3.10)$$

where C_{j0} is the zero biased junction capacitance, V_R the reverse voltage, V_0 the depletion-layer voltage, m the grading coefficient, ϵ_S the materials electrical permittivity, q the stored charge, N_A the doping concentration of the p side of the junction, and N_D the concentration of the n-side junction [83]. The diffusion capacitance (C_D) relates to the switching action of the diode. This capacitance is expressed as follows:

$$C_D = \left(\frac{\tau_T}{V_T} \right) \cdot I, \quad (3.11)$$

where τ_T is the mean transit time (or switching time) of the diode, V_T the thermal voltage of the diode, and I the diode current at the bias point. In the circuit of Figure 3.9 we use two diodes, one for RC differentiation ($D1$) and the other for filtering ($D2$).

The differentiator is compatible with UWB waveforms because the diffusion capacitance that exists at the p-n junction is very small when placed in an RC configuration. A lumped element equivalent circuit of a series diode demonstrates that differentiation occurs as the input (V_{in}) energized the Schottky diode ($D1$ and $D2$) and appears across the (R_{L1}) load (see Figure 3.9B). Application of KCL to this equivalent

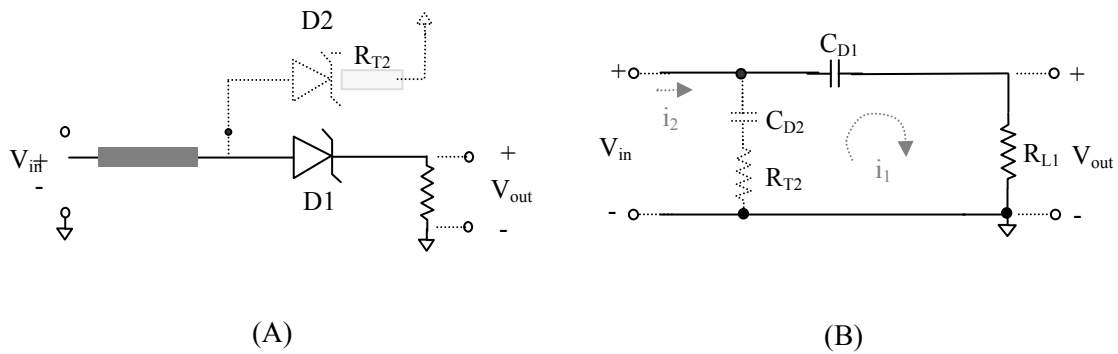


Figure 3.9: A Schottky detector diode differentiator (A) schematic and (B) lumped element equivalent circuit.

circuit provides a means to relate the output (V_{out}) to this input (V_{in}). An analysis of the output in loop 1 (i_1) gives rise to the following relationship:

$$V_{out} = i_1 \cdot R_{L1} = R_{L1} \cdot C_{D1} \cdot \frac{dV_{C_{D1}}}{dt} , \quad (3.12)$$

where R_{L1} is the load, C_{D1} the junction capacitance for diode $D1$, and $V_{C_{D1}}$ the voltage across that diode. This relationship may be expressed in terms of the input by considering that $V_{C_{D1}} = V_{in} - V_{out}$, which produces the following expression when substituted into (3.11) above:

$$V_{out} = R_{L1} \cdot C_{D1} \cdot \frac{dV_{in}}{dt} - \underbrace{R_{L1} \cdot C_{D1} \cdot \frac{dV_{out}}{dt}}_{\text{Unwanted Term}} \quad (3.13)$$

As a result, an unwanted term in (3.12) distorts the waveform. The effects of this term may be minimized by adding a path through Schottky diode $D2$ (see Figure 3.9A).

This path provides a means to describe the input voltage using the following equation:

$$V_{in} = V_{C_{D2}} + (i_2 - i_1) \cdot R_{T2} = V_{C_{D2}} + R_{T2} \cdot C_{D2} \cdot \frac{dV_{C_{D2}}}{dt} \quad (3.14)$$

where i_2 is the loop two current (see Figure 3.9B), $V_{C_{D2}}$ the voltage across diode $D2$ and C_{D2} the junction capacitance. This input may be expressed in terms of the output, as shown by

$$V_{out} = V_{in} - V_{C_{D1}} = V_{C_{D2}} + R_{T2} \cdot C_{D2} \cdot \frac{dV_{C_{D2}}}{dt} - V_{C_{D1}} \quad (3.15)$$

If (3.14) is derivated, the following expression results:

$$\frac{dV_{out}}{dt} = \frac{dV_{C_{D2}}}{dt} + R_{T2} \cdot C_{D2} \cdot \frac{d^2V_{C_{D2}}}{dt^2} - \frac{dV_{C_{D1}}}{dt} \quad (3.16)$$

which may be reduced by considering that $C_{D1} = C_{D2}$ and $V_{C_{D1}} = V_{C_{D2}}$, which yields

$$\frac{dV_{out}}{dt} = R_{T2} \cdot C_{D2} \cdot \frac{d^2V_{C_{D2}}}{dt^2} \quad (3.17)$$

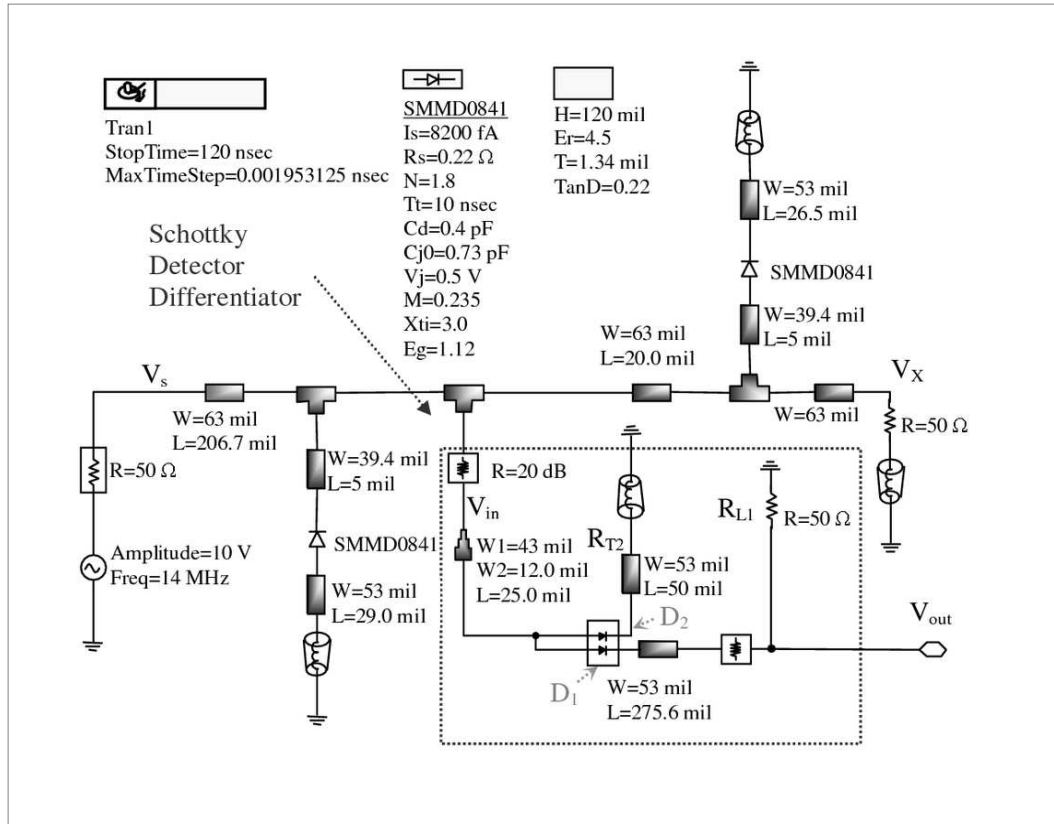
If the expression in (3.16) is substituted for V_{out} on the right side of (3.12) and the expression $C_x = C_{D1}$ and C_{D2} is considered, the final output takes the form as

$$V_{out} = R_{L1} \cdot C_x \cdot \frac{dV_{in}}{dt} - \underbrace{R_{L1} \cdot C_x^2 \cdot R_{T2}}_{\text{2nd Order Differential}} \cdot \frac{d^2V_{C_{D2}}}{dt^2} . \quad (3.18)$$

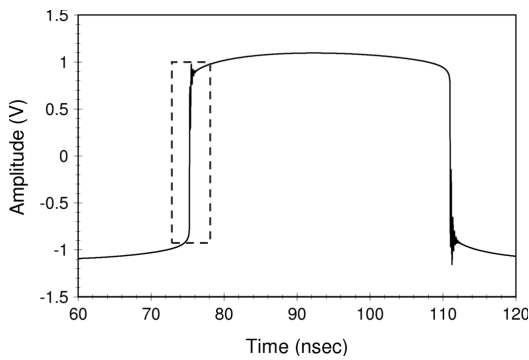
In (3.18) the second order differential is also notable. However, this term may be eliminated by requiring $R_{T2} \ll R_{L1}$, accomplished by grounding the $D2$ diode.

The derivative in (3.18) was verified in simulation by capturing a Schottky detector differentiator circuit using Agilent ADS 2004A (see Figure 3.10A). In this circuit an HSMS-286x series Schottky detector diode was used. This diode typically has a capacitance of 0.25 pF, voltage sensitivity of 35 mV/μW at 2.45 GHz, and 915 MHz to 5.8 GHz operational range. The circuit in Figure 3.10A applies forward and reverse step recovery diodes to transforming a 14 MHz sinusoidal input to a square wave by compressing its rising and falling edges (see Figure 3.10B). This compression of the rising and falling edges is described by Maxwell, Weller, and Harrow [84].

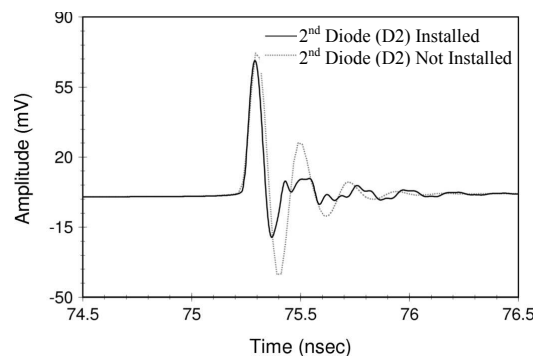
A 20 dB attenuator is used in this circuit to isolate the source (Vs) from the waveforms generated by the Schottky differentiator. When Schottky diode ($D2$) is not installed, a 2nd derivative appears in the output (V_{out}) (see Figure 3.10A) as indicated by equation (3.18). A Gaussian waveform results when this diode is installed. These results demonstrate the capacity for a Schottky diode to differentiate a time-domain waveform.



(A)



(B)



(C)

Figure 3.10: A Schottky detector diode differentiator (A) ADS schematic block, (B) V_x square wave response, and (C) V_{out} output waveform.

3.3.3 Implementation of a practical UWB differentiator

As shown in Figure 3.11, the coupled-line coupler and Schottky detector diode differentiators were combined to implement a multi-port circuit for simultaneous shaping of sub-nanosecond pulses (MCS³P). This circuit produces different UWB waveforms that are aligned to the same reference. In this circuit, a forward and reverse biased Metelics step recovery diode (SMMD-0841) modifies the rising and falling edges of a 14

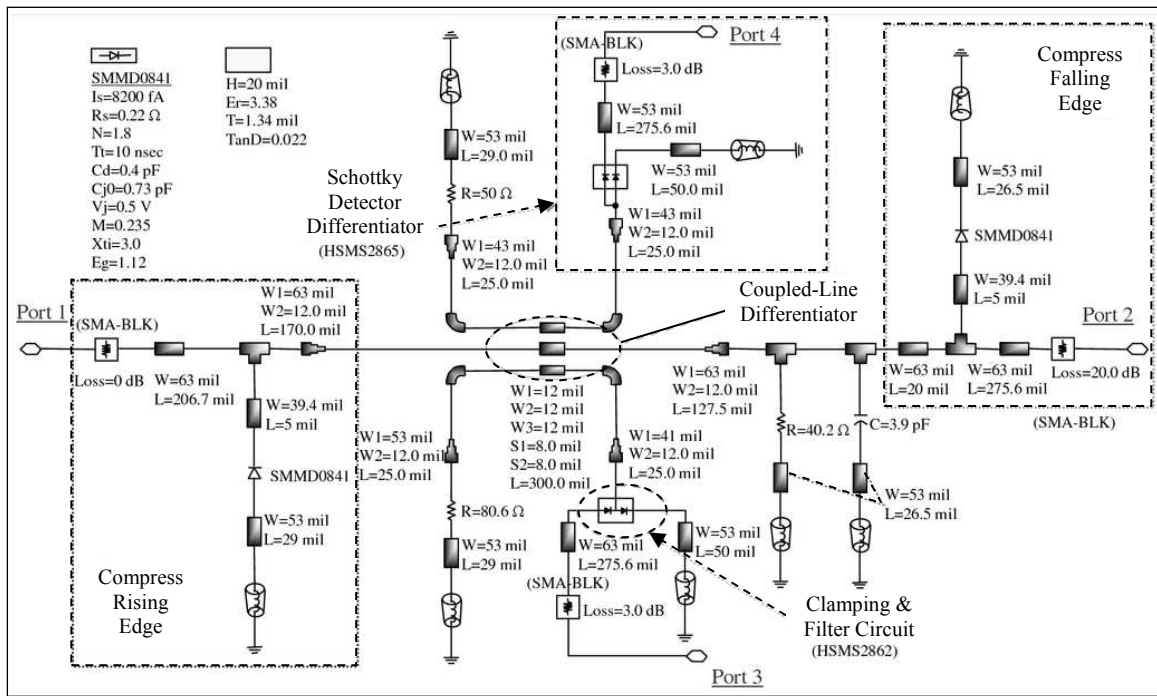


Figure 3.11: Schematic block of the designed MCS³P.

MHz, 10 V_{pp} sinusoidal input, as described above. A three-section coupled-line coupler differentiates the square wave as well as provides a means to isolate the Schottky detector differentiator (in lieu of a 20 dB attenuator). A microstrip, asymmetric three-section

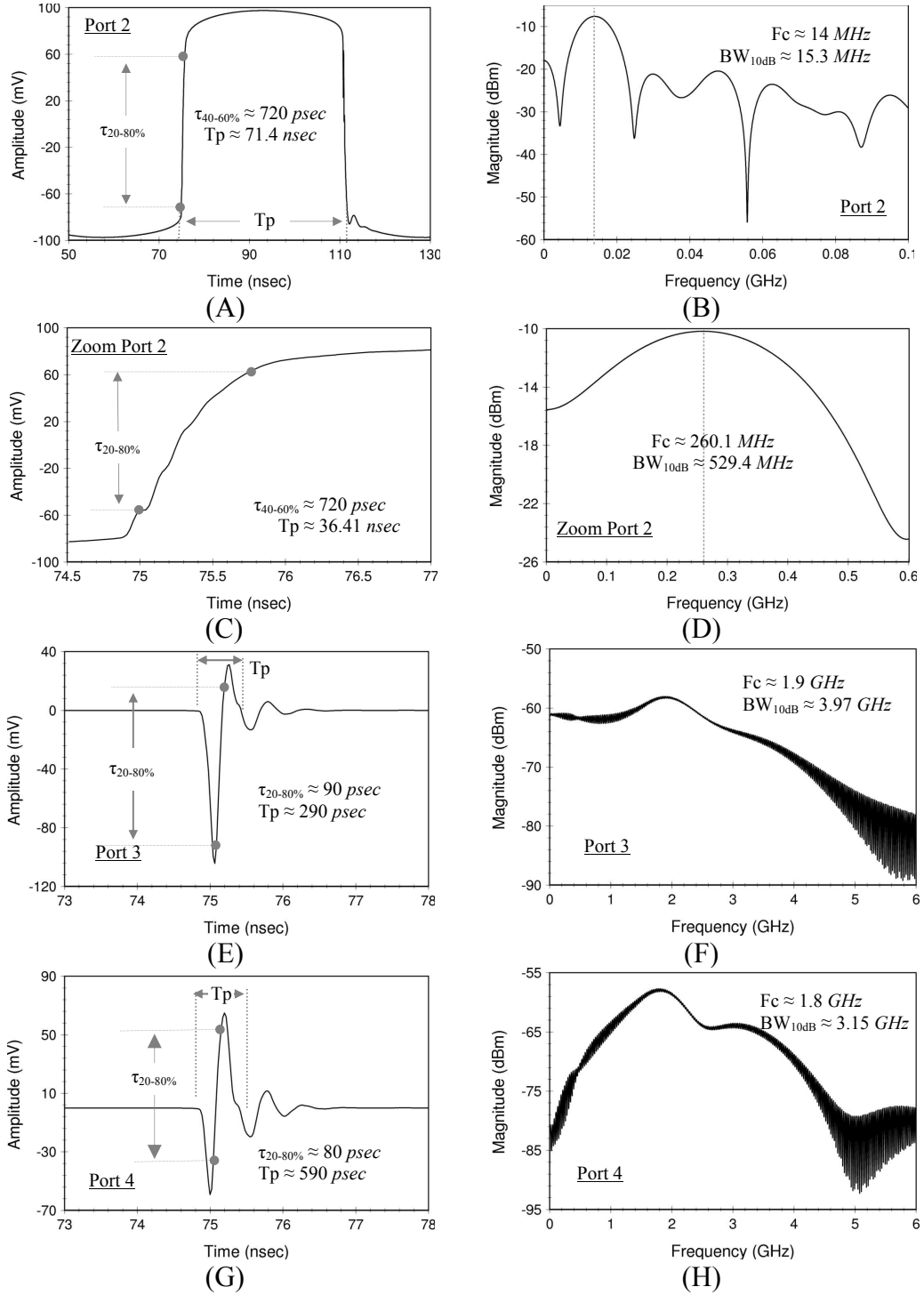


Figure 3.12: Time-domain (A,C,E,G) and frequency-domain (B,D,F,H) responses of multi-port circuit for simultaneous shaping of sub-nanosecond UWB pulses.

coupled-line coupler (model MACLIN3) was used in simulation. On one side of the coupler, the positive going Gaussian was clamped and the negative going Gaussian supplied to the output port through an HSMS-2862 Schottky detector diode (see port 3 in Figure 3.11). The Schottky detector differentiator circuit was placed on the adjacent side of the coupler, from which a monocycle was formed from the Gaussian input (see port 4 in Figure 3.11).

The MCS³P circuit was simulated in ADS 2004A, using a transient/convolution simulator. The waveforms supplied to and generated by the MCS³P are shown in Figure 3.12. In this figure, (A-B) shows the square-wave at port 2, (C-D) the step for the square wave, (E-F) the Gaussian at port 3, and (G-H) the monocycle at port 4. The multi-port circuit generated a square-wave with a 20-80% rise time of 720 *psec*, from which a Gaussian with full-width pulse-duration of 290 *psec* and monocycle with a duration of 590 *psec* were produced. If only the step for the square wave is considered in a Fourier transform, a 529.4 *MHz* bandwidth that meets the FCC UWB specification results (see Figure 3.12D). However, the same edge rate applied to a square wave response does not meet the FCC specification due to the nulls that are introduced at harmonics of the cycle frequency (see Figure 3.12B). This suggests that a fast rise time step-function may be UWB while its square wave response is not. However, the square wave response was used to produce Gaussian and monocycle pulses with a 3.97 *GHz* and 3.15 *GHz* bandwidths, respectively. The signals at ports 3 and 4 were terminated with a 3 *dB* attenuator to control line reflections and port 2 was terminated with a 20 *dB* attenuator to meet the signal level requirement for measurement.

Following simulation, the MCS³P was fabricated on a Rogers Corporation RO4003 substrate ($\epsilon_r = 3.38$, $\tan \delta = 0.022$, and thickness $h = 0.51 \text{ mm}$). Figure 3.13 shows the layout of the implemented MCS³P, which has a Schottky and coupled-line coupler differentiator circuits as discussed in previous sections. The circuit has a dimension of $41.9 \text{ mm} \times 31.8 \text{ mm}$. Dimensions for the transmission lines are given in the schematic of Figure 3.5. The printed circuit board (PCB) was populated with surface

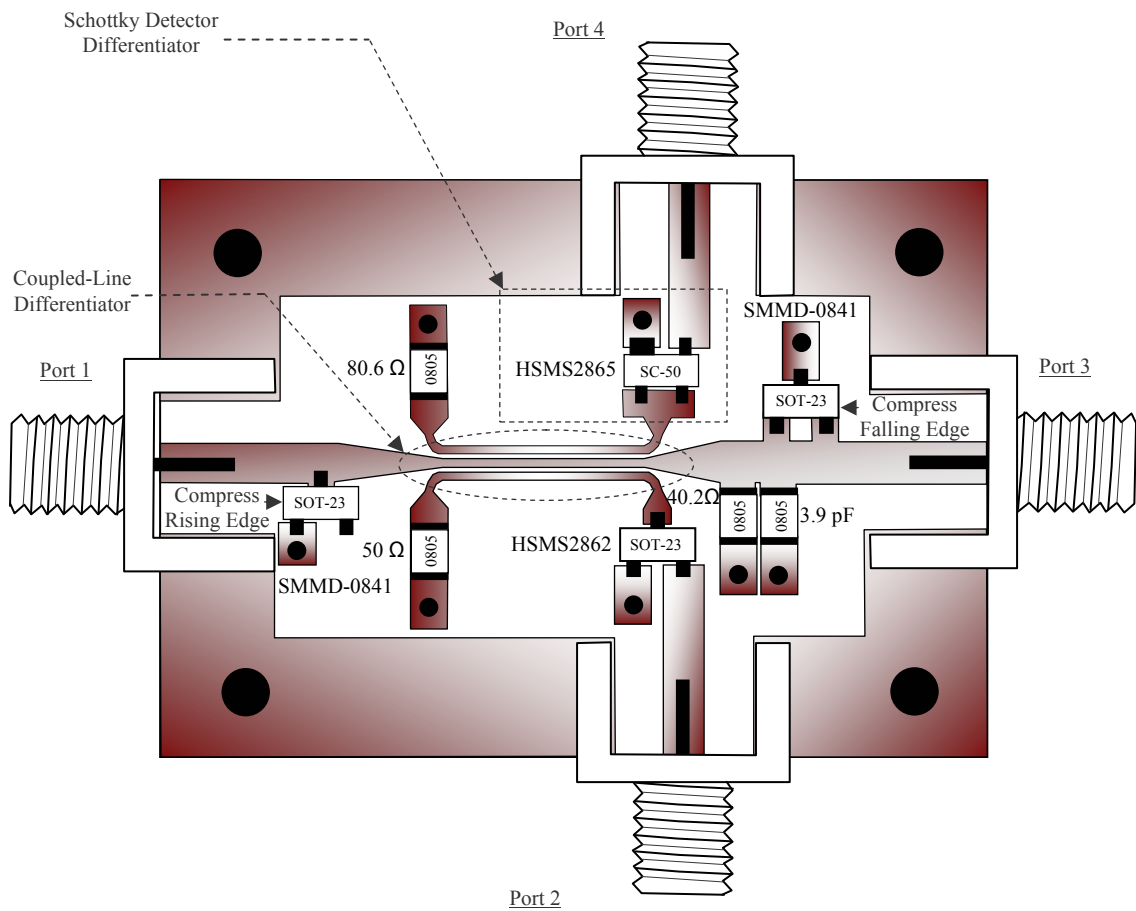


Figure 3.13: Component layout for the MCS³P with SMA connectors attached.

mount components, including 0805 chip capacitors and resistors. Johnson SMA edge mount connectors (142-0761-871) were used to interface with the PCB.

A 20 GHz digitizing oscilloscope (HP 54750A)—configured for 128-bit averaging—was used to measure the response of the MCS³P. As predicted in simulation, waveforms measured at ports 2-4 followed the expected morphology of a square wave, Gaussian, and monocycle shape, respectively. The 20-80% rise time measured for the square wave was 850 *psec* whereas the rise time simulated rise time was 720 *psec*. A good fit was achieved for the amplitude and morphology of simulated and measured square wave (see Figure 3.14A). The Gaussian waveform measured at port 4 demonstrated a pulse-duration that is 100 *psec* greater than simulated (see Figure 3.14B). Finally, the monocycle pulse measured at port 3 (see Figure 3.14C), showed less agreement between simulated and measured data. Since the monocycle was constructed by differentiating the response of a coupled-line derivative, differences in the simulated and measured Gaussian were compounded as the square wave was subjected to the coupled-line followed by Schottky detector differentiation. Nonetheless, a monocycle pulse was distinguishable in the morphology of the measurement. As such, practical implementation of a coupled-line coupler differentiator and Schottky detector differentiator is possible. These differentiators provide alternative approaches to UWB pulse differentiation and support the possibility of using other microwave structures for achieving passive RC networks.

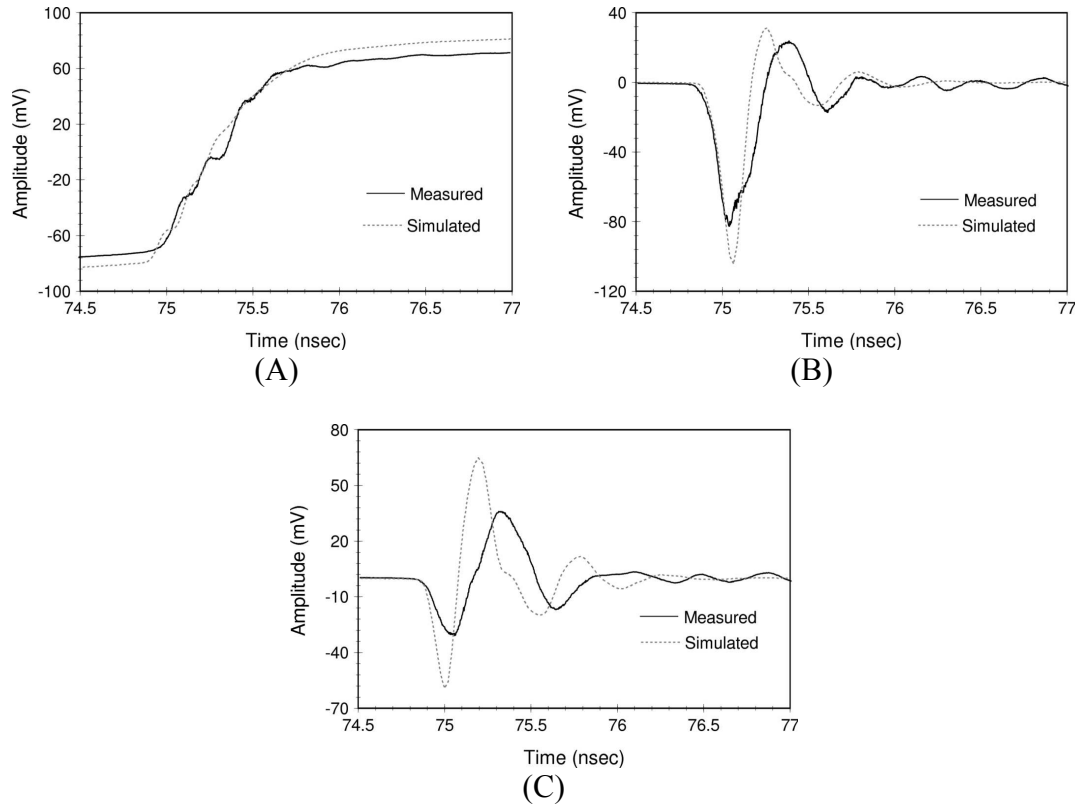


Figure 3.14: Measured and simulated waveforms responses for (A) edge compression sub-circuit, (B) coupled-line coupler differentiator sub-circuit, and (C) Schottky detector differentiator sub-circuit.

3.4 Novel circuits for UWB pulse generation

The unique performance advantages offered by UWB systems, including improved measurement resolution and better clutter suppression, have compelled research toward resolving cost, performance, analysis and design challenges [66, 85, 86]. One of the earliest and most persistent challenges has been pulse generation. A variety of techniques to generate the fast-edge transitions necessary to generate a UWB pulse have been used, including spark gaps, FETs, non-linear transmission lines and step recovery diodes (SRDs) [87, 88]. Of these techniques, SRDs stand out as a means to achieve a

cost-effective and low-noise solution for developing generators with a fixed or tunable pulse-duration [89, 90]. This study applies SRDs to the development of a novel tunable pulse generator based on modifying the design approach.

3.4.1 Tunable pulse-duration UWB generator

Tunable pulse generators are useful in UWB-radar, -radiometric, and -dielectric measurement because they enhance target discrimination by providing a platform for optimizing the absorbed and reradiated power of an isolated target [3]. Optimizing the power presents an opportunity to change penetration depth, radiation intensity, and range resolution by controlling the shape, center frequency, and bandwidth of the spectrum. Tunable generators modify the spectrum shape and center frequency by varying the pulse type through signal differentiation, as discussed above. They modify the spectrum bandwidth by varying the pulse-duration. As such, tunable pulse-duration generators are desirable for time-domain dielectric spectroscopy research because they provide a means to enhance discrimination.

Many tunable pulse-duration generator designs have been proposed in the literature, including those that achieve a variable pulse width by switching in sequential sections of transmission lines, by applying non-linear transmission lines, and by varying circuit impedance [91, 92]. These circuits often require a number of discrete components in addition to power biasing. In addition, they produce waveforms that are no longer Gaussian as more pulses combine for increasing the duration. Although proposed generators have distinct circuit topologies, they convey a similar design approach for

pulse-duration tuning. This approach involves the use of mechanisms for tuning the duration after formation of the Gaussian pulse. In a low-cost, solid-state generator design, this approach is often combined with the use of an SRD that is placed in series with the source [93]. In this study, we explore a new approach to pulse-duration tunable generator design, which requires tuning prior to Gaussian pulse formation. This approach entails applying a shunt SRD configuration to generating a square wave, tuning the rise time associated with the square wave edges, and forming a Gaussian pulse by differentiating the modified square wave. Before, implementing this new approach in a design for fabrication, the following section demonstrates the capacity and limitations associated with using shunt SRDs to generate a square wave and modify the rise time.

3.4.1.1 Validation of new design approach

A new approach to a tunable pulse generator emerges from the consideration that a relationship between pulse-duration and rise time exists. Tian, Sun, and Qu demonstrated that a relationship exists between fall time (or rise time) and pulse-duration [94]. In network theory, Ghosh showed that an impulse function results from the derivative of a unit step-function [95]. In signal processing, Loomis describes an impulse function as the mathematical limit for a Gaussian function as it becomes narrower and taller [96]. If the observations made by Tian, Sun, and Qu are combined with the theories presented by Ghosh, and Loomis to infer the following:

- a step-function with a finite rise time forms a Gaussian following differentiation,
- a tunable Gaussian results from modifying the step-function rise time, and

- an increase in amplitude occurs as the rise time for the step-function decreases.

These observations suggest a new approach to tunable pulse-duration design which requires pulse-duration tuning prior to Gaussian pulse formation. As a result, the first objective in tunable generator design was to apply the SRD towards generating a fast-edge step-function (or square wave) by compressing the rising and falling edges of a source. The second objective was to modify the rise time of the fast-edge, followed by pulse differentiation. As a result, this new approach to tunable generator design is referred to as variable edge-rate compression (VERC).

Application of SRDs in a shunt (double-shunt) configuration provides a means for producing the fast-edge step-function (or square wave) that is required in the VERC approach (see Figure 3.15) [97]. A square wave response is notable in a simple ADS

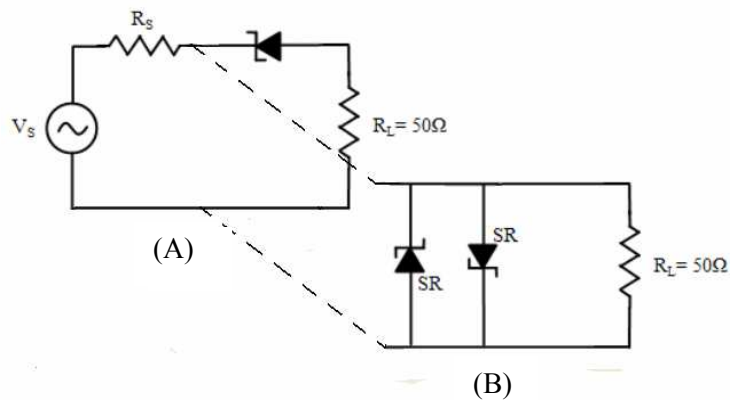
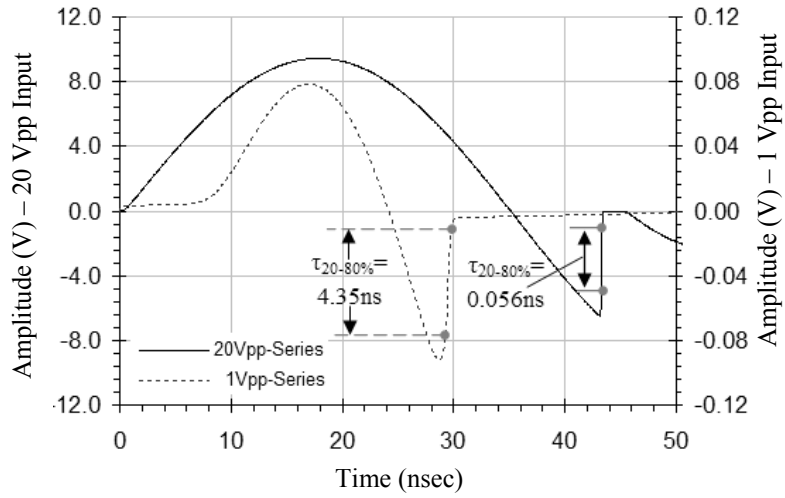


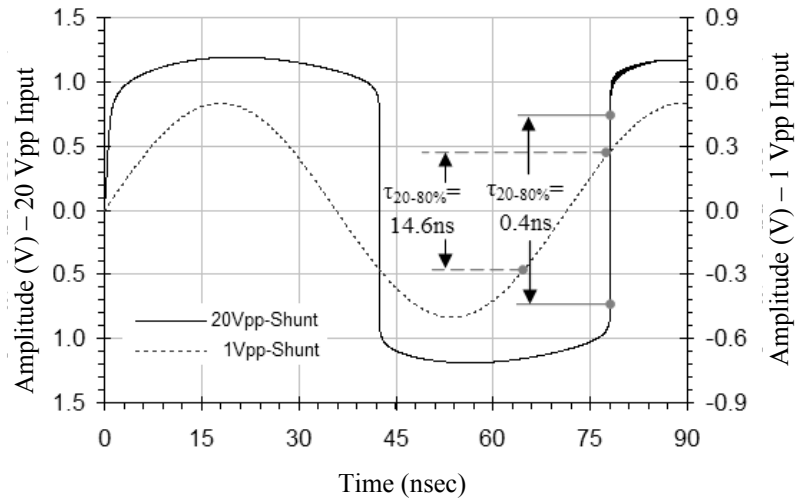
Figure 3.15: SRDs in a series (A) and shunt (B) configuration with power supply.

simulation of a series and double-shunt diode configuration, using a 14 MHz variable amplitude sinusoid. The series configuration demonstrated a 20-80% rise time ranging from .056-4.35 *nsec* (see Figure 3.16A). This corresponds to a FWHM pulse-duration

tuning range of 0.12-9.1 *nsec*. As the tuning voltage is varied from 20 to 1.0 V_{pp} , the step-function voltage decreased to 90 *mV*. In a series configuration, a lower signal-to-noise ratio increasingly challenges the utility of pulses with larger durations. In contrast,



(A)



(B)

Figure 3.16: ADS simulations showing voltage waveforms generated using a 1.0 V_{dd} and 20 V_{dd} 14 *MHz* sources for a series (A) and shunt (B) connected SRD.

the shunt configuration produced step-function amplitudes that decreased less rapidly as the tuning voltage decreased, so that at $1.0 V_{pp}$ this amplitude measured $0.6 V$. The rise time associated with these waveforms ranges from $0.4\text{-}14.6 \text{ nsec}$, which resulted in a wider FWHM pulse-duration tuning range from $0.84\text{-}30.5 \text{ nsec}$ (see Figure 3.16B). Even so, the morphological changes in the waveform of a shunt configuration were more profound over the $1\text{-}20 V_{pp}$ tuning voltage. Voltage adjustments tended to compress the step-function's rising and falling edges so that the waveform approximated a sinusoid at the lower limit and square wave at the upper limit.

Observations made in the above simulation were used to develop a simple circuit to validate the VERC approach (see Figure 3.17). This circuit included a shunt configuration and a variable capacitor for step-function rise time adjustment. Since the

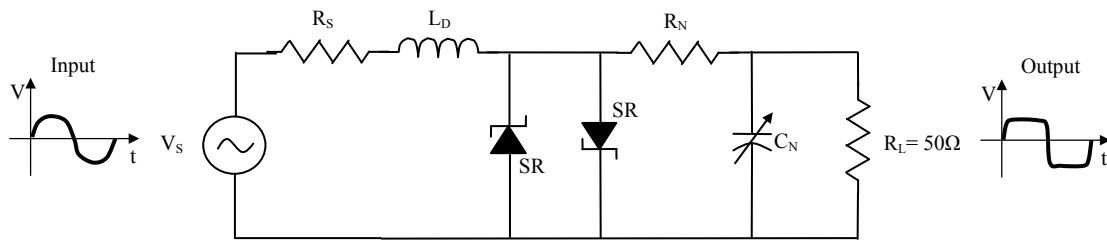


Figure 3.17: Schematic of the variable edge-rate compressor.

slew-rate optimization parameter is responsible for pulse-duration tuning, a variable capacitor was used to alter the resistor-capacitor (RC) time constant in the circuit, which provided a variable slew-rate for the edges of square wave [98]. A Metelics SMMD840 SRD was used to rapidly charge up and snap back on the rising (S_{R1}) and falling (S_{R2}) edges of the source. The SRD (S_{R2}) contributed to the pulse shape, width and low

distortion achieved in this circuit. The edge rate was controlled using a simple RC network where R_N was implemented using a 60Ω chip resistor and C_N a capacitor trimmer with a 1-20 pF range (Sprague-Goodman SG2020). The variable edge-rate compressor was fabricated on a Rogers Corporation high frequency laminate (RT5870) with a relative dielectric constant of 2.33 and a board thickness of 0.787 mm . An Agilent

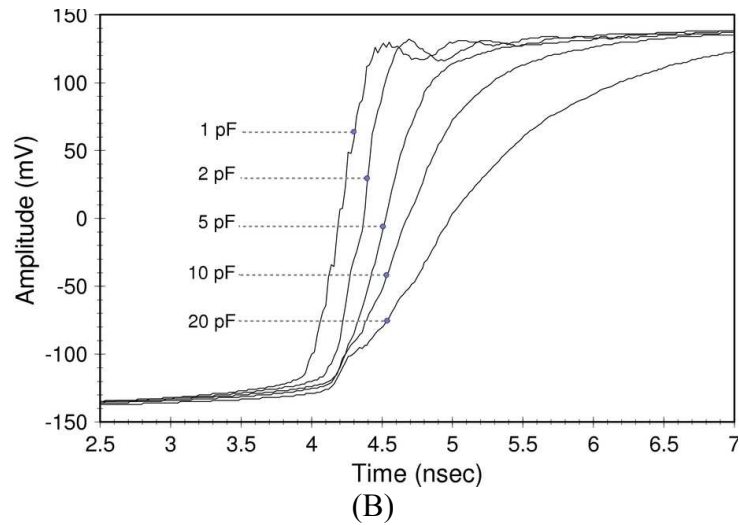
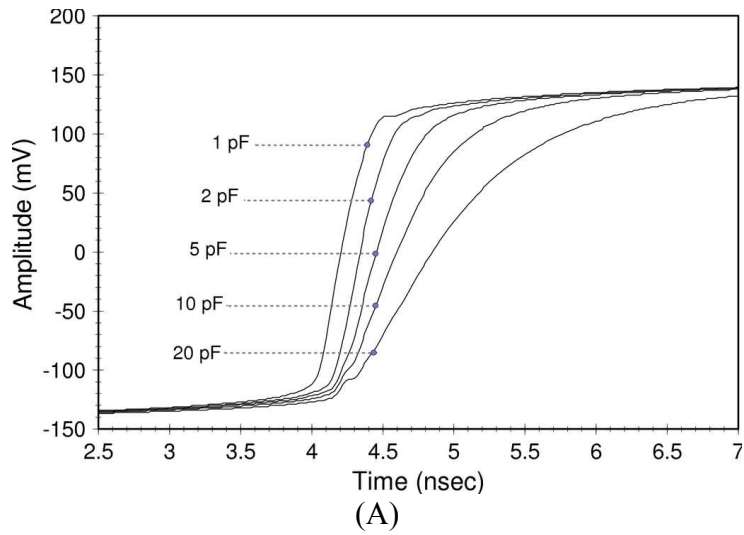


Figure 3.18: ADS simulation (A) and measurement (B) results of the variable edge-rate compression approach, for 1, 2, 5, 10 and 20 pF capacitance values.

33120A arbitrary waveform generator was used to produce the 14 MHz 10 V_{pp} sinusoidal input stimulus, and an HP 54750A digitizing oscilloscope with an HP54715A 20 GHz module was used to capture the output waveform. Data obtained using this setup was compared to ADS 2003A simulations.

The simulation and measurement data were taken on the variable edge-rate compressor. Figure 3.18 demonstrates the tuning range of the compressor as C_N was varied from 1-20 pF. The amplitude associated with the waveforms, in this figure, is a function of the amount of charge that is available from the SRDs at the time of the snap. Consequently, the following observations were made: the voltage decreases with an increase in the circuit's equivalent capacitance, the rise time increases as the amplitude decreases and there is good agreement between simulated and measured data.

3.4.1.2 Circuit design and description

A new tunable UWB pulse generator was developed based on applying a VERC approach (see Figure 3.19). It was implemented with three sub-circuits, including a variable edge-rate compressor, pulse shaper, and RF/microwave differentiator (see appendix D for alternative circuits). The variable edge-rate compressor sub-circuit provided a mechanism for producing a tunable pulse width by allowing slew-rate control. This sub-circuit was constructed using a Metelics SMMD840-SOT23-0S step recovery diode to rapidly charge up and snap back on the rising (SR1) and falling (SR2) edges of the source. Although a sharp falling edge was not typically used in the construction of

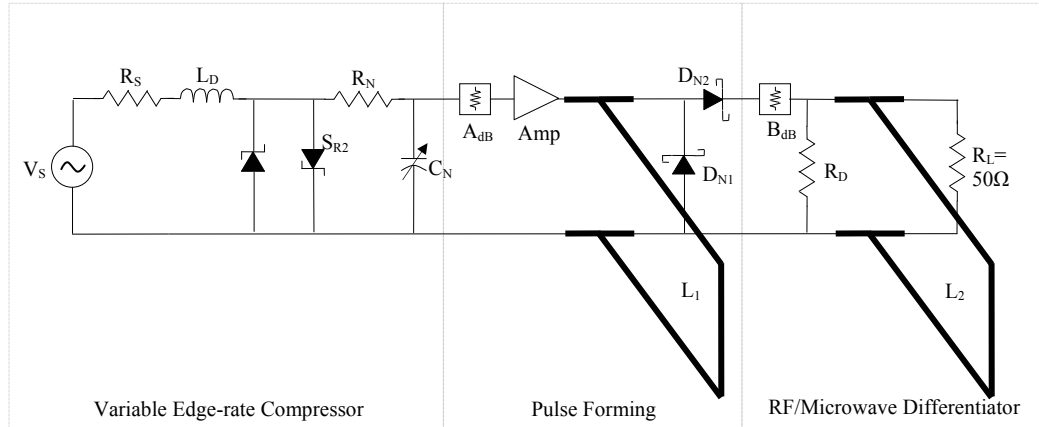


Figure 3.19: Schematic of a tunable UWB generator.

a Gaussian waveform, the corresponding step recovery diode (SR2) contributed to the pulse morphology and low distortion achieved in this circuit. The edge rate associated with the rectangular pulse, which resulted from the variable edge-rate compressor, was controlled with a simple RC network. In this network, an RN of 60 Ω was determined by optimizing the pulse shape in ADS. The RC time constant that provided a means to vary signal rise time by modifying the capacitance, was determined by evaluating the series inductance and shunt capacitance as a 1st order low-pass filter. The cut-off frequency for this filter was obtained from the reciprocal of the step-function rise time. Consequently, the low-pass filter inductance (L'_k) and capacitance (C'_k) were defined by the following equations:

$$L'_k = \frac{R_o \cdot L_k}{\omega_c} \quad (3.19)$$

$$C'_k = \frac{C_k}{R_o \cdot \omega_c} \quad (3.20)$$

where, R_o is the circuit resistance, C_k is the normalized capacitance, L_k is the normalized inductance, and ω_c is the cut-off frequency [99]. A minimum and maximum rise time was used to constrain the filter elements. The minimum rise time was computed by taking 60% of the 70.0 *psec* transition time for the Metelics step recovery diode because it corresponds to the smallest possible 20-80% rise in amplitude. The maximum rise time was computed by taking 60% of the 10.0 *nsec* minority carrier lifetime for the Metelics SRD because it corresponds to the largest 20-80% rise in amplitude. These limits were applied to (3.19) and (3.20) above, using normalized element values, which correspond to a maximally flat pass-band. This endeavor resulted in an inductance range of 4.0-0.35 *nH* and capacitance range of 0.17-14.5 *pF*. Consequently, the L_D and C_N were implemented with a 0.35 *nH* chip inductor and a capacitor trimmer with a 1-20 *pF* range, respectively (Sprague-Goodman SG2020).

The variable edge-rate signal was passed to the pulse shaper sub-circuit, which formed a Gaussian pulse. This sub-circuit consisted of the following: a Picosecond Pulse Labs 5840A-107 amplifier to provide 21 *dB* of gain and 35 *dB* of isolation over a 80 *kHz*-9.3 *GHz* bandwidth; an attenuator of 6 *dB* to help meet the 0 *dBm* input power requirement for the amplifier; and a pulse forming network for differentiating the incoming rectangular pulse (see Figure 3.19). Since the pulse-forming network included a differentiator, the initial value for the lengths L_1 and L_2 was set to a quarter wavelength at the maximum frequency [100]. The maximum frequency was determined from the rise time, so that the length may be expressed by the following equation:

$$Len = 1.2 \cdot \frac{\tau_{10-90\%}}{4 \cdot \sqrt{\epsilon \cdot \mu}} \quad (3.21)$$

where ϵ is the electric permittivity, and μ is the magnetic permeability. The factor of 1.2 was applied to approximate the full rise time from the 10-90% rise time ($\tau_{10-90\%}$). The resulting length was then optimized in ADS to achieve a desirable ripple and overshoot.

The pulse-forming network (see Figure 3.19 above) was constructed from a short circuit stub with a length L_1 of 103 mm and a width of 2.5 mm. Since the resulting Gaussian contained both positive and negative going pulses, an Agilent Technologies Schottky barrier diode package (HSMS2862) was used to clamp the negative going reflections by providing a ground path through D_{N1} as well as blocking through D_{N2} . The resulting Gaussian was then passed to the RF/Microwave differentiator sub-circuit where a monocycle was formed. This sub-circuit contained a DC-18 GHz 3.0 dB attenuator to minimize circuit reflections. It was implemented using a 100 Ω resistor for matching and a short circuit stub L_2 that has a length of 80 mm and width of 1.25 mm. Each sub-circuit was developed on a separate printed circuit board, as shown in Figure 3.20.

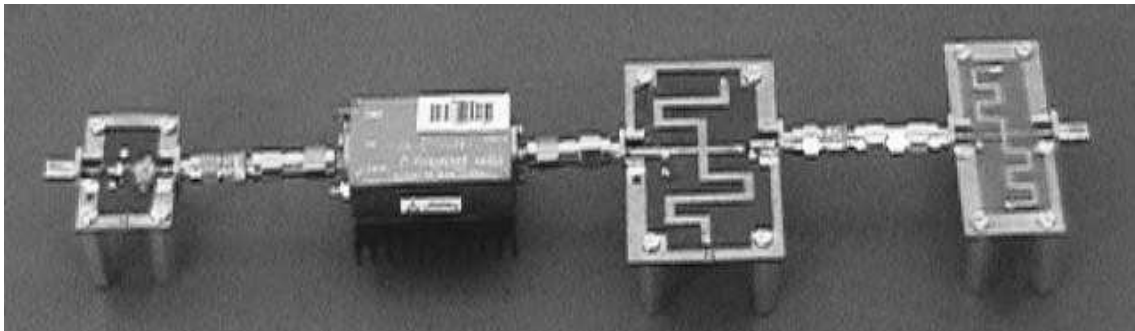
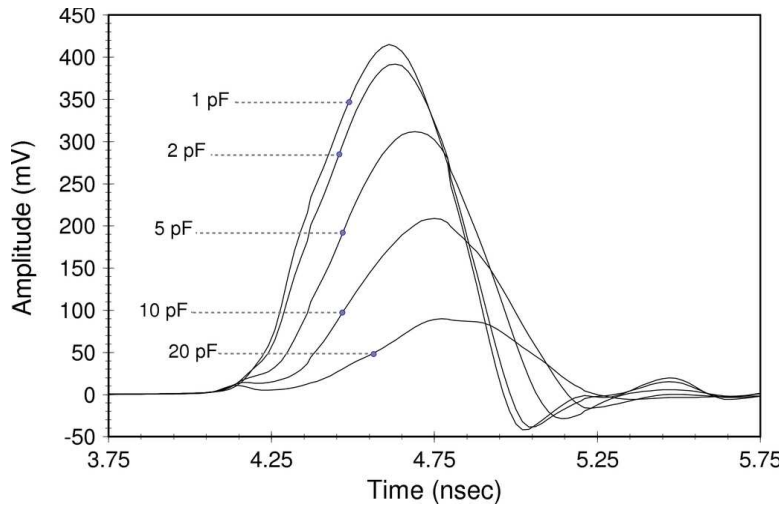


Figure 3.20: Photo of the single-stage tunable UWB pulse generator consisting of a variable edge-rate compressor, amplifier, pulse forming network and RF/microwave differentiator, from left to right.

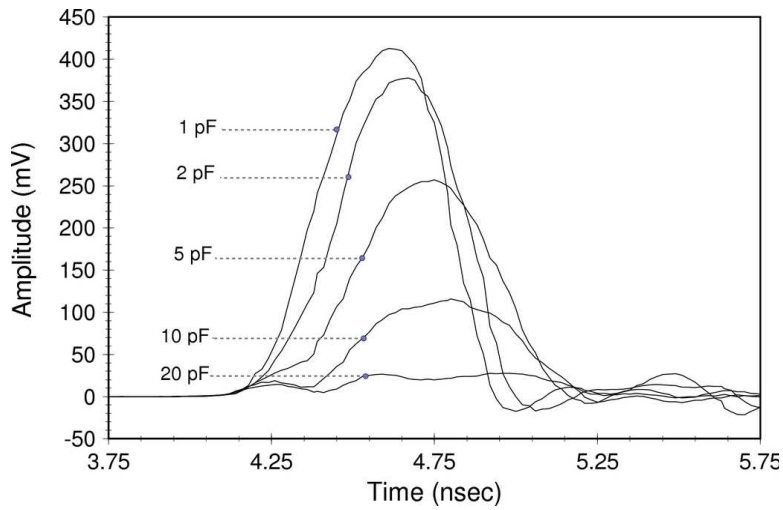
3.4.1.3 Fabrication and measurement

The variable edge-rate compressor and pulse forming networks were fabricated on a Rogers Corporation high frequency laminate (RT5870) with a relative dielectric constant of 2.33 and a board thickness of 0.787 mm . The RF/Microwave differentiator was fabricated on a 0.787 mm FR4 glass epoxy substrate having a relative dielectric constant of 4.2. The setup used to test this generator included the use of an Agilent 33120A arbitrary waveform generator to produce the 14 MHz 10 V_{pp} sinusoidal stimulus that was required at the input of the circuit. The setup also included an HP 54750A digitizing oscilloscope with an HP54715A 20 GHz module to capture the output. The measured data that was obtained from this setup was compared to data simulated using Advanced Design System (ADS) 2003A.

Simulation and measurement data were taken on each sub-circuit above. Measurement data was collected using an HP54750A oscilloscope with an HP54753A, 20 GHz TDR plug-in. Figure 3.21B demonstrates the tuning range of the compressor as the capacitance was varied from $1\text{-}20\text{ pF}$. The amplitude associated with the waveforms, in this figure, was a function of the amount of charge available from the step recovery diodes at the time of the snap. Since voltage amplitude may be expressed mathematically as the equivalent charge over the total capacitance, it is expected that the signal amplitude would decrease with an increase in the circuit's capacitance. As the capacitance was reduced, the signal rise time decreased while the amplitude increased. Good agreement between simulated and measured data may be observed in this figure.



(A)

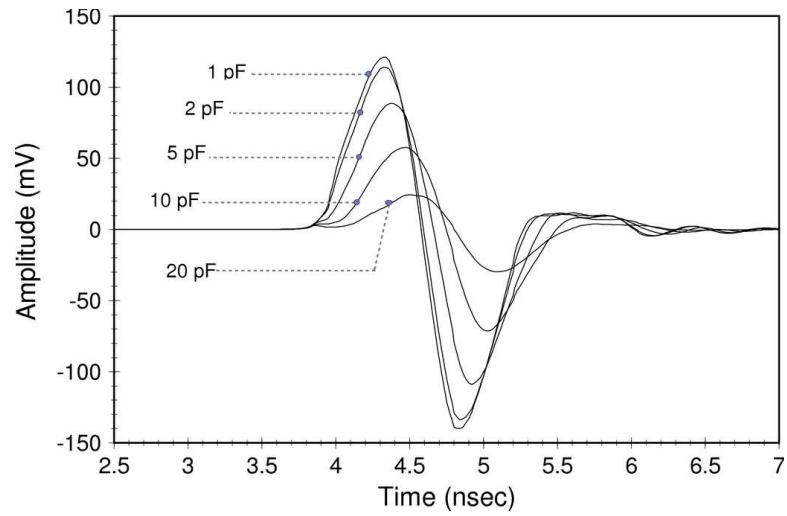


(B)

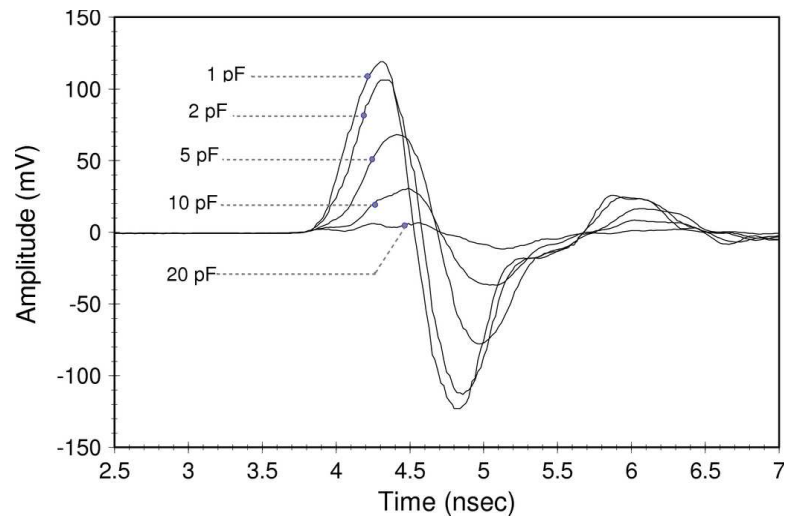
Figure 3.21: Simulated and measured Gaussian waveforms at 1, 2, 5, 10 and 20 pF capacitance with a (A) simulated and (B) measured Gaussian pulse at the output of the pulse shaper, over capacitance.

The Gaussian waveform resulting from the circuit demonstrated a morphology that remained Gaussian throughout the tunable range. It also showed a distinct peak-amplitude and slope that varied as a function of pulse width (see Figure 3.22). However,

the amplitude decreased sharply with an increase in capacitance for measured results; i.e., the simulated amplitude at 20 pF was about 25 mV,



(A)



(B)

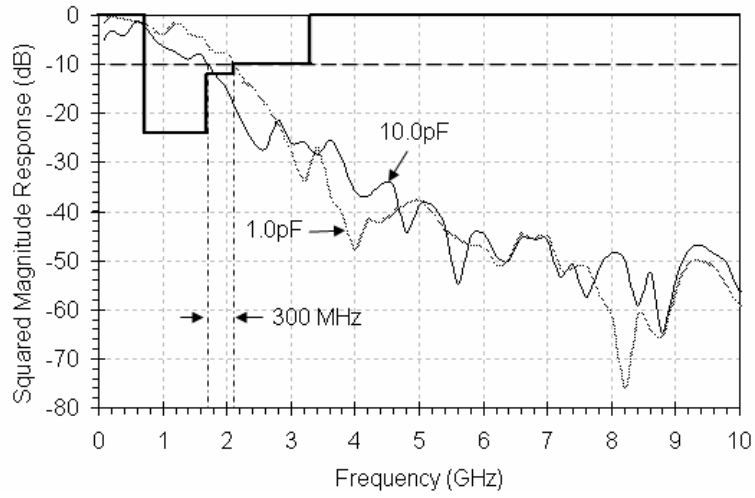
Figure 3.22: Simulated and measured monocycle waveforms at 1, 2, 5, 10 and 20 pF capacitance with (A) simulated and (B) measured monocycle pulse resulting from a 2nd derivative of pulse forming output.

whereas the measured amplitude was about 5 mV . Consequently, the measured amplitude at 20 pF was very close to the ringing noise in the circuit. This Gaussian shape may be restored by increasing amplifier gain at the input of the pulse forming sub-circuit. Figure 3.22A-B shows the simulated and measured waveforms for the differentiated Gaussian [100]. As shown, monocycles result from this differentiation over the $1\text{-}20\text{ pF}$ capacitance range. The differentiator used in this sub-circuit produced pulses that have closely matched amplitudes for the positive and negative going edges. As such, a monocycle having a 1.6 nsec width resulted from differentiating an 800 psec Gaussian.

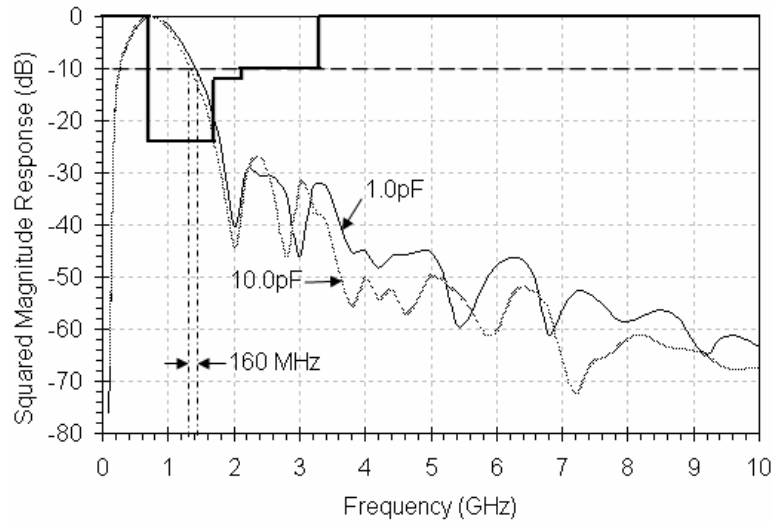
The normalized spectrum associated with the Gaussian and monocycle waveforms above are shown in Figure 3.23. These figures show that the tuning range and bandwidth decreased upon the application of a second derivative in the differentiator sub-circuit. The tuning range measured 300 MHz and 160 MHz , for the Gaussian and monocycle, respectively. The bandwidth associated with the 10 pF capacitance measured 1.4 GHz for the monocycle spectrum (see Figure 3.23B) and 1.7 GHz for the Gaussian spectrum (see Figure 3.23A).

A tunable pulse generator based on a novel mechanism of utilizing step recovery diodes for variable edge-rate compression simplifies UWB generator design by allowing a focus on generating a smooth slope for the step in a rectangular pulse and then developing RF/microwave differentiators. The waveforms that result from this approach demonstrated good Gaussian symmetry throughout a tuning range of 800 psec to 1150 psec using a $1\text{-}20\text{ pF}$ capacitance trimmer. In addition, circuits required only an AC

input and DC supply for the amplifier. They were developed without biasing and contain only eight discrete components.



(A)



(B)

Figure 3.23: Shaped spectrum with FCC mask for medical imaging and normalized frequency response of waveforms generated using 1 and 10 pF capacitance with (A) Gaussian and (B) monocycle responses.

3.5 Summary

In this chapter, a new design approach to tunable pulse generator design was introduced, which involved pulse-duration tuning prior to pulse shaping. This design approach provides a means to divide tunable UWB generator circuit topology into three distinct parts: step-function generation, rise time tuning, and pulse shaping. In step-function generation, an ADS basic diode model was reconfigured to provide a step response. Although the fit between simulated and measured step responses was deemed suitable for designing circuits, parasitics associated with SMA interconnects and vias to ground increased the amount of reflection noise in the circuit. The effect of this noise was more noticeable when tuning the pulse-duration using a variable capacitor, which demonstrated a smaller signal to noise ratio as the capacitance was increased to obtain a larger pulse width.

Through pulse shaping the step-function waveform that was generated using step recovery diodes was differentiated to obtain Gaussian and monocycle pulses. These pulse types are more useful because they meet the FCC UWB specification but also provide a means to shape the spectrum. It was shown that pulse shaping can be accomplished by using any RF/microwave element that has a capacitance, including microstrip transmission line, couplers and diodes. This was evidenced by analyzing the equivalent circuit of various topologies. This analysis revealed unwanted terms in the circuit equations for coupled-line coupler and Schottky detector differentiation circuits. Signal differentiation was achieved in the circuit response by minimizing these terms. In

coupled-line coupler differentiation, the rate of change of the input signal had to be very large to achieve differentiation. In Schottky detector differentiation, a second order derivative was attenuated by adding a parallel diode path to ground. These topologies offer alternatives to UWB pulse shaping and generation, which may solve problems with signal isolation and circuit complexity at the expense of smaller signal amplitudes. However, by applying these topologies within the framework of a new approach, the utility of conventional RF/microwave elements is expanded.

Chapter 4

Dielectric Properties of Lossy Liquids From Transmission-Reflection Measurements

This chapter presents an improved coaxial-line test fixture for transmission-reflection measurement. The National Institute of Standards and Technology (NIST) describes fixtures used for transmission-reflection measurement as suitable only for characterizing solids. However, a simple, low-cost fixture with the capability to contain a liquid specimen is made possible by constructing the fixture from a semi-rigid coaxial-line with DuPont Teflon PolyTetraFluoroEthylene (PTFE) core. This contribution is presented below by providing a background for transmission-reflection measurement and theory for permittivity extraction. To accommodate a Teflon PTFE core, a general solution to the Nicholson-Ross-Weir (NRW) technique is presented where as the formulations available in the literature are based on an air-core assumption. Afterwards, the functionality of the fixture is demonstrated using the NRW technique. Last, sources of uncertainty are discussed followed by a summary.

4.1 Background

Coaxial-line transmission-reflection methods are based on a well-established theoretical framework and are useful in applications permitting cylindrical specimens. They have been applied in a variety of dielectric measurement systems including:

produce and biomaterial [101-104]. These methods are advantageous in dielectric measurement because they utilize transverse electromagnetic (TEM) modes, provide measurement data from which both the complex permittivity as well as permeability may be determined, and produce a broad measurement bandwidth [105, 106]. TEM modal propagation is often the most attractive feature in coaxial-line transmission-reflection methods because it permits simplification of the electromagnetic (EM) analysis used in computing the dielectric properties. This simplification is the result of the orientation of the electric and magnetic field vectors, which are both normal with respect to the direction of propagation for TEM modes. However, transmission-reflection methods suffer from three major problems: air gaps at the sample-fixture interface, half-wavelength resonances, and over-moding [107].

Air gaps are a problem because they may contribute to mode conversion, which results in higher order modes. Mode conversion can occur when an incident wave encounters an interface between materials with different characteristic impedances. As a result, care is taken in the construction of coaxial test-fixtures to achieve two primary goals: dominance of TEM mode propagation in the transmission line and containment of the specimen. However, these two goals are not mutually exclusive because imperfections in the fixture geometry or air gaps at the air-sample interface may significantly alter the propagation coefficient, resulting in higher order modes in the transmission line. These challenges have been mitigated for measuring solids by machining the specimen to precisely fit the specimen holder, adjusting the algorithm for analytical analysis, and eliminating the air gap through the application of conductive

materials to the face of the specimen [108]. Transmission-reflection measurements on liquids have added to these challenges by requiring construction of a holder, which introduces an interface between the fixture's specimen and air-core transmission line, for confining the liquid [109, 110]. Specimen holders for air-core coaxial transmission line fixtures have resulted in mechanically complex fixtures with limited capability for measuring different materials.

In this study, a simple, low-cost, coaxial-line fixture, which eliminated the need for an additional interface between the fixture's specimen and transmission line, was developed for transmission-reflection measurement of liquids. This improvement was accomplished by developing a coaxial-line fixture from a semi-rigid coaxial transmission line, with a Teflon PTFE core instead of an air-core. Although this improvement reduces the complexity and cost of the fixture, a non-air-core approach is unconventional for transmission-reflection measurement. As such, the algorithms, measurement systems, and methods that are presented in the literature are based on an air-core assumption. As a result, a general solution to the Nicolson-Ross-Weir (NRW) algorithm for determining the permittivity is presented in section 4.3. The transmission-reflection measurement fixture, system, methods, and procedures are presented in sections 4.4 and 4.5. Simulation and measurement results along with an analysis are presented in section 4.6. A comparison of results from the NRW algorithm to that of a modified-NRW algorithm and NIST approximation is also shown in section 4.6. Lastly, a discussion of measurement uncertainty is presented in section 4.7, followed by a summary in section 4.8.

4.2 Theory

The utility of an experimental coaxial fixture is realized so long as an analysis of the dielectric properties can be applied. These properties are a function of the physical characteristics of the fixture and electromagnetic method applied to analyze the measurement data. These functions are captured in Maxwell's equations, which describe the relationship between electricity, magnetism, space, and time. Consequently, the time-harmonic form of Maxwell's equations provides a construct for analyzing and understanding the transmission-reflection method for boundary-value electromagnetic problems by rearranging the following equations:

$$\nabla \times \vec{E} = -\vec{M}_i - j\omega\vec{B} \quad , \quad (4.1)$$

$$\nabla \times \vec{H} = -\vec{J}_i + \vec{J}_c + j\omega\vec{D} \quad , \quad (4.2)$$

where the time-harmonic field quantities \vec{E} , \vec{H} , \vec{D} , \vec{B} , \vec{J} , and \vec{M} are functions of space coordinates (x, y, z) and angular frequency (ω) , whereby:

- \vec{E} is the electric field intensity (*volts/meter*),
- \vec{H} is the magnetic field intensity (*amps/meter*),
- \vec{D} is the electric flux density (*coulombs/meter²*),
- \vec{B} is the magnetic flux density (*webers/meter²*),
- $\vec{J}_{i,c}$ is the impressed and conduction electric current densities (*amps/meter²*) and
- \vec{M} is the magnetic current density (*volts/meter²*).

A simultaneous system of equations that is used to determine the complex material properties results from this rearrangement. This is accomplished by applying constitutive relations:

$$\vec{B} = \mu\vec{H} , \text{ and} \quad (4.3)$$

$$\vec{D} = \epsilon\vec{E} , \quad (4.4)$$

to Faraday's law of induction in (4.1) and Ampere's law in (4.2) and taking the curl of both sides, which yields:

$$\nabla \times \nabla \times \vec{E} = -\nabla \times M_i - j\omega\mu(\nabla \times \vec{H}) , \quad (4.5)$$

$$\nabla \times \nabla \times \vec{H} = \nabla \times J_i + \nabla \times J_c + j\omega\epsilon(\nabla \times \vec{E}) , \quad (4.6)$$

where μ is the magnetic permeability and ϵ is the electric permittivity. This operation exposes a coupled relationship between the electric and magnetic fields, which maybe decoupled by substituting the right sides of equations (4.1-4.2) into equations (4.5-4.6).

After rearranging the terms and assuming that there are no sources of electric ($\vec{J} = 0$) or magnetic ($\vec{M} = 0$) current density and no free charge build up ($\nabla \cdot \vec{D} = 0$), the following uncoupled second order wave equations result:

$$\nabla^2 \vec{E} + \omega^2 \mu\epsilon\vec{E} = 0, \quad (4.7)$$

$$\nabla^2 \vec{H} + \omega^2 \mu\epsilon\vec{H} = 0. \quad (4.8)$$

The complex material properties in these equations may be expressed as complex numbers ($\mu' - j\mu''$ and $\varepsilon' - j\varepsilon''$) for isotropic materials or as tensors for anisotropic materials. These equations comprise the fundamental basis for understanding modal propagation in a two-media region and deriving a practical solution for analyzing the dielectric parameters.

Waves can travel in an infinite lossy media in the $\pm z$ direction. If the $-z$ direction is selected, and step-function discontinuities exist about the sample, then the time-dependent fields in (4.7-4.8) may be expanded in terms of a modal representation of forward and reverse traveling waves (\pm), expressed as:

$$E(\vec{r}, t) = \frac{1}{2\pi} \int_{-\infty}^{\infty} d\omega \sum_n \vec{E}_n(\vec{r}_T, \omega) e^{\pm\gamma_n z} e^{j\omega t} \quad (4.9)$$

$$H(\vec{r}, t) = \frac{1}{2\pi} \int_{-\infty}^{\infty} d\omega \sum_n \vec{H}_n(\vec{r}_T, \omega) e^{\pm\gamma_n z} e^{j\omega t} \quad (4.10)$$

where E and H are the field component bounded in the \vec{r} direction and \vec{E}_n and \vec{H}_n are field components along vector \vec{r}_T associated with the modes (n). The propagation constant (γ_n) is defined as:

$$\gamma_n = j \sqrt{\frac{\omega^2 \mu_r \varepsilon_r}{c_0^2} - \left(\frac{2\pi}{\lambda_{nc}}\right)^2}, \quad (4.11)$$

where λ_{nc} is the cut-off wavelength for that mode and c_0 is the speed of light in a vacuum. The simplicity in the transmission-reflection method hinges upon the consideration of transverse field components. If the discontinuities about the sample and in the fixture are

small, the transverse component (T) becomes dominant in a coaxial fixture. As a result, the Fourier transformed fields may be expanded into a complete set of modal functions, which includes the transverse electromagnetic (TEM), transverse electric (TE), and transverse magnetic (TM) field configurations. Consequently, electric and magnetic fields expressed in terms of modes, traveling in the $-z$ direction. Jarvis, Janevic, Riddle and others showed that a TEM assumption may be assumed outside of the specimen because the non-TEM waves generated by a lossy, slightly inhomogeneous specimen are evanescent in the coaxial transmission line. As a result, the electric field may be expressed in terms of scattering parameters (S-parameters) with the following equations:

$$E_I = \underbrace{e^{(-\gamma_{c1}z)}}_{\text{IncidentWaves}} + S_{11}e^{(\gamma_{c1}z)} + \underbrace{\sum_{n=2}^N C_n(\bar{z}_T)e^{(\gamma_{cn}z)}}_{\text{EvanescentWaves}} \quad (4.12)$$

$$E_{II} = \sum_{n=1}^N D_n(\bar{z}_T)e^{(-\gamma_{mn}z)} + E_n(\bar{z}_T)e^{(\gamma_{mn}z)} \quad (4.13)$$

$$E_{III} = \underbrace{S_{21}e^{(-\gamma_{c1}(z-L))}}_{\text{TransmittedWaves}} + \underbrace{\sum_{n=2}^N F_n(\bar{z}_T)e^{(-\gamma_{cn}(z-L_2))}}_{\text{EvanescentWaves}} \quad (4.14)$$

where L_2 is the specimen length, E_I , E_{II} , and E_{III} are the normalized electric fields in regions I, II, and III respectively, C_n , D_n , E_n , and F_n are modal coefficients, and γ_{ci} and γ_{mi} are propagation constants of the n^{th} mode in the core and material respectively [111]. Consequently, if the transmission lines of the fixture are long enough, the contribution by the evanescent fields is negligible, resulting in a simpler set of equations for extracting the material properties from S-parameters.

4.3 General solution to Nicholson-Ross-Weir method

Air-filled coaxial sample holders are often not simple in construction and require an interface for confining liquid test samples. A simple, low-cost construction is possible using a dielectric filled line in which the dielectric itself serves to constrain the sample under test. After constraining the sample under test, consideration must be given to extracting the dielectric properties. Towards this end, the Nicholson-Ross-Weir method provides a solution for extracting the complex relative permittivity (ϵ_r) and permeability (μ_r) of the test sample from measured S-parameters. In an air-core coaxial fixture, this solution involves use of the following published equations:

$$\epsilon_r = -\frac{1}{\mu_0 \epsilon_0} \left(\frac{1}{\omega} \ln(z) \frac{1}{L_2} \right)^2 \frac{1}{\mu_r} \text{ and} \quad (4.15)$$

$$\mu_r = \frac{j}{\omega L_2 \epsilon_0} \ln(z) \left(\frac{1+\Gamma}{1-\Gamma} \right), \quad (4.16)$$

where L is the length, Γ the reflection coefficient, and z the complex propagation constant of the sample [112]. In these equations, Γ is computed from the S-parameters of the sample using the following expression

$$\Gamma_{12} = \frac{1 - (S_{21}^2 - S_{11}^2)}{2S_{11}} \pm \sqrt{\left(\frac{1 - (S_{21}^2 - S_{11}^2)}{2S_{11}} \right)^2 - 1}, \quad (4.17)$$

where S_{11} and S_{21} are the reflection and transmission coefficients associated with the sample under test. To obtain S_{11} and S_{21} for the sample, the S-parameters measured at the calibration reference plane (S'_{11} and S'_{21}) must be rotated through the coaxial

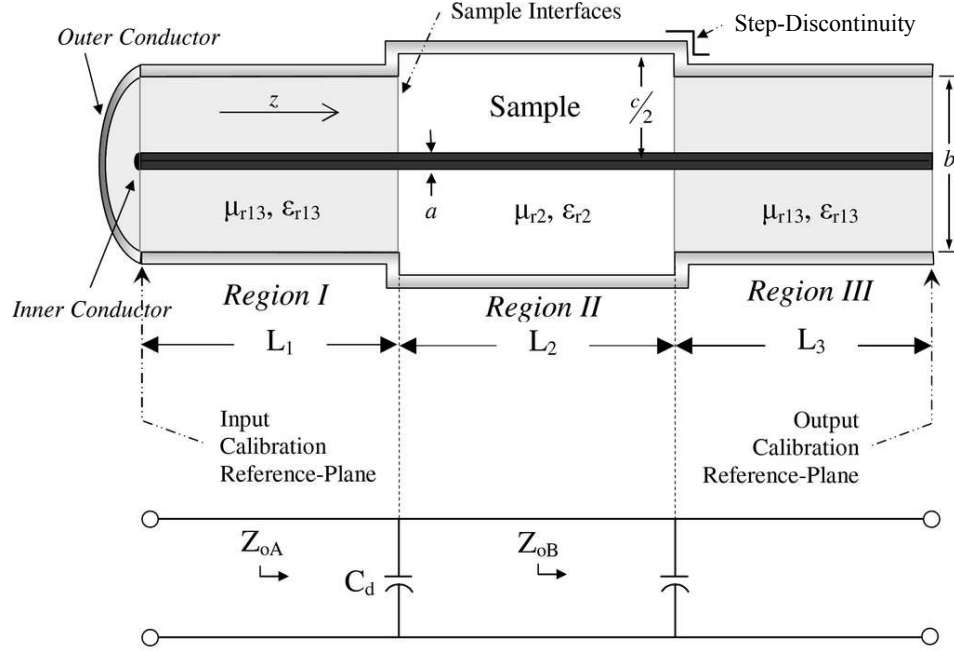


Figure 4.1: Calibration reference-plane and sample interface of coaxial fixture with a relative complex permittivity (ϵ_{r2}) and permeability (μ_{r2}) of specimen so that $\epsilon_{r2} = \epsilon_2' - j\epsilon_2''$ and $\mu_{r2} = \mu_2' - j\mu_2''$.

transmission lines connecting the VNA and fixture (see Figure 4.1). This rotation is accomplished by using the wave propagation equation

$$z = e^{-j\beta_x L_x}, \quad (4.18)$$

where β_x is the phase constant and L_x length of the coaxial cable, to produce the following expressions for the S-parameters at the sample face:

$$S_{11} = S'_{11} e^{j2\beta_1 L_1 \sqrt{\mu_{r13} \epsilon_{r13}}} \text{ and} \quad (4.19)$$

$$S_{21} = S'_{21} e^{j2\beta_1 (L_1 + L_3) \sqrt{\mu_{r13} \epsilon_{r13}}}, \quad (4.20)$$

where μ_{r13} is the relative complex magnetic permeability of regions I and III, ε_{r13} the relative complex electric permittivity of regions I and III, L_1 the length of the coaxial cable in region I, and L_3 the length of the coaxial cable in region III of the fixture. Equations (4.19) and (4.20) are dependent on the material used in the coaxial cables in regions I and III of the fixture. As such, an air-filled line applies (4.15) and (4.16) without alteration, but ε_r and μ_r are modified if a dielectric filled line is assumed. The new equations resulting from this analysis are referred to as a general solution to the NRW method.

A general solution that is not based on an air-core assumption was obtained by considering wave propagation through the sample, where (4.18) was applied so that the sample phase constant (β_2) was used for β_x and sample length (L_2) was used for L_x . Since the phase constant is simply the imaginary component of the complex propagation constant (γ_2 where $\gamma_2 = j\omega\sqrt{\mu_{r2}\varepsilon_{r2}}$), an equation for the complex relative permittivity results by substituting $\omega\sqrt{\mu_{r2}\varepsilon_{r2}}$ for β_2 in (4.18) and solving for ε_{r2} , which yields the same equation as in (4.15). Although this equation is of the same form as an air-core solution, it gives rise to different results, partly because the reflection coefficient (Γ_{12}) is different for a dielectric filled core due to the effect of a non-air-core interface at the $\varepsilon_{r1}/\varepsilon_{r2}$ boundary. This effect is more apparent in the general expression for the complex magnetic permeability (μ_{r2}). To derive an expression for μ_{r2} , a second equation is needed because ε_{r2} and μ_{r2} are mathematically coupled in (4.15). The second equation

was developed by expressing the reflection coefficient at the interface between regions I and II (Γ_{12}) in terms of characteristic impedances (Z_1, Z_2), which may be written as follows:

$$\Gamma_{12} = \frac{Z_2 - Z_1}{Z_2 + Z_1} = \frac{\sqrt{\mu_{r2}/\epsilon_{r2}} - \sqrt{\mu_{r1}\mu_0/\epsilon_{r1}\epsilon_0}}{\sqrt{\mu_{r2}/\epsilon_{r2}} + \sqrt{\mu_{r1}\mu_0/\epsilon_{r1}\epsilon_0}}. \quad (4.21)$$

By substituting (4.14) for ϵ_{r2} into (4.20) and solving for μ_{r2} , the following relationship results

$$\mu_{r2} = \frac{j}{\omega L_2 \epsilon_0} \ln(z) \left(\frac{1 + \Gamma_{12}}{1 - \Gamma_{12}} \right) \sqrt{\frac{\mu_{r1}}{\epsilon_{r1}}}. \quad (4.22)$$

Equations (4.15) and (4.22) comprise a general solution to the NRW method for dielectric analysis. The analysis used to derive these expressions was simplified by assuming that the effects of the coaxial step in the outer conductor are negligible. However, the following sections will show that these effects can not be ignored.

4.4 Coaxial-line test fixture construction

The coaxial-line test fixture was constructed from a 119.6 mm long, 50 Ω copper-jacketed, PTFE-filled, semi-rigid EZ-form (EZ-250) cable with standard SMA plug connectors (see Figure 4.2). The specimen holder, located at the center of the test fixture, was constructed by removing a 44.2 mm section of the cables outer copper-jacket and Teflon PTFE core. Care was taken not to breach the silver-coated center conductor while performing this modification. In addition, the walls of the PTFE core were made smooth and perpendicular to the center conductor.

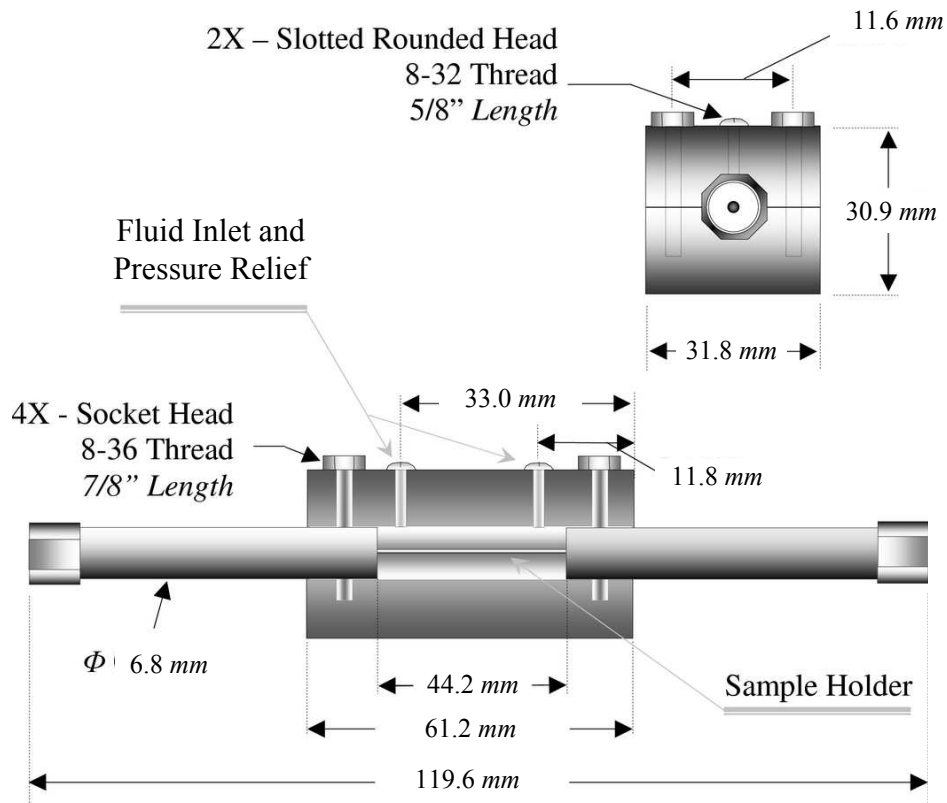


Figure 4.2: Coaxial transmission line fixture for dielectric measurements of lossy liquids whereby the sample holder is constructed from a semi-rigid coaxial line with fluid inlet and pressure relief.

The exposed center conductor in the machined cable was enclosed using a machined 774.2 mm^2 solid copper bar. The bar was cut to a length of 61.2 mm and then sliced into two equal halves along the length. The simplest approach to machining the enclosure to house the exposed coax involved drilling a 6.4 mm diameter trench through the center of two halves for the solid copper bar. The machined bar was further modified to provide four threaded holes for combining the two halves. Threaded inlet and outlet pressure-relief valves were constructed above the specimen holder using screws that were machined to provide a smooth internal surface for the coax. When assembled, this

enclosure resulted in a 0.8 mm step-discontinuity at the PTFE-specimen interface, due to removal of the copper jacket from the semi-rigid coax. The characteristic impedance (Z_0) for the semi-rigid transmission line may be described by the equation:

$$Z_0 = \sqrt{\frac{\mu}{\varepsilon}} \frac{\ln(b/a)}{2\pi}, \quad (4.23)$$

where b and a are the outer and inner conductor diameters (see Figure 4.1 above) , which produced a 49.2 Ω characteristic impedance for a Teflon ($\varepsilon=2.07$) dielectric. This characteristic impedance value was used for regions I and III coaxial transmission line (Z_{oA}). (Note: A coaxial step in the outer conductor for the sample holder in region II produced a characteristic impedance (Z_{oB}) of 56.7 Ω for a Teflon dielectric.) Somlo showed that a step capacitance (C_d) may be used to describe the coaxial step in the outer conductor, expressed as

$$C_d(\alpha, \tau) \approx \varepsilon_{r13} \pi a \times \frac{\varepsilon_0 \varepsilon_{r2}}{100 \cdot \pi} \left[\frac{\alpha^2 + 1}{\alpha} \ln\left(\frac{1 + \alpha}{1 - \alpha}\right) - 2 \ln\left(\frac{4\alpha}{1 - \alpha^2}\right) \right] \dots \quad (4.24)$$

$$+ \varepsilon_{r13} \pi a \times 4.1 \times 10^{-15} (0.8 - \alpha)(\tau - 1.4),$$

where $\alpha = (b - a)/(c - a)$, $\tau = c/a$ and a, b , and c are radii of the coaxial test fixture [113]. This equation is noteworthy because it shows that the coaxial step introduces a capacitance that is a function of the complex relative permittivity of the test sample.

4.5 The utility of Teflon for PTFE core

Teflon PTFE is a registered trademark of DuPont Company. It is a commonly used dielectric in coaxial transmission line construction because of its broadband electrical- and environmental-stability [9]. Characterized by a low dielectric constant, low dissipation factor, high arc-resistance as well as a high surface and volume resistivity, PTFE is well suited in the construction of RF/microwave coaxial transmission lines. These remarkable electrical properties are achieved through the control of five factors: the presence of macroscopic flaws, extent of microporosity, percent crystallinity, molecular weight, and degree of orientation. These physical characteristics may lead to increased analytical complexity for extracting material properties from measured data if the liquid specimen is partially absorbed into the PTFE at the specimen boundaries. PTFE mechanical and chemical properties must also be considered in its application as a transmission-reflection measurement test fixture. Fortunately, PTFE has remarkable mechanical and chemical properties as well. Its resolubility assures a distinct boundary that makes data analysis simpler. Furthermore, PTFE offers some chemical resistance to corrosive reagents, which allows for testing over a broad range of specimens, including biomaterial. The non-adhesive nature of PTFE supports methods for preparing consecutive test specimens with minimum fixture preparation. Moreover, its mechanical flexibility at low temperatures as well as stability at high temperatures adds ease in fixture manufacturing and provides an environment for testing over temperature. As a result, the electrical, mechanical and chemical properties of PTFE make it a useful core in transmission-line test fixtures.

4.6 Frequency-domain simulation and measurement

The sections below present simulation and measurement data for the coaxial test fixture. Since there is a step-discontinuity in the specimen holder, simulations are shown for both the condition of continuity and step-discontinuity at the PTFE-specimen interface. These conditions were controlled in simulation by adjusting the outer diameter of the specimen holder (TL2). A curve was fitted to the error associated with a comparison of the two simulations to produce an equation used to adjust the NRW solution for permittivity. Due to the effects of half-wavelength resonances, the measurement data was processed using several other methods to determine the approach that provided the closest Cole-Cole approximation over frequency. These results were compared to a new method for resolving the permittivity of dilute lossy liquids.

4.6.1 Simulation results and analysis

Simulation of the coaxial test fixture was accomplished using Agilent Advanced Design System (ADS) 2004A. As shown in Figure 4.3, the coaxial test fixture was constructed in ADS using an input/output port (I/O) defined by TL3 and TL4 and a specimen holder (TL2). Coax TL5 represents a bulkhead connector that was inserted in the fixture to facilitate connecting the fixture to a coaxial cable. This bulkhead and coaxial cable was given a combined length of 1626 *mm* whereas TL6 was sized to 152.4 *mm* long. The I/O ports (TL3 and TL4) were assigned an inner and outer conductor diameter of 1.63 *mm* and 6.4 *mm*, respectively. To capture the step-discontinuity at the

TL6/TL3 and TL4/TL5 interfaces, the inner diameter of the outer conductor for the specimen holder measured 5.31 mm and 6.4 mm, respectively.

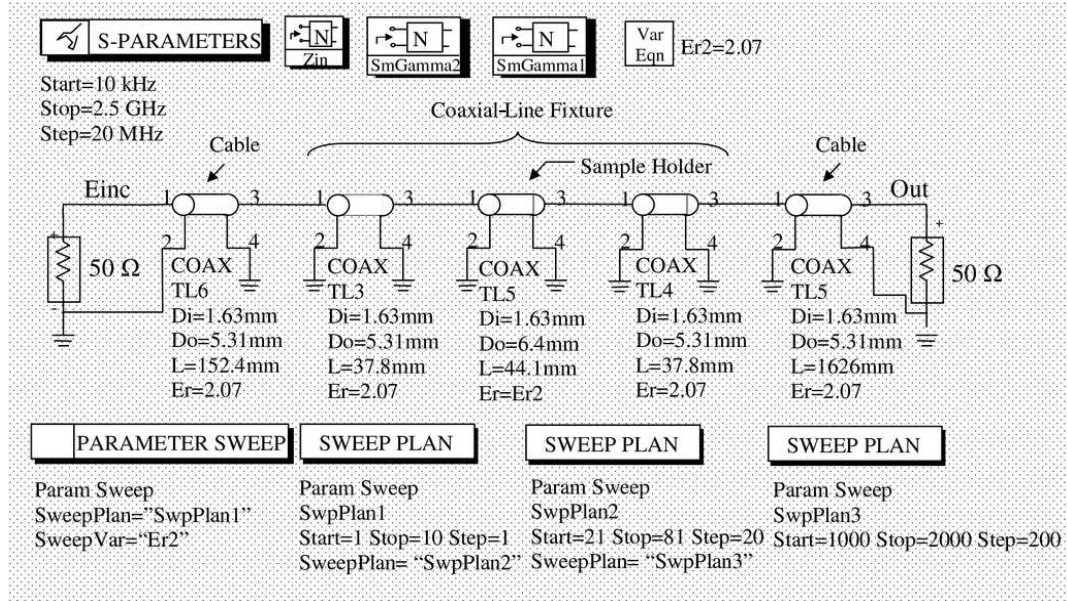
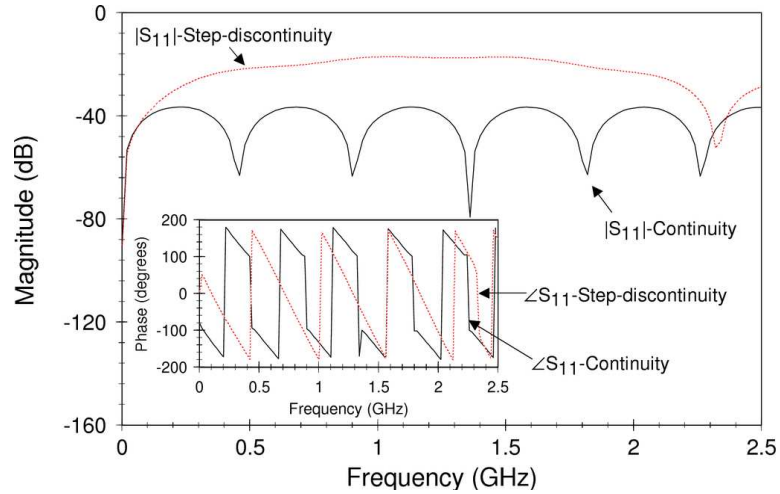
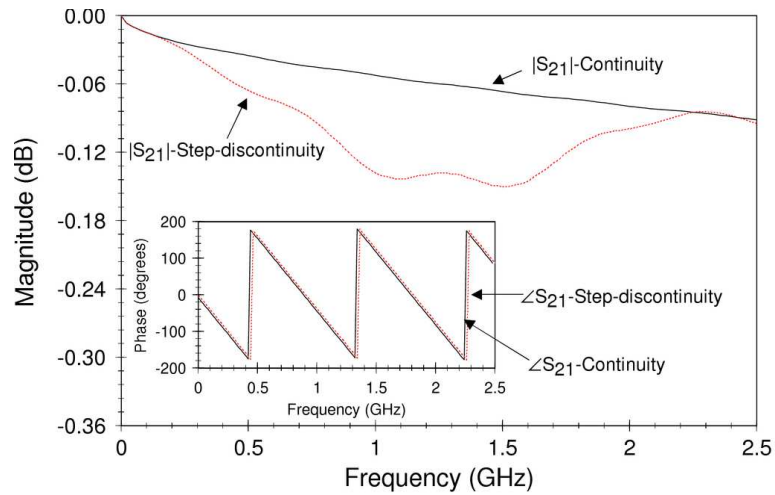


Figure 4.3: ADS schematic block of a coaxial fixture for computing the complex relative permittivity from S-parameter simulation data.

The coaxial fixture was captured in an ADS schematic for computing the complex relative permittivity from S-parameter simulation data. Dielectric parameters were computed for the sample (ϵ_r) by adding the equation sets for (4.15) and (4.22) in the data display. The effects of TL6 and TL5 were de-embedded to provide the S-parameters referenced to the PTFE-specimen interfaces located at TL3/TL2 and TL4/TL2. The S-parameters in the measurement plane (see Figure 4.4A-B) showed an increased reflection magnitude under the condition of a step-discontinuity. These frequency dependent differences showed that the step-discontinuity in the fixture can not be ignored. To correct NRW results for the effects of the coaxial step, one may transform the characteristic impedance of the fixtures sample holder from a $\sim 50.0 \Omega$ coax to a 56.7Ω



(A)



(B)

Figure 4.4: A simulated comparison of the de-embedded S-parameters for an unaltered holder with a 5.31 to 6.35 mm diameter, where (A) is phase and magnitude of S_{11} and (B) S_{21} (TL5/TL6 de-embedded).

coax or decompose the measured S-parameters into a lumped element equivalent circuit and add the step capacitance (4.24). As discussed in section 4.4, there is a dependency on the relative complex permittivity of the material under test, which complicates these approaches. A more simple approach to data correction was used by applying the S-

parameters in Figure 4.4 to compute the complex relative permittivity for a fixture with and without a step-discontinuity. In a plot of the permittivity resulting from this computation (see Figure 4.5), the weaknesses in the NRW method were readily apparent. At about 2.3 GHz a resonance effect occurred in the simulated data, which was accompanied by a sharp spike and drop in ϵ_r' , as well as negative going transients in ϵ_r'' . Rhode and Scharz identifies this phenomena as half-wavelength resonance, which occurs when the sample length is equivalent to multiples of one-half wavelength in the material [114]. As a result of half wavelength resonance, there was a loss in measurement

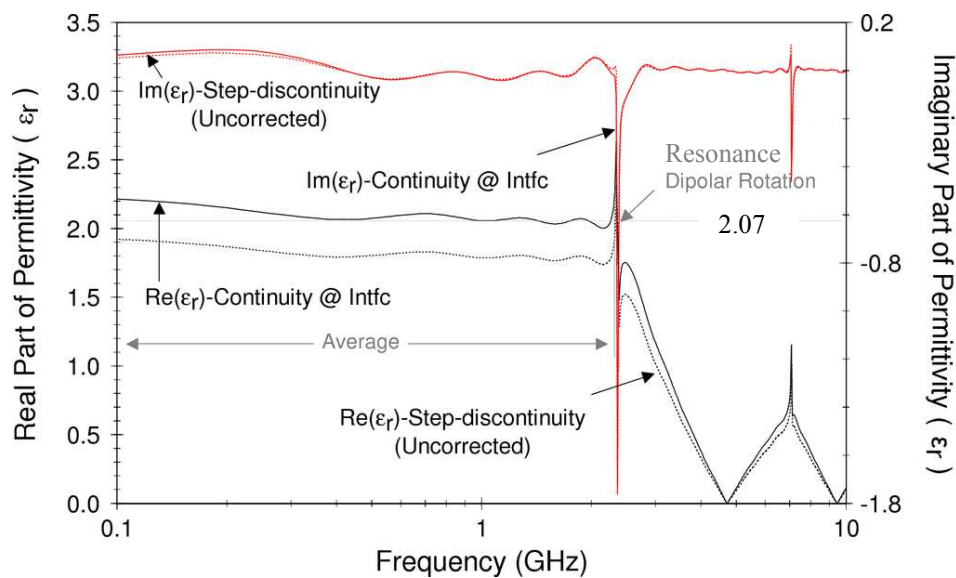


Figure 4.5: A simulation of the real and imaginary part of ϵ_r for a specimen holder that transitions smoothly (continuous) at PTFE-specimen interface.

accuracy and the characteristic relaxation of the simulated sample material (Teflon, $\epsilon_r=2.1$) could not be resolved (see Chapter 5 for a solution to this problem). Nonetheless, the morphology of the complex relative permittivity corresponding to a fixture with and

without a step-discontinuity were similar. Only an amplitude difference for ε_r' was observed.

As a result, a simple approach to correcting for the effects of the coaxial step was developed. This approach entailed

- computing the permittivity with and without a step-discontinuity over several simulated sample values for $\varepsilon_{r,2}$,
- calculating an error for the difference between the computed permittivity values,
- fitting a difference equation to the calculated error, and
- correcting the NRW permittivity in (4.15) using the difference equation.

A comparison of the computed permittivity with (outer conductor diameter, $\Phi=6.4$ mm) and without ($\Phi=5.31$ mm) a step-discontinuity present was used calculate an error, which was plotted over 1-1000 range for $\varepsilon_{r,2}$ (see Figure 4.6 below). The error associated with a coaxial step moved from 12-30% as $\varepsilon_{r,2}$ changed. This error data were fitted to an equation using a custom equation in MATLAB. This custom equation was constructed as:

$$Adjust = A \exp \frac{B}{\varepsilon_r'} . \quad (4.25)$$

where ε_r is the real part of the relative permittivity, and constants A and B are 0.159 and 0.0725, respectively. Application of this adjustment to correct the NRW permittivity

resulted in a good fit between the fixtures with and without continuity at the PTFE-specimen interface.

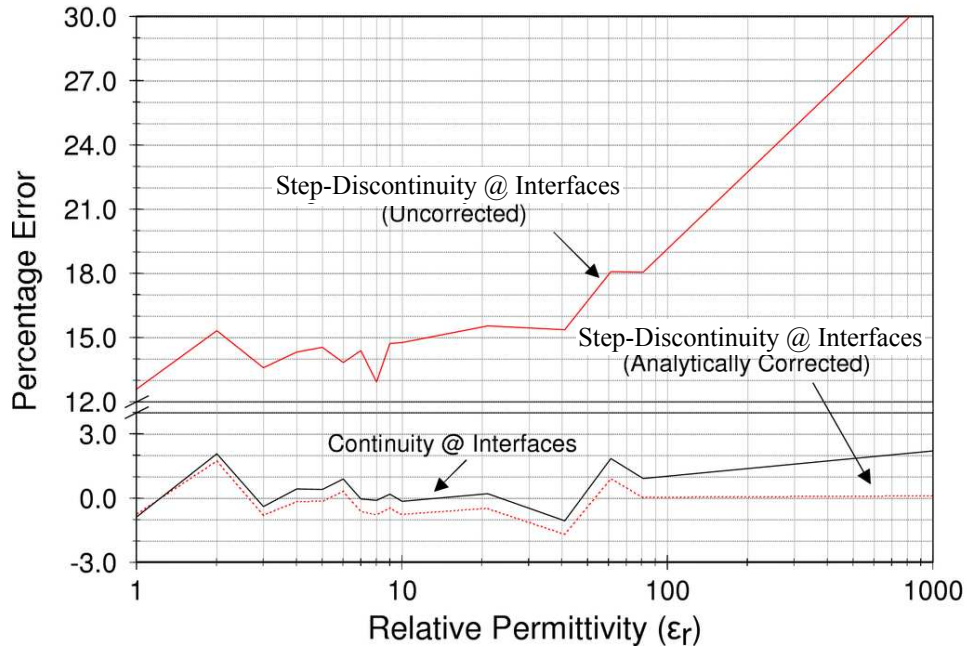


Figure 4.6: A simulated comparison of the error associated with the real part of ϵ_r , for a continuous specimen holder against ones with a discontinuity at the PTFE-specimen (PTFE-S) interface. Note: the step-discontinuity occurs as the I/O port (5.31 mm ID) transitions to the specimen holder (6.4 mm ID).

In table Table 4.1, measurement errors were taken for a maximum, minimum, and average error value associated with the permittivity, with application of the NRW algorithm. The average error corresponded to a measurement across all frequencies until half-wavelength resonance was reached. These three error measurements corresponded to PTFE-specimen interface with and without a step-discontinuity. However, the data associated with the step-discontinuity was adjusted using (4.25). Error measurements over an ϵ_r range of 1-2000 demonstrated better performance for the analytically corrected step-discontinuity at higher permittivity measurements (see Table 4.1).

Table 4.1: Half-wavelength resonance frequency ($f_{r1/2}$) and percentage error for measurement of ϵ_r in fixture with a continuous and corrected step-discontinuity interface.

ϵ_r	$f_{r1/2}$ (GHz)	Continuity @ PTFE-Specimen Interface						Step-Discontinuity @ PTFE-Specimen Interface					
		Real Part of ϵ_r			Error (%)			Real Part of ϵ_r			Error (%)		
		Min	Max	Avg	Min	Max	Avg	Min	Max	Avg	Min	Max	Avg
1	3.72	0.8	1.6	1.0	-20.0	56.8	0.6	0.8	1.2	1.0	-19.4	21.9	0.7
3	1.96	2.8	3.2	3.0	-5.2	6.5	0.4	2.9	3.2	3.0	-3.6	6.9	0.8
5	1.48	4.2	5.2	5.0	-16.2	4.6	-0.4	4.2	5.2	5.0	-15.4	5.0	0.1
7	1.26	6.4	7.3	7.0	-8.8	3.8	0.0	6.5	7.3	7.0	-7.6	4.2	0.6
9	1.12	8.6	9.3	9.0	-4.6	3.4	-0.2	8.7	9.3	9.0	-2.8	3.7	0.4
21	0.72	17.3	21.5	21.0	-17.6	2.6	-0.2	17.7	21.6	21.1	-15.6	2.9	0.5
41	0.52	39.0	43.4	41.4	-4.9	5.9	1.0	40.5	43.3	41.7	-1.3	5.5	1.7
81	0.36	72.3	83.6	80.2	-10.7	3.3	-0.9	74.5	83.6	81.0	-8.0	3.2	0.0
200	0.22	175.9	204.1	192.7	-12.1	2.0	-3.6	180.3	204.5	195.3	-9.8	2.2	-2.3
400	0.14	343.0	407.8	383.6	-14.2	2.0	-4.1	351.1	408.8	389.8	-12.2	2.2	-2.6
800	0.08	735.7	813.5	776.6	-8.0	1.7	-2.9	745.1	817.5	791.5	-6.9	2.2	-1.1
2000	0.04	1895	2017	1945	-5.3	0.9	-2.7	1937	2044	2000	-3.2	2.2	0.0

4.6.2 Measurement system and procedures

The hardware used to take physical measurements consisted of a coaxial test fixture, network analyzer, PC, syringe, MATLAB, and cables (see Figure 4.7). The cables were used to attach the fixture to the VNA. The coaxial test fixture was used to house the specimen. Data extracted from the VNA was processed in MATLAB using equations (4.16) and (4.23) for the NRW algorithm. Prior to data measurement, a full 2-Port (SOLT) calibration was performed on the VNA (Agilent 8753D) over a 30 kHz-6.0 GHz range. After removal of the inlet and outlet valves, the specimen holder was washed

with ethanol and then air-dried. The specimen holder was then rinsed once with the dilute liquid specimen to be tested, before filling it with the specimen using a syringe. Next, a VNA measurement was performed using 16-bit averaging. After saving the data to the PC, another ethanol wash was performed on the fixture.

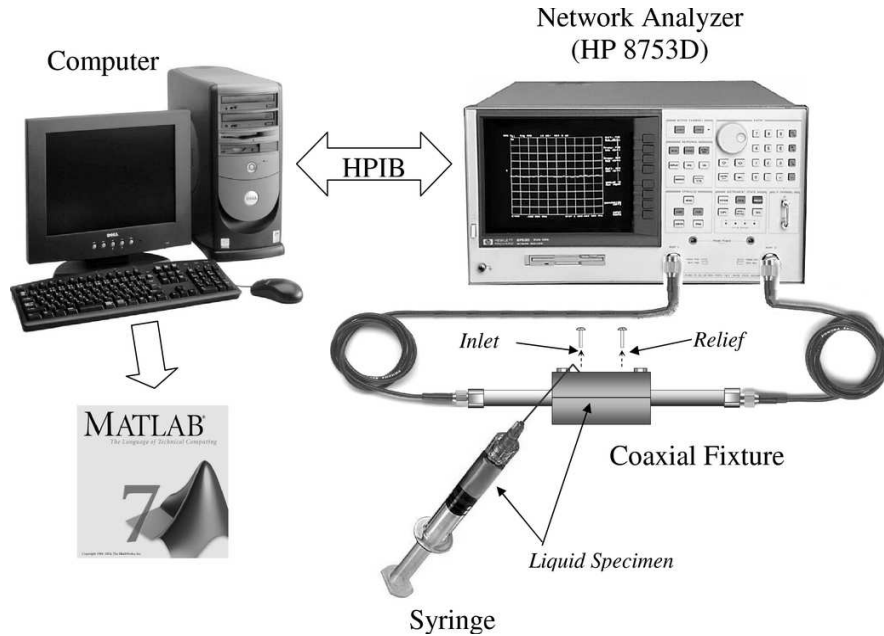


Figure 4.7: Experimental setup for dielectric characterization using transmission-reflection techniques.

In this measurement system, data were taken on several dilute solutions including ethanol, methanol, and de-ionized water. Ethanol data was used to tune the lengths of the coaxial cable (L_1 , L_2 , and L_3) to minimize the difference between the static permittivity (ϵ_s)—lowest frequency measure of ϵ_r' —produced by the corrected NRW algorithm and that obtained from the National Institute of Standards and Technology (NIST) dispersion tables [115]. The NIST dispersion tables provide model parameters ϵ_s , ϵ_o , and λ_c ,

which allows computation of the complex dielectric constant over frequency when applied to the Debye dispersion equation (see Table 4.2 below). The Debye dispersion equation is described by

$$\varepsilon = \varepsilon' - j\varepsilon'' = \varepsilon_s + \frac{\varepsilon_o - \varepsilon_s}{1 + (j\omega\tau)}, \quad (4.26)$$

where ε_s is the complex static permittivity (located at $\lambda = 0$), ε_o is the complex optical permittivity (located at $\lambda = \infty$), and τ is the characteristic relaxation time. The relaxation time may be described by the following equation:

$$\tau = \frac{\lambda_c}{2\pi c} = \frac{1}{2\pi f_c}, \quad (4.27)$$

where λ_c and f_c are the cut-off wavelength and frequency, respectively. The Debye dispersion model provides a complete description for the complex relative permittivity, whereas the NRW technique suffers from losses due to half-wavelength resonance effects. As a result, only the static permittivity parameter is useful for comparison with the corrected NRW results. The corrected NRW measurement data for ethanol, methanol, and de-ionized water were compared to the NIST static permittivity.

Table 4.2: NIST approximations of the Debye model parameters for ethanol, methanol and de-ionized water at 27°C.* Note: the critical wavelength associated with ethanol was assumed.

	ε_s	ε_o	λ_c (cm)
Ethanol	24.01	4.22	22.94*
Methanol	32.25	5.56	8.6
DI-Water	77.67	5.2	1.49

4.6.3 Measurement results and analysis

The plots in Figure 4.8 compare the results of applying the NRW technique (4.25) and modified-NRW algorithms against the Cole-Cole representation for air, ethanol, methanol, and de-ionized water at room temperature. In air (see Figure 4.8A), the test fixture yielded good measurement data for the real part of the complex permittivity (ϵ_r') to $f_{r1/2}$.

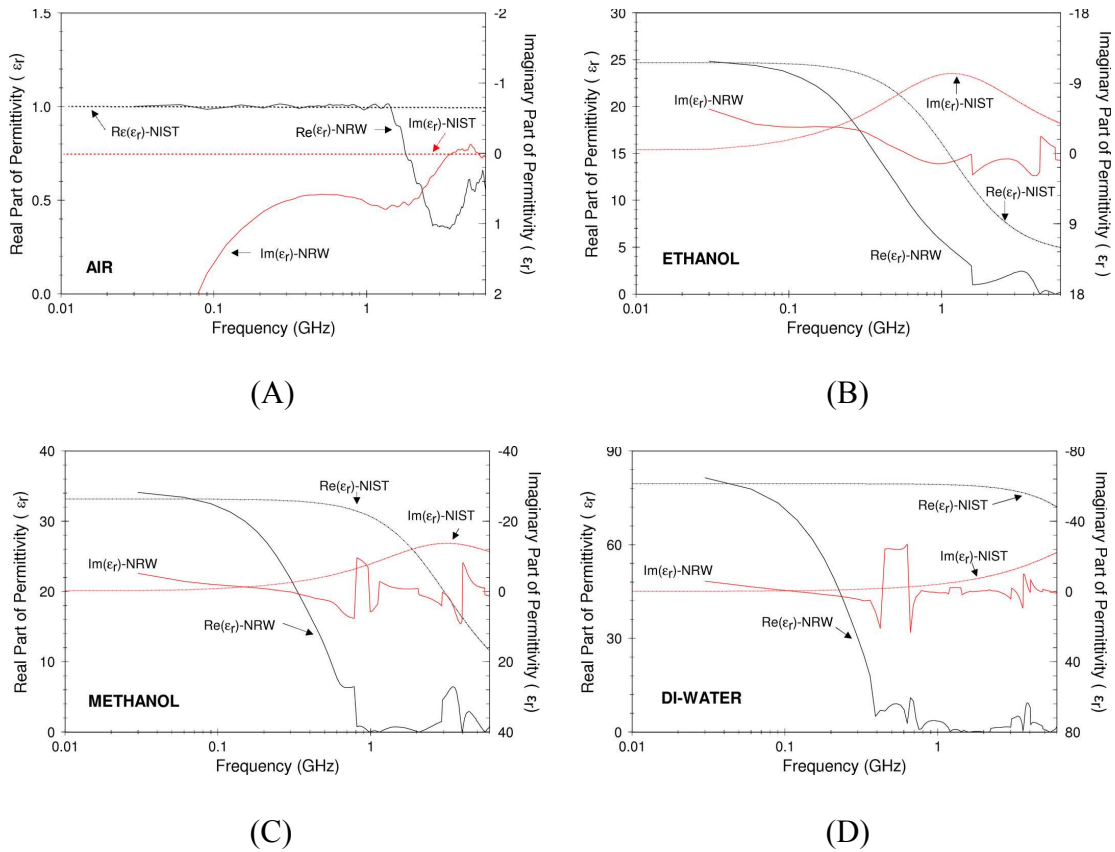


Figure 4.8: Permittivity measurement comparison of the corrected Nicholson-Ross-Weir (NRW) algorithm to NIST Debye dispersion data for (A) air, (B) methanol, (C) ethanol and (D) DI-water.

Similarly, a measurement of the real part of the complex permittivity for methanol (see Figure 4.8B), ethanol (see Figure 4.8C), and de-ionized water (see Figure 4.8D) showed good agreement with the NIST Debye dispersion, up to the resonant frequency ($f_{r1/2}$).

The static permittivity for methanol measured 34.1, ethanol 24.8 and di-water 81.4.

These measurements produce a low-frequency error of less than 3.0% as compared to the NIST standards (see Figure 4.9). However, the error grew exponentially, starting at 70 MHz, due to half-wavelength resonance effects.

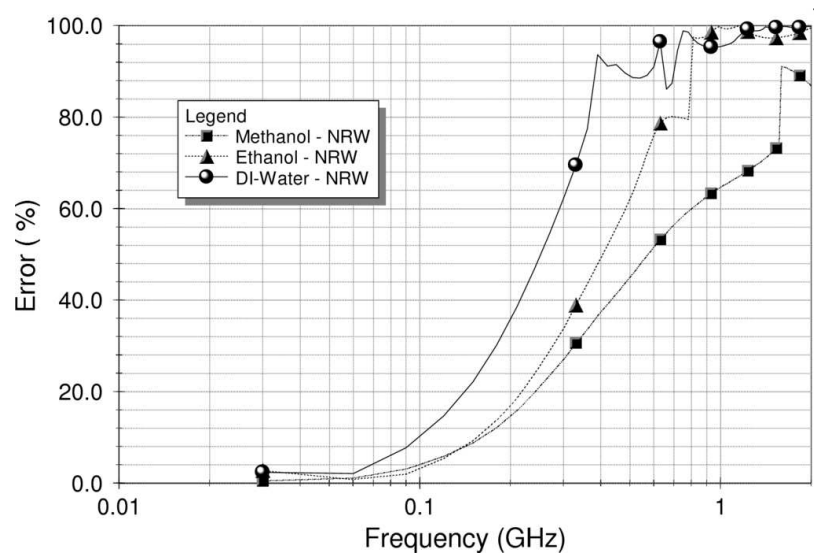


Figure 4.9: Percentage error for dilute substances using NRW algorithm.

The measure for the imaginary part of the complex relative permittivity (ϵ_r'') produced by the corrected NRW algorithm did not show good agreement with NIST data, and was unrealistic. This loss of resolution originates from not choosing the correct root in evaluating of the natural log of the propagation constant in (4.15) and (4.22). This natural log is expressed as $\ln(z)$ and is equal to the imaginary part $j(\theta + 2\pi n)$, where the

root $n = 0, \pm 1, \pm 2 \dots \infty$. Rhode and Schwarz reported that the choice of this root may be achieved by analyzing the group delay or by estimating the group delay from a good initial guess for ϵ_r and μ_r . In any event, estimating the group delay is random and weakens the case for selecting a Nicholson-Ross-Weir technique for analysis.

4.7 Measurement uncertainty and error

The sources of error in the above measurement were due to: an imperfect calibration of the VNA, inexact physical description of fixture dimensions, imprecise measurement of temperature for estimating the permittivity for the NIST standard calibration standards, and uncertainty associated with step-discontinuity computation. However, the most significant contributors to uncertainty in the VNA measurement were the imperfect analysis of the fixture dimensions and step-discontinuity. Assessment of dielectric properties using the NRW technique was based on the assumption that the fixture dimensions did not include problems with eccentricity or imperfect geometries. Eccentricity is a problem whereby the center conductor is not perfectly centered in the transmission line. Imperfect fixture geometries captures problems associated with imperfections due to machining of the fixture. A combination of these problems adds uncertainty because they were considered negligible, although an inspection confirmed the existence of small scratches on the inner conductor, and imperfections on the side-walls of the sample holder.

4.8 Summary

A reduction in the complexity for coaxial-line test fixtures for transmission-reflection measurement was obtained by applying a non-air-core assumption to the dielectric of the fixture. This assumption provided a means to construct a simple low-cost fixture with the capability to contain liquid specimens by using a Teflon PTFE filled transmission line. However, development of a coaxial fixture with a PTFE core required reformulation of the NRW equation set based on a non-air-core assumption. An outer step-discontinuity at the PTFE-sample interfaces of the fixture was allowed to simplify machining, which introduced a shunt capacitance that is dependent upon the dielectric properties of the material under test. This dependency introduced some measurement error while using the NRW technique and motivated the development of alternative approaches for extraction of the dielectric properties. Even so, frequency-domain measurements in air, ethanol, methanol, and de-ionized water demonstrated a viable fixture that could be applied to the measurement of a variety of specimens.

Chapter 5

A Genetic Algorithm Approach to the Electromagnetic Characterization of Materials in a Coaxial Fixture

This chapter presents a genetic algorithm (GA) approach to the electromagnetic characterization of materials, which offers a means to circumvent the problems of half-wavelength resonance in the Nicholson-Ross-Weir technique and local minima in iterative techniques. Moreover, the GA presented in this chapter offers an improvement over Oswald's genetic approach by expanding the parametric limits of the genome and incorporating a measure for magnetic permeability [116]. These improvements allow for computation of the dielectric properties over a wider range of materials. The above contributions are presented below by first providing background information on permittivity models. Next, the genetic algorithm is introduced and then applied to the measurement of traceable materials, including ethanol, methanol, and de-ionized water. Lastly, the chapter concludes with an evaluation of uncertainty and a summary.

5.1 Background and motivation

Electromagnetic characterization is of interest in a broad spectrum of research disciplines [111, 117, 118]. In this research, electromagnetic characterization of biomaterials is of interest. Biomaterial characterization often entails sample preparation,

data measurement and property determination [102, 107]. Due to limitations in previous techniques, researchers have focused mainly on enhancing the ease and accuracy of computing the dielectric properties for materials [119]. The Nicholson-Ross-Weir technique is perhaps the most heavily referenced technique in coaxial-line transmission-reflection measurements [104]. It provides an explicit means for computing the permeability and permittivity from measured S-parameters. However, this technique suffers from half-wavelength resonance effects, which results in a loss in measurement resolution at half wavelength multiples of the sample length [120, 121]. Iterative approaches based on the Debye model provide a means to circumvent this problem by assuming that the dielectric behavior of the material will follow a trend [122].

Accordingly, NIST describes three other techniques, including the NIST short-circuit-line (SCL) technique, new non-iterative technique, and iterative technique [123]. The SCL technique is not suitable for transmission-reflection measurement, the new non-iterative technique does not provide a measure for permeability, and the iterative technique suffers from a problem of local minimum [124].

To address these problems, Oswald and others presented a novel method for determining the dielectric properties of dispersive media using a weighted superposition of many Debye models in a genetic algorithm. Oswald's algorithm is based on the assumption that the magnetic permeability is equal to one. This technique included five model parameters and was applied towards the measurement of materials that had relative static permittivity which spanned a range between 6-12 [116]. Incorporating additional model parameters in order to increase the range of measurable materials and expanding

the range for the genome parameters increases the size of the search space for the algorithm. Consequently, an algorithm that is capable of measurement over a broad range of materials significantly challenges the ability for the algorithm to converge upon a meaningful solution. Nonetheless, the complex permittivity associated with various biomaterials span a broad range [125]. Furthermore, a priori information may not always be available to limit the search space. Therefore, a technique that offers the capability to measure a broad range of materials is useful in biomaterials measurement.

5.2 Overview of genetic algorithms

Genetic algorithms are adaptive heuristic search engines, which exploit historical information to direct random convergence towards an optimal solution within a designated search space. Inspired by evolutionary biology, genetic algorithms apply a genome, which comprises a possible solution to the problem, towards an objective function that provides a measure of the solution fit. This genome is then modified or evolved by genetic operators called selection, crossover, and mutation. It is then passed through the objective function again and the process repeats until the genome evolves into the best approximation within the constraints of the GA. The genome structure is called a genetic representation. Although the genetic representation remains constant, the values assigned to the alleles—the structural components of the genome—are variable. The numerical limits or bounds for these variables define the population from which the genome is constructed. Consequently, a single genome is assembled from a population through the selection process, in which the GA selects values from the population based

on pre-defined stochastic schemes. Following selection, the assembled genomes, which often include two parents, are modified through a process called crossover in which the two parents share alleles to construct a child. This child genome may be mutated so that randomly selected alleles are further modified to provide different features from the parents (see Figure 5.1). The objective or fitness function is central to GA performance [126].

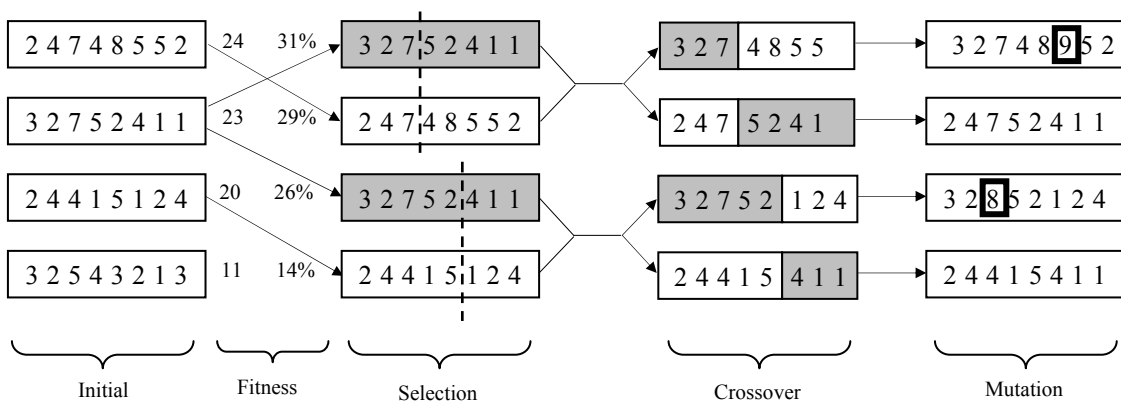


Figure 5.1: Evolutionary process of a genetic algorithm.

5.3 Genetic-based approach for parametric extraction

The problems of half-wavelength resonance associated with the NRW technique and local minimum associated with other iterative techniques were circumvented by first assuming that the dielectric behavior of the material follows a trend. Peter Debye noted a trend in the materials properties and developed a dielectric relaxation model that relates dipole moments to dielectric constant and relaxation time, as seen in the equation

$$\epsilon_r(\omega) = \epsilon_s + \frac{\epsilon_o - \epsilon_s}{1 + j\omega\tau}, \quad (5.1)$$

where $\varepsilon_r(\omega)$ is the relative complex dielectric constant, ε_s is the static permittivity at the low-frequency limit, ε_∞ is the optical permittivity at the high frequency limit, ω is the angular frequency, and τ is the characteristic relaxation time of the medium [127].

Havriliak and Negami introduced an empirical modification to account for asymmetry and broadness in the relaxation process of some polymers [128]. This modification resulted in:

$$\varepsilon_r(\omega) = \varepsilon_s + \frac{\varepsilon_o - \varepsilon_s}{[1 + (j\omega\tau)^{1-\alpha}]^\beta} \quad (5.2)$$

where α is the distribution parameter which describes the asymmetry of the spectra and β is the broadness. K.S. Cole, R.H. Cole, and D.W. Davidson also introduced variants to the Debye model for special cases [129]. Oswald and others presented a novel method for determining the dielectric properties of dispersive media using a weighted superposition of many Debye models. The present research extends Oswald's work by applying a genetic algorithm to characterization of three traceable standards namely ethanol, methanol and de-ionized water. A measure of air is also included. These measurements were taken in an experimental transmission-reflection fixture, which has an outer step-discontinuity at the material interfaces.

This research applied a library called GALIB, that was supplied by MIT, towards the construction of a genetic algorithm using C++ [130]. Like other algorithms, this software required definition of the objective function, genetic representation and operators to work. The genetic representation used in construction of the GA for this research included a structure containing nine alleles (see Table 5.1). These alleles

comprise the dielectric model parameters used to define the genetic representation. The range selected for the dielectric model parameters was determined by including the limits associated with dielectric measurement data that was compiled by the National Bureau of Standards (now NIST) [115].

Table 5.1: Genetic representation for genome construction in permittivity extraction GA.

bit	Allele	Effective Range
1	ϵ_s -- Relative Complex Static Permittivity	$1 \leq \epsilon_s \leq (\text{NRW}_{\text{Approx}} \cdot 1.025)$
2	ϵ_o -- Relative Complex Optical Permittivity	$1 \leq \epsilon_o \leq 13$
3	τ_{re} -- Electric Relaxation Time	$10^{-16} \leq \tau_{re} \leq 10^{-7}$
4	σ_{dc} -- DC Conductivity	$(\text{NRW}_{\text{Approx}} \cdot 0.1) \leq \sigma_{dc} \leq (\text{NRW}_{\text{Approx}} \cdot 0.5)$
5	μ_s -- Relative Complex Static Permeability	$1 \leq \mu_s \leq 2$
6	μ_o -- Relative Complex Optical Permeability	$1 \leq \mu_o \leq 2$
7	τ_{rm} -- Magnetic Relaxation Time	$10^{-16} \leq \tau_{rm} \leq 10^{-7}$
8	α -- Cole-Cole Asymmetry Parameter	$0 \leq \alpha \leq 1$
9	β -- Havrilak-Negami Broadness Parameter	$0 \leq \beta \leq 1$

A process of trial and error was used to select the genetic operators and other GA configuration parameters, with the goal of balancing the run time and data fit following algorithm convergence. To achieve these goals the GA was configured to run for 300 generations. It was also configured for a total of 64 populations containing 500 data points for each of the alleles. A probability of 50% was applied to the mutation and 90% to the crossover probability (see Table 5.2).

Table 5.2: Parameter set for genetic algorithm performance.

Parameter	Value
Scaling Type	No Scaling
Selector Type	Rank Selector
Number of Generations	300
Population Size	500
Number of Populations	64
Mutation Probability	0.5
Crossover Probability	0.9
Replacement Percentage	.05

The objective function used in this GA provided an estimate for the goodness of fit between the measured and computed S-parameters. Since the GALIB library only supports the construction of a single objective function, components contributing to this fitting function were summed (see Figure 5.2). Thus, error values were constructed by summing the differences in the measured and calculated S-parameter magnitudes and the difference in the sign associated with the phase angle for both S_{11} and S_{21} . Since the total difference obtained by summing the error in magnitude was much less than 1 and the total differences obtained by summing the error in phase angle was much greater than one, weights were applied to these sums to balance the effect of each component on the error value, in order to control optimization. Consequently, the total sum for the difference in S-parameter magnitude was increased by a factor of 1000. The total phase angle sign error was cubed to compel an exponential increase in attention by the GA library with successive increases in the number of phase angle sign mismatches.

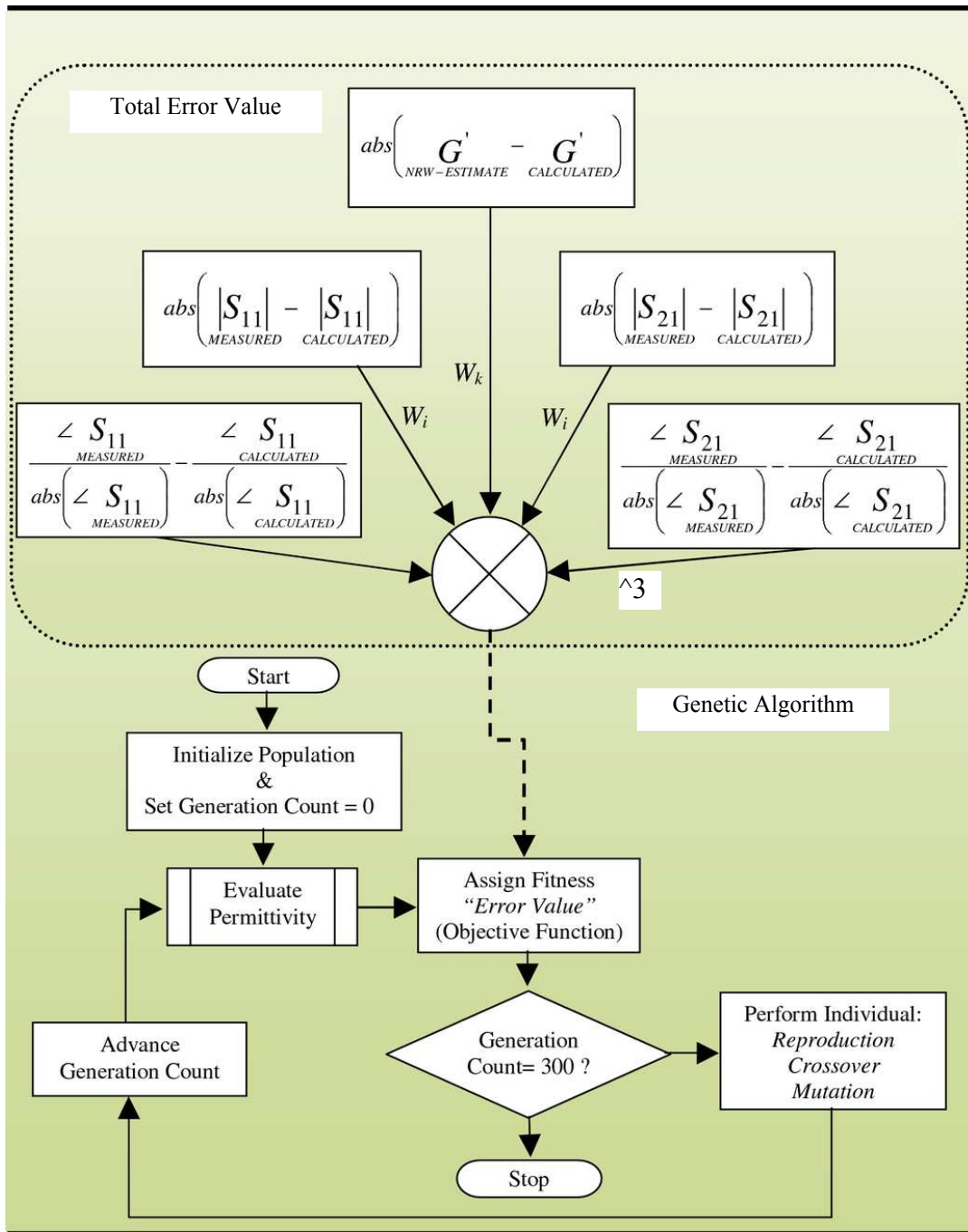


Figure 5.2: Flow chart for the GA, which demonstrates the components of the objective function.

The genetic approach to parametric extraction was implemented in four stages in order to mitigate the effects of introducing additional model parameters and expanding the genome range. Stage one was designed to provide an explicit calculation for the NRW complex permittivity, which was used to limit the search range for the static permittivity of stage two. In stage two, range limits were placed about the relaxation time so that ten different search ranges were created. These search ranges were continuous and incremented for ten different runs of the GA. In each run, the GA would find the best genome associated with the relaxation time search range.

Next, the best of ten was selected, and the genome was passed to stage three. In stage three, the Cole-Cole α parameter was set to vary in range from zero to one. Like the relaxation time of stage two, the optical permittivity of stage three was subdivided, and the best of ten was selected over subsequent GA runs. The other alleles of the genome were limited to vary in a range of $\pm 2.5\%$ of the stage two values. In stage four, the β parameter was allowed to vary in a range from zero to one for a Havrilak-Negami fit. In addition, the best genome from stage three was used to set the range limits associated with the allele for stage four by varying it from $\pm 1\%$ (see Figure 5.3). In this genetic approach, α and β parameters were introduced in stages to discourage impractical solutions by the GA. It was observed that the GA would arbitrarily find values for these parameters if introduced in stage two. In order to reduce the randomness of finding values for these parameters for successive runs, the GA was forced to determine the best fit using the Debye model parameters first, then Cole-Cole, and last Havrilak-Negami model parameters. As a result, the α and β parameters were used to refine the GA fit.

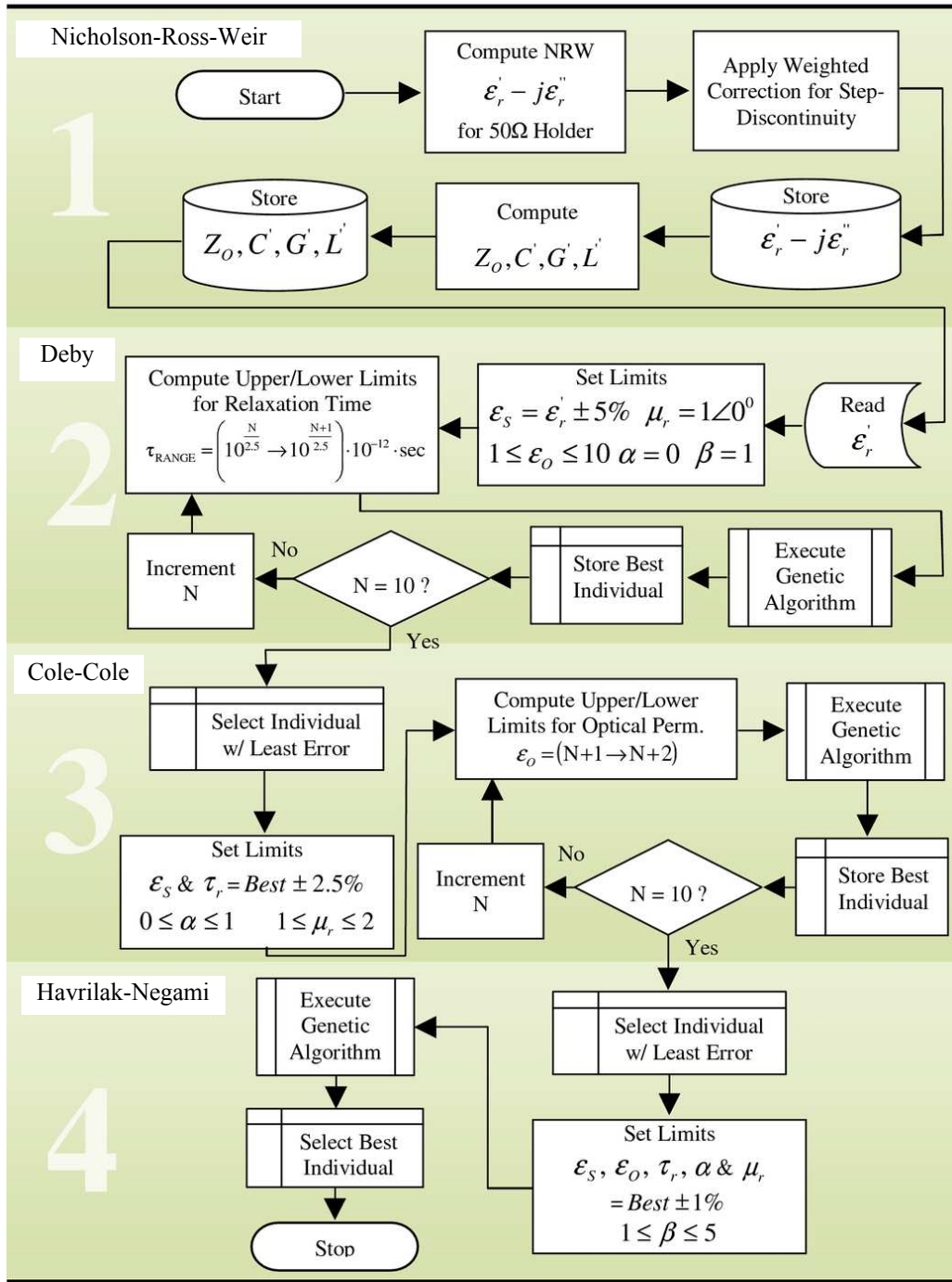


Figure 5.3: Flow chart of the genetic algorithm for permittivity determination.

5.4 Calculated S-parameters for comparison in GA objective function

The calculated S-parameters used for comparison with those measured with the VNA were determined by computing characteristic impedance (Z_w) and wave propagation constant (γ) from the GA parameters, which includes the static permittivity (ϵ_s), optical permittivity (ϵ_o), relaxation time (τ), dc conductivity (σ_{dc}), alpha dispersion parameter (α), beta dispersion parameter (β), static permeability (μ_s), and optical permeability (μ_o). These parameters are place into the following equations for computing the complex relative permittivity and permeability

$$\epsilon_r = \epsilon_s + \frac{\epsilon_{o(physical)} - \epsilon_s}{[1 + (i\omega\tau)^{1-\alpha}]^\beta} - j \frac{\sigma_{dc}}{\omega\epsilon_0} \text{ and} \quad (5.3)$$

$$\mu_r = \mu_s + \frac{\mu_o - \mu_s}{[1 + (i\omega\tau)^{1-\alpha}]^\beta}. \quad (5.4)$$

The frequency dependent values for ϵ_r and μ_r were used to compute the lumped element distributed transmission line parameters, which include

$$C_{Prime} = \frac{2\pi\epsilon_0 \text{Re}(\epsilon_r)}{\log\left(\frac{a}{c}\right)} \text{ (F/m)}, \quad (5.5)$$

$$G_{Prime} = \frac{2\pi\omega\epsilon_0 \text{Im}(\epsilon_r)}{\log\left(\frac{a}{c}\right)} \text{ (mhos/m)}, \quad (5.6)$$

$$L_{Prime} = \frac{\mu_r\mu_0}{2\pi} \log\left(\frac{a}{c}\right) \text{ (H/m)}, \text{ and} \quad (5.7)$$

$$R_{\text{Prime}} = \frac{1}{2\pi} \left(\frac{\rho_a}{a} + \frac{\rho_b}{b} \right) (\Omega/\text{m}), \quad (5.8)$$

where a and b are the inner and outer conductor diameters of the sample holder, ρ_a is the surface resistance of silver so that $\rho_a = \sqrt{\mu_0 \omega / 2 \times 59.6 \times 10^6}$ and ρ_b is the surface resistance of copper so that $\rho_b = \sqrt{\mu_0 \omega / 2 \times 63.1 \times 10^6}$. These distributed parameters were used to compute the characteristic impedance of the line and the wave propagation constant as represented by the following equations:

$$Z_w = \sqrt{\frac{R_{\text{Prime}} + j\omega L_{\text{Prime}}}{G_{\text{Prime}} + j\omega C_{\text{Prime}}}} \text{ and} \quad (5.9)$$

$$\gamma = \sqrt{(R_{\text{Prime}} + j\omega L_{\text{Prime}}) \times (G_{\text{Prime}} + j\omega C_{\text{Prime}})}. \quad (5.10)$$

Finally, the equations in (5.9) and (5.10) were used to compute the S-parameters

$S_{11_Calculated}$ and $S_{21_Calculated}$, expressed as follows:

$$S_{11_Calculated} = (Z_w^2 - Z_{ref}^2) \times \frac{\tanh(\gamma \times L_2)}{2Z_w Z_{ref} + (Z_w^2 + Z_{ref}^2) \times \tanh(\gamma \times L_2)} \text{ and} \quad (5.11)$$

$$S_{21_Calculated} = \frac{2(Z_{ref} Z_w)}{2(Z_{ref} Z_w) \cosh(\gamma \times L_2) + \sinh(\gamma \times L_2) \times (Z_w^2 + Z_{ref}^2)}. \quad (5.12)$$

These calculated values were used for comparison with the measured S-parameters in the objective function of the GA.

5.5 Performance results for the genetic algorithm

In this section, GA performance was assessed by conducting a frequency-domain measurement on air, ethanol, methanol, and de-ionized water using the vector network analyzer (VNA). The goodness of fit was evaluated along with a comparison of the traceable standards. Lastly, algorithm repeatability was determined through a type-A evaluation of the GA data obtained by running it ten times on the same set of data and observing the variations. Other sources of error were assumed to be negligible.

5.5.1 Measurement procedure

The hardware used to take dielectric measurements consisted of the following: a coaxial test fixture (see Chapter 4, Figure 4.2), HP8753D VNA, Intel PC, syringe, C++ based GA, and 12-inch SMA cables. The SMA cables were used to attach from the coaxial fixture to the VNA. Prior to data measurement, a full 2-port (SOLT) calibration was performed on the VNA over a 30 *kHz*-6.0 *GHz* range. After removal of the inlet and outlet screws, from the specimen holder portion of the test fixture, an ethanol wash was applied followed by the test specimen. Last, the VNA measurement data was captured using 16-bit averaging, extracted from the VNA, and processed with the GA.

5.5.2 Algorithm convergence using traceable standards

The transmission coefficient (S_{21}) for ethanol demonstrated good transmission at DC (see Figure 5.4A-D). The corresponding magnitude rolls off exponentially with an increase in frequency. As a result, the magnitude for the reflection coefficient (S_{11})

demonstrated a good impedance match at DC, which contributed to maximum power transfer at DC. The phase associated with ethanol for S_{11} rolls off very slowly, so that it appeared constant, above 500 MHz. In the 2nd stage of the GA, the measured and computed phases did not match very well, especially for S_{11} . Stage 3 of the GA resulted in improvement in the goodness of fit for the S-parameters. In this stage, the agreement between the calculated and measured phase for S_{11} improved notably, while this agreement for the phase of S_{21} improved only for frequencies below about 1.0 GHz.

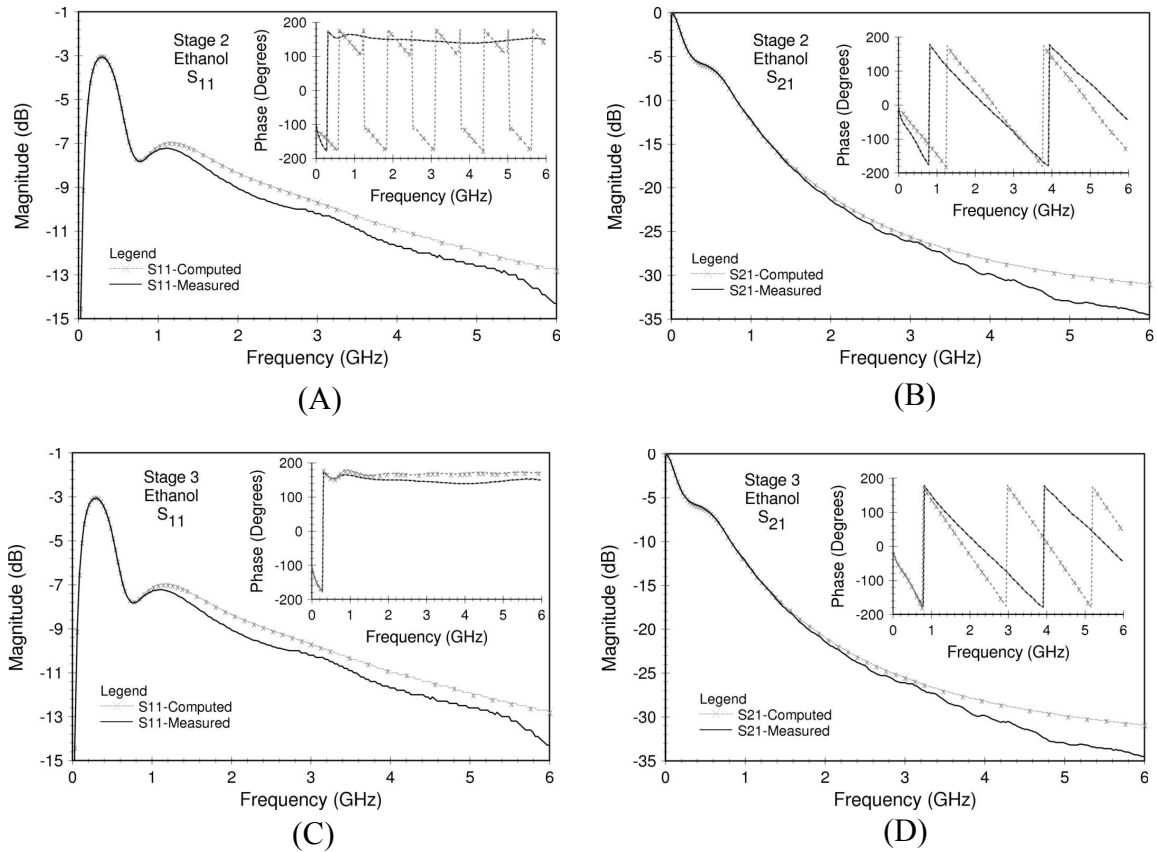


Figure 5.4: Measured versus calculated S-parameters for ethanol comparing (A) reflection and (B) transmission coefficients of 2nd GA stage, and (C) reflection and (D) transmission coefficients of 3rd stage at 27°C.

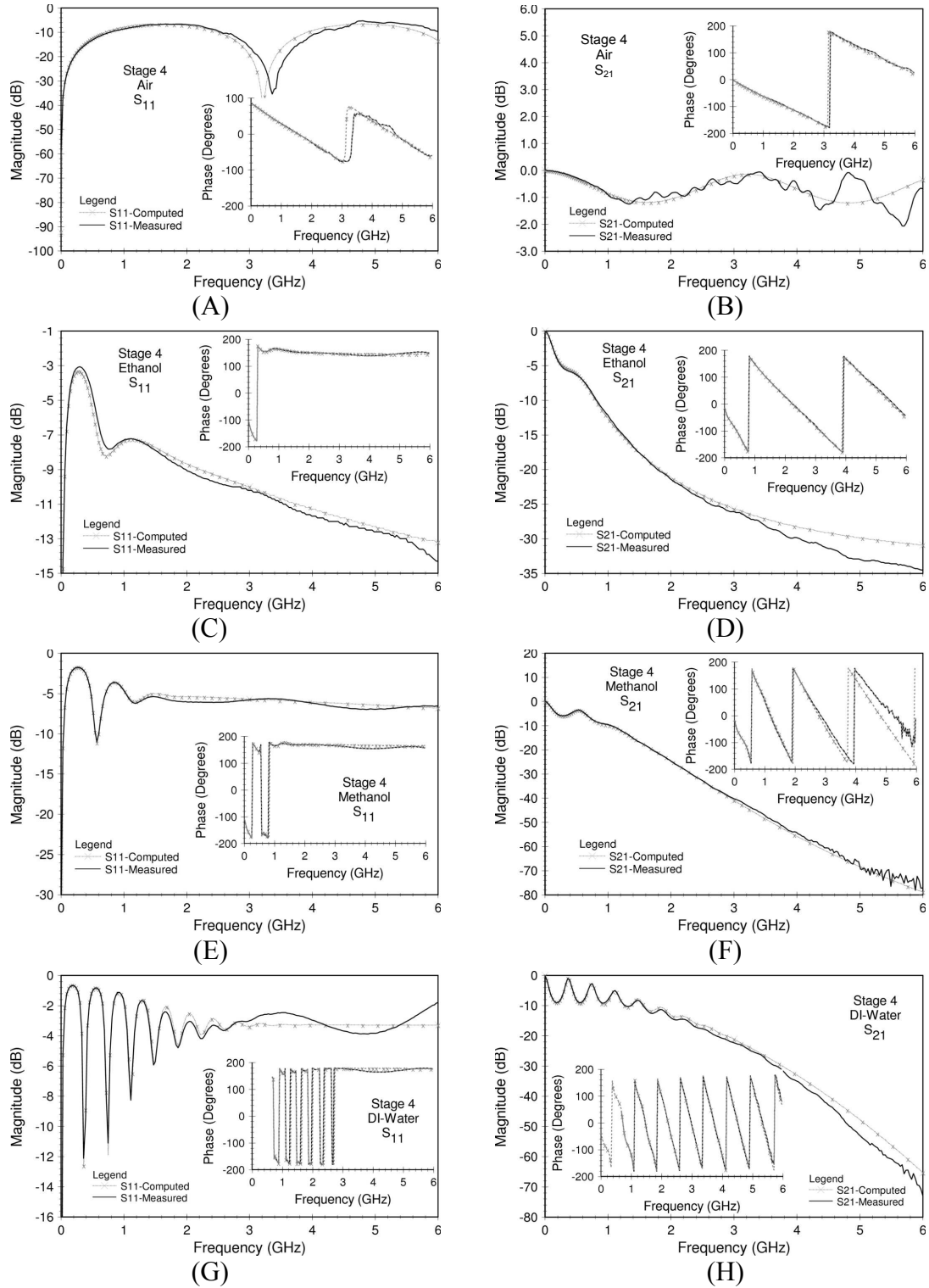
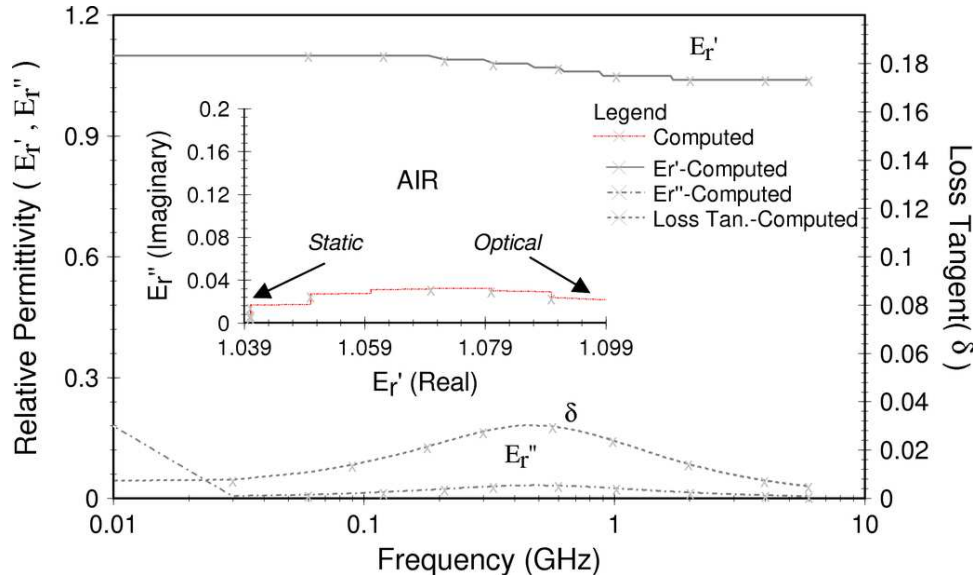


Figure 5.5: Measured versus computed S-parameters from 3rd GA stage for measurements of S11-S21 in (A-B) air, (C-D) ethanol, (E-F) methanol and (G-H) de-ionized water at 27°C.

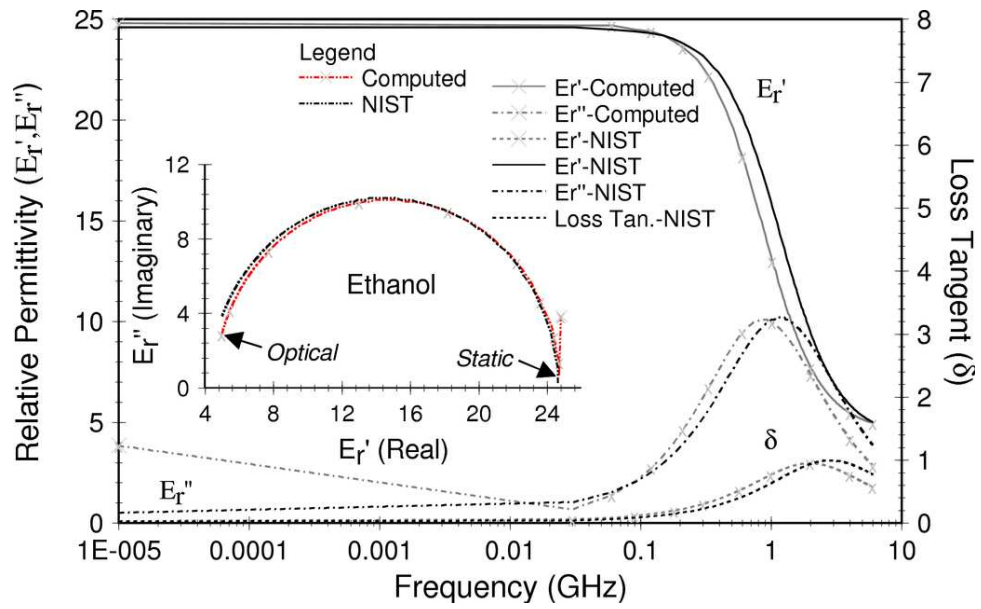
Finally, the stage four S-parameter fit was considered in assessing the performance of the GA. The algorithm provided a good fit between calculated and measured results for the S_{11} and S_{21} phase and magnitude for all of the dilute substance, over a 6.0 GHz bandwidth (see Figure 5.5A-G). In general, a better fit was observed at lower frequencies. The fit associated with the S_{21} phase for methanol showed less agreement at 6.0 GHz than any of the other substances. Conversely, the fit associated with S_{11} phase for ethanol showed the best fit. As a result, the GA demonstrated the ability to converge upon parameters, which provided a good solution for ethanol, methanol, de-ionized water, and air.

5.6 Error and uncertainty

The error and uncertainty in the measurement of ethanol, methanol and de-ionized water was evaluated by exploring goodness of fit between the NIST approximation for complex relative permittivity and that which was computed from S-parameter measurement data using the GA. The loss constant, real and imaginary parts of the electric permittivity, and complex plane plot are provided for air and ethanol (see Figure 5.6A-B) as well as methanol and de-ionized water (Figure 5.7A-B). Recall that the complex plane plot provides a means to determine if multiple dispersions exist based on the morphology of the semi-circle (see Chapter 2, Figure 2.2). The static and optical permittivity as well as relaxation time, which resulted from the GA, closely fit NIST data. The NIST approximations for the Debye model parameters for ethanol, methanol and de-ionized water yielded a static permittivity of 24.01, 32.25 and 77.67, respectively

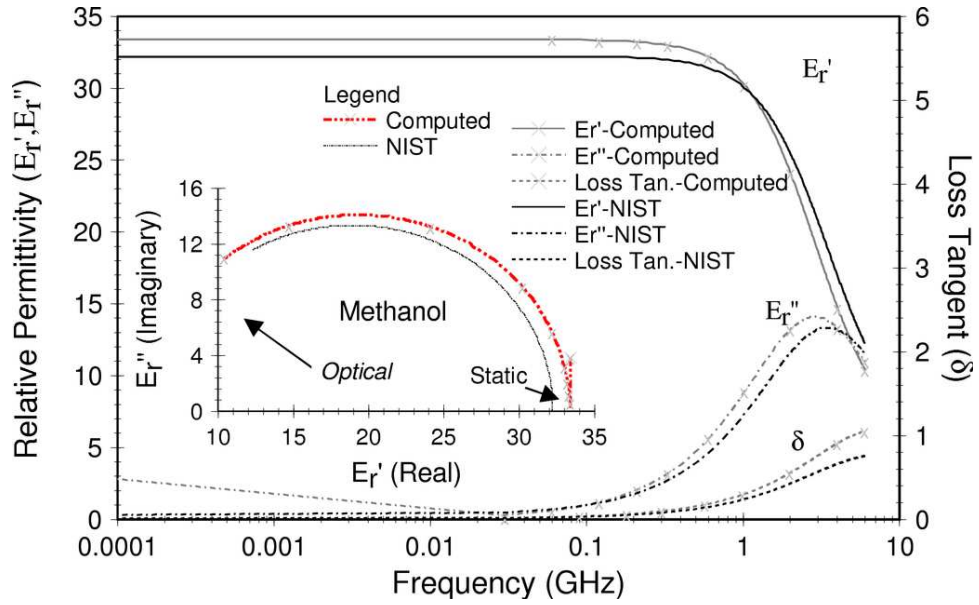


(A)

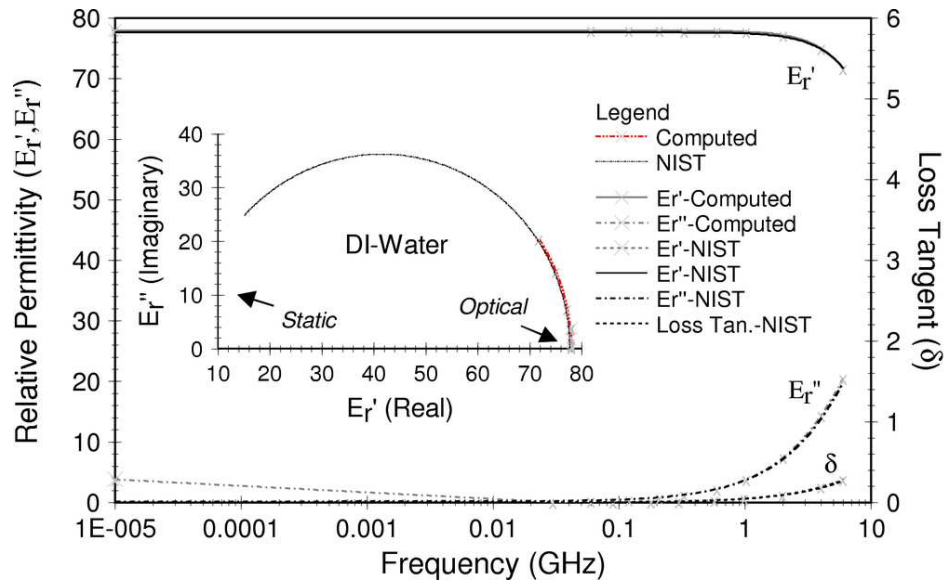


(B)

Figure 5.6: The complex permittivity and loss tangent for a stage 4 solution in the genetic algorithm for (A) air and (B) ethanol, at 27°C.



(A)



(B)

Figure 5.7: The complex permittivity and loss tangent for a stage 4 solution in the genetic algorithm for (A) methanol and (B) de-ionized water, at 27°C.

(see Table 4.2 in Chapter 4). The GA computed average values of 24.63, 33.32 and 77.93 for ethanol, methanol and de-ionized water respectively, from measured S-parameters. Methanol fit less precisely than measures for ethanol and de-ionized water. A good fit between measured and NIST results over frequency was observed. The measurements were taken at room temperature, which was recorded at 27°C using a mercury thermometer. It was assumed that the thermometer accurately reflected the fixture temperature and that room temperature remained constant during testing.

The standard uncertainty associated with the Debye model parameters was determined by running the GA for ten iterations on the same set of data. Based on a 90% confidence level, it was determined that the genetic algorithm yielded genomes within less than 1% of the mean. Approximations for air and ethanol yielded very low uncertainties for static permittivity and relaxation time. However, the uncertainty associated with the optical permittivity for de-ionized water was high. In fact, the sample size (n) required to achieve a distribution about the mean for de-ionized water was determined to be 1052 (see Table 5.3). This sample size represents the number of times the GA must be run for a given uncertainty ($u_i(\bar{x})$) over a 90% confidence interval, in order to achieve a 0.794% error. The equation used to compute the size is expressed as,

$$n = \left(Z_{\alpha/2} \cdot \frac{u_i(\bar{x})}{.00794} \right)^2, \quad (5.13)$$

where $Z_{\alpha/2}$ is the z score in a standard normal distribution (Z) table. Consequently, due to variability in the GA as it computes dielectric data for de-ionized water, many more iterations were required for the GA to produce normally distributed data.

Table 5.3: GA uncertainty ($u_i(\bar{x})$) and sample size (n) required for measurement of air, ethanol, methanol and de-ionized water at a 90% confidence level.

Material	ϵ_s		ϵ_o		λ_c (cm)	
	$\bar{x} \pm u_i(\bar{x})$	n	$\bar{x} \pm u_i(\bar{x})$	n	$\bar{x} \pm u_i(\bar{x})$	n
Air	$1.05 \pm 7.4\text{E-}16$	1	$1.00 \pm 1.4\text{E-}17$	1	$2.69 \pm 1.3\text{E-}3$	1
Ethanol	24.63 ± 0.062	1	4.61 ± 0.028	2	34.45 ± 0.29	3
Methanol	33.32 ± 0.097	1	5.88 ± 0.044	3	10.81 ± 0.053	2
DI-Water	77.93 ± 0.0131	1	3.17 ± 0.498	1052	1.54 ± 0.0106	2

It was determined that uncertainty was high for the optical permittivity in de-ionized water because of the large value for the relative static permittivity. In the imaginary component of the complex permittivity, the static permittivity (ϵ_s) is reduced by the optical permittivity (ϵ_o) as shown in the Debye expression below:

$$\epsilon_r(\omega) = \epsilon_s + \frac{\epsilon_o - \epsilon_s}{1 + (j\omega\tau)} \quad (5.14)$$

Therefore, a large relative distance between the static and optical permittivity results in greater uncertainty for the optical permittivity term in the GA. As a result, the objective function was modified to reduce the variability of the optical permittivity term. Since the optical permittivity is defined by the imaginary component of the complex permittivity

(see equation (5.3)), the conductance (G_{Prime} - see equation (5.6)) of the sample contributes most to variations in the optical permittivity (see Appendix C). Consequently, variability was reduced by adding a comparison between a NRW estimated conductance in stage one of the GA and calculated conductance in subsequent stages (see Figure 5.8).

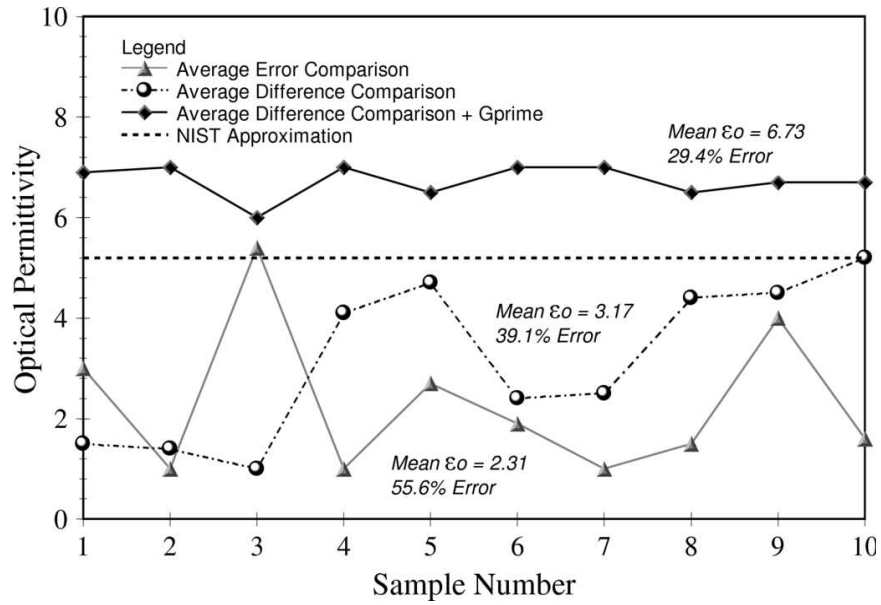


Figure 5.8: The uncertainty for various methods of representing the error associated with the fit between measured and computed S-parameters.

As a result, the statistical uncertainty associated with the Debye model parameter in de-ionized water was greatly reduced. Consequently, the sample size required for a normal distribution was decreased to eleven (see Table 5.4).

Table 5.4: A comparison of GA uncertainty in measurement of de-ionized water using two methods for comparing the difference in the measured and computed S-parameter values.

Objective Statement	Material	ϵ_s		ϵ_o		λ_c (cm)	
		$\bar{x} \pm u_i(\bar{x})$	n	$\bar{x} \pm u_i(\bar{x})$	n	$\bar{x} \pm u_i(\bar{x})$	n
$\Delta_{\text{Magnitude}}$	DI-Water	$77.93 \pm 1.31\text{E-}2$	1	$3.17 \pm 4.98\text{E-}1$	1052	$1.54 \pm 1.06\text{E-}2$	2
$\Delta_{\text{Magnitude}} + G_{\text{Prime}}$	DI-Water	$77.95 \pm 1.2\text{E-}2$	1	$6.73 \pm 1.1\text{E-}1$	11	$1.58 \pm 1.7\text{E-}3$	1

5.7 Summary

This genetic algorithm provided an enhancement to Oswald's approach by supporting a broader range of materials through the application of a Havrilak-Negami model, by extending the limits of the genome and by adding additional model parameters including magnetic permeability. However, these modifications increased the difficulty for the GA to converge upon a solution and increased the variability. These challenges were mitigated through a staged approach and by modifying the objective function. As a result, the algorithm provided an enhancement to available approaches enabling a means for effective convergence over a large parametric range.

Chapter 6

Ultra-Wideband/RF-Microwave Measurement System

This chapter presents the theory, architecture, measurement procedures, and calibration methods for a time-domain dielectric spectroscopy (also called an ultra-wideband/RF-microwave) measurement system used to characterize the dielectric properties of materials. Theory for converting the system's time-domain waveforms to S-parameters is introduced in section 6.2, following a brief background on UWB measurement. Next, the UWB measurement system architecture is described along with an algorithm for time-domain conversion. In section 6.4, the S-parameters resulting from this conversion were applied to calibrating and validating the measurement system using traceable standards. Lastly, this chapter concludes with a discussion of measurement uncertainty and error.

6.1 Background

Time-domain dielectric spectroscopy (or ultra-wideband) measurement systems have received increasing attention since Sperry and Lincoln Laboratory sought to understand the wideband properties of an Electronic Scanning Radar (ESR) [131]. Afterwards, Barney Oliver introduced a constructive approximation for impulse excitation with the development of a sampling oscilloscope at Hewlett Packard in 1962

[132]. This work led to the expectation that UWB offers unique performance advantages and soon found application in measuring the dielectric properties of natural materials [117]. Because these advantages include improved measurement resolution and clutter suppression, time-domain based UWB measurement systems offer the possibility for a more accurate measurement of dielectric properties than systems based in the frequency-domain [133]. Many applications require accurate knowledge of complex relative permittivity and permeability, including the design of radar absorbing material, design of transmission line circuits, and electromagnetic wave propagation analysis [134].

Generally, the techniques employed in the measurement of complex relative permittivity and permeability include application of low voltage and low electric field strengths [135]. Time-domain based UWB techniques are the most commonly used in low voltage applications. Pulse generators are used in UWB techniques to achieve a bandwidth of 500 *MHz* or more. Several time-domain measurement systems employ generators with a pulse-width of 1.0 *ns*, a material cross-sectional area of about 5.9 *in*² and sensors to pick up the signal [136]. The measurement system presented in this work employs a 290 *psec* Gaussian pulse generator for measuring a material with a 0.05 *in*² cross-sectional area, which is makes it more amenable to measurement of biomaterials since the sample size may be small. As a preliminary step, these properties were determined by converting the measured time-domain signals to S-parameters and using these parameters to compute the dielectric material properties.

6.2 Theory for time-domain reflectometry

Time-domain reflectometry (TDR) is a measurement technique that can be used to evaluate the characteristic of a transmission line. This impedance is used to relate magnetic permeability and electric permittivity to the propagation constant, which may be determined using the S-parameters. As a signal ($E_{inc}(t)$) propagates down a transmission line, its attenuation increases and phase changes over distance traveled (see Figure 6.1A). This propagation is captured by a coefficient described by the following

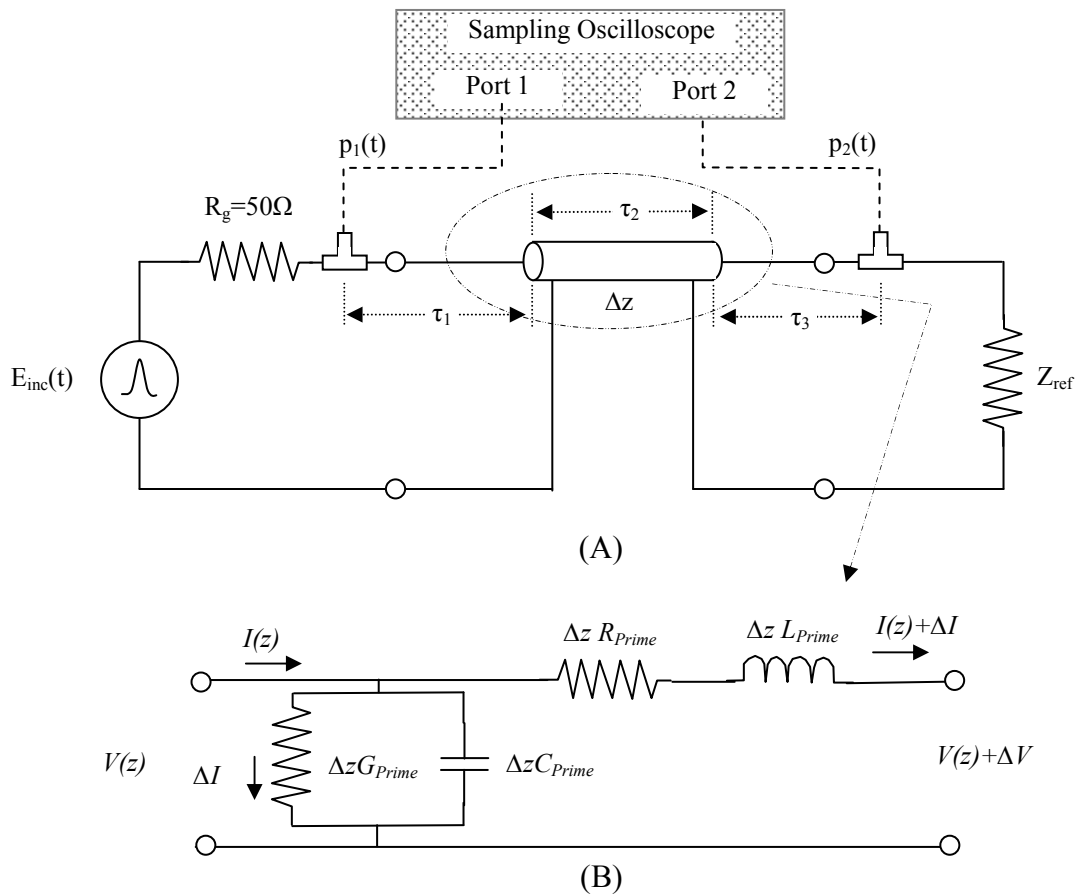


Figure 6.1: Diagrams for (A) time-domain reflectometry system configuration and (B) classical lumped element equivalent model for a transmission line.

equation: $\gamma = \alpha + j\beta$, where α is the attenuation per unit length (nepers/meter) and β is the phase per unit length (radians/m). As shown in Figure 6.1B, attenuation is affected by the amount of resistance (R_{prime}) and conductance (G_{prime}) per unit length of transmission line. The phase is affected primarily by the amount of inductance (L_{prime}) and capacitance (C_{prime}) per unit length. Propagation constant may be expressed in terms of these lumped element values by evaluating the circuit response of the transmission line in Figure 6.1B.

In Chapter 5, equations (5.11) and (5.12) demonstrates that γ may be determined for any transmission line length ($\Delta z = L_2$) by computing S-parameters S_{11} and S_{21} for the network. The S-parameters may be determined by performing a Fourier transform of the time-domain signal received at ports 1 and 2 of Figure 6.1A and dividing them by the incident waveform, so that:

$$S_{11}(\omega) = \frac{\mathfrak{F}(P_1(t))}{\mathfrak{F}(E_{inc}(t))} \text{ and} \quad (6.1)$$

$$S_{21}(\omega) = \frac{\mathfrak{F}(P_2(t))}{\mathfrak{F}(E_{inc}(t))}, \quad (6.2)$$

where $P_1(t)$ and $P_2(t)$ are the total signals reflected onto port 1 and transmitted to port 2, respectively. An expression for $P_1(t)$ and $P_2(t)$ in terms of the incident waveform may be formulated by considering wave propagation using a bounce diagram (see Figure 6.2). If the transmission lines not terminated in a perfectly matched load ($Z_0 = Z_L$), the

incident signal will continue to bounce between the ports until attenuated. An imperfect match may occur as a result of applying a load that does not match the characteristic impedance of the line or using a transmission line with regions having different dielectric properties.

In this research, a line with different dielectric properties is of interest, therefore the bounce diagram in Figure 6.2 is segmented into three regions, where Regions 1 and 3 are the input and output lines that connect a material under test (Region 2) to ports 1 and 2, respectively. As a result, if a wave $e_0(t)$ is incident on a transmission line and

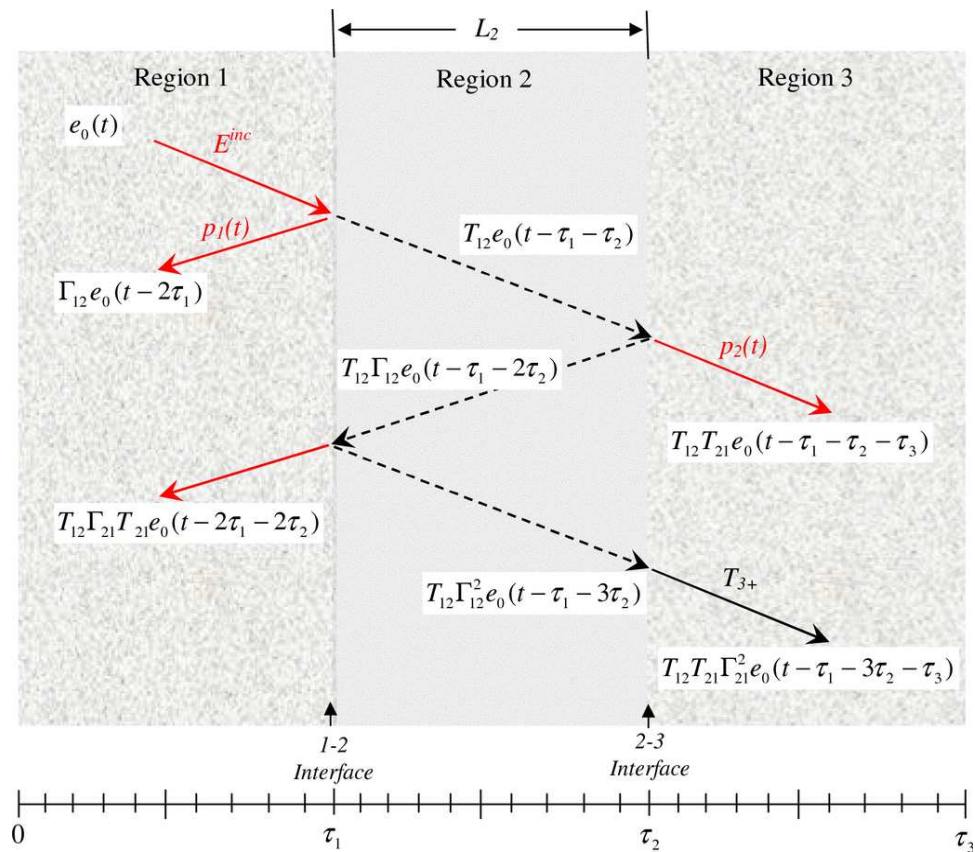


Figure 6.2: Bounce diagram for the time-domain waveform for the incident signal in the fixture.

encounters a material of a different permittivity, part of the wave will be reflected and part will be transmitted into Region 3. The length (L_2) represents the total length of material in the transmission line, τ_1 the propagation time from port 1 to the 1-2 sample interface, τ_2 the one-way propagation time through the sample, and τ_3 the propagation time from port 2 to the 2-3 sample interface. Consequently, the signal measured at port 1 may be expressed as:

$$P_1(t) = \Gamma_{12} \cdot e_0(t - 2\tau_1) + \dots \quad (6.3)$$

$$\sum_{n=0}^{\infty} T_{21}(t) \cdot \left\{ \left(\Gamma_{21}^* \right)^{2n+1} \left[T_{12} \cdot e_0(t - 2\tau_1 - 2(n+1)\tau_2) \right] \right\},$$

where Γ_{12}^* is a convolution of the reflection coefficient at the Region 1-2 interface, T_{12} and T_{21} are the transmission coefficients, and n represents the reflection number [105].

The total signal transmitted may be represented by the following equation:

$$P_2(t) = T_{21} \cdot \left\{ e_0(t - \tau_1 - \tau_2 - \tau_3) \cdot T_{21}(t) \right\} + \dots \quad (6.4)$$

$$\sum_{n=0}^{\infty} T_{21}(t) \cdot \left\{ \left(\Gamma_{21}^* \right)^{2(n+1)} \left[T_{12} \cdot e_0(t - \tau_1 - (3 + 2n)\tau_2 - \tau_3) \right] \right\}.$$

Equations (6.3) and (6.4) include an infinite number of reflections and transmissions, respectively. Following application of Fourier transform to (6.3) and (6.4) the S-parameters of (6.1) and (6.2) take form as:

$$S_{11}(\omega) = \Gamma_{12}(\omega) \cdot e^{-j\omega\tau_1} + \dots \quad (6.5)$$

$$\sum_{n=0}^{\infty} T_{21}(\omega) \cdot T_{12}(\omega) \cdot \left\{ \left(\Gamma_{21}(\omega) \right)^{2(n+1)} e^{-j2\omega[\tau_1 + (n+1)\tau_2]} \right\} \text{ and}$$

$$S_{21}(\omega) = T_{12}(\omega) \cdot T_{21}(\omega) \cdot e^{-j\omega(\tau_1 + \tau_2 + \tau_3)} + \dots \quad (6.6)$$

$$\sum_{n=0}^{\infty} T_{21}(\omega) \cdot T_{12}(\omega) \cdot \left\{ \Gamma_{21}(\omega) \right\}^{2(n+1)} e^{-j\omega[\tau_1 + (3+2n)\tau_2 + \tau_3]} \}.$$

The above S-parameter require an infinite sum of the reflected and transmitted signals at the two-ports of the fixture. Knoop provided a means for approximating the infinite sequences in (6.1) and (6.2) by applying the following well known relationship:

$$\sum_{n=0}^{\infty} x^n = \frac{1}{1-x}, \text{ for } |x| < 1, \quad (6.7)$$

where x is any variable. Since, the S-parameters are normalized by the incident waveform, (6.7) may be applied so that the relationships in (6.5) and (6.6) may be expressed by the equations:

$$S_{11}(\omega) = \Gamma_{12}(\omega) \cdot e^{-j\omega\tau_1} + \frac{T_{12}(\omega) \cdot T_{21}(\omega) \cdot \Gamma_{21}(\omega) \cdot e^{-j2\omega(\tau_1 + \tau_2)}}{1 - \Gamma_{21}(\omega)^2 \cdot e^{-j2\omega\tau_2}} \text{ and} \quad (6.8)$$

$$S_{21}(\omega) = T_{12}(\omega) \cdot T_{21}(\omega) \cdot e^{-j\omega(\tau_1 + \tau_2 + \tau_3)} + \frac{T_{12}(\omega) \cdot T_{21}(\omega) \cdot \Gamma_{21}(\omega)^2 \cdot e^{-j\omega(\tau_1 + 3\tau_2 + \tau_3)}}{1 - \Gamma_{21}(\omega)^2 \cdot e^{-j2\omega\tau_2}}, \quad (6.9)$$

which require determination of the reflection (Γ_{21}) and transmission coefficients (T_{12} and T_{21}) as well as time constants (τ_1 , τ_2 and τ_3).

6.2.1 Resolving the propagation times and coefficients

Equations (6.3) and (6.4) provide a formulation for extracting the S-parameters from time-domain data. However, this form requires resolution of the propagation

constants and coefficients, to include: propagation time constants τ_1 , τ_2 and τ_3 ; transmission coefficients T_{12} and T_{21} ; and reflection coefficients Γ_{12} and Γ_{21} . For computational ease, the transmission coefficients are considered as a single variable, expressed as $(T_{12} \cdot T_{21})$, and the transmission line is assumed to be balanced, which allows an equality for the reflection coefficients ($\Gamma_{12} = -\Gamma_{21}$). Time constant τ_1 is determined by taking the half the time between the waveform incident in Region 1 and the first reflection. Time constant τ_2 is determined by taking the time between the reflection at the 1-2 and 2-3 interfaces. Lastly, time constant τ_3 is determined from the expression:

$$\tau_3 = T - (\tau_1 + \tau_2) , \quad (6.10)$$

where T is the time between the incident and transmitted signals.

These time constants are used in conjunction with the reflection ($p_1(t)$) and transmission ($p_2(t)$) components of the bounce diagram to resolve the reflection and transmission coefficient, which are related by the following expression:

$$p_1(t) = \Gamma_{12} \cdot e_0(t - 2\tau_1) , \quad (6.11)$$

where $p_1(t)$ is the waveform reflected from the 1-2 interface and measured using a sampling oscilloscope, at port 1. The transmitted component $p_2(t)$ is observed at port 2 and expressed by:

$$p_2(t) = T_{12} \cdot T_{21} \cdot e_0(t - \tau_1 - \tau_2 - \tau_3) . \quad (6.12)$$

Equations (6.11) and (6.12) provide two equations and two unknowns through which the transmission coefficients $T_{12}(\omega) \cdot T_{21}(\omega)$ and reflection coefficient $\Gamma_{12}(\omega)$ are used to resolve the S-parameters from time-domain measurements. However, it is important that the transmission line of Region 2 is long enough to ensure adequate separation between the reflections off the 1-2 and 2-3 interfaces. Inadequate separation may result in an inseparable composite-reflection. The following section addresses isolation and clear-time in the transmission line.

6.2.2 Isolation and clear-time considerations

Time isolation is required between the transmission line reflections in order to compute coefficients needed for determining the S-parameters from time-domain data. The time isolation required at the 1-2 and 2-3 interfaces in order to provide adequate separation for the reflections may be described in terms of the length (L_2) for a given pulse width (τ_w), see below:

$$L_2 > \frac{\tau_w}{2} \cdot \frac{c_0}{\sqrt{\epsilon_{r2}}} . \quad (6.13)$$

A longer sample length is required as the pulse width of the incident signal increases. Since the length is inversely proportional to the sample permittivity, then a lower bound on the permittivity results for a given sample length. A fixed sample length of 45.72 mm accommodates measurement of a minimum relative permittivity of 2.7 using a 290 psec signal. Equation (6.13) provides a means to evaluate the length of the transmission line

between port 1 and the sample interface 1-2. The clear-time required to ensure isolation between the incident pulse and first reflection requires the first transmission line be at least 51.82 mm . The transmission time of Region 3 must be at least twice the length of that for Region 1 in order to ensure that secondary reflections on the transmission line are delayed until the primary reflections arriving at port 1 and the transmission arriving at port 2 are captured.

6.3 System-level architecture of the UWB measurement system

The UWB measurement system consisted of a UWB Gaussian pulse generator, 12 MHz arbitrary waveform generator, an experimental coaxial-line test fixture, a 20 GHz oscilloscope, Intel PC, syringe, MATLAB-based algorithm, and 13- and 26-inch SMA cables. The cables were used to attach an experimental coaxial-line test fixture to the oscilloscope through a Gaussian pulse generator. Data extracted from the oscilloscope was processed using a MATLAB-based algorithm for converting the oscilloscope data to S-parameters. Next, a Nicholson-Ross-Weir algorithm was used to compute the dielectric properties from the S-parameters (see Figure 6.3).

In this measurement system a 12 MHz , 10 V_{pp} sinusoidal waveform was applied to the input of the UWB Gaussian pulse generator using an HP33120A arbitrary waveform generator. The HP33120A provided stimulus to an UWB pulse generator, constructed using a shunt step recovery diode and a short circuit-stub, which produced a 290 $psec$ inverted Gaussian pulse. This generator launched an incident wave down the L_1 transmission line and into port 1 of the oscilloscope. Part of this wave front was reflected

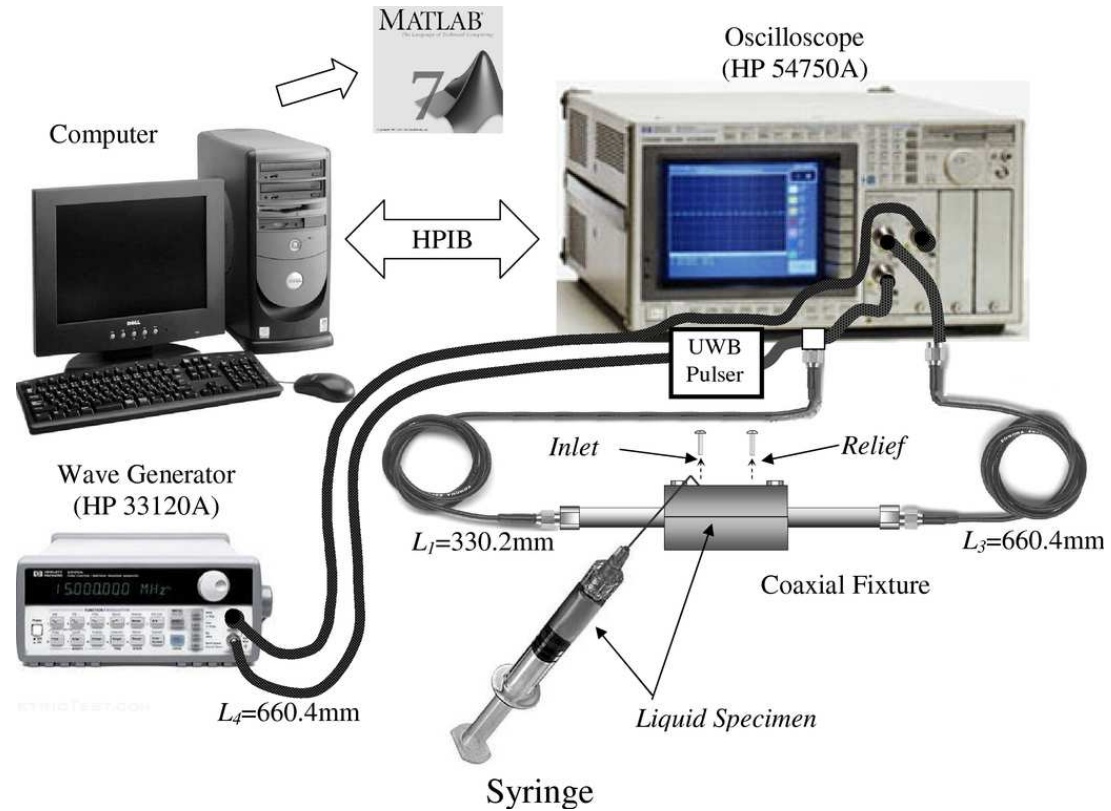


Figure 6.3: Complex ultra-wideband/RF-microwave measurement system for time-domain extraction of dielectric properties of materials.

from the 1-2 and 2-3 interfaces back to port 1, and the remainder was transmitted to port 2 of the oscilloscope through L_3 , which was made from 26-inch of SMA coaxial cable. The oscilloscope used to collect these waveforms was a 20 GHz digital sampling oscilloscope (HP54750A) setup to trigger on the HP33120A. The oscilloscope was also set to 128-bit sampling and produced an ASCII formatted output files for further processing. These files were processed using a data acquisition and analysis algorithm that was developed in MATLAB and used for converting the data to S-parameters (Appendix D).

6.4 Calibration and validation of UWB measurement system

The sections below present calibration methods and validation data for the UWB measurement system. Although clear-time considerations limit the measurable permittivity to greater than 2.7, measurements were taken for air, ethanol, methanol, and de-ionized water. The data for these measurements was processed using the aforementioned NRW technique to provide a means to validate the system through a comparison of the complex relative permittivity.

6.4.1 Measurement procedures

After removal of the inlet and outlet valves, the specimen holder was washed with ethanol and then air-dried. The specimen holder was then rinsed once with the dilute liquid test sample before filling the sample holder with it. Once the inlet and outlet valves were replaced, an oscilloscope measurement was performed. To ensure continuity in the S-parameter data, the trigger was stopped prior to saving the measurement data. Next, the test sample was used to calibrate and then validate the measurement system.

The ASCII formatted files from the oscilloscope were read by the data acquisition and analysis algorithm. The time and magnitude values for ports 1 and 2 were assigned to a matrix of variables. Next, the program was used to perform a peak search to provide a means to compute the propagation time constants as well as boundaries for isolating waveforms. These isolated pulses were then processed for S-parameter conversion.

Finally, the dielectric parameters were determined from these S-parameters using the NRW technique.

6.4.2 UWB measurement system calibration

The UWB measurement system was calibrated by adjusting the lengths L_1 and L_3 , of the transmission lines. The value for lengths L_1 and L_3 was adjusted to 335.8 and 655.32 *mm*, respectively. Initial values of 330.2 and 660.4 *mm* were measured for these lengths, but they were adjusted to achieve a better fit between the NIST approximation and computed results for relative permittivity of ethanol. Details and results of this calibration are covered in the measurement system validation below.

6.4.3 UWB measurement system validation

The UWB measurement system was validated to confirm that the adjustments made to the transmission line lengths resulted in a robust measurement system, which is capable of computing the dielectric properties for a wide range of materials. To provide a measure for this goal, the calibrated measurement system was validated by measuring the complex permittivity for several dilute liquids, including ethanol, methanol and de-ionized water. Air was also measured to confirm a loss of measurement resolution for samples with a permittivity less than 2.7, as shown in section 6.2.2. These measurements were initiated by capturing the signals at ports 1 and 2 of the oscilloscope (see Figure 6.4). Distinctions were observed in the captured waveforms for the dilute liquids, following the -350 *mV*, 290 *psec* Gaussian excitation incident on the measurement

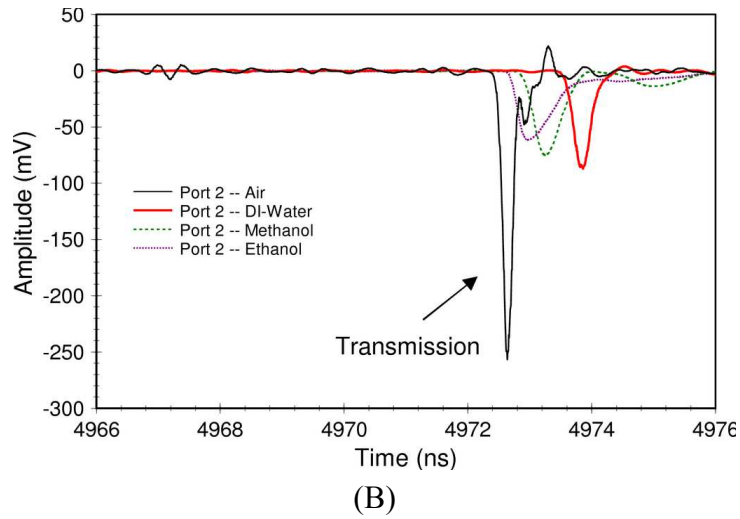
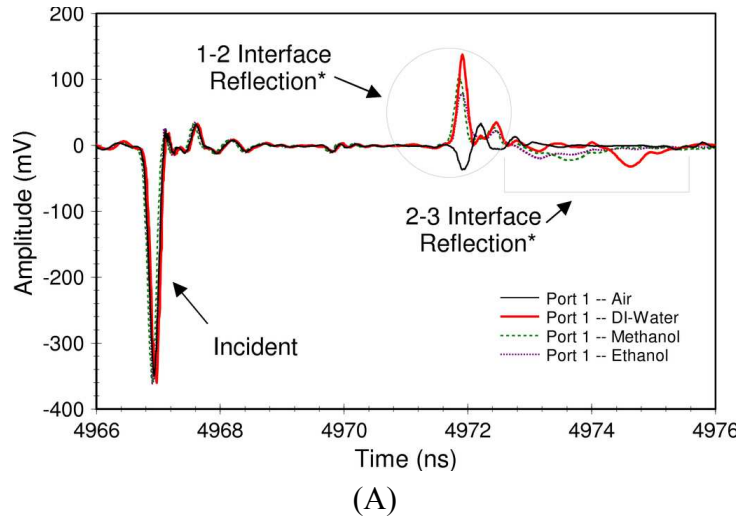


Figure 6.4: Contextual view of measured waveforms at (A) port 1 and (B) port 2 of the oscilloscope.

system. The pulses generated at the 1-2 and 2-3 interfaces were opposite in polarity. Since the lengths associated with transmission lines L_1 and L_3 are related by the expression: $L_3 = 2L_1$, then the reflections from the 2-3 interface arrived at port 1 (see Figure 6.4A) at about the same time as the port 2 transmissions (see Figure 6.4B). The waveform morphology changed in each dilute liquid. These morphological distinctions were best observed after the waveforms were separated for further processing.

The waveforms in Figure 6.4A-B, were separated into four components to support further processing. These components included an incident (E_0), transmitted (E^{tran}), reflection from Region 1-2 interface ($p_1(t)$), and reflection from Region 2-3 interface ($p_2(t)$). About 25 psec of jitter was observed in the measurement. It was determined that this jitter originated from the arbitrary waveform generator (see Figure 6.5A). The reflection at the Region 1-2 interface (Figure 6.5B) demonstrated a smaller amplitude in

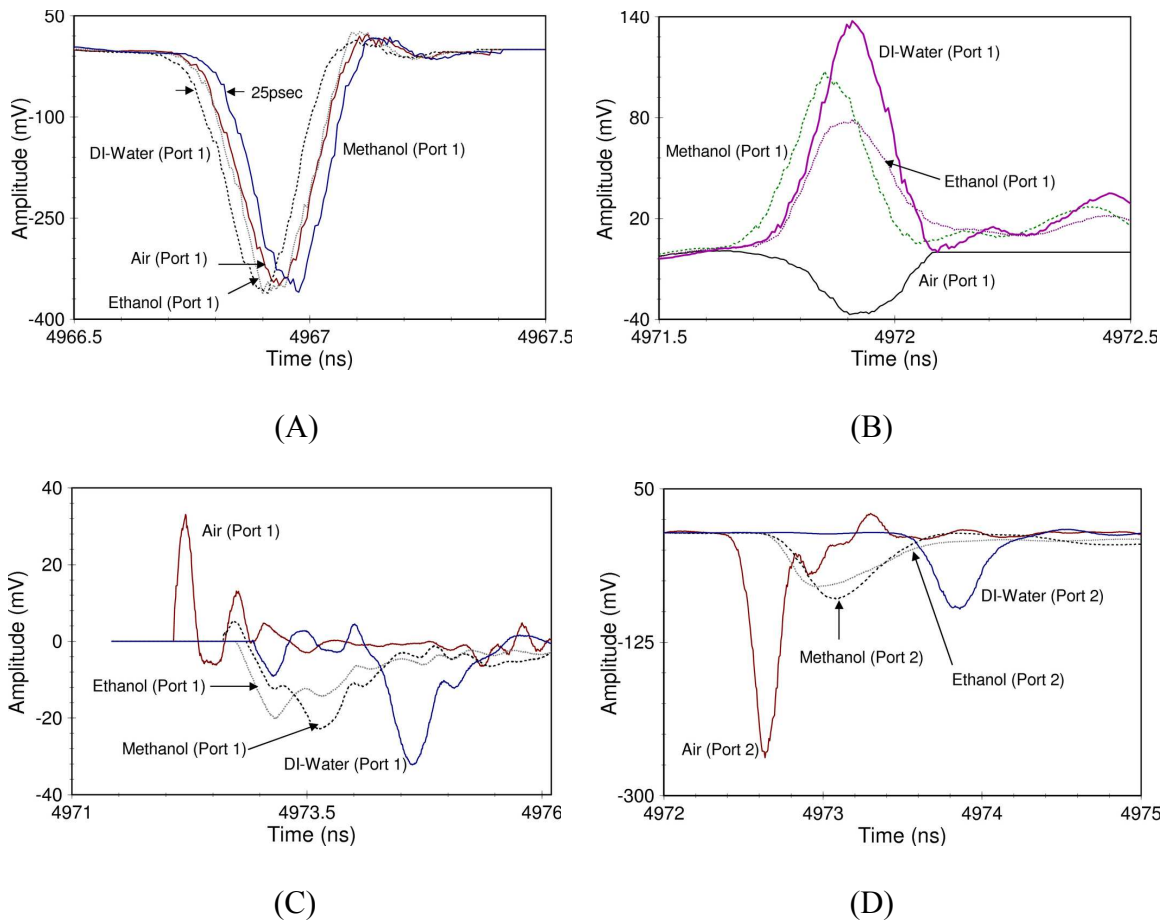
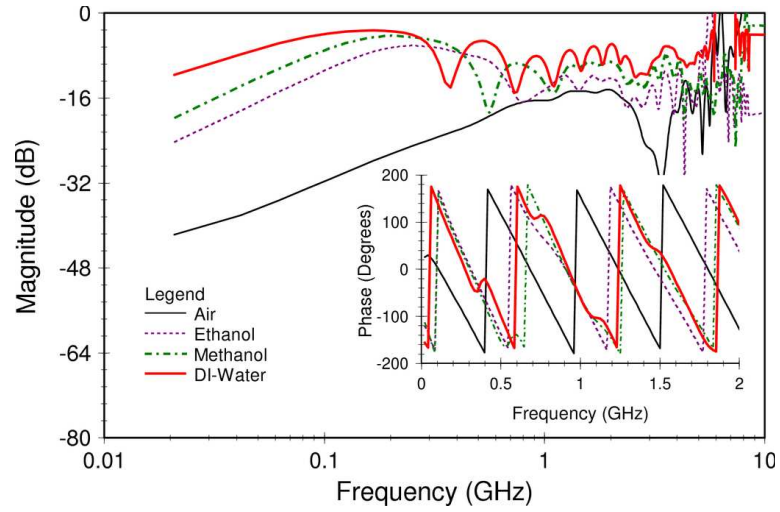
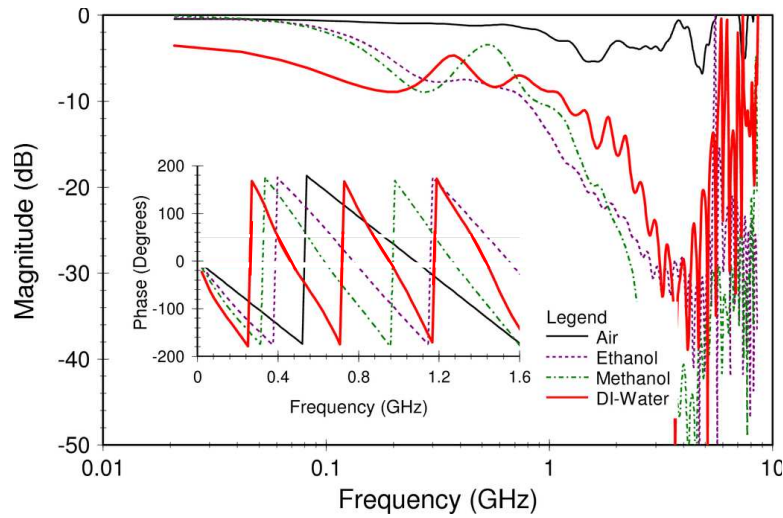


Figure 6.5: Isolation waveforms for the (A) incident, (B) interface 1-2 reflected, (C) interface 2-3 reflected and (D) transmitted signals using the data acquisition and analysis algorithm.

air and larger amplitude for de-ionized water. Air took on a negative going value for the reflection as compared to the other dilute liquids because its permittivity was lower than the PTFE-Teflon coaxial-cable feeding the sample holder. The reflections from the



(A)



(B)

Figure 6.6: Computed S-parameters (A) S_{11} and (B) S_{21} from time-domain waveforms.

Region 2-3 interface (Figure 6.5C) were of similar morphology for all the dilute liquids and opposite in polarity from those at the 1-2 interface. In the transmitted waveform, the S-parameter for air showed a larger magnitude than the dilute liquids, measuring -250 mV (see Figure 6.5D). As observed in the contextual view, the morphology of the transmissions for the dilute liquids was distinct. A Rician distribution was observed for ethanol and methanol, while water took on more of a normal distribution.

The above separated waveforms were Fourier transformed and applied for S-parameter conversion using equations (6.11) and (6.12) above. The resulting S-parameters demonstrated trends that were consistent with observation made in the time-domain signals in Figure 6.6A-B. These parameters demonstrated phase and

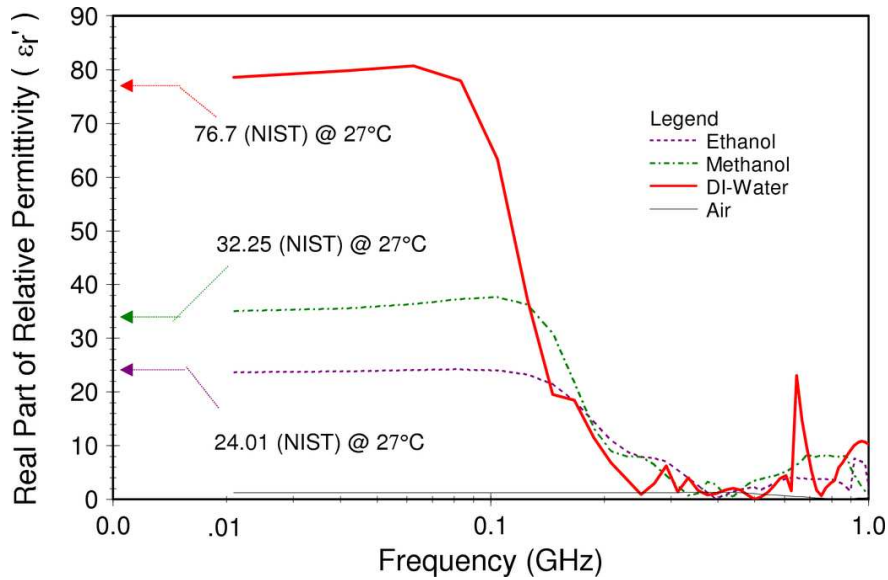


Figure 6.7: The resulting real parts of the complex relative permittivity, obtained using NRW technique.

magnitude differences for air, ethanol, methanol, and de-ionized water. These differences allowed for distinction in the dilute liquids up to 0.2 GHz. As observed in the time-domain waveforms, S-parameter computations for water demonstrated the highest reflection and lowest transmission. The phase of S_{11} associated with air was opposite that of the other measurements, which also supports the time-domain observation of inverted polarity in Figure 6.5B. Correlations between the time- and frequency-domain components provided confidence that the time to S-parameter conversion was successful to 0.2 GHz.

These S-parameters were applied to the NRW algorithm, which resulted in distinctions between the solutions (see Figure 6.7). As expected, the measure for air was inaccurate due to the lower limit of the fixture. However, the measure for ethanol, methanol, and de-ionized water closely approximates NIST data for static permittivity.

6.5 Measurement uncertainty and error

The error associated with computing the scattering parameters in the UWB system is affected by the accuracy of characterizing the impedance and dielectric properties of the coaxial transmission lines and the sample holder. Consequently, the sources of error include:

- Imperfect matching at the oscilloscope ports,
- Imperfect reference impedance,
- Imperfect matching of sample length,

- Imperfect calibration standard due to temperature variations,
- Noise introduced by Gaussian pulse generator, and
- Uncertainty associated with computational assumptions.

The most significant contributors to uncertainty in this measurement system are the imperfect estimation of the transmission line lengths, position of the material within the line, material size, and reference impedance. In this research, the transmission lines were measured to the ports of the oscilloscope. In addition, it was assumed that the reference impedance was 50Ω with no imaginary component. Very small adjustments to the measured length of transmission lines were made to compensate for imperfections in the fixture geometry.

6.6 Summary

Electromagnetic characterization of the dielectric properties of materials in an UWB measurement system was made possible through a number of assumptions, which tended to reduce the measurement accuracy and range. Assumptions associated with the reference impedance, temperature, and propagation mode allowed for measurement to about 200 MHz using NRW technique for analysis. These modifications led to the development of a simple and low-cost UWB measurement system, which is capable of measuring a broad range of materials.

Chapter 7

An Investigation of Isolated B16-F10 Tumor Cells in Liquid Medium

This chapter presents a study of B16-F10 isolated tumor cells suspended in McCoy's liquid medium. In this study, frequency- and time-domain measurement systems are used to characterize the cell suspension. In the first section, a background on model selection and justification for using cancer cell cultures is discussed. The next section presents materials and methods to culture, count, and control the cell suspension. Afterward, results and analysis are presented for several volumes of suspended B16 cells. A statistical analysis and discussion follows presentation of results for the frequency- and time-domain measurement systems. These results contribute to biomedical research by demonstrating the capacity of dielectric spectroscopy to characterize and quantify isolated B16 tumor cells.

7.1 Background

Enactment of the United States Department of Agriculture's (USDA) Animal Welfare Act (AWA) has guided selection of a biomedical research model for this study [137]. Animal models are desirable because they provide a more complex physiological environment as well as a means to extrapolate data for human testing. However, alternative techniques to animal testing were considered in fulfillment of requirements set

forth by the Institutional Animal Care and Use Committee (IACUC) at the University of South Florida [138, 139]. As a result, a non-animal model was used in this study because it provided the most ethical and suitable choice for a preliminary investigation.

Alternatives for non-animal models fall into several categories including living systems, nonliving systems, and computer simulations. In-vitro techniques are the most commonly recognized living systems and are central elements in biological research [140]. These techniques do not involve direct use of vertebrate animals but may include organ, tissue, and cell cultures. Cell cultures are favored because they are based on established methods. They are easily sustained by controlling atmosphere, humidity, temperature, pH, and nutrients [141, 142]. The pH and nutrients for the cell culture are supplied through the liquid medium in which it was placed. This research employs a living system comprised of B16-F10 tumor cells in liquid medium.

7.2 Materials and methods

The B16-F10 tumor line was derived by injecting B16 tumor cells into syngeneic C57BL/6 mice and harvesting the secondary growth after 2-3 weeks. This tissue was then placed in a culture and injected into new syngeneic mice. The process was repeated ten times and given the designation F10. The B16 line is desirable because it shows stable metastatic properties, even after many tissue subcultures [143]. American Type Culture Collection (ATCC) supplied the primary B16-F10 tissue culture for this research, so harvesting tissue from mice was unnecessary.

However, growing the cells in culture was mandatory to achieve the large cell counts required for experimentation. McCoy's medium consists of a combination of inorganic salts, amino acids, vitamins, sugars, and other materials, which provides a better culturing environment for growing large volumes of cells in a shorter period of time than other medium types, i.e. Dulbecos [144]. As a result, the tissue culture laboratory at USF recommends McCoy's liquid medium (Cat No. 10-50-CV, 5A Iwakata and Grace Modification) for culturing a B16 cell line. This line required 5-8 days in culture to achieve the desired cell count.

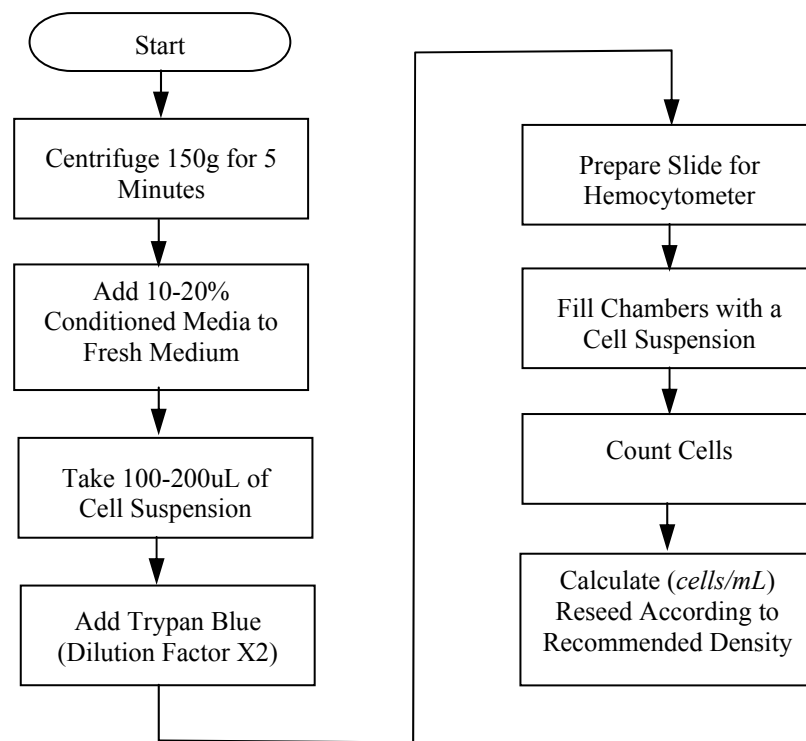


Figure 7.1: Flow chart of the process for preparing a cultured B16-F10 tumor cell for counting and measurement.

After we removed the cells from culture, we processed them in accordance with the flow chart in Figure 7.1. Cell counts were verified using a hemocytometer (No. 0267110; Fisher Scientific). To prepare the cells for counting, a pipette was used to transfer the cell suspension from the culture flask to a centrifuge tube. Next, the cell suspension was placed in a centrifuge for 5 minutes in order to concentrate the cells to a minimum of 10^5 *cells/mL*, as required for measurement using the hemocytometer method. Afterwards, the cells were re-suspended in a smaller volume by removing the excess medium and replacing it with 10-20% conditioned medium. A 100-200 *uL* sample of cell suspension was collected and placed in a separate tube. Trypsan blue was added, and a micropipette was used to transfer 20 *uL* to both chambers located at the edges of the hemocytometer. The prepared hemocytometer was then placed under a microscope for cell counting, using the procedure outlined by the manufacturer [145].

The cell count was used to determine the amount of cell suspension and medium that was needed to achieve the desired volumetric cell counts, from which we formed the following test groups: 0, 1, 2 and 3 M *cells/mL* of McCoy's 5A medium. Aseptic techniques were used in the handling of the suspensions, including the use of sterile pipettes and fixture for each test group (see Figure 7.2). An ethanol wash was used to sterilize the fixture. Following the ethanol wash, the fixture was flushed with McCoy's medium to remove any other residue. Lastly, the cell suspensions were shaken throughout the test to keep the cells from settling at the bottom of the suspension. They were also drawn into the pipette and released back into the tube several times, to keep the suspension in animation.

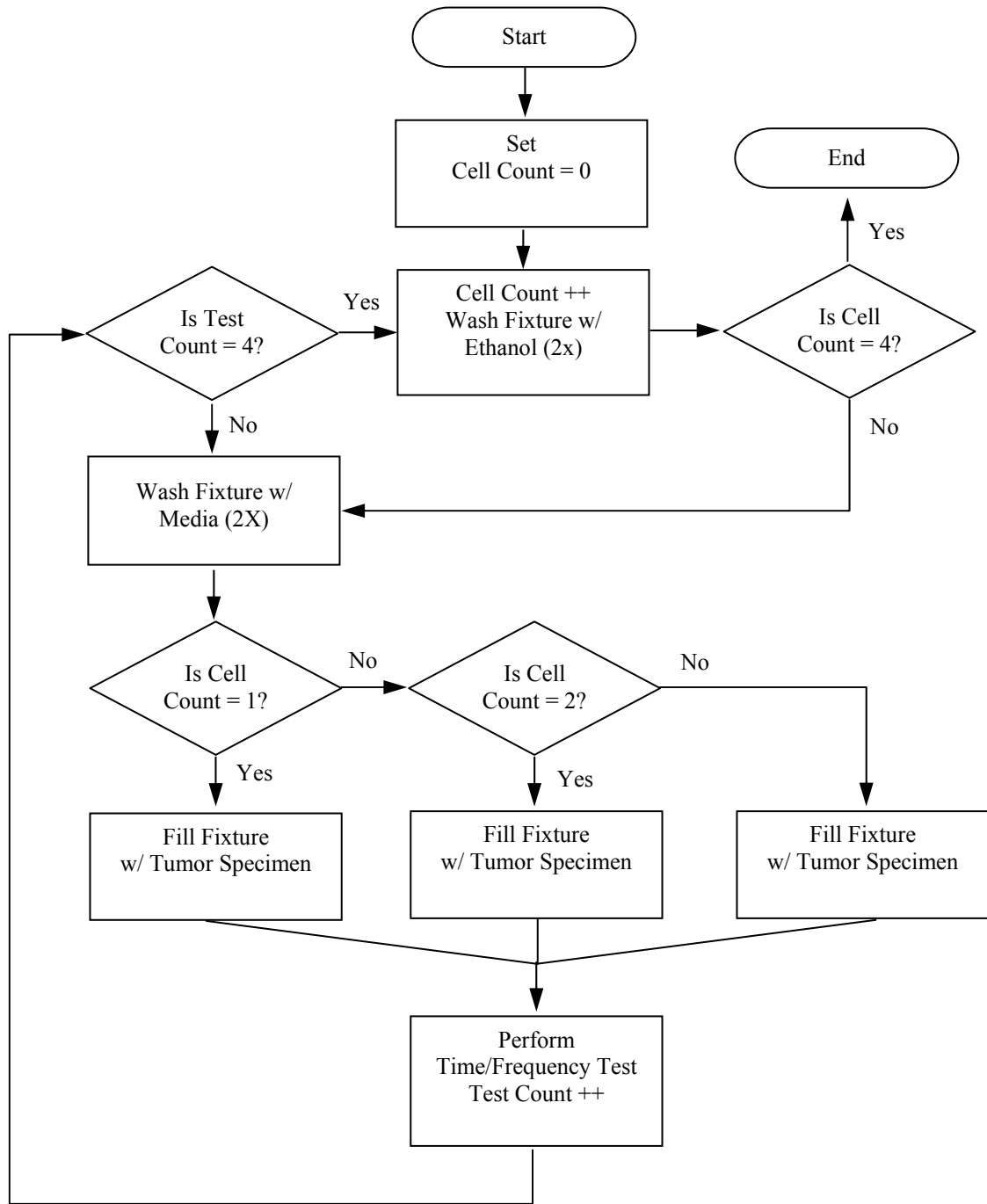


Figure 7.2: Process flow for preparation and measurement of B16-F10 tumor cell suspension.

7.3 Approach to evaluating statistical uncertainty

Sources of statistical error and uncertainty in frequency and time-domain characterization of B16 tumor cells include the following: error associated with the cell count, uncertainty associated with the statistical convergence in the genetic algorithm and uncertainty associated with measurement variability across the entire population. These sources of error and uncertainty were evaluated following time- and frequency-domain characterization of the B16 tumor cells.

The error associated with the cell count originated from use of the hemocytometer and extraction of a liquid test sample from the population. The sources of error for the hemocytometer include statistical error associated with the estimated count, chamber fill variations, distributional differences of the sampled cells, and conventional inconsistencies in counting cells that fall on the boundary lines. The count was averaged across three grids to obtain the total cells for this experiment. Nielsen, Smyth, and Greenfield reported a 15% error associated with a three grid test [146]. Pipette extraction of a test sample from the population also contributed to cell count error. In pipette extraction, a 1.5 *mL* cell suspension sample was drawn into a pipette, from a test tube that contained a larger mixture volume, for placement in the test fixture. An even cell distribution was assumed for the suspension. Variation in the cell distribution affects the volume of cells drawn from the population. Therefore, the cells are agitated to keep them in suspended animation. Cell count is also affected by cell adhesion to the walls of the

test tube. Although it is difficult to measure the contribution of these sources of error, cell counting error shows up as uncertainty for the entire population of measurement data.

The uncertainty associated with the statistical convergence of the genetic algorithm was determined by running the GA on the same test sample for ten iterations and recording the results for each iteration. A type-A evaluation of standard uncertainty ($\nu(x_i)$) was performed on the iteration data ($X_{i,k}$) by first determining the sample mean (x_i) as described in the following equation:

$$x_i \equiv \bar{X}_i = \frac{1}{n} \sum_{k=1}^n X_{i,k}, \quad (7.1)$$

where k is the independent observation over n iterations. This sample mean was used to compute the standard uncertainty, which is expressed by

$$\nu(x_i) = s(\bar{X}_i) = \sqrt{\frac{1}{n(n-1)} \sum_{k=1}^n (X_{i,k} - \bar{X}_i)^2}. \quad (7.2)$$

The standard uncertainty is also called the estimated standard deviation of the mean ($s(\bar{X}_i)$). It is used in this research to describe the lack of certainty in GA convergence on the complex relative permittivity.

The uncertainty associated with the entire population of measurement data was evaluated by applying a paired t-test for hypothesis testing. A one-tail test was carried out to verify the null hypothesis that: there is no difference between comparison groups of cell concentrations, which include a comparison of the following groups: 3 and 2

million cells per milliliter (M *cells/mL*), 2 and 1 M *cells/mL*, and 1 and 0 M *cells/mL*.

These test were conducted at a 90% confidence level. The difference in the means (Δx_i) of the comparison groups m and w was determined by equation: $\Delta x_i = x_m - x_w$, where x_m and x_w are the statistical means for m and w , respectively. The variance associated with this difference is defined by

$$Var(\Delta x_i) = \left[\frac{(n_m - 1)\sigma_m^2 + (n_w - 1)\sigma_w^2}{n_m + n_w - 2} \right] \left(\frac{1}{n_m} + \frac{1}{n_w} \right), \quad (7.3)$$

where n_m and n_w are the number of test samples in each group, and σ_m^2 and σ_w^2 are variances. The difference in the mean and their variances were used to form a t-statistic ($t = \Delta x_i / \sqrt{Var(\Delta x_i)}$) for hypothesis testing. The t-statistic was used to determine the area under the curve of a t-distribution given the significance level (α). The null hypothesis was rejected if this area was less than α .

7.4 Approach and methodology

B16 cell suspensions consisting of 0, 1, 2 and 3 M *cells/mL* in McCoy's 5A medium were characterized to determine how well frequency- and time-domain measurement systems are able to characterize ITCs. The frequency-domain system consisted of an HP8753D vector network analyzer, which was used to capture S-parameters for the cell suspensions (see Figure 7.3). Data resulting from this measurement were used to asses the capacity to characterize and quantify ITCs in the frequency-domain, by computing the dielectric properties for several volumes of cell

suspensions. These properties were determined from the frequency-domain measurement data using the genetic algorithm described in Chapter 6. However, due to limiting effects of large random uncertainty introduced by the GA, only the static permittivity, provided by the NRW algorithm was used to evaluate the entire population. For the time-domain measurement system, transmitted and reflected waveforms were captured using an HP54750A oscilloscope and processed with a MATLAB-based algorithm for conversion to S-parameters. Next, the genetic as well as the NRW algorithms were used to compute dielectric properties of the B16-F10 suspension. A statistical analysis followed the use of each measurement system.

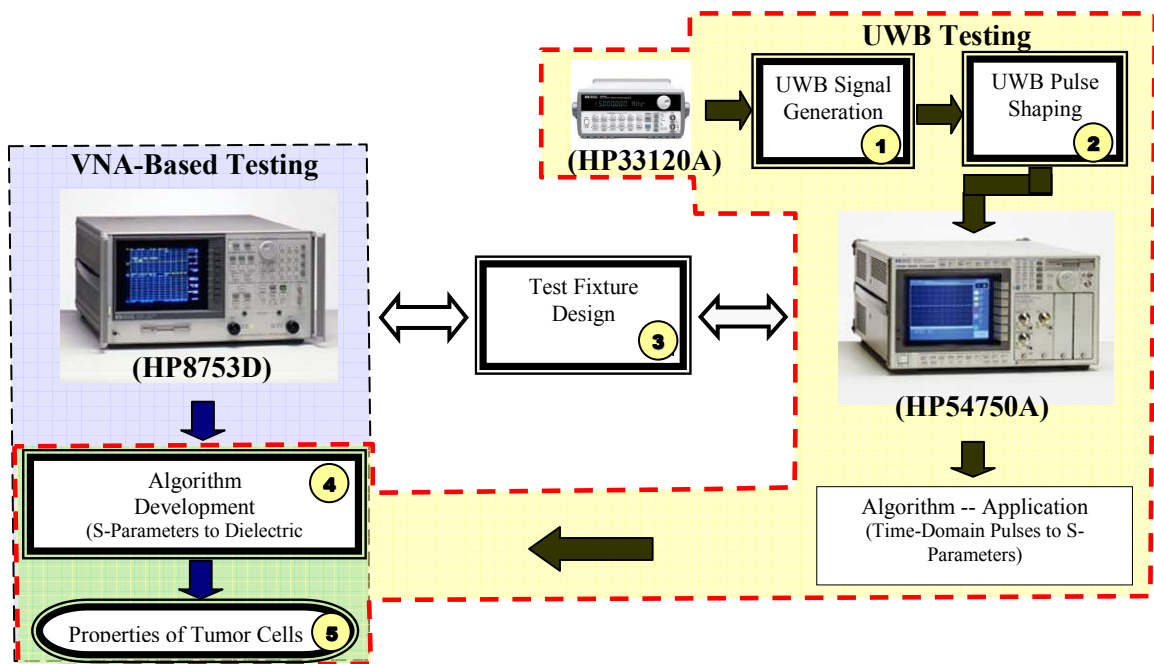


Figure 7.3: Flow for time- and frequency-domain electromagnetic characterization of B16 suspension.

7.5 Results and analysis for frequency-domain measurement

The frequency-domain measurement system is based on using an HP8753D VNA, through which S-parameters are acquired with well-established procedures. A calibrated VNA minimizes measurement uncertainty due to the cable length and connectors by establishing a reference plane at the ports of the test fixture. Data measurement groups consisting of 0, 1, 2 and 3 M *cells/mL*, which contained a population of 8 samples per group, were collected using the frequency-domain measurement system. This data was processed with genetic and NRW algorithms and then analyzed for uncertainty. In genetic algorithm data processing, a single test-set consisting of 0, 1, 2, and 3 M *cells/mL* in McCoy's liquid medium was arbitrarily selected. Henceforth, this frequency-domain test-set is referred to as test-set #3. Comments for interpreting the results are held for the discussion that follows a statistical analysis.

7.5.1 Frequency-domain data analysis using the GA

The graphs in Figure 7.4 illustrate how well the GA is able to fit the Havrilak-Negami model using test-set #3 data. Parameters used to achieve this fit include the static and optical permittivity as well as relaxation time. A good fit was achieved up to about 1.0 *GHz* for the phase and magnitude of S_{11} (see Figure 7.4 A, C, E and G). However, the fit of S_{21} data was not as good (see Figure 7.4 B, D, F and H). The GA provided a better match for a S_{21} below 200 *MHz*.

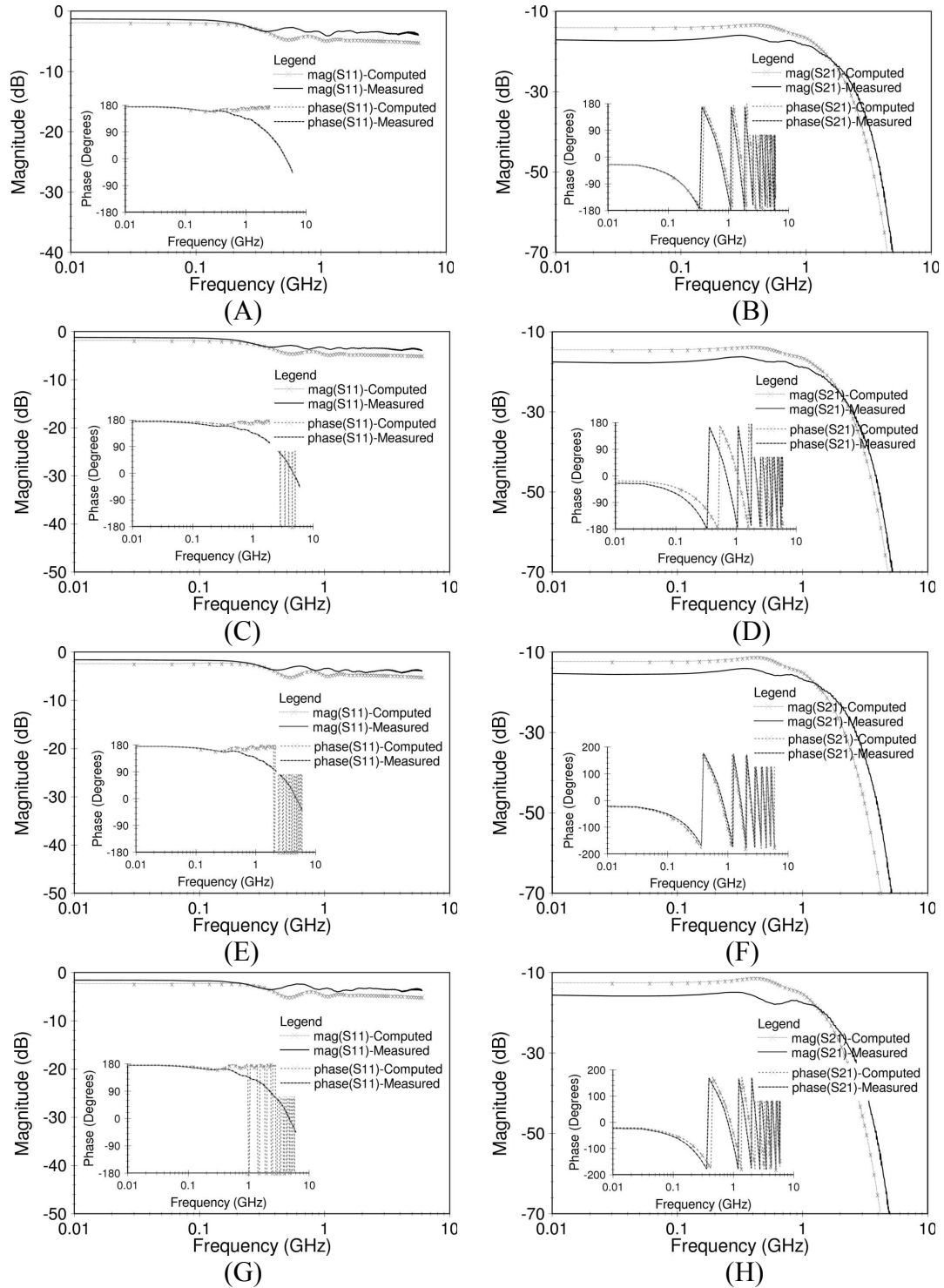


Figure 7.4: A comparison of the VNA measured and GA computed results for S_{11} and S_{21} of the 3rd frequency-domain test, for (A)-(B) 3 M, (C)-(D) 2 and, (E)-(F) 1 M *cells/mL*, (G)-(H) McCoy's medium.

The complex permittivity that resulted from fitting the S-parameters to a Havrilak-Negami model showed morphological distinction over a frequency of 300 MHz (see Figure 7.5). This range provides a measure for the static permittivity, which measured

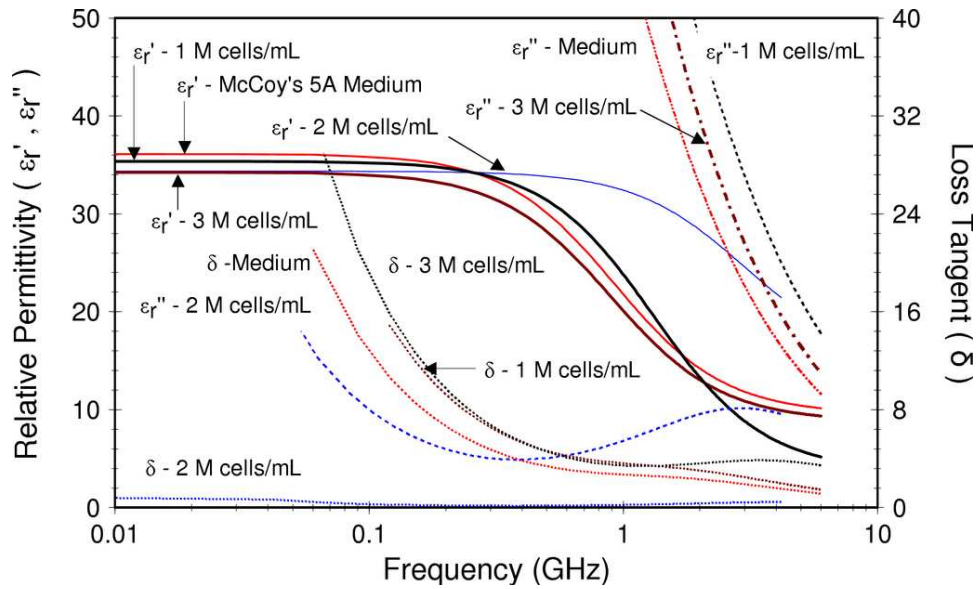


Figure 7.5: GA produced complex permittivity for B16 cell suspension for frequency-domain measurement data (test-set #3).

between 32.9 to 37.5 for test-set #3. However, as the roll-off approached the optical permittivity, the real part of the complex permittivity converged at about 2 GHz before settling out in a range from 5.7 to 8.4. Electromagnetic characterization of materials supports cell quantification if any of the dielectric properties moves proportionally with an increase in cell count per volume. Neither the optical permittivity, relaxation time, nor magnetic permittivity followed such a trend (see Table 7.1). However, the static permittivity showed some distinction.

Table 7.1: Extracted GA parameters for frequency-domain measurement data (test-set #3).

	ϵ_{static}	$\epsilon_{\text{optical}}$	τ_{relax}	μ_s	μ_i
3 M <i>cells/mL</i>	32.93	5.77	1.774E-10	1.05	1.04
2 M <i>cells/mL</i>	33.61	8.38	7.091E-10	0.99	0.99
1 M <i>cells/mL</i>	36.75	8.40	2.327E-10	1.09	1.06
0 M <i>cells/mL</i> (McCoy's Medium)	37.44	7.25	1.229E-10	1.11	1.04

7.5.2 Uncertainty analysis of GA performance

The static permittivity for the test-set #3 of the GA demonstrated distinct values for different volumes of B16-F10 tumor cells. However, the GA produced different values for the static permittivity each time it was executed on the same measurement data. A type-A evaluation of the standard uncertainty associated with ten iterations of the GA on test-set #3 produced upper and lower bounds for the confidence limits, which overlapped. This test showed a margin of error of about $\pm 8\%$ for the computed static permittivity. The error produces a 90% confidence interval that is wider than the difference being resolved for 0-3 M *cells/mL*. Consequently, the GA produced results which showed great statistical variability (see Table 7.2). Since the NRW algorithm is not based on a statistical convergence and provides an estimate using an explicit formula

for computing the static permittivity, it was applied to analyzing the population of measurement data. As discussed previously, the downside of applying the NRW technique is the problem of half-wavelength resonance, which prevents analysis of relaxation effects in the material.

Table 7.2: Type-A evaluation on a 90% confidence interval of frequency-domain GA test-set #3.

Group	NRW	Genetic Algorithm ($\bar{X}_{3,k}$)					
		x_3	$\nu(x_3)$	Margin of Error	Confidence Limits		
					$x_3 \pm t_{(\alpha/2, N-1)} \frac{\nu(x_3)}{\sqrt{N}}$	Lower Bound	Upper Bound
3 M cells/mL	ϵ_{static}	33.77	31.64	4.42	$\pm 8.1\%$	29.08	34.20
	$\epsilon_{\text{optical}}$	-	8.28	0.02	$\pm 0.2\%$	8.26	8.29
	τ_{relax}	-	0.72	0.01	$\pm 0.6\%$	0.72	0.72
2 M cells/mL	ϵ_{static}	34.52	32.36	4.52	$\pm 8.1\%$	29.74	34.99
	$\epsilon_{\text{optical}}$	-	8.40	0.02	$\pm 0.2\%$	8.39	8.41
	τ_{relax}	-	0.73	0.01	$\pm 0.8\%$	0.73	0.74
1 M cells/mL	ϵ_{static}	36.28	33.88	4.73	$\pm 8.1\%$	31.14	36.62
	$\epsilon_{\text{optical}}$	-	7.37	0.05	$\pm 0.4\%$	7.35	7.40
	τ_{relax}	-	0.92	0.03	$\pm 1.6\%$	0.91	0.94
McCoy's 5A Medium	ϵ_{static}	36.88	34.57	4.83	$\pm 8.1\%$	31.77	37.37
	$\epsilon_{\text{optical}}$	-	7.54	0.06	$\pm 0.4\%$	7.50	7.57
	τ_{relax}	-	0.92	0.056	$\pm 0.9\%$	0.91	0.92

7.5.3 Frequency-domain data analysis using Nicholson-Ross-Weir

The non-iterative NRW algorithm computed a relative complex permittivity that demonstrated better distinction than the GA's estimate (see Figure 7.6). As such, the static permittivity decreased with an increase in the cell volume under test. Application of the NRW technique to the population of suspension tests resulted in estimates of the static

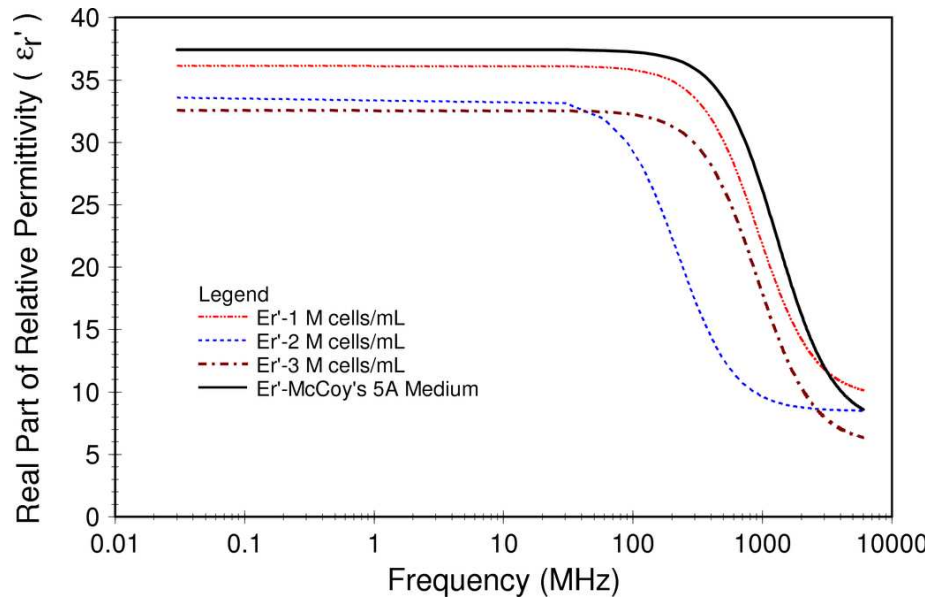


Figure 7.6: The real part of the NRW complex permittivity for frequency-domain test-set #3.

permittivity. With the exception of two outliers in the measurement of McCoy's medium, the static permittivity for each of the cell suspensions was distinct across the entire population of samples and each test group showed little variation within the group \

except that for 1 M *cells/mL* (see Figure 7.7). This variation is explored in detail in the following section, followed by the reasons for it.

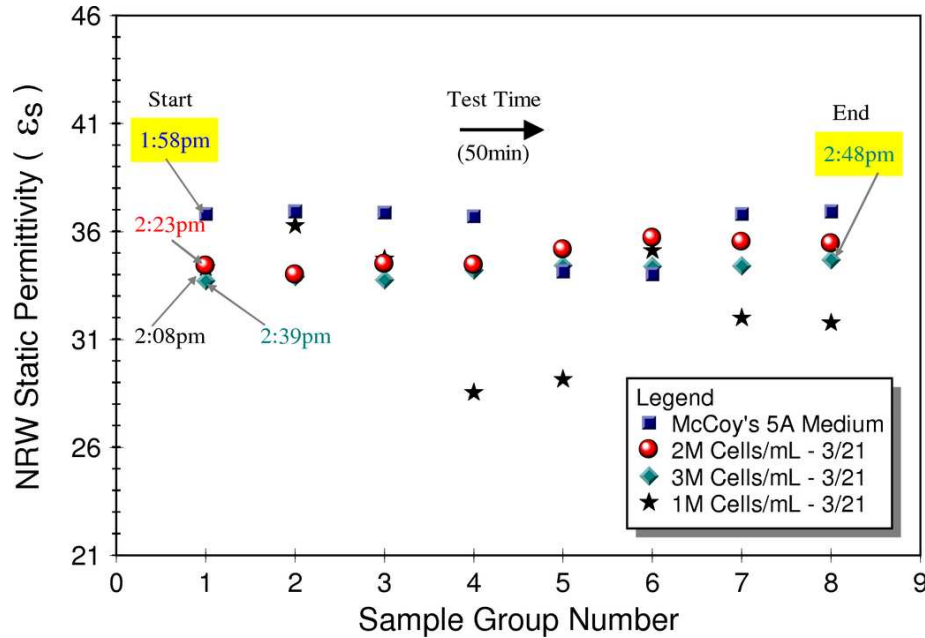


Figure 7.7: The NRW static permittivity for test population of B16 suspensions in frequency-domain.

7.5.4 Uncertainty analysis of NRW performance

An evaluation of the standard uncertainty at a 90% confidence level showed a smaller margin of error using the NRW algorithm to calculate the population means corresponding to 0, 2 and 3 M *cells/mL*, than the genetic algorithm. McCoy's medium as well as 2 and 3 M *cells/mL* also followed a trend, and the confidence limits showed less overlap (see Table 7.3 below). However, the margin of error for 1 M *cells/mL* was greater. As a result, the group means appears to be different.

Table 7.3: Type-A evaluation at a 90% confidence level for frequency-domain NRW data population.

Group	x_i	$v(x_i)$	Margin of Error	Confidence Limits	
				$x_i \pm t_{(\alpha/2, N-1)} \frac{v(x_i)}{\sqrt{N}}$	
				Lower Bound	Upper Bound
3 M <i>cells/mL</i>	34.199	0.355	± 0.60%	33.993	34.405
2 M <i>cells/mL</i>	34.909	0.633	± 1.81%	34.541	35.277
1 M <i>cells/mL</i>	32.744	2.845	± 8.69%	31.090	34.398
0 M <i>cells/mL</i>	36.163	1.278	± 3.53%	35.420	36.906

A paired t-test was conducted to determine the significance of these differences. The null hypothesis that: there is no difference in the static permittivity, was rejected for each of the comparison groups as the area under the one-tail t-distribution was less than the significance level ($\alpha = 0.1$) (see Table 7.4). As a result, the B16 test using frequency-domain measurement system, showed distinct differences in the data, despite the variability in the sample for 1 M *cells/mL*.

Table 7.4: One-tail paired t-test at a 90% confidence level for frequency-domain NRW data population.

Comparison	Δx_i	$Var(\Delta x_i)$	t-statistic	Likelihood ($v=11$)	Verdict (Null Hypothesis)
3 and 2 M <i>cells/mL</i>	5.94	15.13	1.53	0.077	Reject
2 and 1 M <i>cells/mL</i>	5.42	3.29	2.99	0.006	Reject
3 and 1 M <i>cells/mL</i>	11.37	12.13	3.26	0.004	Reject
1 and 0 M <i>cells/mL</i>	2.30	0.54	3.14	0.005	Reject

7.5.5 Discussion of frequency-domain measurement

Measurement and analysis of data in the frequency-domain was challenged with difficulties in GA convergence, variability in the population, and the occurrence of several outliers in the 1 M *cells/mL* population group. The GA failed to produce a good fit for the data above 1 *GHz*. Since the Havrilak-Negami model was the objective for data fitting, the appropriateness of this model for testing B16 ITCs is questionable. However, it is important to account for the effects of an imprecise calibration. Imprecise calibration of the fixture dimensions, which includes the sample length, transmission line length, inner/outer conductor radii, and permittivity estimate for the PTFE core, were based on the assumption that the estimate used for ethanol is accurate. In addition, this dielectric estimate is a function of temperature, which introduces more error and uncertainty. As a result, fixture calibration was effected by the uncertainty associated with the calibration standard and temperature. It also introduces error into the measurement, which impacts the goodness of fit achieved by the algorithm. As a reminder, the GA statistically selects from the population as it converges upon a solution. Because, the starting point may not be the same, the end-point may show some statistical variability. If a precise fit is not obtained, greater uncertainty may be introduced.

A NRW algorithm over the entire population showed variability for 1 M *cells/mL*, which contained several outliers. These outliers may have resulted from a number of factors, including bacterial contamination, cellular cross contamination, cell death, and nutritionally deficient medium. However, it is likely that these effects were due to

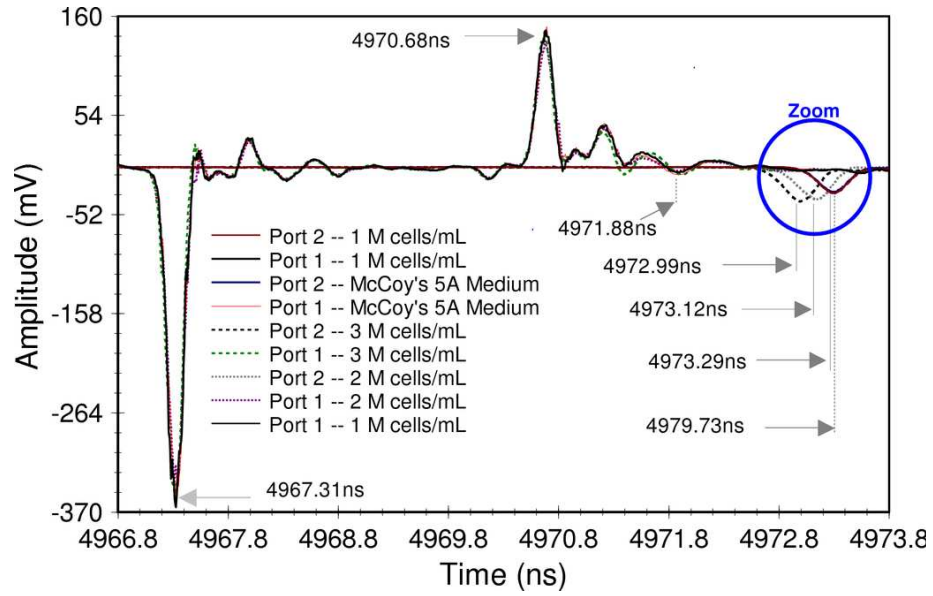
contamination from trace elements of ethanol that remained in the fixture, as the measurement technique was being improved. Despite this measurement error, the static permittivity showed statistical distinction following characterization of the cell suspensions. The data also followed a trend that allowed for correlating the characteristics to cell quantity, with limited resolution.

7.6 Results and analysis for time-domain measurement

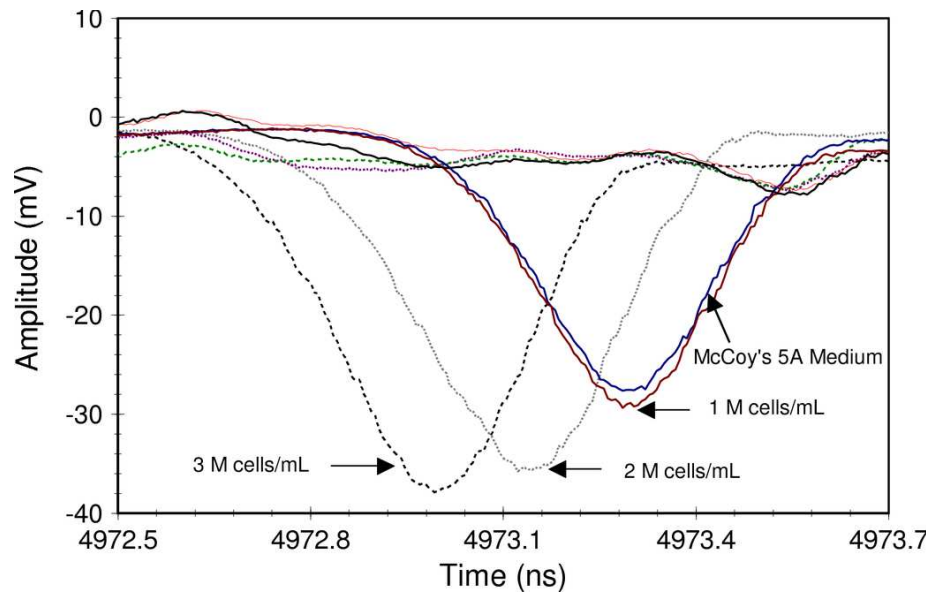
The frequency-domain measurement results provided confidence that different concentrations of B16 cancer cells may be distinguished electrically. It also provided a baseline for evaluating permittivity in the time-domain measurement system. In this measurement system a Gaussian pulse was launched down a transmission line towards the test specimen. This launched pulse, and its reflections were captured using HP54750A 20 GHz oscilloscope, set up for 128-bit averaging. In addition, the transmission through the specimen was captured (see Figure 7.8A above). Next, these reflections were processed for permittivity determination. The results of this measurement are presented below, which includes processing using genetic and NRW algorithm. This section concludes with a discussion of these results.

7.6.1 Time-domain data analysis using the GA technique

A single test-set consisting of 0, 1, 2 and 3 M *cells/mL* in McCoy's medium was arbitrarily selected from the population for processing using the GA. For this test-set, a contextual view of the waveforms resulting from a two-port time-domain measurement of



(A)



(B)

Figure 7.8: A contextual view of two-port time-domain measurement of (A) waveforms transmitted and reflected from specimen interface for B16 suspension test #2 with (B) zoom on through transmission.

the transmissions and reflections in the fixture showed morphological distinction (see Figure 7.8B). Although the group delay and magnitude associated with 1 M *cells/mL* and McCoy's medium was similar, the UWB waveforms interacted differently to various concentrations of B16 cells suspensions. The magnitude of reflections on the first port was smaller for 3 M *cells/mL* than for the other B16 cell suspensions of test-set #2. Furthermore, 3 M *cells/mL* showed less loss than the other B16 cell suspensions.

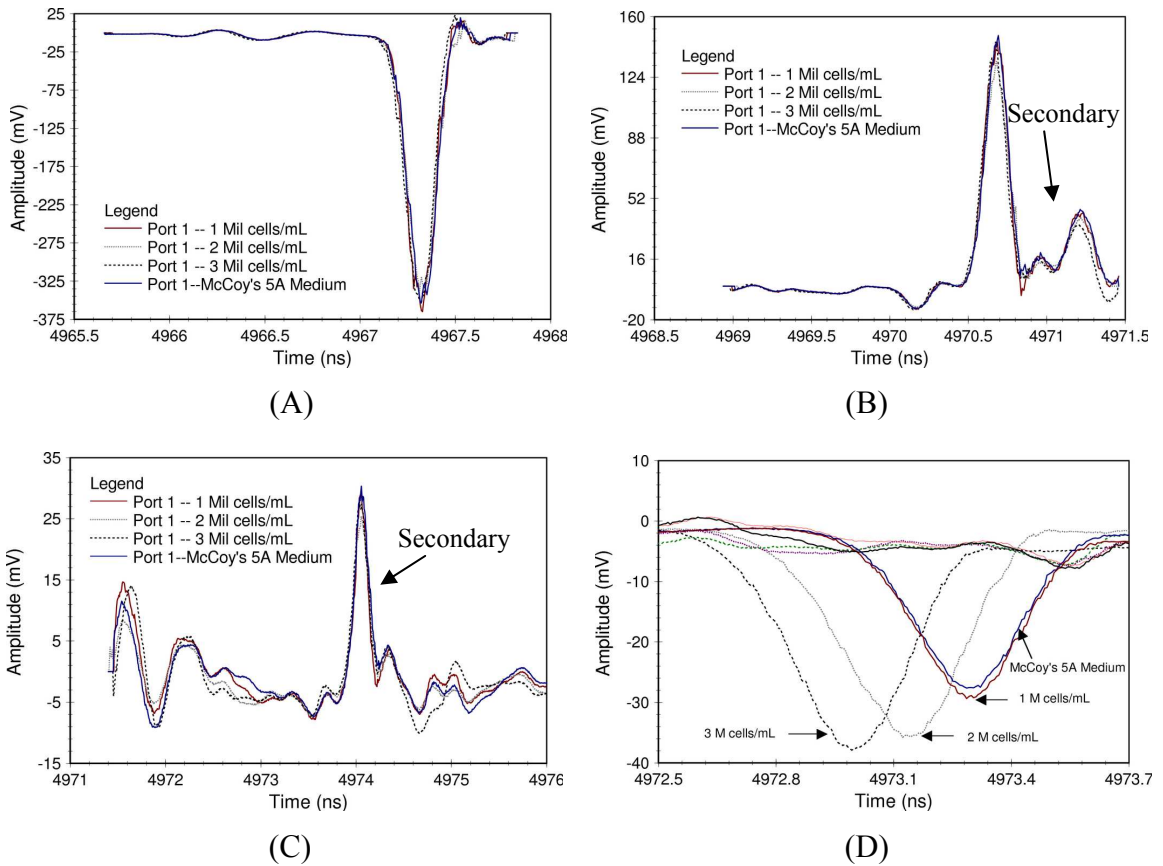
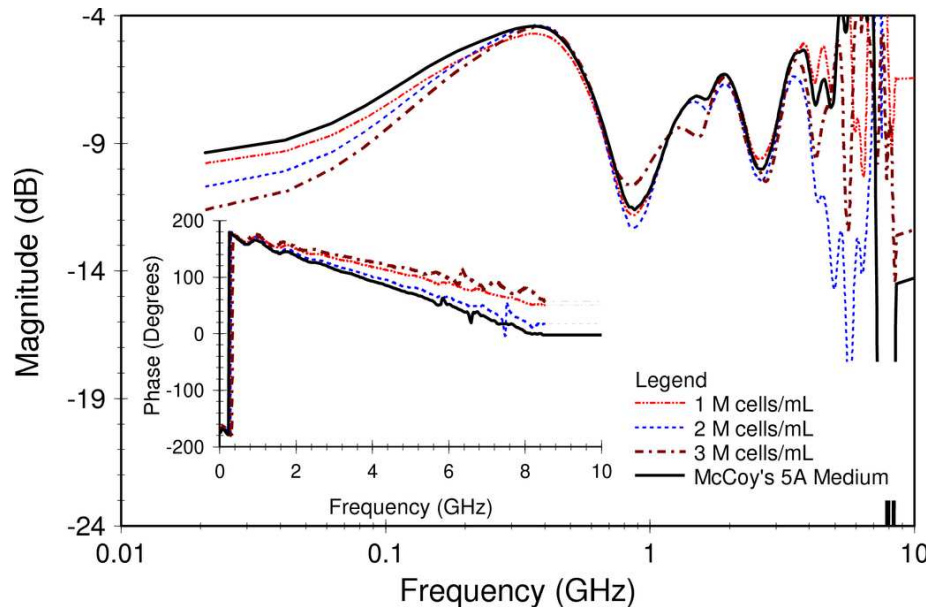


Figure 7.9: Pre-processing for converting time-domain data to S-parameters in B16 test-set #2, where (A) is waveform launched down fixture, (B) reflected from 1st and (C) 2nd interfaces, and (D) transmitted through.

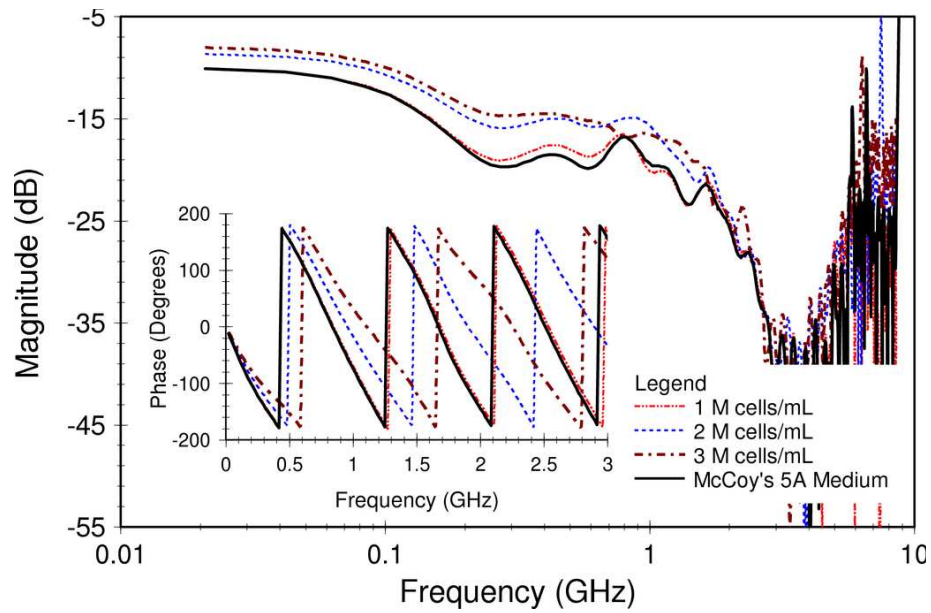
Isolation of the time-domain waveforms for computing the S-parameters required deciding on the position of the boundaries for windowing on the primary reflections (see Figure 7.9). Secondary reflections originating from energy reflected by the input port of the pulse generator were placed within the bounds of the isolated waveforms to reduce the measurement error associated with ethanol. The most pronounced secondary effects were noted in the reflections at the PTFE-specimen interfaces. Courtney and Bowden required capturing only the primary reflections [105]. However, the fixture applied by Courtney-Bowden strictly required a 50 Ω match and probes to pick up the transmitted and reflected waveforms. As such, there was no need to deal with large secondary reflections. Next, the isolated waveforms were pre-processed for conversion to S-parameters by performing a Fourier transform on the waveform reflecting back to port 1 from the specimen interface (Figure 7.9B) and dividing it by the transform of the launched pulse (Figure 7.9A) for the construction of S_{11} . Similarly, S_{21} was constructed by dividing the Fourier transform of the waveform transmitted to port 2 by the incident waveform (Figure 7.9D).

Table 7.5: Computed time intervals for test-set #2 of B16 cell suspensions.

	τ_1 (ns)	τ_2 (ns)	τ_3 (ns)	τ_4 (ns)
3 M <i>cells/mL</i>	1.6758	0.6357	3.3604	5.6719
2 M <i>cells/mL</i>	1.6846	0.60058595	3.5273	5.8125
1 M <i>cells/mL</i>	1.6787	0.60058590	3.6797	5.9590
0 M <i>cells/mL</i> (McCoy's Media)	1.6875	0.6035	3.6797	5.9707



(A)



(B)

Figure 7.10: Computed S-parameters (A) S11 and (B) S21 associated with a conversion of time-domain measurement data for the test #2 of B16 cell suspensions.

The data in Table 7.4 shows the computed time intervals required in the conversion of time-domain waveforms to S-parameters for test-set #2. As observed from this table, the total time between the launched Gaussian signal at port 1 and received at port 2 (τ_4) increased in duration with a decreasing cell count. This time measured 5.67 *nsec* for 3 M *cells/mL* and 5.97 *nsec* for medium. Application of these times in the conversion of time-domain measurement data (see Chapter 4) resulted in S-parameters that showed distinction in the phase of S_{21} and amplitude of S_{11} (see Figure 7.10). This distinction was evident in a plot of the magnitude for S_{11} and S_{21} up to a frequency of 600 *MHz* and 1 *GHz*, respectively. A comparison of McCoy's medium and 1 M *cells/mL* showed the least noticeable distinction, especially for S_{21} , but the phase and magnitudes were slightly advanced so that this measure supported a definite pattern for the cell concentrations. The S-parameter magnitudes computed for S_{11} showed that McCoy's medium is less reflective than when concentrated with 3 M *cells/mL*. As such, the transmission coefficient increased proportionately with an increase in the cell concentration. A shift in the phase for the transmission coefficient also accompanied an increase in the cell concentration.

These S-parameters were applied to the GA for permittivity extraction. Graphs in Figure 7.11 illustrate how well the GA was able to fit the Havrilak-Negami model to the data of test-set #2. A good fit was achieved for the phase and magnitude of S_{11} up to about 200 *MHz* (see Figure 7.11A, C, E & G). The fit of measured and computed data for S_{21} showed a better phase match in the frequency-domain test.

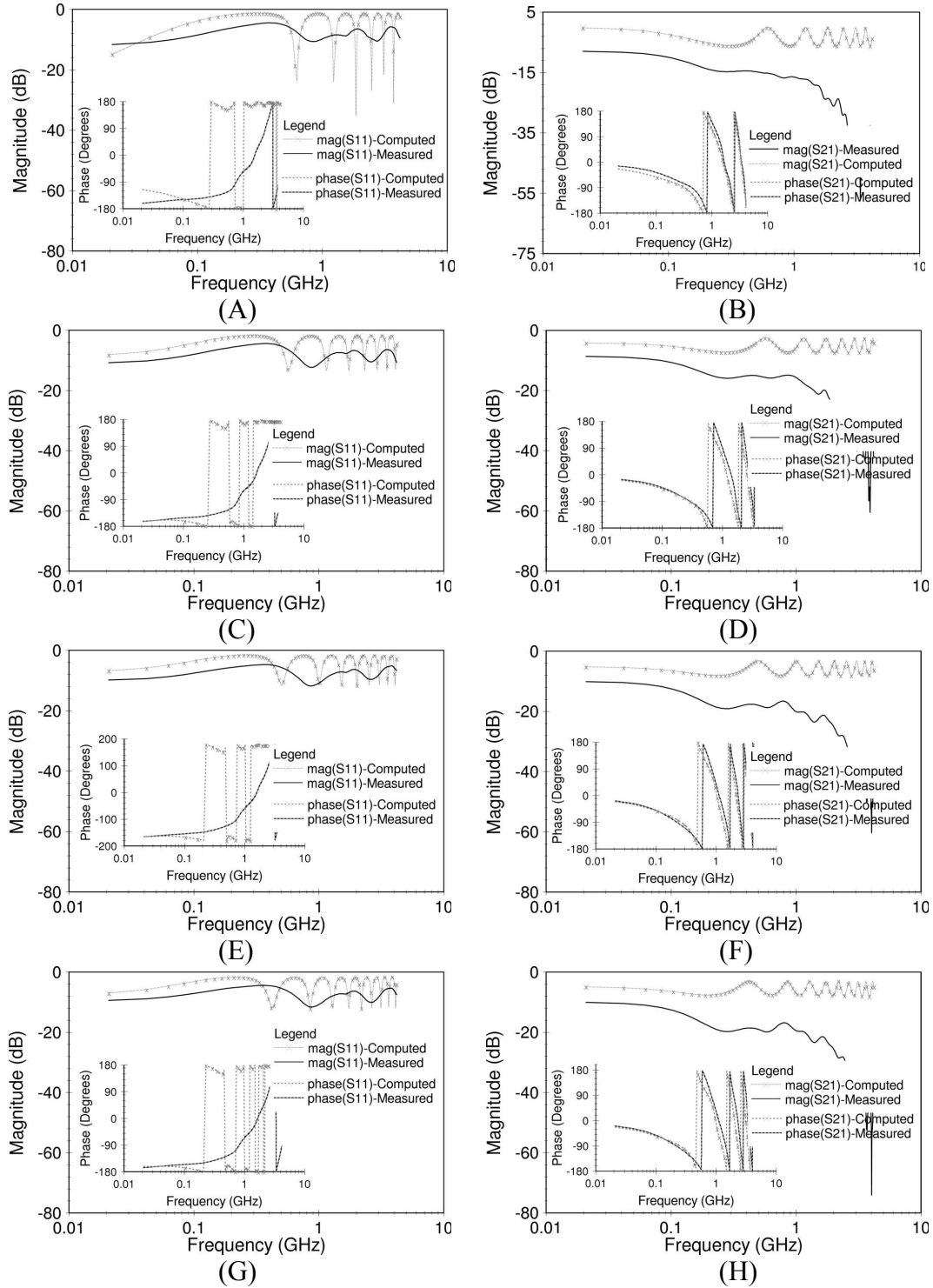


Figure 7.11: A comparison of measured and computed results for S_{11} and S_{21} of the 3rd test, for (A-B) 3 M cells/mL, (C-D) 2 M cells/mL, (E-F) 1 M cells/mL, (G-H) McCoy's 5A medium.

(see Figure 7.11B, D, F and H). Although, the UWB test is challenged with additional uncertainty due to added transmission line length and impedance matching, it displayed better distinction in the test groups for the complex relative permittivity, although the low-frequency match between measured and computed data was poor for a single test-set.

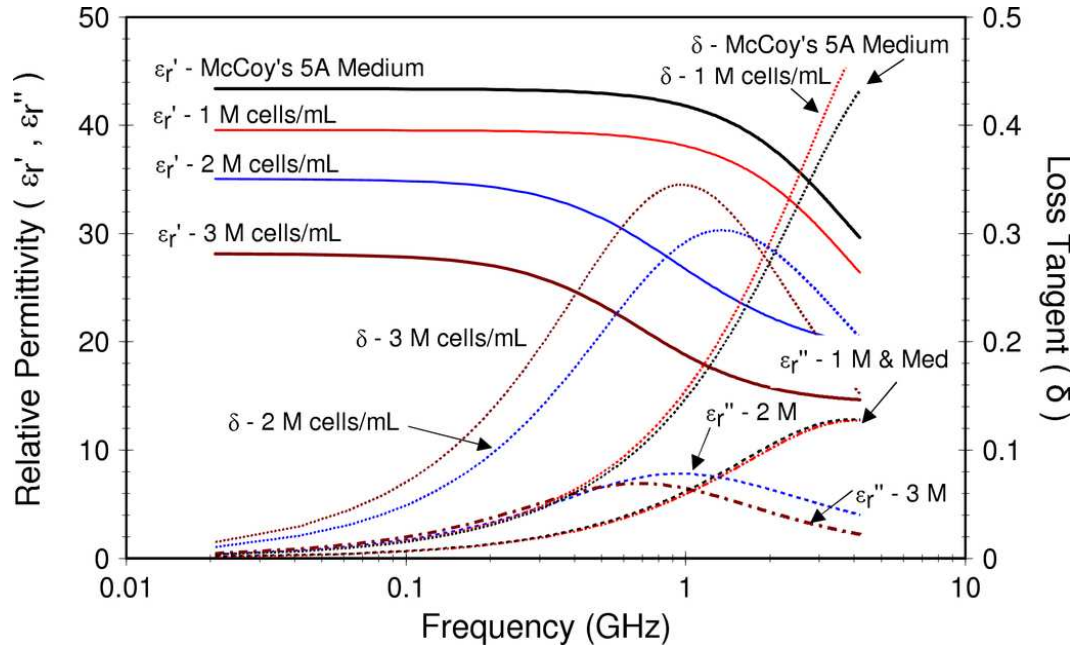


Figure 7.12: Complex permittivity for B16 cell suspension using the GA on test-set #2.

Furthermore, the real and imaginary components of the complex permittivity associated with this test-set were also clearly distinct (see Figure 7.12). Although the GA yielded very distinct values for the complex relative permittivity in the time-domain dielectric spectroscopy system, the raw score associated with the goodness of fit was worse than that measured using the VNA data (see Table 7.6).

Table 7.6: Extracted GA parameters for time-domain measurement data (test-set #2).

	ϵ_{static}	$\epsilon_{\text{optical}}$	τ_{relax}	U_s	U_i	A_s
3 M <i>cells/mL</i>	31.60	11.9	2.389E-07	0.992	0.989	0.34
2 M <i>cells/mL</i>	32.37	14.9	5.356E-11	0.980	0.980	0.12
1 M <i>cells/mL</i>	39.37	15.5	3.094E-11	1.012	1.012	0.00
0 M <i>cells/mL</i> (Medium)	44.19	16.2	3.874E-11	0.989	0.989	0.15

7.6.2 Uncertainty analysis of GA performance

A type-A evaluation of the standard uncertainty was performed on the B16 suspensions to assess the repeatability of using the GA. In this test, a t-distribution was applied at a 90% confidence level. The statistical measure for this uncertainty over ten iterations of the GA for test-set #2 data showed great variability in the dielectric parameters (see Table 7.7). This analysis yielded an uncertainty with a minimum of 3.87 for the static permittivity. Unlike in the frequency-domain, the confidence limits did not overlap as much across the test-set. As a result, the GA performed better with time-domain data. However, for consistency, the NRW technique was used to process the time-domain data for the remainder of the population.

7.6.3 Time-domain data analysis using NRW technique

Application of the NRW technique demonstrated distinction in the real and imaginary parts of the complex permittivity up to about 200 MHz (see Figure 7.12A-B).

Above 200 MHz the effects of impedance mismatch at the input port as well as the uncertainty associated with the lengths of transmission lines begins to dominate the

Table 7.7: Type-A evaluation on a 90% confidence interval of time-domain test-set #2.

Group	NRW	Genetic Algorithm ($X_{2,k}$)					
		x_2	$\nu(x_2)$	Margin of Error	Confidence Limits		
					$x_2 \pm t_{(\alpha/2, N-1)} \frac{\nu(x_2)}{\sqrt{N}}$		
					Lower Bound	Upper Bound	
3 M cells/mL	ϵ_{static}	29.97	27.75	3.87	$\pm 8.1\%$	25.51	29.99
	$\epsilon_{\text{optical}}$	-	16.68	0.29	$\pm 1.0\%$	16.51	16.84
	τ_{relax}	-	0.19	0.01	$\pm 3.1\%$	0.18	0.20
2 M cells/mL	ϵ_{static}	35.47	32.40	4.5	$\pm 8.1\%$	29.79	35.01
	$\epsilon_{\text{optical}}$	-	19.52	0.26	$\pm 0.8\%$	19.37	19.67
	τ_{relax}	-	0.07	0.003	$\pm 2.4\%$	0.07	0.07
1 M cells/mL	ϵ_{static}	42.84	39.44	5.49	$\pm 8.1\%$	36.26	42.63
	$\epsilon_{\text{optical}}$	-	15.94	5.49	$\pm 20.0\%$	12.75	19.12
	τ_{relax}	-	0.03	0.001	$\pm 1.8\%$	0.03	0.03
0 M cells/mL (Medium)	ϵ_{static}	46.23	41.89	5.82	$\pm 8.1\%$	38.51	45.25
	$\epsilon_{\text{optical}}$	-	18.03	0.45	$\pm 1.4\%$	17.77	18.28
	τ_{relax}	-	0.04	0.001	$\pm 1.7\%$	0.03	0.04

measurement data. Although the primary limitation in using the NRW technique is half-wavelength resonance effects, its occurrence seemed to provide some distinction in the

B16 cell suspensions. As in the frequency-domain test, the static permittivity for test #2 showed the highest values for McCoy's medium and lowest for 3 M *cells/mL*.

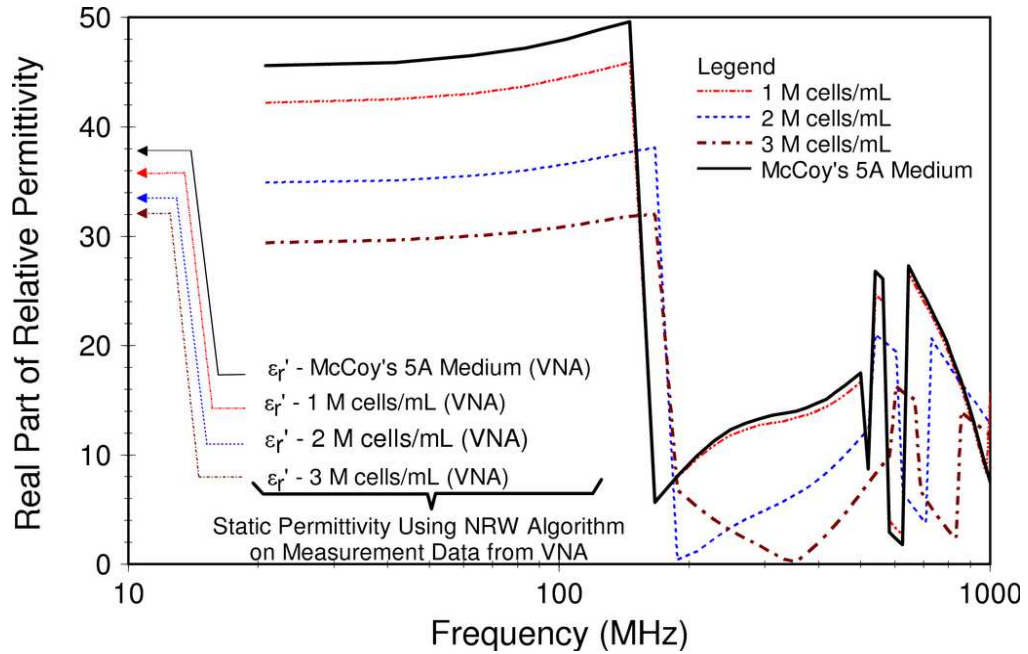


Figure 7.13: The real part of the NRW complex permittivity in the time domain.

A test over the entire population of B16 cell suspensions yielded distinguishable UWB measures for the cell suspensions. The time-domain test demonstrated distinction in all the suspensions including 1 M *cells/mL* (see Figure 7.14). However, a strong upward trend was observed in the NRW plot of permittivity for the B16 cell suspensions. The trend is more pronounced for 3 M *cells/mL* (see discussion for more details).

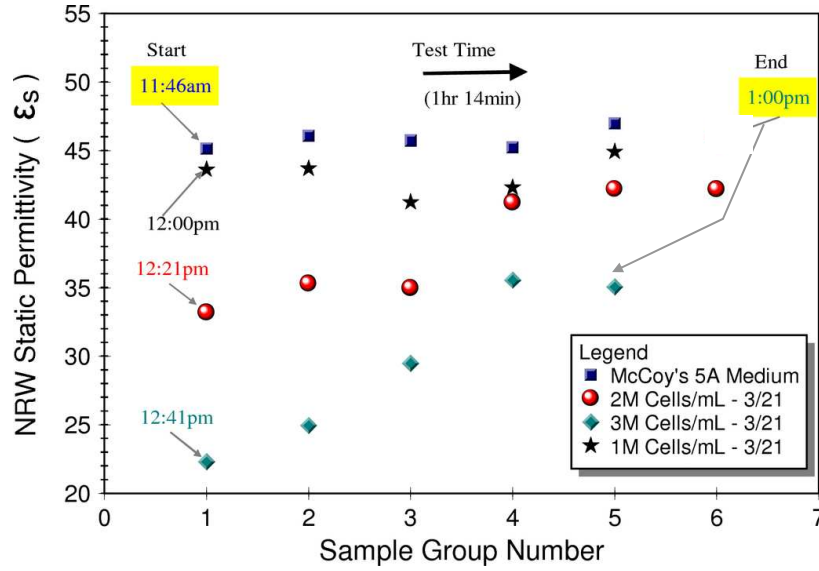


Figure 7.14: The NRW static permittivity for the population of tests of B16 suspensions in the time domain.

7.6.4 Uncertainty analysis of NRW performance

A type-A evaluation of the standard uncertainty across the entire population demonstrated that a distinction could be made between McCoy's medium, 1 and 2 M *cells/mL* (see Table 7.9). Although there was statistical overlap between the confidence

Table 7.8: Type-A evaluation at a 90% confidence level for time-domain NRW data population.

Group	x_i	$\nu(x_i)$	Margin of Error	Confidence Limits	
				Lower Bound	Upper Bound
3 M <i>cells/mL</i>	32.247	8.591	± 17.9%	26.478	38.015
2 M <i>cells/mL</i>	38.188	4.120	± 7.24%	35.422	40.955
1 M <i>cells/mL</i>	43.612	1.666	± 2.56%	42.493	44.730
0 M <i>cells/mL</i>	45.917	0.681	± 1.0%	45.460	46.374

intervals associated with 2 and 3 M *cells/mL* at a 90% confidence level, the mean appeared to be distinct for UWB measurement. A t-test demonstrated that the null hypothesis may not be rejected for each comparison group, as in frequency-domain dielectric spectroscopy (see Table 7.9). However, unlike the frequency-domain test there was no significant difference in a comparison of 3 and 1 M *cells/mL*.

Table 7.9: One-tail paired t-test at a 90% confidence level for time-domain NRW data population.

Comparison Group	Δx_i	$Var(\Delta x_i)$	t-statistic	Likelihood ($\nu=11$)	Verdict (Null Hypothesis)
3 and 2 M <i>cells/mL</i>	0.71	0.08	2.52	0.015	Reject
2 and 1 M <i>cells/mL</i>	2.17	1.89	1.58	0.072	Reject
3 and 1 M <i>cells/mL</i>	1.46	1.84	1.07	0.155	Accept
1 and 0 M <i>cells/mL</i>	3.42	2.16	2.33	0.021	Reject

7.6.5 Discussion of time-domain measurement

Measurement and analysis of data in the time-domain showed significant improvement in GA performance as compared to frequency-domain data. This performance is due to a larger spread in the permittivity for time-domain data. A $\pm 8.1\%$ margin of error was noted for the GA performance in both the time- and frequency-domain measurement. An 18% difference between the time- and frequency-domain data was observed for measurement of 0 M *cells/mL*. The time-domain measurement system

was calibrated in ethanol, which was less dispersive than McCoy's medium. As a result, the reflections off the 2nd specimen interface (see Figure 7.9) for McCoy's medium was less distinctive than for ethanol (see Figure 6.4). This occurrence is due to the inability to precisely locate the peak for estimate the time interval (τ_3) used to compute the S_{21} S-parameter. McCoy's medium showed greater dispersion and more loss than the dilute substances used to calibrate the instrument. Moreover, a secondary line reflection, which appears in the measurement of both the dilute substance as well as McCoy's medium, interferes with the B16 measurement data (compare Figure 7.9C and Figure 6.4C). As a result, the measurement of time-domain data was less precise. However, this lack of precision resulted in a larger spread in the data, which gives the appearance of better GA performance.

The time-domain results also showed no statistical distinction between 1 and 3 M *cells/mL*. The upward trend in the data population in Figure 7.14 is the cause of this occurrence. Originally, it was thought that this trend was due to cell death because the occurrence appears to be a function of time and cell count. This thought was later dismissed after considering the difficulty in maintaining an evenly distributed population of tumor cells in suspension. It is believed that the population contained a higher concentration of cells towards the bottom of test tube. The pipette was inserted towards the bottom of the tube when drawing a test sample from the population. As a result, fewer cells were drawn from the population with each test.

7.7 Summary

Characterizing and quantifying ITCs in medium is difficult because of the requirement for an evenly distributed population of cells. Besides cell growth and death, which occurs in a cell culture, assuring an evenly distributed population of cells is non-trivial and is a central problem in a transmission-reflection measurement of ITCs. In flow cytometry, this distribution problem is solved by the “flow” of liquids in the analysis. Regardless, this study demonstrated that ITCs can be characterized using dielectric spectroscopy, as well as related to cell quantity. The resolution associated with the quantity measured is a function of uncertainty in the measurement system. The calibration accuracy for the measurement system and convergence of the genetic algorithm were primary sources of uncertainty. The advantage of a wide measurement bandwidth available in the time-domain measurement system can not be assessed without accurately computing the S-parameters.

Chapter 8

Summary and Future Recommendations

This research provided novel UWB electronics, design methods, genetic and NRW algorithms, and frequency- and time-domain measurement systems. These tools were applied to an investigation on the use of dielectric spectroscopy to characterize and quantify isolated B16 tumor cells in McCoy's liquid medium. In developing practical systems for measurement, many challenges were encountered, which included designing UWB electronics to generate sub-nanosecond pulses, compensating for imperfections in the fixture construction, and extracting accurate dielectric properties using the algorithms.

Designing UWB electronics to generate sub-nanosecond pulses was a challenge because of the early stages of advancement for UWB technology. At the start of this research, adequacy of the tools for evaluating UWB pulses was questioned by researchers. Furthermore, the FCC had not yet settled on a definition for UWB classification. As a result, development of UWB electronics required fundamental tasks, which included: modeling of diodes for simulation, establishing an approach for UWB generator design, and exploring various topologies for waveform generation. These tasks resulted in the development of two new circuits including: a MCS³P circuit that contained unique Schottky detector and coupled-line differentiators and pulse-duration tunable UWB generator that applied a novel VERC approach.

Secondly, compensating for imperfections in the fixture construction was a challenge. The fixture was designed with the goal to measure a small sample within a simple and low-cost structure. This goal was achieved by developing a coaxial-line fixture with a step-discontinuity, which complicated NRW analysis. However, the fixture construction did not mitigate challenges with sample preparation and processing. Problems associated with cell preparation, which included unevenly distributed cells in suspension and lengthy measurement times, had a noticeable impact on the results. This research related trends in the permittivity to how the cells were distributed in the population from which they were drawn. In future research, a method for ensuring an even distribution of cells or consistent sampling could reduce variation in the measurement results. In addition, the length of time required for measurement of each sample was approximately two minutes. This time is reflective of the difficulty in taking T/R measurements in the fixture, which included inserting and removing the sample as well as cleaning the fixture for each test. Because the cell suspension is a living system, the cells are not static. During this time cell death and growth occurred, which changed the cell morphology and the medium pH. In this study, cell death and growth had a negligible impact because the resolution was only 1.0 M *cells/mL*. However, variations due to cell dynamics may become more important as a need to increase cell count accuracy rises.

Finally, extracting accurate dielectric properties using the NRW and genetic algorithms was a challenge in developing practical systems for measurement. Algorithm development was a challenge because of the need to calibrate the fixture. Calibration

entailed accurately describing the fixture dimensions, which included defining the transmission line lengths and describing the step-discontinuity at the specimen interface. The transmission line lengths were tuned in the algorithms using a time-consuming manual entry process. For future research, it recommended a GA be written to tune these lengths, since data associated with the calibration standard is already known. The problems associated with the step-discontinuity were solved in part by modifying the NRW algorithm and development of a GA to circumvent the shortcomings of the former. However, the GA was the source of a new set of problems, which included weak convergence upon a solution. Convergence could be improved with multiple objective functions, which is not available in the GALib software. Therefore, capturing an algorithm in a GA package that supports multiple objective statements is also recommended.

Although these challenges were significant, some challenges were not revealed until the frequency- and time-domain systems were applied to the measurement of tumor cells. Application of these tools of research showed that dielectric spectroscopy has the capacity for characterizing and quantifying ITCs in medium, through measurement of the complex electric permittivity. It also demonstrated that different volumes of cancer cells were electrically distinctive in a frequency- and time-domain measurement system, so long as the cell volumes are large enough to overcome the sources of uncertainty. Time-domain dielectric spectroscopy provided more distinct measurement data than frequency-domain dielectric spectroscopy, but the challenges associated with identifying the cell count and maintaining a homogeneous cell distribution did not permit drawing any

certain conclusion. Consequently, more research is needed to improve measurement procedures, which should include an instrument for accurately counting large cell volumes and a method for controlling and monitoring the distribution of tumor cells in medium. Consequently, reproducing accurate cell counts for congruency in measurement, establishing a consistent pulse-duration from the tunable UWB generator for measurement comparison, and reducing the execution time for sample measurement are recommended for future tests.

In conclusion, patients with cancer are typically faced with a tough choice based on limited information. Microscopic metastases could disseminate from the primary mass to the regional lymph nodes and then into distant sites, which lowers the probability of cure. Although the Mayo Clinic Surgical trials showed that survival was significantly improved when initial management began with an elective lymph node dissection, some patients may be subjected to an operation when they do not have a metastasis in a lymph node [147]. However, if the patient delays lymph node dissection until the metastasis is clinically palpable, the probability of cure sharply declines. Detecting, characterizing and quantifying ITCs, may provide an answer to this dilemma. However, tools of research are required to conduct the experiments needed to assess its prognostic significance. Dielectric spectroscopy has the potential to provide data that can not be obtained by conventional methods. It offers another modality from which information can be assembled for increased prognostic value.

References

1. Naume, B., Borgen, E., Kvalheim, G., Kåresen, R., Qvist, H., Sauer, T., Kumar, T. and Nesland, J.M., *Detection of Isolated Tumor Cells in Bone Marrow in Early-Stage Breast Carcinoma Patients: Comparison with Preoperative Clinical Parameters and Primary Tumor Characteristics*. *Clinical Cancer Research*, 2001. 7: p. 4122-4129.
2. Singletary, S.E., Greene, F.L. and Sobin, L.H., *Classification of Isolated Tumor Cells: Clarification of the 6th Edition of the American Joint Committee on Cancer Staging Manual*. *Cancer*, 2003. 98(12): p. 2740-2741.
3. Cserni, G., *Further Axillary Metastases Associated With Isolated Tumor Cells in Sentinel Lymph Nodes of Breast Cancer Patients*. *Annals of Surgery*, 2006. 243(2): p. 287.
4. Wiedswang, G., Borgen, E., Kåresen, R., Qvist, H., Janbu, J., Kvalheim, G., Nesland, J.M., and Naume, B., *Isolated Tumor Cells in Bone Marrow Three Years after Diagnosis in Disease-Free Breast Cancer Patients Predict Unfavorable Clinical Outcome*. *Clinical Cancer Research*, 2004. 10(16): p. 5342-5348.
5. Wiedswang, G., Borgen, E., Kåresen, R., Qvist, H., Janbu, J., Kvalheim, G., Nesland, J.M., and Naume, B., *Detection of Isolated Tumor Cells in Bone Marrow Is an Independent Prognostic Factor in Breast Cancer*. *Clinical Cancer Research*, 2003. 21(18): p. 3469-3478.
6. Uchikura, K., Takao, S., Nakajo, A., Miyazono, F., Nakashima, S., Tokuda, K., Matsumoto, M., Shinchi, H., Natsugoe, S. and Aikou, T., *Intraoperative Molecular Detection of Circulating Tumor Cells by Reverse Transcription-Polymerase Chain Reaction in Patients With Biliary-Pancreatic Cancer Is Associated With Hematogenous Metastasis*. *Annals of Surgical Oncology*, 2002. 9(4): p. 364-370.
7. Hermanek, P., Hutter, R.V., Sobin, L.H. and Wittekind, C., *Classification of Isolated Tumor Cells and Micrometastasis*. *Cancer*, 1999. 86(12): p. 2668-2673.

8. Sobin, L.H., *TNM, Sixth Edition: New Developments in General Concepts and Rules*. Seminars in Surgical Oncology, 2003. 21(1): p. 19-22.
9. Cserni, G., Bianchi, S., Boecker, W., Decker, T., Lacerda, M. Rank, F., and Wells, C.A., *Improving the Reproducibility of Diagnosing Micrometastases and Isolated Tumor Cells*. Cancer 2004. 103(2): p. 358-367.
10. Pasteur, Aventis. *The Reality: Understanding the Nature of Cancer*. [cited 2004]; Available from:
http://www.cancervaccines.com/pff/reality_understanding_cancer.cfm.
11. *Intense Lymph Node Processing*. 2007 1 Sep. 2006 [cited 2007 July 5]; Available from: <http://www.palpath.com/MedicalTestPages/agardspub.htm>.
12. Abati, A. and Liotta, L.A., *Looking Forward in Diagnostic Pathology*. Cancer, 1996. 78(1): p. 1-3.
13. Herbert, G., Sohn, V. and Brown, T. , *The impact of nodal isolated tumor cells on survival of breast cancer patients*. The American Journal of Surgery, 2007. 193(5): p. 571-574.
14. Weaver, D.L., Krag, D.N., Manna, E.A., Ashikaga, T., and Harlow, S.P., and Bauer, K.D., *Comparison of Pathologist-Detected and Automated Computer-Assisted Image Analysis Detected Sentinel Lymph Node Micrometastases in Breast Cancer*. Methods in Pathology, 2003. 16(11): p. 1159-1163.
15. Mesker, W.E., Torrenge, H., Sloos, W.C., Vrolijk H., Tollenaar, R.A., de Bruin, P.C., van Diest, P.J. and Tanke, H.J., *Supervised automated microscopy increases sensitivity and efficiency of detection of sentinel node micrometastases in patients with breast cancer*. Journal of Clinical Pathology, 2004. 57: p. 960-964.
16. Morales, A.R. and Nassiri, M., *Automation of the Histology Laboratory*. Lab Medicine, 2007. 38(7): p. 405-410.
17. Lee, Y.J., Moon, H.G., Park, S.T., Choi, S.G., Hong, S.C., Jung, E.J., Joo, Y.T., Jeong, C.Y. and Ha, W.S., *The value of intraoperative imprint cytology in the assessment of lymph node status in gastric cancer surgery*. Gastric Cancer, 2005. 8: p. 245-248.
18. Beck, H.P., Brammer, I., Zywiets, F. and Jung H., *The Application of Flow Cytometry for the Quantification of the Response of Experimental Tumors to Irradiation*. Cytometry, 1981. 2(1): p. 44-46.

19. Robinson, J.P., *Flow Cytometry*, in *Encyclopedia of Biomaterials and Biomedical Engineering*. 2004, Marcel Dekker, Inc.: New York. p. 630-639.
20. *Flow Cytometry: Current Trends and Future Outlook*, in *Biocompare Surveys and Reports*. 2006. p. 2-4.
21. Paraskevas, C.D., Vassiliou P. and Dervos, C.T. *Temperature Dependent Dielectric Spectroscopy in Frequency-domain of High-Voltage Transformer Oils Compared to Physicochemical Results*. in *IEEE International Conference on Dielectric Liquids*. 2005: IEEE.
22. Asami, K., Gheorghiu, E., and Yonezawa, T., *Real-time monitoring of yeast cell division by dielectric spectroscopy*. *Biophysical Journal*, 1999. 76(6): p. 3345-3348.
23. Gheorghiu, E., *Characterizing cellular systems by means of dielectric spectroscopy*. *Bioelectromagnetics*, 1998. 17(6): p. 475-482.
24. Prodan, C., Mayo, F., Claycomb, J.R., and Miller, J.H., *Low-frequency, low-field dielectric spectroscopy of living cell suspensions*. *Journal of Applied Physics*, 2004. 95(7): p. 3754-3756.
25. Raicu, Valerica, *A simple theoretical and practical approach to measuring dielectric properties with an open-ended coaxial probe*. *Measurement Science and Technology*, 1995. 6(4): p. 410-414.
26. Krzyzagórski, M., Adamski, W., Komisarczuk, J., and Kitliński, M. *Transmission line method for liquid or loose material diagnosis*. in *12th International Conference on Microwaves and Radar*. 1998. Krakow, Poland.
27. Garner, A.L., Yang, J., Chen, N., Kolb, J., Loftin, K.C., Swanson, R.J., Beebe, S., Joshi, R.P., and Schoenbach, K.H. *Effects of electrical pulses on the dielectric properties of biological cells*. in *2003 Annual Report Conference on Electrical Insulation and Dielectric Phenomena*. 2003. Albuquerque, New Mexico: IEEE Dielectrics and Insulation Society.
28. Liu, J.C., Wu, C.Y., Lou, D.C., and Liu, C.Y., *Picosecond pulse shaping circuits with inverse Gaussian monocycle waveforms*. *Jnl of C.C.I.T*, 2005. 34(1): p. 1-9.
29. Golub, T. R., Slonim, D. K., Tamayo, P., Huard, C., Gaasenbeek, M., Mesirov, J. P., Coller, H., Loh, M. L., Downing, J. R., Caligiuri, M. A., Bloomfield, C. D. and Lander E. S., *Molecular Classification of Cancer: Class Discovery and Class Prediction by Gene Expression Monitoring*. *Science*, 1999. 286(5439): p. 531-537.

30. Rao, Nannapaneni Narayanna, *Elements of Engineering Electromagnetics*, 3rd ed. 1991, Prentice Hall, Inc.: Englewood Cliffs. p. 90-106.
31. Toll, John S., *Causality and the Dispersion Relation: Logical Foundations*. Physical Review, 1956. 104(6): p. 1760-1770.
32. *Application Note 1217-1*, in *Basics of measuring the dielectric properties of materials*, HP Literature Number 5091-33003. 1992: Hewlett Packard Company. p. 1-16.
33. Hamburger, F., *Polar Molecules, Their Contribution to energy loss in dielectrics*. Physical Review, 1930. 35: p. 1119-1124.
34. Schwan, H.P. *Electrical Properties of Tissue and Cell Suspensions: Mechanisms and Models*. in *The 16th Annual International Conference of the IEEE Engineering Advances: New Opportunities for Biomedical Engineers*. 1994. Baltimore, MD, USA: IEEE.
35. Martinsen, ØG., Grimnes, S., Schwan, H.P., *Interface Phenomena and Dielectric Properties of Biological Tissue*, in *Encyclopedia of Surface and Colloidal Science*. 2002, Marcel Dekker, Inc.: New York. p. 2463-2652.
36. Wagner, K.W., *Explanation of the dielectric fatigue phenomena on the basis of Maxwell's concept*. Arch, 1914. Arch. Elektro. Technol.(2): p. 371.
37. Maxwell, J.C., *Treatise on Electricity and Magnetism*. 1873: Oxford University Press.
38. Cole, K.S. and Cole, R.S., *Dispersion and Absorption in Dielectrics: I. Alternating Current Characteristics*. Journal of Chemical Physics, 1941. 9: p. 341-351.
39. Davidson, D. W. and Cole, R. H., *Dielectric relaxation in glycerol, propylene glycol, and n-propanol*. Journal of Chemical Physics, 1951. 19: p. 1484-1490.
40. Negami, S. and Negami, S., *A complex plane representation of dielectric and mechanical relaxation processes in some polymers*. Polymer, 1967. 8(4): p. 161-210.
41. Asami, Koji, *Characterization of heterogeneous systems by dielectric spectroscopy*. Progress in Polymer Science, 2002. 27: p. 1617-1659.

42. Hanai, T., Koizumi, N., and Irimajiri, A., *A Method for determining the dielectric constant and the conductivity of membrane-bounded particles of biological relevance*. Biophys. Struct. Mechanism, 1975. 1: p. 285-294.
43. Gheorghiu, E., *The dielectric behaviour of suspensions of spherical cells: a unitary approach*. Journal of Physics, A: Math. Gen., 1994. 27: p. 3883-3893.
44. Irimajiri, A., Hanai, T., and Inouye, A., *A dielectric theory of "Multi-stratified Shell" model with its application to a lymphoma cell*. Journal of Theoretical Biology, 1979. 78: p. 251-269.
45. Ermolina, I., Polevaya, Y., and Feldman, Y., *Study of Normal and Malignant White Blood Cells by Time-domain dielectric spectroscopy*. IEEE Transactions on Dielectrics and Electrical Insulation, 2001. 8(2): p. 253-261.
46. Pelster, R., *Dielectric spectroscopy of confinement effects in polar materials*. Physical Review B, 1999. 59(14): p. 9214-9228.
47. Maxwell, J.C., *A treatise of electricity and magnetism*. 1954, Dover: (Originally Clarendon Press, 1891). p. 310-314.
48. Sun, T., Gawad, S., Green, N.G. and Morgan, H., *Dielectric Spectroscopy of Single Cells: Time Domain Analysis Using Maxwell's Mixture Equations*. Journal of Physics D: Applied Physics, 2007. 40(1): p. 1-8.
49. Boniconro, A., Cametti, C., and Biasio, A.D., *Effect of volum ion polarisation on Maxwell-Wagner dielectric dispersions*. Journal of Physics D: Applied Physics, 1980. 13(8): p. 1529-1535.
50. Bonet, S., Ginzburg, B.Z., Morgan, H., Wilson, G. and Zaba, B., *Time-domain dielectric spectroscopy applied to cell suspensions*. Physics in Medicine and Biology, 1993. 38(4): p. 511-520.
51. Freeman, M.S., Nottenburg, R.N., and DuBow, J.B., *An automated frequency-domain technique for dielectric spectroscopy of materials*. Journal of Physics, E: Scientific Instrumentation, 1979. 12: p. 899-902.
52. Feldman, Yu, *Time-domain dielectric spectroscopy: Advantages and disadvantages*, in *Seventh International Conference on Dielectric Materials Measurement and Applications*. 1996, IEE: University of Bath, UK.
53. Feldman, Y., Ermolina, I., and Hayashi, Y., *Time domain dielectric spectroscopy study of biological systems*. IEEE Transactions on Dielectrics and Electrical Insulation, 2003. 10(5): p. 729-753.

54. Nath, S., Urbanek, D.C., Kern, S.J., and Berg, M.A., *High-resolution Raman spectra with femtosecond pulses: An example of combined time- and frequency-domain spectroscopy*. Physical Review Letters, 2006. 97: p. 1-4.
55. Deng, J., Schoenbach, K.H., Buescher, E.S., Hair, P.S., Fox, P.M., and Beebe, S.J., *The effects of Intense submicrosecond electrical pulses on cells*. Biophysical Journal, 2003. 84: p. 2709-2714.
56. Liu, J., Dohler, M., Allen, B., and Ghavami, M., *Power loss modeling of short-range ultra wideband pulse transmissions*. IEE Proceedings of Communications, 2006. 153(1): p. 144-152.
57. Reinhardt, Rachel. *A comparison of damped waves and Gaussian waveforms*. 1997 [cited 2007; Available from: http://www.aetherwire.com/UWBWG_Archive/attach/DSWFinal.pdf].
58. Raicu, V., Kitagawa, N. and Irimajiri, A., *A quantitative approach to dielectric properties of the skin*. Phys. Me. Biol., 2000. 45: p. L1-L4.
59. Santos, J.L., Garcia, D. and Eiras, J.A., *Dielectric Characterization of Materials at Microwave Frequency Range*. Materials Research, 2002. 6(1): p. 97-101.
60. Safarik, I. and Safarikova, M., *Magnetic techniques for the isolation and purification of proteins and peptides*. BioMagnetic Research and Technology, 2004. 2(7): p. 1-17.
61. Sillerud, L.O., Popa, S.G. Coutsia, E.A., Sheltraw, D., Kuethe, D. and Adolphi, N., *Research results on biomagnetic imaging of the lung tumors*. Advanced Biomedical and Clinical Diagnostic Systems III., 2005. 5692: p. 1-10.
62. Lawrence, K.C., Nelson, S.O. and Barley, P.G., *Flow-through coaxial sample holder design for dielectric properties measurement from 1 to 350 MHz*. IEEE Transactions on Instrumentation and Measurement, 1998. 47(2): p. 354-361.
63. Folgero, Kjetil, *Broad-Band Dielectric Spectroscopy of low-permittivity fluids using one measurement cell*. IEEE Transactions on Instrumentation and Measurement, 1998. 47(4): p. 881-885.
64. *Code of Federal Regulation, Title 47, Chapter 1, Part 15, Radio Frequency Devices, Sub-Part F, Ultra-Wideband Operation*, Commission, Federal Communications, Editor. 2003. p. 767-768.

65. Harmuth, H.F., *Introduction to Ultra-Wideband Radar Systems: Transmitter Signature and Target Signature of Radar Signals*. 1995, Boca Raton, FL: CRC Press. p. 435-451.
66. Barrett, Terence W., *History of UltraWideBand Communications and Radar: Part I, UWB Communications*. Microwave Journal, Euro-Global Edition, 2001. 44(1): p. 22-56.
67. Fontana, R., *Recent system applications of short-pulse ultra-wideband (UWB) Technology*. Transactions on Microwave Theory Techniques, 2004. 52(9): p. 2087-2104.
68. Zhou, B., Shao, W. and Wang G., *UWB Microwave Imaging for Early Breast Cancer Detection: Effect of Coupling Medium On Resolution*, in *Asia Pacific Radio Science Conference*. 2004, URSI: Qingda, China. p. 431-434.
69. Sedra, A.S. and Smith, K.C., *Microelectronic Circuits*. 1998, New York: Oxford University Press, Inc.
70. Boff, A., Moll, J., and Shen, R. *A new high-speed effect in solid-state diodes*. in *International Solid State Circuits Conference*. 1960. University of Pennsylvania: IEEE.
71. Wang, C., Zeng, F., and Yao, J., *All-fiber ultrawideband pulse generation based on spectral shaping and dispersion-induced frequency-to-time conversion*. IEEE Photonics Technology Letters, 2007. 19(3): p. 137-139.
72. Hafdallah, H., Ouslimani, A., Vernet, G., and Adde. R., *Picosecond pulse shaping and compression with FETs*. Electronic Letters, 1993. 29(4): p. 414-415.
73. Afshari, E. and Hajimiri, A., *Nonlinear transmission Lines for pulse shaping in silicon*. IEEE Journal of Solid-State Circuits, 2005. 40(3): p. 744-751.
74. Mollfulleda, A., Miskovsky, P., and Mateu, J. *Robust passive shaping network for impulse radio and UWB signal generator*. in *2005 IEEE MTT-S International Microwave Symposium*. 2005. Long Beach, California: IEEE.
75. Wilson, D. *RC and RL Transient Responses*. 2003 [cited 2007 August 12]; Available from: http://www.wilsonware.com/electronics/rc_and_rl.htm.
76. Ciamulski, T. and Gwarek, K., *On eliminating crosstalk within multiconductor transmission lines*. IEEE Microwave And Wireless Components Letters, 2004. 14(6): p. 298-300.

77. Barr, A.W., *Analyzing crosstalk and ground bounce in multiconductor systems using SPICE circuit simulation*. AMP Journal of Technology, 1993. 3: p. 10-20.
78. *HSMS-286x Series*, in *Surface Mount Microwave Schottky Detector Diodes Technical Data*. 2001, Agilent Technologies, Inc. p. 1-16.
79. Sedra, A.S. and Smith, K.C., *Microelectronics circuits*. 1998, Oxford University Press, Inc.: New York. p. 197-198.
80. *Application Note*, in *Basics of Schottky Barrier Diodes*. 2007, Microwave Device Technology, Inc: Westford, MA. p. 47-52.
81. Sedra, A.S. and Smith, K.C., *Microelectronics circuits*. 1998, Oxford University Press, Inc.: New York. p. 137-146.
82. Sedra, A.S. and Smith, K.C., *Microelectronic circuits*. 1998, Oxford University Press, Inc.: New York. p. 131-136.
83. Sedra, A.S. and Smith, K.C., *Microelectronic circuits*. 1998, Oxford University Press, Inc.: New York. p. 146-155.
84. Maxwell, E., Weller, T., and Harrow, J. *A tunable Ultra-Wideband pulse generator using a variable edge-rate signal*. in *IEEE Asia Pacific Conference on Circuits and Systems*. 2006. Singapore: IEEE.
85. Fontana, R., *Recent system applications of short-pulse ultra-wideband (UWB) Technology*. IEEE Transactions on Microwave Theory Techniques, 2004. 52(9): p. 2087-2104.
86. Engler, H.F., *Technical Issues in Ultra-Wideband Radar Systems*. 1995: CRC Press, Inc. p. 11-50.
87. Agee, F.J., Baum, C.E., Prather, W.D., et al., *Ultra-wideband source and antenna research*. IEEE Transactions on Plasma Science 2000. 28(5): p. 1624-1630.
88. Prather, W., Baum, C.E., Lehr, J.M. et al., *Ultra-wideband source and antenna research*. IEEE Transactions on Plasma Science, 2000. 28(5): p. 860-873.
89. Han, J. and Nguyen C., *A New Ultra-Wideband, Ultra-Short Monocycle Pulse Generator with Reduced Ringing*. IEEE Microwave And Wireless Components Letter, 2002. 12(6): p. 1-3.
90. *Pulse and waveform generation with step recovery diodes*, in *Application Note 918*. 1968, Palo Alto, CA: Agilent Technologies.

91. Han, J. and Nguyen C., *Ultra-Wideband Electronically Tunable Pulse Generators*. IEEE Microwave And Wireless Components Letter, 2004. 14(3): p. 112-114.
92. Han, J. and Nguyen C. *Microstrip Impulse Generators with Tunable Pulse-duration for Ultra-Wideband Applications*. in *Asia Pacific Microwave Conference*. 2003. Seoul Korea.
93. Lesha, M.J. and Paoloni, F.J., *Generation of balanced sub nanosecond pulses using step-recovery diodes*. Electronic Letters, 1995. 31(7): p. 510-511.
94. Tian, Z., Sun, Z., and Qu, S., *Tunable pulse-width, electro-optically cavity-dumped, rf-excited Z-fold waveguide CO2 laser*. Review of Scientific Instruments, 2005. 76: p. 1-3.
95. Ghosh, Smarajit, *Network Theory: Analysis and Synthesis*. 2005, Prentice-Hall: New Delhi, India. p. 289-290.
96. Loomis, J. *Signal Processing Notes*. 1997 5 Sep. [cited 2007 August 21]; Available from:
<http://www.engr.udayton.edu/faculty/jloomis/ece561/notes/intro/signals.html>.
97. Maxwell, E., Weller, T., and Harrow, J. *Enhanced Tunable Ultra-Wideband Pulse Generation Based on Variable Edge-Rate Compression*. in *Radar Conference, 2006. 3rd European*. 2006. Manchester, UK: IEEE.
98. Johnson, H. and Graham, M., *High Speed Digital Design: A Handbook of Black Magic*. 1993, Prentice Hall: New Jersey.
99. Pozar, D.M., *Microwave Engineering*. 2nd ed. 1998, John Wiley & Sons: New York. p. 422-496.
100. Hsue, C., Cheng T. and Chen H., *Implementation of First-Order and Second order Microwave Differentiators*. IEEE Transactions on Microwave Theory and Techniques, 2004. 52(5).
101. Nelson, S., Forbus, J. and Lawrence, K., *Permittivity of fresh fruits and vegetables at 0.2 to 20 GHz*. Journal of Microwave Power and Electromagnetic Energy, 1994. 29: p. 81-93.
102. Pethig, R., *Dielectric Properties of Biological Materials: Biophysical DNA Medical Applications*. IEEE Transactions on Electrical Insulation, 1984. EI-19: p. 453-474.

103. Williams, T.C., Stuchly, M.A. and Saville, P., *Modified Transmission–Reflection Method for Measuring Constitutive Parameters of Thin Flexible High-Loss Materials*. IEEE Transactions on Microwave Theory and Techniques, 2003. 51(5): p. 1560-1566.
104. Boughriet, A.H., Legrand, C. and Chapoton A., *Noniterative Stable Transmission/Reflection Method for Low-Loss Material Complex Permittivity Determination*. IEEE Transactions on Microwave Theory and Techniques, 1997. 45(1): p. 52-57.
105. Courtney, C., Motil, W., Bowen, T. and Blocher, S., *Measurement Methods and the Characterization of the Electromagnetic Properties of Materials*. 1996, Voss Scientific/Philips Laboratory.
106. Cravey, R.L., Tiemsin, P.I., Bussell, K., Dudley K.L., *Dielectric Property Measurement in the Electromagnetic Properties Measurement Laboratory*, Administration, National Aeronautics and Space, Editor. 1995, Langley Research Center. p. 1-16.
107. Venkatesh, M.S. and Raghavan G.S., *An Overview of Dielectric Properties Measuring Techniques*. Canadian Biosystems Engineering, 2005. 47: p. 7.15-7.30.
108. Nicholson, A. M., Ross, G. F., *Measurement of the Intrinsic Properties of Materials by Time-Domain Techniques*. IEEE Transactions on Instrumentation and Measurement, 1970. IM-19(4): p. 377-382.
109. Afsar, M.N., Birch, J.R. and Clarke, R. N., *The measurement of the properties of materials*. Proceedings of the IEEE, 1986. 74(1): p. 183- 199.
110. Mattar, K.E., Watters, D.G. and Brodwin, M.E., *Influence of wall contacts on measured complex permittivity spectra at coaxial line frequencies*. IEEE Transactions on Microwave Theory and Techniques, 1991. 39(3): p. 532.
111. Baker-Jarvis, J.R., Geyer, R.G., Grosvenor, C.A., Holloway, C.L., Janezic, M.D., Johnk, R.T. and Riddle, B.F., *Measuring the Permittivity and Permeability of Lossy Materials: Solids, Liquids, Metals, Building Materials, and Negative-Index Materials*, Commerce, U.S. Department of, Editor. 2005, National Institute of Standards and Technology. p. 1-149.
112. Shenhui, J., Ding, D., and Quanxing, J. *Measurement of electromagnetic properties of materials using transmission/reflection method in coaxial line*. in *Asia-Pacific Conference on Environmental Electromagnetics*. 2003. Hangzhou, China: IEEE.

113. Somlo, P.I., *The Computation of Coaxial Line Step Capacitances*. IEEE Transactions on Microwave Theory and Techniques, 1967. 15(1): p. 48-53.
114. *Application Note: Measurement of dielectric material properties*. 2006: Rhode and Schwarz. p. 6.
115. Buckley, F. and Maryott, A.A., *Tables of Dielectric Dispersion Data for Pure Liquids and Dilute Solutions*, Commerce, United States Department of, Editor. 1958, National Bureau of Standards (now NIST). p. 1-102.
116. Oswald, B., Doetsch J. and Roth K., *A new computational technique for processing transmission-line measurements to determine dispersive dielectric properties*. Geophysics, 2006. 71(2): p. K31-K35.
117. Oswald, B., Erni, D., Benedickter, H.R., Bachtold, W. and Fluhler, H. *Dielectric Properties of Natural Materials*. in *Antennas and Propagation Society International Symposium*. 1998. IEEE: Atlanta, GA.
118. S. O. Nelson, J. Forbus, and K. Lawrence,, *Permittivity of fresh fruits and vegetables at 0.2 to 20 GHz.*. Journal of Microwave Power and Electromagnetic Energy, 1994. 29: p. 81-93.
119. Gorriti, A.G. and Slobb, E.C., *A New Tool for Accurate S-Parameters Measurements and Permittivity Reconstruction*. IEEE Transactions on Geoscience and Remote Sensing, 2005. 43(8): p. 1727-1735.
120. Mohammed N. Afsar, James R. Birch, and R. N. Clarke, *The measurement of the properties of materials*. Proceedings of the IEEE, 1986. 74(1): p. 183-199.
121. Havrilla, M.J. and Nyquist D.P., *Electromagnetic Characterization of Layered Materials via Direct and De-embed Methods*. IEEE Transactions on Instrumentation and Measurement, 2006. 55(1): p. 158-163.
122. Baker-Jarvis, J., *A Generalized Dielectric Polarization Evolution Equation*. IEEE Transactions on Dielectrics and Electrical Insulation, 2000. 7(3): p. 374-386.
123. Commerce, U.S. Department of, 1993, *Transmission/Reflection and Short-Circuit Line Methods for Measuring Permittivity and Permeability*.
124. Technologies, Agilent, *Agilent Basics of Measuring the Dielectric Properties of Materials*, in *Application Note*. 2006, Agilent Technologies.

125. Joines, W. T., Zhang, Y., Li, C. and Jirtle, R. L., *The Measured Electrical Properties of Normal and Malignant Human Tissues from 50 to 900 MHz*. American Association of Physics and Medicine, 1994. 21(4): p. 547-550.
126. Rahmat-Samii, Y. and Michielssen, E., ed. *Electromagnetic Optimization by Genetic Algorithms*. Wiley Series in Microwave and Optical Engineering, ed. Chang, K. 1999, New York: John Wiley & Sons, Inc. p. 1-27.
127. Debye, P., *Polar Molecules*. 1929, Chemical Catalog Co: New York.
128. Havriliak, S. and Negami, S., *A complex plane representation of dielectric and mechanical relaxation processes in some polymers*. *Polymer*, 1967. 8(4): p. 161.
129. Cole, K. S., Cole, R.H. , *J. Chem. Phys*, 1941. 9: p. 341.
130. Wall, Matthew. *GAlib Documentation version 2.4* [cited 2006]; Available from: <http://lancet.mit.edu/galib-2.4/>.
131. Barrett, Terence W. *History of UltraWideBand (UWB) Radar & Communications: Pioneers and Innovators*. in *Progress in Electromagnetics Symposium*. 2000. Cambridge, MA.
132. Ross, G.F. *The evolution of UWB technology*. in *Proceedings of Radio and Wireless Conference 2003*. IEEE: Sarasota, FL.
133. Hussain, M.G., *Ultra-Wideband Impulse Radar-an Overview of the Principles*. *IEEE Aerospace and Electronics Systems Magazine*, 1998. 13(9): p. 9-14.
134. Nicolson, A.M., Mitchell, P.G., Mara, R.M. and Auckenthaler, A.M., *Time domain measurement of microwave absorbers*, in *Final Technical Report AFAL-TR-71-353*, Air Force Avionics Laboratory, Air Force Systems Command, Wright-Patterson AFB, November 1971, DTIC No. AD-892162.
135. Cole, R.H., *Evaluation of dielectric behavior by time-domain spectroscopy, I. Dielectric response by real time analysis, II. Complex Permittivity*. *Journal of Physics and Chemistry*, 1975. 79(14): p. 1459-1474.
136. Staebell, K. and Misra, D., *An Experimental Technique for Permittivity Measurement of Materials at Microwave Frequencies*. *IEEE Microwave Theory and Techniques*, 1990. 38: p. 337-339.

137. AWA/AWR, USDA-APHIS [Animal Welfare Act/Animal Welfare Regulations, US Department of Agriculture-Animal and Plant Health Inspection Service], 2002, Animal Welfare Act and Animal Welfare Regulations, Code of Federal Regulations, Title 9, Chapter 1, Subchapter A-animal welfare.
138. Balls M., Goldberg A., Fentem J., Broadhead C., Burch R., Resting M., Frazier J., Hendriksen C., Jennings M., van der Kamp M., *The Three Rs: The Way Forward. Alternatives to Laboratory Animals*, 1995. 23: p. 838-866.
139. *The Ethics of Research Involving Animals*. 2005, London: Nuffield Council on Bioethics. p. 31-57.
140. NRC (National Research Council). *Models for Biomedical Research: A New Perspective*, in *A report by the Committee on Models for Biomedical Research*. 1985, Washington, DC: National Academy Press. p. 12-13.
141. Bennett, B.T., Brown, M.J., Schofield, J.C., *Essentials For Animal Research a Primer For Research Personnel*. 1994, Beltsville, Md: Animal Welfare Information Center, USDA. p. 9-17.
142. Ohira T., Ohe Y., Heike Y., Podack E.R., Olsen K.J., Nishio K., Nishio M., Miyahara Y., Funayama Y., Ogasawara H., et al., *In vitro and in vivo growth of B16F10 melanoma cells transfected with interleukin-4 cDNA and gene therapy with the transfectant*. *Journal of Cancer Research and Clinical Oncology*, 1994. 120(11): p. 631-635.
143. Fidler, Isaiah J., *Biological Behavior of Malignant Melanoma Cells Correlated to Their Survival in Vivo*. *Cancer Research*, 1975. 35(1): p. 218-224.
144. Freshney, R.I., *Culture of Animal Cells: A Manual of Basic Technique*. 2nd ed. 1987, Alan R. Liss, Inc.: New York. p. 131-140.
145. Freshney, R.I., *Culture of Animal Cells: A Manual of Basic Technique*. 2nd ed. 1987, Alan R. Liss, Inc.: New York. p. 227-244.
146. Nielsen, L.K., Smyth, G.K. and Greenfield P.F., *Hemocytometer Cell Count Distributions: Implications of Non-Poisson Behavior*. *Biotechnology Progress*, 1991. 7(6): p. 560-563.
147. Balch, C.M., Cascinelli, N.S., Frankin, H., Soong, S.J., et al. , *Cutaneous Melanoma, 3rd Ed: Elective Lymph Node Dissection: Results of Prospective Randomized Surgical Trials*. 1998, St. Louis Missouri: Quality Medical Publishing, Inc. p. 210-211.

Appendices

Appendix A: Quantitative description for Gaussian pulse

UWB signal propagation in the frequency-domain is of great interest because RF/Microwave characteristics are mainly described by frequency-domain measures, through which parameters important in component selection, design, and evaluation are readily identifiable, i.e. cut-off frequency, bandwidth and center frequency. The utility of these parameters is not fully realized if an imprecise time-domain formulation is applied for transformation to the frequency-domain. Consequently, this section presents a simple approach for formulating a more precise ideal Gaussian PDF and demonstrates that evaluating it in terms of 10-90% rise time offers a practicable Gaussian function, a mathematical approach to identifying points for axis shifting, and a starting point for math-based periodic signal evaluation.

A.1 Methodology

This section approaches reformulation of the ideal Gaussian for UWB measurement systems by first exposing the complications with standard deviation and the error that results from an unsuitable interpretation. Next, the basic Gaussian PDF in equation (A.1) is used to develop a relationship between standard deviation rise time and 10-90% rise time. This relationship was applied to the construction of a more appropriate and accurate formula. Consequently, this section includes an expression in terms of 10-90% rise time. This expression was applied to the construction of a second expression that provides a double-sided distribution on the positive time-axis. A 3rd expression that demonstrates periodicity was also constructed from the double-sided formulation.

Appendix A: (Continued)

Following construction of each expression, they will be validated using the knee frequency, which is described by the following formula:

$$F_{knee} = \frac{1}{2 \cdot \tau} \quad (A.1)$$

where F_{knee} is the knee frequency and τ is the pulse rise time. Graphically, F_{knee} corresponds to the point in a log-frequency scale (Bode plot) where the spectral amplitude is down by half from the -4.0 dB/decade roll-off. It will be used for validation because it simultaneously accomplishes the goals of verifying formulation accuracy in the time-domain as well as provides an opportunity to identify and formularize morphological trends in the frequency-domain. Use of the knee frequency accomplishes these goals because it is graphically resolved following a time to frequency-domain transformation. Any formulation inaccuracies are translated through this transformation and affect the resulting waveform. Consequently, validity will be determined by comparing the expected rise time to the actual rise time, whereby the expected rise time refers to the value applied to the time-domain formula and the actual rise time the value measured from the frequency plot of F_{knee} .

A.2 Standard deviation rise time

Standard deviation rise time (τ_{σ}) describes the time required for voltage to traverse from maximum to the 1st standard deviation. The standard deviation engenders confusion because any interpretation for this variable mathematically satisfies the unity,

Appendix A: (Continued)

symmetry, and area requirements for Gaussian PDF classification, but may not be useful or valid for UWB measurement system applications. Logically, a direct replacement of standard deviation with an arbitrary rise time measure produces what should be interpreted as a standard deviation rise time and not the 10-90% rise time that is used in practice. This can be demonstrated by considering the following example: if a 10-90% rise time (τ_{10-90}) of 1.0 *nsec* is directly substituted for σ_x in (A.1), it can be expected that τ_{10-90} would be measurable in the resulting waveform. However, τ_{10-90} measures to 1.68 *nsec* instead; see Figure A.1 below.

Consequently, a direct substitution of τ_{10-90} for σ_x results in a waveform with 68% error in the time axis. It can be concluded that directly substituting 10-90% rise time for standard deviation does not yield a precise formula and τ_{10-90} is not equivalent to σ_x . Furthermore, if the 1.0 *nsec* rise time is applied to equation 2, an expected knee frequency of 0.5 *GHz* results. However, an actual F_{Knee} located at approximately 0.31 *GHz* results following a Fourier transformation, see Figure A.2 below. Since the actual and expected knee frequencies are not in agreement, the frequency-domain is not practicable, i.e., frequency-domain measures such as the 10 *dB* bandwidth, is located at approximately 0.35 *GHz* instead of the expected 0.55 *GHz*. Consequently, when an imprecise interpretation is applied to standard deviation, frequency-domain data is inaccurate and the PDF's utility is diminished to morphological trending, exclusively.

Appendix A: (Continued)

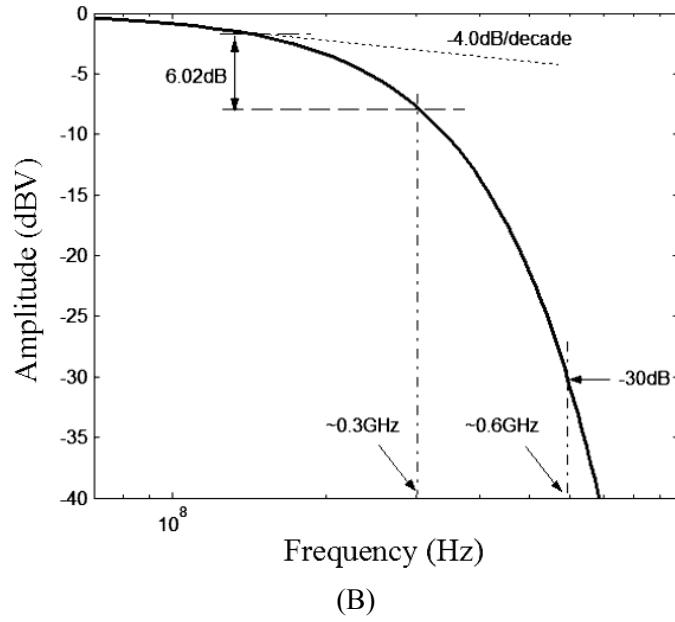
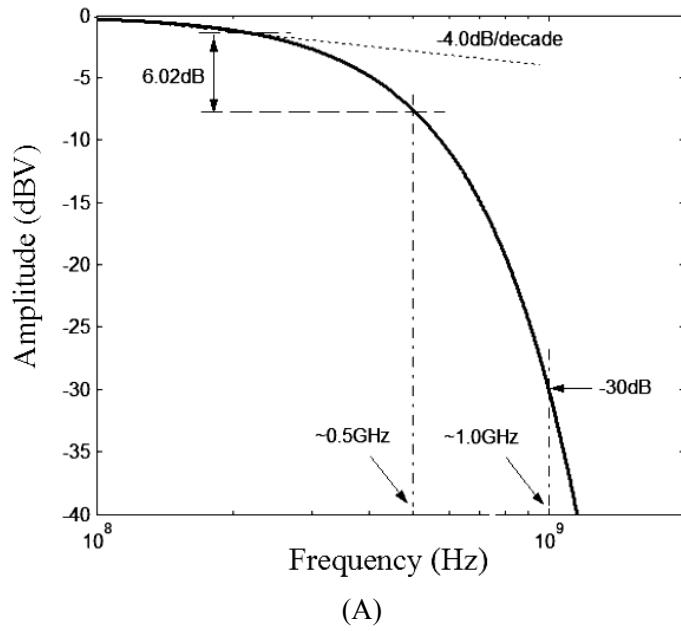


Figure A.1: Imprecise rise time for (A) Gaussian of a normalized 1.0 nsec pulse and (B) normalized spectrum with imprecise interpretation for F_{Knee} using a 1.0 nsec Gaussian pulse.

Appendix A: (Continued)

A.3 Formulation of Gaussian pulse based on 10-90% rise time

A more precise formulation could enhance the utility of the Gaussian function beyond a simple morphological comparison. Since diminished utility results from an imprecise interpretation for standard deviation, it stands to reason that a more practicable Gaussian function can be created by applying a precise interpretation for standard deviation, which can be accomplished by accurately scaling the time-axis, when 10-90% is used. Thus, the scaling factor required to represent the Gaussian formula in terms of 10-90% rise time is precisely determined by constructing a mathematical relationship between 10-90% rise time (τ_{10-90}) and standard deviation rise time (τ_σ). This relationship can be developed by substituting τ_σ for σ_x and $t_{x\%}$ for α in (A.1), which yields:

$$t_{x\%} = \sqrt{-2 \cdot \tau_\sigma^2 \cdot \ln(g(t_{x\%}, \tau_\sigma))} \quad (\text{A.2})$$

where x is the percent amplitude and $g(t_{x\%}, \tau_\sigma)$ the voltage level. Since the τ_{10-90} measure provides the time required for voltage to traverse from 10% to 90% of maximum, as shown by the equation:

$$\tau_{10-90} = |t_{10\%} - t_{90\%}| \quad (\text{A.3})$$

an equation relating τ_{10-90} and τ_σ may be developed when $t_{10\%}$ and $t_{90\%}$ are each substituted for $t_{x\%}$ in (A.2). Applying these instantaneous time values to (A.3) produces the following relationship:

Appendix A: (Continued)

$$\tau_{10-90} = \tau_{\sigma} \sqrt{-2} \cdot \left| \sqrt{\ln(0.9)} - \sqrt{\ln(0.1)} \right| \approx 1.687 \tau_{\sigma} \quad (\text{A.4})$$

that provides an exact scaling factor for equating standard deviation to 10%-90% rise time. Moreover, this relationship gives rise to the following expression:

$$g(t, \tau_{10-90}) = \frac{1}{\tau_{10-90} \cdot \sqrt{2\pi} \cdot C} \cdot e^{-\frac{t^2}{2(C \cdot \tau_{10-90})^2}} \quad (\text{A.5})$$

$$C = \frac{1}{\sqrt{-2} \cdot \left(\sqrt{\ln(0.9)} - \sqrt{\ln(0.1)} \right)} \approx 0.5928 \quad (\text{A.6})$$

where C is the scaling factor and A is the distribution amplitude. This scaling factor allows conversion of the x-axis from units in standard deviation to units in time. It also compresses the time-axis, which reveals that the standard deviation unit is larger than that of time, which would yield a spectrum with measures located at lower frequencies. The density function that results from application of the scaling factor C provides a more meaningful and accurate resolution of time- and frequency-domain measures as can be validated by applying F_{knee} . If a Fourier transform of (A.6) is plotted and a 10-90% rise of 1.0 *nsec* is applied, then the Bode plot in Figure A.3 results. Graphical analysis of this plot yields an actual knee frequency that agrees with the expected value of 0.5 *GHz* (see Figure A.2). This valid formula has a utility beyond morphological trending.

A.4 Mathematical approach to identifying points for axis shifting

The expression above provides an algebraic basis for considering a more useful formula by shifting the waveform along the time-axis. Axis shifting is necessary for a

Appendix A: (Continued)

practical Gaussian formulation to ensure the entire distribution is captured on the positive x-axis. Use of the negative axis for electrical waveforms is not conventional for measurement system applications since the x-axis represents time. Therefore, the objective of axis shifting is to move the distribution horizontally along the time-axis so that the Gaussian starts from zero. However, axis shifting introduces error because the basic ideal Gaussian distribution has an asymptotic tail and it is necessary to select a threshold along it. This threshold finitely bounds the distribution and provides a finite shifting point. The threshold error is described by a ratio of the area bounded by the selected thresholds and the total area. If the selected thresholds are represented in increments of standard deviation, then this error may be described by:

$$Error = 1 - \frac{\int_{-x \cdot C \cdot \tau}^{x \cdot C \cdot \tau} g(t, \tau_{10-90}) dt}{\int_{-\infty}^{\infty} g(t, \tau_{10-90}) dt} \quad (A.7)$$

where one standard deviation ($x=1$) produces an error of 31.7% which corresponds to a distribution that comprises only 68.3% of the total Gaussian area. However, a threshold located at four standard deviations is arbitrarily selected in this section because it results in only a .03% error, which comprises 99.97% of the Gaussian area. Consequently, the amount of error can be negligible depending on the threshold selected for shifting. Since Gaussian distributions are generally shifted in increments of standard deviation, a mathematical approach to identifying these points for axis shifting is exposed by the

Appendix A: (Continued)

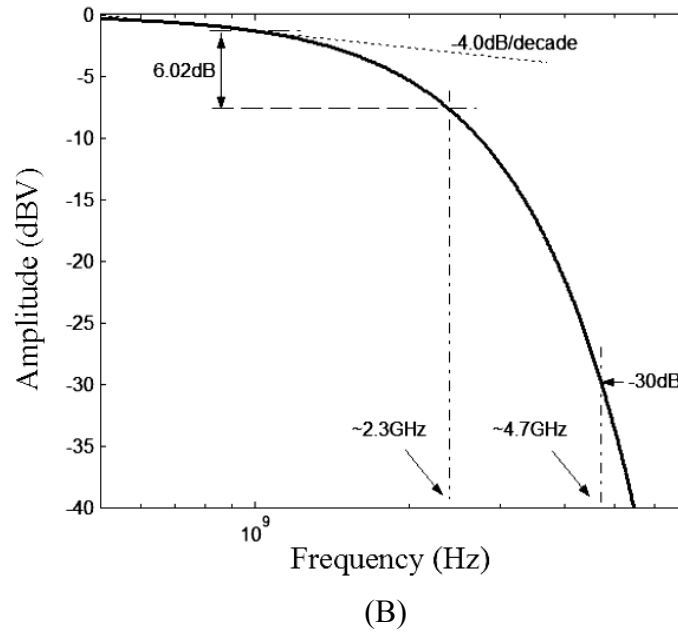
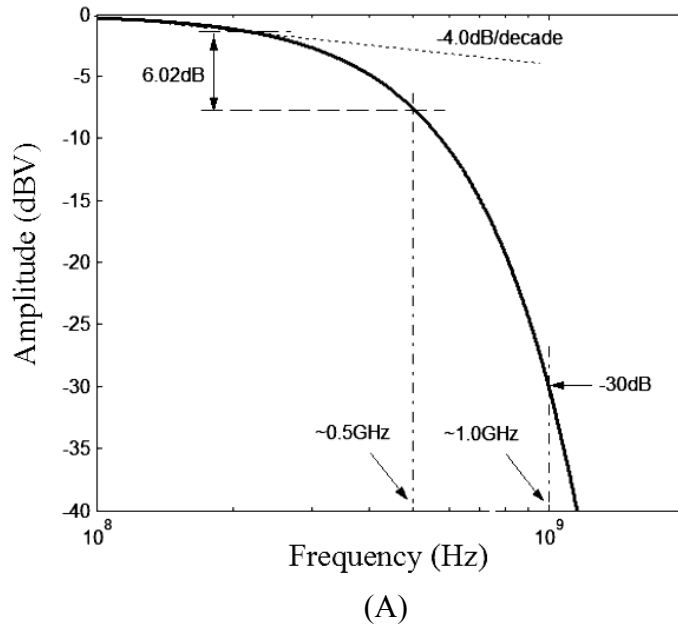


Figure A.2: Normalized spectrum with F_{knee} for (A) a 1.0 nsec 10-90% rise time and (B) normalized spectrum with F_{knee} for 1.0 nsec pulse width using 10-90% rise time interpretation.

Appendix A: (Continued)

relationship between 10-90% to standard deviation. This approach entails selecting the amount of error in terms of standard deviation, transforming it through a scaling factor C and fitting it to (A.6). Therefore, in order to completely shift the Gaussian pulse into the positive time axis, it is necessary to horizontally move the pulse to the right by four standard deviations, resulting in the second expression intended for this section, which is conveyed by:

$$g(t, \tau_{10-90}) = \frac{1}{\tau_{10-90} \cdot \sqrt{2\pi} \cdot C} \cdot e^{-\frac{(t-m_{4\sigma})^2}{2(C \cdot \tau_{10-90})^2}} \quad (\text{A.8})$$

where $m_{4\sigma} = 4 \cdot C \cdot \tau_{10-90}$ is a time shift of four standard deviations. This expression may be validated by selecting a 0.21 *nsec* rise time for (A.8), which corresponds to an expected F_{knee} of 2.37 *GHz*. Following transformation and graphical resolution of (A.8), an actual F_{knee} may be verified from Figure A.4, below. Consequently, the use of the above approach to identifying points for axis shifting gives rise to a valid formula that has a time-domain waveform on the positive time-axis, which leads to increased utility for both the time- and frequency-domain waveforms.

A.5 A starting point for periodic signal evaluation

The density function of (A.6) also exposes a starting point for periodic signal evaluation through the relationship that exists between 10-90% and standard deviation. Based on (A.8), a four standard deviation shift is equivalent to a single side of the Gaussian pulse, so the pulse width may be described by twice $m_{4\sigma}$. Therefore, periodicity

Appendix A: (Continued)

requires a pulse repetition with an increment of pulse width, which is mathematically equivalent to the product of $(2n+1)$. This relationship can be used in the construction of the final expression derived in this section:

$$g(t, \tau_{10-90}) = A \cdot \sum_{n=0}^{\infty} e^{-\frac{[t-(2n+1)m_{4\sigma}]^2}{2(C \cdot \tau_{10-90})^2}} \quad (\text{A.9})$$

where $n=0,1,2\dots$ describes the number of pulses. This expression serves as a starting point for math-based periodic signal evaluation, because it provides a foundation for producing a train of Gaussian pulses of any size. Also, application of a 0.21 nsec rise time, which corresponds to a pulse width of 1.0 nsec , to (A.9) produces a time-domain plot that contains two pulses which are centered at 1.0 nsec and 3.0 nsec using this rise time and $n=1$, see Figure A.5. Moreover, the formulation is valid since the actual knee frequency of 2.3 GHz , observed from this spectral-amplitude plot (see Figure A.6), agrees with the expected value. The enhanced utility of this plot may be demonstrated by considering the nulls that appears as the spectrum rolls-off. Measurement of these nulls reveals that they are located at 0.5 GHz harmonics, which is equivalent to reciprocal of the 2.0 nsec period. Consequently, time-domain information is both observable and measurable from the spectral amplitude plot. Furthermore, because the pulse width is 1.0 nsec and period is 2.0 nsec , the duty cycle of this waveform is 50/50. Duty cycle is defined as the ratio of pulse width to pulse period. Since the pulse period is determined by the $(2n + 1)$ factor then this formulation may be modified for a more application specific duty cycle.

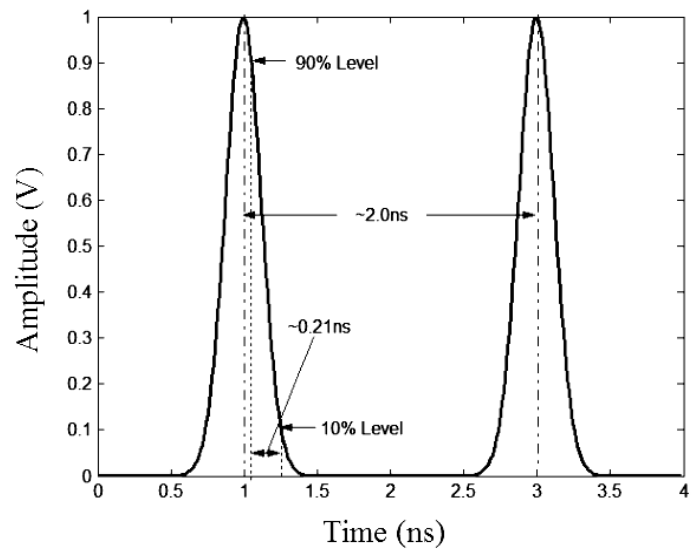
Appendix A: (Continued)

A.6 Results and discussion

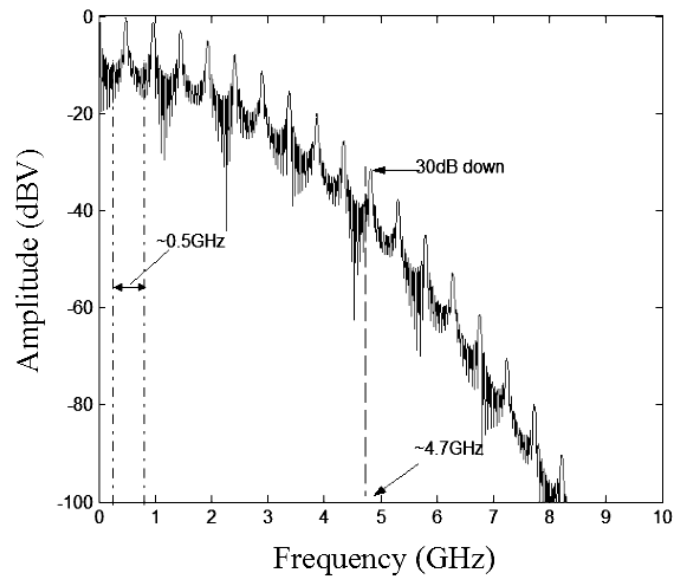
There are many measures for rise time including center slope, maximum slope, standard deviation, 20-80% and 10-90%. However, 10-90% rise time measure is most appropriate because it is used most heavily in practice, and it circumvents the need for PDF evaluation at asymptotic end-points in the first expression (A.6). This offers an advantage over immediately resolving the asymptotic end-points by providing an unaltered basis from which shifted and periodic functions are developed.

Unlike 10-90% rise time, the knee frequency requires the user to identify the spectrums natural roll-off prior to application. The natural roll-off defines the longest flat frequency response for a continuously decreasing gain and is the same for a given waveform (i.e., square wave, sinusoid, Gaussian). However, it is graphically resolved. As a result, formula validation is accomplished using an imprecise measure. Nevertheless, it is the most appropriate measure for formula validation because it is completely established in the frequency-domain, which more greatly demonstrates enhanced utility. As such, F_{knee} illuminates other frequency-domain characteristics such as rise time that is located at 30 *dB* down in the Bode plots of Figures A.3 and A.4 and cycle time (see Figure A.6). The morphological trends associated with these characteristics are noticeable using an imprecise formulation but are measurable using the formulas above.

Appendix A: (Continued)



(A)



(B)

Figure A.3: Normalized periodic (A) 1.0 nsec pulse and (B) normalized spectrum for pulse train with a 1.0 nsec pulse width.

Appendix A: (Continued)

Notwithstanding, there are two sources of error in (A.8) and (A.10): threshold resolution error and scaling error. Threshold error is associated with limiting the Gaussian distribution in order to shift it onto the positive time axis or introducing periodicity. This error is unavoidable but it can be predetermined with an impact to overall signal frequency in a periodic waveform; decreasing the error requires a longer Gaussian asymptote, which increases the cycle time. In addition, because of the asymptotic nature of the Gaussian, this error affects the minimum signal amplitude of the waveform. Since the shifted and periodic waveforms never begin at zero amplitude, this minimum will appear as direct current. On the other hand, the scaling error is associated with the accuracy of scaling the time-domain Gaussian using the standard deviation to 10-90% relationship. This error affects how well an expected and actual measure correlates as it passes through the formula. Both sources of error may be adjusted to have a negligible impact on the practicability of the formula

Correctly interpreting standard deviation in the basic Gaussian distribution leads to a pursuit to establish a mathematical relationship between 10-90% and standard deviation which is key to constructing a density function that provides a more meaningful and accurate resolution of time- and frequency-domain measures. These measures are most meaningful as the utility of the density function is extended beyond a simple morphological comparison and most accurate as the actual and expected measures are in agreement. As such, this density function allows measurement of pulse width, rise time, and cycle time from the amplitude-spectrum by correlations observed between the time-

Appendix A: (Continued)

and frequency-domains. Thus, a practicable Gaussian function results from the simple approach of reformulating the ideal PDF. Even so, the utility of the Gaussian function is more greatly enhanced by the establishment of the time-domain waveform on the positive axis through shifting and the introduction of periodicity. Consequently, these formulations provide a more useful starting point for exploring the fundamental properties of UWB pulses and towards enhancing techniques for pulse generation.

Appendix B: MATLAB code for Courtney and Motil technique

The code required to convert time-domain data that is collected using the oscilloscope to S-parameters is captured using MATLAB because it provides an interface which lends itself to graphically monitoring dynamic changes to the source code. In processing time-domain data, the user is required to adjust the window about the primary wave reflections in the system. These adjustments are monitored and confirmed using a graphical representation of the waveforms. However, the first task for MATLAB is to read the measurement data into a matrix. This data is then processed, using the aforementioned windowing technique in order to convert the time-domain representation to S-parameters. It is then post-processed by applying the Nicholson-Ross-Weir Technique to these S-parameters for yielding the dielectric properties of materials.

B.1 Data pre-processing

The purpose of pre-processing is to convert the time-domain data to S-parameters. This frequency-domain data is obtained by applying the Courtney and Motil technique. This technique entails developing the S-parameters by dividing the Fourier transform of the primary wave reflections from the specimen faces and the transmitted wave by the incident pulse. To obtain the primary reflections, it is necessary to isolate the reflections and transmissions in the measurement data. This is accomplished in the code below by providing a means to place a window about the waveforms. These computations also depend on an accurate measure of the group delays through the system. These group delays are obtained automatically by a peak search that is designed in to the code.

```

1  fronIncdt = +80;    fronWaveA = +400;
2  fronWaveB = 76;    fronTrans = 1400;
3  backIncdt = -53;   backWaveA = -06;
4  backWaveB = -712; backTrans = -0;

5  switch1 = 0;    switch2 = 0;
6  switch3 = 0;    switch4 = 0;

7  applyZeroFront=1; applyZeroBack=1;

8  Reducelastpoint1 = 0;
9  Reducelastpoint2 = 0;
10 Reducelastpoint3 = 0;
11 Reducelastpoint4 = 0;

12 ReduceFirstpoint = fronIncdt;

13 [Null,T0IndxMin_Size]= size(Vg_pulse0);
14 [Null,T1IndxMin_Size]= size(Vg_pulse1);

15 if (sign(Vg_pulse0(T0Indx1))==-1)
16 midpoint1 = round((T0Indx2 - T0Indx1));
17 firstpoint1=T0Indx1-FindIndex(-
    0.003,Vg_pulse0(T0Indx1:midpoint1+T0In
    dx1),0,1)-ReduceFirstpoint;
18 else
19 midpoint1 = round((T0Indx2 - T0Indx1));
20 firstpoint1=T0Indx1-
    FindIndex(0.006,Vg_pulse0(T0Indx1:midp
    oint1+T0Indx1),0,0)-ReduceFirstpoint;
21 end
22 lastpoint1=T0Indx1+(T0Indx1-
    firstpoint1)+1+backIncdt;

23 firstpoint2 = lastpoint1 + fronWaveA;
24 lastpoint2=T0Indx2+(T0Indx2-firstpoint2)+
    backWaveA;

25 firstpoint3 = lastpoint2 + 1+fronWaveB;
26 midpoint3 = T0IndxMin_Size+backWaveB;

27 firstpoint4 = 1+fronTrans;
28 midpoint4 = T1IndxMin_Size+backTrans;

29 % ETHANOL
30 switch1=1; window1 = 3;
31 %points of span E
32 switch2=1; swindow2=1; window2 = 4;
33 %points of span p1(t)
34 switch3=0; swindow3=40; window3 = 4;
35 %points of span p2(t)
36 switch4=0;window4 = 186;

37 %points of span T
38 if (switch1 == 1)
39 T0Indx1_Low = firstpoint1;
40 T0Indx1_High = lastpoint1 +
    Reducelastpoint1;
41 elseif (switch1 == 2)
42 T0Indx1_Low = T0Indx1 - window1;
43 T0Indx1_High = T0Indx1 + window1;
44 elseif (switch1 == 3)
45 T0Indx1_Low = swindow1 + 1;
46 T0Indx1_High = T0Indx1 + window1;
47 else
48 T0Indx1_Low = firstpoint1;
49 T0Indx1_High = firstpoint2-1;
50 end

51 i = 1;
52 while (i <= T0IndxMin_Size)
53 if (i >= T0Indx1_Low & i <= T0Indx1_High)
54 Incident(i) = Vg_pulse0(i);
55 elseif (i > T0Indx1_High & applyZeroBack ==
    0)
56 Incident(i) = Vg_pulse0(T0Indx1_High);
57 elseif (i < T0Indx1_Low & applyZeroFront ==
    0)
58 Incident(i) = Vg_pulse0(T0Indx1_Low);
59 else
60 Incident(i) = 0;
61 end
62 i = i + 1;
63 end

64 Fs = 1/(TimeV0(3)-TimeV0(2));
65 NFFT =
    4*(floor(length(TimeV0)/64)*64);
66 StdFreq = Fs*(0:NFFT/20)/NFFT;
67 Pwatts_Incident = abs(fft(Incident,NFFT)) ;

68 p1YMin = floor(min(Incident)/(10^-3));
69 r1YMin = sign(p1YMin)*5-(p1YMin-
    roundn(p1YMin/5,0)*5);
70 Y1Min = r1YMin + p1YMin;
71 p1YMax = ceil(max(Incident)/(10^-3));
72 r1YMax = sign(p1YMax)*5-(p1YMax-
    roundn(p1YMax/5,0)*5);
73 Y1Max = r1YMax + p1YMax;

74 figure ('Color',[1,1,1])
75 set(gca,'FontSize',11)

```

Appendix B: (Continued)

```

76 subplot(2,1,1)
77 plot(TimeV0/(10^-9),Incident/(10^-3),'r');
78 hold on
79 axis([XMin XMax Y1Min Y1Max ]);
80 xlabel('Time (ns)','FontSize',12);
81 ylabel('Amplitude (mV)','FontSize',12);
82 title('Preprocessed Incident
      Waveform','FontSize',14);
83 subplot(2,1,2)
84 plot(StdFreq/(10^9),20*log10(Pwatts_Incident
      (1:length(StdFreq))),'r');
85 grid off;
86 hold off;
87 xlabel('Freq (GHz)','FontSize',12);
88 ylabel('Amplitude (dBV)','FontSize',12);
89 title('FFT of Incident
      Waveform','FontSize',14);

90 if (switch2 == 3)
91     T0Indx2_Low = swindow2 + 1;
92     T0Indx2_High = T0Indx2 + window2;
93 elseif (switch2 == 2)
94     T0Indx2_Low = T0Indx1_High + 1;
95     T0Indx2_High = T0Indx2 + window2;
96 elseif (switch2 == 1)
97     T0Indx2_Low = firstpoint2;
98     T0Indx2_High = lastpoint2 +
        Reducelastpoint2;
99 else
100    T0Indx2_Low = firstpoint2;
101    T0Indx2_High = firstpoint3-1;
102 end

103 i = 1;
104 while (i <= T0IndxMin_Size)
105     if (i >= T0Indx2_Low & i <= T0Indx2_High)
106         Reflected_A(i) = Vg_pulse0(i);
107     elseif (i < T0Indx2_Low & applyZeroFront ==
        0)
108         Reflected_A(i) = Vg_pulse0(T0Indx2_Low);
109     elseif (i > T0Indx2_High & applyZeroBack ==
        0)
110         Reflected_A(i) = Vg_pulse0(T0Indx2_High);
111     else
112         Reflected_A(i) = 0;
113     end
114     i = i + 1;
115 end

116 Pwatts_Reflected_A =
        abs(fft(Reflected_A,NFFT));

117 p2YMin = floor(min(Reflected_A)/(10^-3));
118 r2YMin = sign(p2YMin)*5-(p2YMin-
        roundn(p2YMin/5,0)*5);
119 Y2Min = r2YMin + p2YMin;
120 p2YMax = ceil(max(Reflected_A)/(10^-3));
121 r2YMax = sign(p2YMax)*5-(p2YMax-
        roundn(p2YMax/5,0)*5);
122 Y2Max = r2YMax + p2YMax;

123 if (abs(p2YMin) > abs(p2YMax))
124     SignA = +1;
125 else
126     SignA = -1;
127 end

128 figure ('Color',[1,1,1])
129 set(gca,'FontSize',11)
130 subplot(2,1,1)
131 plot(TimeV0/(10^-9),Reflected_A/(10^-3),'r');
132 hold on;
133 V = axis;
134 axis([XMin XMax Y2Min Y2Max ]);
135 xlabel('Time (ns)','FontSize',12);
136 ylabel('Amplitude (mV)','FontSize',12);
137 title('Preprocessed Refected Waveform from
      A','FontSize',14);

138 subplot(2,1,2)
139 plot(StdFreq/(10^9),20*log10(Pwatts_Reflected_A(1:length(StdFreq))),'r');
140 grid off;
141 hold off;
142 xlabel('Freq (GHz)','FontSize',12);
143 ylabel('Amplitude (dBV)','FontSize',12);
144 title('FFT of Reflected Waveform on
      A','FontSize',14);

145 if (switch3 == 3)
146     T0Indx3_Low = swindow3 + 1;
147     T0Indx3_High = T0Indx3 + window3;
148 elseif (switch3 == 2)
149     T0Indx3_Low = T0Indx2_High + 1;
150     T0Indx3_High = T0Indx3 + window3;
151 elseif (switch3 == 1)
152     T0Indx3_Low = firstpoint3;

```

Appendix B: (Continued)

```

153 T0Indx3_High = lastpoint3 +
    Reducelastpoint3;
154 else
155 T0Indx3_Low = firstpoint3;
156 T0Indx3_High = midpoint3;
157 end
158 i = 1;
159 while (i <= T0IndxMin_Size)
160 if (i >= T0Indx3_Low & i <= T0Indx3_High)
161 Reflected_B(i) = Vg_pulse0(i);
162 elseif (i < T0Indx3_Low & applyZeroFront ==
    0)
163 Reflected_B(i) = Vg_pulse0(T0Indx3_Low);
164 elseif (i > T0Indx3_High & applyZeroBack ==
    0)
165 Reflected_B(i) = Vg_pulse0(T0Indx3_High);
166 else
167 Reflected_B(i) = 0;
168 end
169 i = i + 1;
170 end

171 Pwatts_Reflected_B =
    abs(fft(Reflected_B,NFFT));

172 p3YMin = floor(min(Reflected_B)/(10^-3));
173 r3YMin = sign(p3YMin)*5-(p3YMin-
    roundn(p3YMin/5,0)*5);
174 Y3Min = r3YMin + p3YMin;
175 p3YMax = ceil(max(Reflected_B)/(10^-3));
176 r3YMax = sign(p3YMax)*5-(p3YMax-
    roundn(p3YMax/5,0)*5);
177 Y3Max = r3YMax + p3YMax;

178 figure('Color',[1,1,1])
179 set(gca,'FontSize',11)
180 subplot(2,1,1)
181 plot(TimeV0/(10^-9),Reflected_B/(10^-3),'r');
182 hold on;
183 axis([XMin XMax Y3Min Y3Max]);
184 xlabel('Time (ns)','FontSize',12);
185 ylabel('Amplitude (mV)','FontSize',12);
186 title('Preprocessed Reflected Waveform from
    B','FontSize',14);

187 subplot(2,1,2)
188 plot(StdFreq/(10^9),20*log10(Pwatts_Reflecte
    d_B(1:length(StdFreq))),'r');
189 grid off;
190 hold off;

191 xlabel('Freq (GHz)','FontSize',12);
192 ylabel('Amplitude (dBV)','FontSize',12);
193 title('FFT of Reflected Waveform on
    B','FontSize',14);

194 if (switch4 == 3)
195 T1Indx1_Low = T0Indx1 + window1 + 1;
196 T1Indx1_High = T1Indx1 + window4;
197 elseif (switch4 == 2)
198 T1Indx1_Low = T0Indx1 + window1 + 1;
199 T1Indx1_High = T1Indx1 + window4;
200 elseif (switch4 == 1)
201 T1Indx1_Low = firstpoint4;
202 T1Indx1_High = lastpoint4 +
    Reducelastpoint4;
203 else
204 T1Indx1_Low = firstpoint4;
205 T1Indx1_High = midpoint4;
206 end

207 i = 1;
208 while (i <= T1IndxMin_Size)
209 if (i >= T1Indx1_Low & i <= T1Indx1_High)
210 Transmitted(i) = Vg_pulse1(i);
211 elseif (i > T1Indx1_High & applyZeroBack ==
    0)
212 Transmitted(i) = Vg_pulse1(T1Indx1_High);
213 elseif (i < T1Indx1_Low & applyZeroFront ==
    0)
214 Transmitted(i) = Vg_pulse1(T1Indx1_Low);
215 else
216 Transmitted(i) = 0;
217 end
218 i = i + 1;
219 end

220 Pwatts_Transmitted =
    abs(fft(Transmitted,NFFT));

221 p4YMin = floor(min(Transmitted)/(10^-3));
222 r4YMin = sign(p4YMin)*5-(p4YMin-
    roundn(p4YMin/5,0)*5);
223 Y4Min = r4YMin + p4YMin;
224 p4YMax = ceil(max(Transmitted)/(10^-3));
225 r4YMax = sign(p4YMax)*5-(p4YMax-
    roundn(p4YMax/5,0)*5);
226 Y4Max = r4YMax + p4YMax;

227 figure('Color',[1,1,1])
228 set(gca,'FontSize',11)

```

Appendix B: (Continued)

```
229 subplot(2,1,1)
230 plot(TimeV1/(10^-9),Transmitted/(10^-3),'r');
231 hold on;
232 axis([XMin XMax Y4Min Y4Max ]);
233 xlabel('Time (ns)','FontSize',12);
234 ylabel('Amplitude (mV)','FontSize',12);
235 title('Preprocessed Transmitted
        Waveform','FontSize',14);
236 subplot(2,1,2)
237 plot(StdFreq/(10^9),20*log10(Pwatts_Transmitted(1:length(StdFreq))),'r');
238 hold on;
239 plot(StdFreq/(10^9),20*log10(Pwatts_Incident
        (1:length(StdFreq))),'b');
240 grid off;
241 hold off;
242 xlabel('Freq (GHz)','FontSize',12);
243 ylabel('Amplitude (dBV)','FontSize',12);
244 title('FFT of Transmitted
        Waveform','FontSize',14);
```

B.2 Data post-processing

In the post-processing phase, the spectrums for transmission and reflection coefficients are applied to the development of S-parameters that are used for computing the dielectric properties of materials. The first set of S-parameters (S11_P1 and S21_P2) provides a frequency-domain representation of the measurements located at ports 1 and 2. However, it is necessary to rotate these S-parameters to the sample interfaces. Consequently, the second set of S-parameters (S11Fx and S21Fx) rotates out the transmission line leading to the fixture. However, these S-parameters do not account for the effects of the fixture itself. Consequently, a 3rd set of S-parameters (S11 and S21) are provided which accounts for the transmission line lengths of the fixture. Since the fixture contains an outer step-discontinuity, the effects of this step are applied to the Courtney and Motil technique by transforming the transmission line into a lumped element model and modifying the capacitance element of the model. Next, the modified lumped

Appendix B: (Continued)

elements are transformed back to S-parameters, and the Nicholson-Ross-Weir Technique is used to compute the dielectric properties.

```

1  calibrate4=1;
2  Calibrate2 = 1.0;
3  Calibrate3 = 1;
4  Calibrate = 1;

5  tau1x = tau1*Calibrate;
6  tau2x = tau2*Calibrate*Calibrate3;
7  tau3x = tau3*Calibrate;

8  j = sqrt(-1);
9  Eo = 8.854*(10^-12);
10 Uo = 4*pi*(10^-7);
11 Co = 2.99792458*(10^8);
12 GHz = 10^9;
13 PI = 3.14;
14 ZREF_est = 69;
15 n=0;

16 %%%%%%%%%%%STARTV%
17 %      Coax Definitions
18 %%%%%%%%%%%
19 Tune_Coax1 = 0.17104947;
20 Tune_Coax2 = -0.156;
21 Tune_Slot = 0;
22 Tune_Er13 = 0;
23 Tune_Ur13 = 0;

24 Er13Fx = 2.0689;
25 Ur13Fx = 0.9999;
26 LCoax1 = 11.8
27 LCoax2 = 23.6;
28 LinFx = 0.0254;

29 Er13 = 2.0689;
30 Ur13 = 0.9999;
31 Ls2 = 1.8013;
32 MFreqLwr = 1*10^6;
33 MFreqUpr = 25*10^6;
34 xmax = 1;
35 LTot = 4.3859;

36 Lr1 = (LTot-Ls2-Tune_Slot)/2;
37 Lr3 = (LTot-Ls2-Tune_Slot)/2;

38 % Computations
39 L1 = (Lr1+0)*.0254 + Tune_Coax1*.0254;
40 L2 = Ls2*.0254 + Tune_Slot*.0254;
41 L3 = (Lr3+0)*.0254 + Tune_Coax2*.0254;
42 Er13t = Er13 + Tune_Er13;
43 Ur13t = Ur13 + Tune_Ur13;
44 E13 = Eo*Er13t;
45 U13 = Uo*Ur13t;
46 Er13tFx = Er13Fx;
47 Ur13tFx = Ur13Fx;
48 E13Fx = Eo*Er13tFx;
49 U13Fx = Uo*Ur13tFx;

50 L1Fx = (LCoax1)*.0254;
51 L3Fx = (LCoax2)*.0254;

52 coax_B = 0.250 * .0254;
53 coax_C = 0.209 * .0254;
54 coax_A = coax_B;
55 coax_D = 0.0641 * 0.0254;

56 Modify = Calibrate2;
57 k=1;
58 while (k <= length(StdFreq))

59 %%%%%%%%%%%STARTV%
60 % s-Param From Time-Domain Measure
61 %%%%%%%%%%%

62 w(k) = 2*pi()*StdFreq(k);

63 Gma12(k) =
        (Modify)*SignA*Pwatts_Reflected_A(
        k)/Pwatts_Incident(k);

64 Gma21(k) = -Gma12(k);

65 T12_T21(k) =
        Pwatts_Transmitted(k)/(Pwatts_Inciden
        t(k));

66 T21_T12(k) = T12_T21(k);

```


Appendix B: (Continued)

```

67 R11n(k) = T21_T12(k)*Gma21(k)*exp(-
    j*2*w(k)*(tau1x+tau2x));
68 R21n(k) =
    T12_T21(k)*(Gma21(k)^2)*exp(-
    j*w(k)*(tau1x+(3*tau2x)+tau3x));
69 Sn(k) = (1-((Gma21(k)^2)*exp(-
    j*2*w(k)*tau2x))*(Modify);
70 S11_P1(k) = ((exp(-j*2*w(k)*tau1x)
    *Gma12(k)+(R11n(k)/Sn(k)))*exp(-
    j*w(k)*sqrt(E13Fx*U13Fx)*LinFx);
71 S21_P2(k) = (exp(-
    j*w(k)*(tau1x+tau2x+tau3x))*T12_T21
    (k)+(R21n(k)/Sn(k));
72 S11Fx(k) =
    S11_P1(k)*exp(j*2*w(k)*sqrt(E13Fx*
    U13Fx)*L1Fx);
73 S21Fx(k) =
    S21_P2(k)*exp(j*w(k)*sqrt(E13Fx*U1
    3Fx)*(L1Fx+L3Fx));
74 %%%%%%%%%%%STARTV%
75 % Ref s-Params to P1 & P2 Measurement
76 %%%%%%%%%%%
77 S11(k) =
    S11Fx(k)*exp(j*2*w(k)*sqrt(E13*U13
    )*L1);
78 S11Re(k) = real(S11(k));
79 S11Im(k) = imag(S11(k));
80 S21(k) =
    S21Fx(k)*exp(j*w(k)*sqrt(E13*U13)*(
    L1+L3));
81 S21Re(k) = real(S21(k));
82 S21Im(k) = imag(S21(k));
83 %%%%%%%%%%%STARTV%
84 % Recompute the Gamma12 parameter
85 %%%%%%%%%%%
86 Xn(k) = sqrt(((S11(k)^2-
    S21(k)^2)^2)-2*(S11(k)^2)+1-
    2*(S21(k)^2));
87 Yn(k) = (S11(k)^2)-(S21(k)^2)+1;
88 Gma12r(k) = (Yn(k)-
    Xn(k))/(2*S11(k));
89 %%%%%%%%%%%STARTV%
90 %Frequency Dependent Material Prop
91 %%%%%%%%%%%
92 z(k) = ((S11(k)+S21(k)-Gma12r(k))/(1-
    (S11(k)+S21(k))*Gma12r(k)));
93 C1(k) = -((Co/(L2*w(k)))*log(z(k)))^2;
94 C2(k) =
    (Ur13t/Er13t)*(((1+Gma12r(k))/(1-
    Gma12r(k)))^2);
95 Era(k) = sqrt(C1(k)/C2(k));
96 EraRe(k) = real(Era(k));
97 EraIm(k) = imag(Era(k));
98 Ura(k) = sqrt(C1(k)*C2(k));
99 UraRe(k) = real(Ura(k));
100 UraIm(k) = imag(Ura(k));
101 k = k+1;
102 end
103 k=1;
104 while (k <= length(StdFreq))
105 Cd2_manual = calibrate4*Era(2)*(4.792E-
    12/0.807945);
106 Cd5_manual = 0*Era(2)*(4.792E-
    6/0.807945);
107 Cdc_NRW(k) = 0;
108 Cp_est(k) =
    (Era(k)*(2*PI*Eo))/(log(coax_A/coax_
    D));
109 C_est(k) = Cp_est(k)+2*Cd2_manual;
110 R_est(k) = 0;
111 G_est(k) =
    2*Cd5_manual+((2*PI)*(EraIm(k)*Eo*
    w(k)+Cdc_NRW(k)))/(log(coax_A/coa
    x_D));
112 L_est(k) =
    (Ura(k)*Uo/(2*PI))*(log(coax_A/coax_
    D));

```

Appendix B: (Continued)

```

113 ZWh_est(k) =
    sqrt((R_est(k)+j*w(k)*L_est(k))/(G_est
    (k)+j*w(k)*C_est(k)));

114 Gmah_est(k) =
    sqrt((R_est(k)+j*w(k)*L_est(k))*(G_est
    t(k)+j*w(k)*C_est(k)));

115 S11m_est(k) = ((ZWh_est(k)^2)-
    (ZREF_est^2))*tanh(Gmah_est(k)*L2)/
    ((2*ZWh_est(k)*ZREF_est)+(tanh(Gm
    ah_est(k)*L2)*((ZWh_est(k)^2)+(ZRE
    F_est^2))));

116 S21m_est(k) =
    2/(2*cosh(Gmah_est(k)*L2) +
    sinh(Gmah_est(k)*L2)*((ZWh_est(k)/Z
    REF_est)+(ZREF_est/ZWh_est(k))));

117 V1_nrw(k) = S21m_est(k) +
    S11m_est(k);
118 V2_nrw(k) = S21m_est(k) - S11m_est(k);

119 X_nrw(k) = (1-
    V1_nrw(k)*V2_nrw(k))/(V1_nrw(k)-
    V2_nrw(k));
120 Gma12_1ne(k) = X_nrw(k) +
    sqrt((X_nrw(k)^2) - 1);
121 Gma12_2ne(k) = X_nrw(k) -
    sqrt((X_nrw(k)^2) - 1);

122 if (abs(Gma12_1ne(1)) <= 1)
123 Gma12re(k) = Gma12_1ne(k);
124 else
125 Gma12re(k) = Gma12_2ne(k);
126 end
127 z_nrw(k) = (V1_nrw(k)-Gma12re(k))/(1-
    V1_nrw(k)*Gma12re(k));

128 logz_B(k) = log(z_nrw(k));

129 angleS(k) =
    atan2(imag(logz_B(k)),real(logz_B(k)))
    ;

130 magS(k) = abs(logz_B(k));

131 A_nrw(k) = magS(k)*exp(j*angleS(k) +
    2*PI*n);

132 C1a(k) = -
    (((Co/(L2*w(k)))*A_nrw(k))^2);

133 C2a(k) =
    ((sqrt(Ur13t/Er13t)*((1+Gma12re(k))/(
    1-Gma12re(k))))^2);

134 Er(k) = sqrt(C1a(k)/C2a(k));
135 ErRe(k) = real(Er(k));
136 ErIm(k) = imag(Er(k));

137 Ur(k) = sqrt(C1a(k)*C2a(k));
138 UrRe(k) = real(Ur(k));
139 UrIm(k) = imag(Ur(k));

140 U_NRW(k)=1;

141 Prop_NRW(k) =
    j*w(k)*sqrt(Er(k)*U_NRW(k))/Co;

142 Alpha_NRW(k)= real(Prop_NRW(k));

143 Beta_NRW(k) = imag(Prop_NRW(k));

144 Rsurf_NRW(k)= 1/Alpha_NRW(k);

145 Cdc_NRW(k) =
    (2/(w(k)*Uo*UrRe(k)))*((1/Rsurf_NR
    W(k))^2);

146 k = k+1;
147 end

148 run plotproces

```

Appendix B: (Continued)

B.3 Summary

In the post-processing phase above two techniques are applied to arrive at the dielectric properties: Courtney-Motil and Nicholson-Ross-Weir. Each technique serves a role in computing the dielectric properties of materials. The Courtney-Motil technique in the pre-processing step provides a means to compute the S-parameters from time-domain measurement and the Nicholson-Ross-Weir technique converts these S-parameters to dielectric properties of materials. Since a genetic algorithm that requires measurement data in the form of S-parameters is used in an alternative approach, the s-paramaters are developed in the post-processing phase so that a set of parameters in which the fixture is not extracted is available. As a result, this phase contains several incremental sets of S-parameters. The last set of S-parameters was developed to provide a means to accounts for the fixture step-discontinuity. This step is technique dependent and is not necessary in the GA approach because the conductor diameters are apart of the formulation.

Appendix C: C++ code for genetic algorithm

Source code for the GA used to analyze the dielectric properties of materials is provided below. This code consists of header and the source files. They include code for acquiring the measurement data for processing, de-embedding the effects of the fixture from measured S-parameters, comparing measured S-parameters to those computed using Havrilak-Negami model parameters and setting up the GA. These “getdielectric()” source code supplies the main executable, through which the other source code in this program is executed.

C.1 Measurement data acquisition

The header and source files below are for reading in the VNA and pre-processed oscilloscope S-parameter measurement data files into the following arguments: MyFreq, MyS11_real MyS11_imag, MyS21_real MyS21_imag, MyS12_real MyS12_imag, MyS22_real, and MyS22_imag. A maximum row count of 4096 is allowed in this program, and data must be arranged into 9 columns in the above order. This code is designed to handle data that is exported from an HP 5 series VNA. However, this does not preclude its operation with other files, so long as the format is consistent with the above (including a 196-bit header). This program will fill the remainder of the data with zeros if the row count is longer than the actual file. Also, since the matrix size is set to 4096, so the variables may have to be sized accordingly. Lastly, data is output to "OUTPUT.txt".

Appendix C: (Continued)

```

1  /* -----
Header-File
2  -----*/
3  #ifndef INCLUSION_GUARD_extractVNA_H
4  #define INCLUSION_GUARD_extractVNA_H

5  #include <fstream>
6  #include <iostream>
7  #include <iomanip>
8  #include <cstdlib>
9  #include <stdlib.h>
10 #include <complex>
11 #include <math.h>
12 #include <cmath>

13 #define PI 3.141592653589793238462643

14 using namespace std;
15 void OpenFile(ifstream& fid);
16 void OpenFile(ofstream& fod);

17 const int IN_FILE = 402;
18 float Switch;
19 float MyFreq[IN_FILE];
20 float MyS11_real[IN_FILE];
21 float MyS11_imag[IN_FILE];
22 float MyS21_real[IN_FILE];
23 float MyS21_imag[IN_FILE];
24 float MyS12_real[IN_FILE];

45 /* -----
Source-File
46 -----*/
47 #include "extractVNA.h"

48 float getVNAdata()
49 {
50 using namespace std;

51 ifstream fid; //naming the input file for the
    program
52 ofstream fod; //naming the output file for the
    program

53 fod.setf(ios::scientific);
54 fod.setf(ios::showpoint);
55 fod.precision(8);

25 float MyS12_imag[IN_FILE];
26 float MyS22_real[IN_FILE];
27 float MyS22_imag[IN_FILE];

28 float MyS11_mag[IN_FILE];
29 float MyS11_phase[IN_FILE];
30 float MyS21_mag[IN_FILE];
31 float MyS21_phase[IN_FILE];
32 float MyS12_mag[IN_FILE];
33 float MyS12_phase[IN_FILE];
34 float MyS22_mag[IN_FILE];
35 float MyS22_phase[IN_FILE];

36 int rowNum;
37 int rowSel;

38 typedef complex<float> fcmplx;

39 fcmplx MyS11m[IN_FILE];
40 fcmplx MyS21m[IN_FILE];
41 fcmplx MyS12m[IN_FILE];
42 fcmplx MyS22m[IN_FILE];

43 fcmplx j(0,1);

44 #endif //
    INCLUSION_GUARD_extractVNA_H

56 fid.open("Med_T3b.S1"); rowNum = 201;
57 //*****//
58 // Switch==1 real/imaginary //
59 // Switch==2 dB/Angle //
60 // Switch==3 magnitude/Angle //
61 //*****//
62 Switch = 3;

63 OpenFile(fid);

64 //Open the output file
65 fod.open("OUTPUT.txt");
66 OpenFile(fod);

67 fid.seekg (196, ios::beg);

68 if (Switch == 1) {

```



Appendix C: (Continued)

```

69 for (int i=0; i < rowNum; i++)
70 {
71 fid >> MyFreq[i] >>
72 MyS11_real[i] >> MyS11_imag[i] >>
    MyS21_real[i] >> MyS21_imag[i] >>
    MyS12_real[i] >> MyS12_imag[i] >>
    MyS22_real[i] >> MyS22_imag[i];
73 MyS11m[i]=(MyS11_real[i]+j*MyS11_imag[i]
    );
74 MyS21m[i]=(MyS21_real[i]+j*MyS21_imag[i]
    )
    MyS12m[i]=(MyS12_real[i]+j*MyS12_im
    ag[i]);
75 MyS22m[i]=(MyS22_real[i]+j*MyS22_imag[i]
    );
76 }}

77 if (Switch == 2) {
78 for (int i=0; i < rowNum; i++)
79 {
80 fid >> MyFreq[i] >>
81 MyS11_mag[i] >> MyS11_phase[i] >>
82 MyS21_mag[i] >> MyS21_phase[i] >>
83 MyS12_mag[i] >> MyS12_phase[i] >>
84 MyS22_mag[i] >> MyS22_phase[i];

85 MyS11_real[i]=pow(10,MyS11_mag[i]/20)*co
    s(MyS11_phase[i]*float(PI/180);
86 MyS11_imag[i]=pow(10,MyS11_mag[i]/20)*s
    in(MyS11_phase[i]*float(PI/180);
87 MyS21_real[i]=pow(10,MyS21_mag[i]/20)*co
    s(MyS21_phase[i]*float(PI/180);
88 MyS21_imag[i]=pow(10,MyS21_mag[i]/20)*s
    in(MyS21_phase[i]*float(PI/180);
89 MyS12_real[i]=pow(10,MyS12_mag[i]/20)*co
    s(MyS12_phase[i]*float(PI/180);
90 MyS12_imag[i]=pow(10,MyS12_mag[i]/20)*s
    in(MyS12_phase[i]*float(PI/180);
91 MyS22_real[i]=pow(10,MyS22_mag[i]/20)*co
    s(MyS22_phase[i]*float(PI/180);
92 MyS22_imag[i]=pow(10,MyS22_mag[i]/20)*s
    in(MyS22_phase[i]*float(PI/180);

93 MyS11m[i]=(MyS11_real[i]+j*MyS11_imag[i]
    );
94 MyS21m[i]=(MyS21_real[i]+j*MyS21_imag[i]
    );
95 MyS12m[i]=(MyS12_real[i]+j*MyS12_imag[i]
    );

96 MyS22m[i]=(MyS22_real[i]+j*MyS22_imag[i]
    );
97 }}

98 if (Switch == 3) {
99 for (int i=0; i < rowNum; i++)
100 {
101 fid >> MyFreq[i] >>
102 MyS11_mag[i] >> MyS11_phase[i] >>
103 MyS21_mag[i] >> MyS21_phase[i] >>
104 MyS12_mag[i] >> MyS12_phase[i] >>
105 MyS22_mag[i] >> MyS22_phase[i];

106 MyS11_real[i]=MyS11_mag[i]*cos(MyS11_p
    hase[i]*float(PI/180));
107 MyS11_imag[i]=MyS11_mag[i]*sin(MyS11_
    phase[i]*float(PI/180));
108 MyS21_real[i]=MyS21_mag[i]*cos(MyS21_p
    hase[i]*float(PI/180));
109 MyS21_imag[i]=MyS21_mag[i]*sin(MyS21_
    phase[i]*float(PI/180));
110 MyS12_real[i]=MyS12_mag[i]*cos(MyS12_p
    hase[i]*float(PI/180));
111 MyS12_imag[i]=MyS12_mag[i]*sin(MyS12_
    phase[i]*float(PI/180));
112 MyS22_real[i]=MyS22_mag[i]*cos(MyS22_p
    hase[i]*float(PI/180));
113 MyS22_imag[i]=MyS22_mag[i]*sin(MyS22_
    phase[i]*float(PI/180));

114 MyS22m[i]=(MyS11_real[i]
    +j*MyS11_imag[i]);
115 MyS12m[i]=(MyS21_real[i]
    +j*MyS21_imag[i]);
116 MyS21m[i]=(MyS12_real[i]
    +j*MyS12_imag[i]);
117 MyS11m[i]=(MyS22_real[i]
    +j*MyS22_imag[i]);
118 }}

119 for (int i=0; i < rowNum; i++)
120 {
121 fod << MyFreq[i]
122 << " " << MyS11_real[i] << " " <<
    MyS11_imag[i] << " " << MyS21_real[i]
    << " " << MyS21_imag[i] << " " <<
    MyS12_real[i] << " " << MyS12_imag[i]
    << " " << MyS22_real[i] << " " <<
    MyS22_imag[i] << endl;

```

Appendix C: (Continued)

```

123 }
124 fid.close();
125 fod.close();
126 return 0;
127 } // End function main

128 void OpenFile(ifstream& fid)
129 {
130 if (fid.fail())
131 { system("cls");//clears the screen
132 cout<< "Input file opening failed.\n";

133 exit(1);}
134 } // End function OpenFile

135 void OpenFile(ofstream& fod)
136 {
137 if (fod.fail())
138 {
139 system("cls");//clears the screen
140 cout<< "Output file opening failed.\n";
141 exit(1);
142 }} // End function OpenFile

```

C.2 S-parameters of fixture

The following header and source files are designed to take the S-parameters that are read in from Section C.1 above, and de-embed the effects of the fixture. As a result, the fixture dimensions are used re-compute S-parameters at the specimen interface. These S-parameters are then stored for comparison with those computed in Section C.3 below.

```

1  /* -----
Header-File
2  -----*/
3  #ifndef
    INCLUSION_GUARD_calMSPParam_H
4  #define
    INCLUSION_GUARD_calMSPParam_H

5  /*%%%%%%%%%%%%%%%%%%%%%%%%%%%%START
6  %   Constants to be used
7  %%%%%%%%%%%%%%%%%%%%%%%%%%%%%*/
8  float w[IN_FILE];
9  fcplx S11m[IN_FILE];
10 fcplx S21m[IN_FILE];
11 fcplx S12m[IN_FILE];
12 fcplx S22m[IN_FILE];

13 fcplx phaseS11m[IN_FILE];
14 fcplx magniS11m[IN_FILE];
15 fcplx phaseS21m[IN_FILE];
16 fcplx magniS21m[IN_FILE];

17 float Eo = 8.8541878176*(1E-12);
18 float Uo = 4*PI*(1E-7);
19 float Co = 2.99792458*(1E8);
20 float GHz = 1E9;

21 /%%%%%%%%%%%%%%%%%%%%%%%%%%%%STOP^%
22 %   Coax Definitions
23 %%%%%%%%%%%%%%%%%%%%%%%%%%%%%*/
24 float Tune_Coax2 = 0.0;
25 float Tune_Coax1 = 0.13236;
26 float Tune_Slot = 0;
27 float Tune_Er13 = 0;
28 float Tune_Ur13 = 0;

```

Appendix C: (Continued)

```

29 float Er13    = 2.0689;
30 float Ur13    = 1 - 0.0000003;
31 float Ur13i   = 0;
32 float LCoax1  = 0;
33 float LCoax2  = 0;
34 float Ls2     = 1.80122;
35 float xmax    = 6; // Upper Freq for plots
36 float LTot    = 3.936654;

37 float Lr1     = (LTot-Ls2-Tune_Slot)/2;
38 float Lr3     = (LTot-Ls2+Tune_Slot)/2;

39 float L1=(Lr1+LCoax1)*.0254 +
      Tune_Coax1*.0254;
40 float L2     = Ls2*.0254 + Tune_Slot*.0254;
41 float L3=(Lr3+LCoax2)*.0254 +
      Tune_Coax2*.0254;
42 float Er13t  = Er13 + Tune_Er13;
43 float Ur13t  = Ur13 + Tune_Ur13;
44 float E13    = Eo*Er13t;
45 float U13    = Uo*Ur13t;
46 #endif //
      INCLUSION_GUARD_calMSPParam_H

47 /* -----
48 C-File
49 -----*/
50 #include "calMSPParam.h"

51 float getMSPParam()
52 {
53 using namespace std;

54 fcplx S11_T11;
55 fcplx Zin_T1;

56 fcplx S11Re;
57 fcplx S11Im;

58 fcplx Zreal;
59 fcplx Zimag;

60 fcplx S11_Treal;
61 fcplx S11_Timag;

62 fcplx S21_T21;
63 fcplx Zin_T2;

64 fcplx S21Re;
65 fcplx S21Im;

66 fcplx Zreal2;
67 fcplx Zimag2;
68 fcplx S21_Treal;
69 fcplx S21_Timag;

70 for(int k=0; k < rowNum; k++)
71 {
72 w[k] = 2*PI*MyFreq[k];

73 S11_T11 =
      MyS11m[k]*exp(j*float(2)*w[k]*sqrt(E13
      *U13)*L1);

74 S21_T21 =
      MyS21m[k]*exp(j*w[k]*sqrt(E13*U13)*(
      L1+L3));

75 S11m[k] = S11_T11;
76 S21m[k] = S21_T21;

77 }

78 return 0;
79 }

```



Appendix C: (Continued)

C.3 Dielectric properties of specimen

The following header and source files are designed to compute the frequency dependent dielectric properties based on the Havrilak-Negami model parameters, which are supplied by the genetic algorithm. These properties are used to compute S-parameters at the specimen interface, which are used in a metric for evaluating the goodness of fit between the measured and computed results.

```
1  /* -----
Header-File
2  -----*/
3  #ifndef
    INCLUSION_GUARD_calHSPParam_H
4  #define
    INCLUSION_GUARD_calHSPParam_H
5  fcmplx ZREF = fcmplx(ZREF_est);
6  fcmplx ZWh[IN_FILE];
7  fcmplx Gmah[IN_FILE];
8  fcmplx S11h[IN_FILE];
9  fcmplx S21h[IN_FILE];
10 fcmplx S12h[IN_FILE];
11 fcmplx S22h[IN_FILE];
12 fcmplx phaseS11h[IN_FILE];
13 fcmplx magniS11h[IN_FILE];
14 fcmplx phaseS21h[IN_FILE];
15 fcmplx magniS21h[IN_FILE];
16 float Ereal[IN_FILE];
17 float Eimag[IN_FILE];
18 fcmplx Ureal[IN_FILE];
19 fcmplx Uimag[IN_FILE];
20 fcmplx ErHKp[IN_FILE];
21 fcmplx ErHK[IN_FILE];
22 fcmplx UrHKp[IN_FILE];
23 fcmplx UrHK[IN_FILE];
24 fcmplx Cprime[IN_FILE];
25 fcmplx Gprime[IN_FILE];
26 fcmplx Lprime[IN_FILE];
27 fcmplx Rprime[IN_FILE];
28 fcmplx AdjustEr[IN_FILE];
29 fcmplx AdjustUr[IN_FILE];
30 fcmplx Rsurfa[IN_FILE];
31 fcmplx RsurfaA[IN_FILE];
32 fcmplx RsurfaD[IN_FILE];
33 float Gn; float Ps;
34 fcmplx Um;
35 #endif //
    INCLUSION_GUARD_calHSPParam_H
36 -----
Source-File
37 -----*/
38 #include "calHSPParam.h"
39 #include <cmath>
40 #include <complex>
41 #include <stdio.h>
42 float getHSPParam(float Es, float Ei, float Tne,
    float Ui, float Us, float Tnu, float Cs, float
    As, float Bs)
```



Appendix C: (Continued)

```

43 {
44 float coax_A = 0.250 * 0.0254;
45 float coax_D = 0.0641 * 0.0254;
46 fcmplx HybTan[IN_FILE];

47 for (int k=0; k < rowNum; k++)
48 {
49 ErHKp[k] = Es+((Ei-Es)/pow((float (1) +
      j*w[k]*Tne),1-As))-
      j*(float(1)*Cs/(w[k]*Eo));
50 ErHK[k] = (real(ErHKp[k])) -
      j*(imag(ErHKp[k]));
51 Ereal[k] = real(ErHK[k]);
52 Eimag[k] = imag(ErHK[k])+Cs/(w[k]*Eo);

53 UrHKp[k] = Us+((Ui-Us)/pow((float (1) +
      j*w[k]*Tnu),Bs));/-
      j*(float(1)*Cs/(w[k]*Eo));
54 UrHK[k] = (real(UrHKp[k])) -
      j*(imag(UrHKp[k]));
55 Ureal[k] = real(UrHK[k]);
56 Uimag[k] = imag(UrHK[k]);/+Cs/(w[k]*Eo);

57 Cprime[k] =
      (Ereal[k]*2*PI*Eo)/(log(coax_A/coax_D)
      );
58 Gprime[k] =
      (2*PI*(Eimag[k]*Eo*w[k]))/(log(coax_A/
      coax_D));

59 Lprime[k] =
      ((UrHK[k])*Uo/float(2*PI))*float(log(coa
      x_A/coax_D));

60 RsurfaA[k] = sqrt(
      float(1)*Uo*w[k]/(float(2*59.6E6) ));
61 RsurfaD[k] = sqrt(
      float(1)*Uo*w[k]/(float(2*63.1E6) ));
62 Rprime[k] =
      ((RsurfaA[k]/coax_A)+(RsurfaD[k]/coax_
      D))/float(PI);
63 ZWh[k] =
      sqrt((Rprime[k]+j*w[k]*Lprime[k])/(Gpri
      me[k]+j*w[k]*Cprime[k]));
64 Gmah[k] =
      sqrt((Rprime[k]+j*w[k]*Lprime[k])* (Gpri
      me[k]+j*w[k]*Cprime[k]));
65 HybTan[k] = tanh(Gmah[k]*L2);
66 S11h[k] = (pow(ZWh[k],2)-
      pow(ZREF,2))*tanh(Gmah[k]*L2)/((float
      (2)*ZWh[k]*ZREF)+(tanh(Gmah[k]*L2)*
      (pow(ZWh[k],2)+pow(ZREF,2))));
67 S21h[k] = float (2)/float
      (2)*cosh(Gmah[k]*L2) +
      sinh(Gmah[k]*L2)*((ZWh[k]/ZREF)+(ZR
      EF/ZWh[k]));

68 }
69 return 0;
70 }

```

C.4 S-parameter comparison

The following header and source code is used to compare the S-parameters for the measurement data (see Section C.2) and computed results (see Section C.3). Both sets of S-parameters are rotated to the specimen interface. This code passes a single metric,

Appendix C: (Continued)

which increases with a decrease in the goodness of fit, to the objective function of the genetic algorithm.

```

1  -----
Header-File
2  -----*/
3  #ifndef
    INCLUSION_GUARD_compSPParam_H
4  #define
    INCLUSION_GUARD_compSPParam_H
5  float S11_Compare[IN_FILE];
6  float S21_Compare[IN_FILE];
7  float S11a_Compare[IN_FILE];
8  float S21a_Compare[IN_FILE];
9  float Sum21_Error;
10 float Sum11_Error;
11 float Sum21a_Error;
12 float Sum11a_Error;
13 float SumG_Error;
14 float Avg_Error;
15 float Avg11a_Error;
16 float Avg21a_Error;
17 float Avg11b_Error;
18 float Avg21b_Error;
19 float Angle11m[IN_FILE];
20 float Angle21m[IN_FILE];
21 float Angle11h[IN_FILE];
22 float Angle21h[IN_FILE];
23 float Avg11_Error;
24 float Avg21_Error;
25 float AvgGma_Error;
26 float Sum11m_Error=0;
27 float Sum21m_Error=0;
28 float min_error=1e9;
29 #endif //
    INCLUSION_GUARD_compSPParam_H
30 -----
Source-File
31 -----*/
32 #include "compSPParam.h"
33 float getCompare()
34 {
35 using namespace std;
36 float w2 = 1;
37 float w1 = 1;
38 float start_count = 1;
39 float stop_count = rowNum;
40 Sum21_Error=0; Sum11_Error=0;
41 Sum11a_Error=0; Sum21a_Error=0;
42 SumG_Error=0; Sum11m_Error=0;
43 Sum21m_Error=0;
44 for(int k=start_count; k <
    stop_count; k++)
45 {
46 Angle11m[k]=atan2(imag(S11m[k]),
    real(S11m[k]))*float(180/PI);
47 Angle21m[k]=atan2(imag(S21m[k]),
    real(S21m[k]))*float(180/PI);
48 Angle11h[k]=atan2(imag(S11h[k]),
    real(S11h[k]))*float(180/PI);
49 Angle21h[k]=atan2(imag(S21h[k]),
    real(S21h[k]))*float(180/PI);
50 S11_Compare[k]=abs(abs(S11m[k]) -
    abs(S11h[k]));

```



Appendix C: (Continued)

```

51 Sum11_Error= (S11_Compare[k]) +      Angle21h[k]/abs(Angle21h[k]))
    Sum11_Error;                        Sum21m_Error = float(0) +
                                        Sum21m_Error;
52 S21_Compare[k]=abs(abs(S21m[k])-    62 else Sum21m_Error = float(1) +
    abs(S21h[k]));                      Sum21m_Error;
53 Sum21_Error= (S21_Compare[k]) +    63 }
    Sum21_Error;
54 S11a_Compare[k]=abs(abs(Angle11m   64 Avg11_Error = Sum11_Error;
    [k])-abs(Angle11h[k]));           65 Avg21_Error = Sum21_Error;
55 Sum11a_Error= (S11a_Compare[k])    66 Avg11a_Error =
    + Sum11a_Error;                   Sum11a_Error/(stop_count-
                                        start_count);
56 S21a_Compare[k]=abs(abs(Angle21m   67 Avg21a_Error =
    [k])-abs(Angle21h[k]));           Sum21a_Error/(stop_count-
                                        start_count);
57 Sum21a_Error=(S21a_Compare[k])+    68 Avg11b_Error = Sum11m_Error;
    Sum21a_Error;                     69 Avg21b_Error = Sum21m_Error;
58 SumG_Error = SumG_Error +          70 Avg_Error =
    abs(abs(G_est[k])-                Avg11_Error*float(10) +
    abs(Gprime[k]));                 Avg21_Error*float(15) +
                                        Avg11b_Error + Avg21b_Error +
                                        Avg11a_Error*float(1.2) +
                                        Avg21a_Error;
59 if (Angle11m[k]/abs(Angle11m[k])   71 return
    ==
    Angle11h[k]/abs(Angle11h[k]))
    Sum11m_Error = float(0) +
    Sum11m_Error;
60 else Sum11m_Error = float(1) +
    Sum11m_Error;
61 if (Angle21m[k]/abs(Angle21m[k])
    ==

```

C.5 NRW estimation

The following header and source files are designed to compute an estimate for the static permittivity and conductivity that are used to limit the search space for the genetic algorithm. These estimates are computed using the NRW technique. The DC

Appendix C: (Continued)

conductivity is not computed directly. It is interpolated from the AC conductivity and amplified to provide an upper limit on the search space for this parameter.

```

1  /* -----
Header-File
2  -----*/
3  #ifndef INCLUSION_getNRW_H
4  #define INCLUSION_getNRW_H

5  /*%%%%%%%%%%%%%%%%%%%%%%%%%%%%%%%%%%%%%%%%%%%%%%%%%%%%%%%%%%%%%%%%%%%%%%%%%%%%%%START
6  %   Constants to be used
7  %%%%%%%%%%%%%%%%%%%%%%%%%%%%%%%%%%%%%%%%%%%%%%%%%%%%%%%%%%%%%%%%%%%%%%%%%%%%%%%*/
   /

8  fcplx ZREF_est = fcplx(50.0,0);

9  float Calibrate = 1;
10 fcplx Prop_NRW[IN_FILE];
11 fcplx Alpha_NRW[IN_FILE];
12 fcplx Beta_NRW[IN_FILE];
13 fcplx Rsurf_NRW[IN_FILE];
14 fcplx Cdc_NRW[IN_FILE];
15 fcplx dcCondT_NRW;

16 fcplx S11m_est[IN_FILE];
17 fcplx S21m_est[IN_FILE];
18 fcplx ZWh_est[IN_FILE];
19 fcplx Gmah_est[IN_FILE];

20 fcplx S11nrw[IN_FILE];
21 fcplx S21nrw[IN_FILE];
22 fcplx Cprimenrw[IN_FILE];
23 fcplx Gprimenrw[IN_FILE];
24 fcplx Lprimenrw[IN_FILE];
25 fcplx Rsurfانrw[IN_FILE];
26 fcplx Rprimenrw[IN_FILE];
27 fcplx ZWhnrw[IN_FILE];
28 fcplx Gmahnrw[IN_FILE];

29 fcplx Cp_est[IN_FILE];
30 fcplx rho_est[IN_FILE];
31 fcplx cndvty[IN_FILE];
32 fcplx Gp_est[IN_FILE];
33 fcplx Temp_est[IN_FILE];

34 fcplx Cp_est2[IN_FILE];

35 fcplx rho_est2[IN_FILE];
36 fcplx cndvty2[IN_FILE];
37 fcplx Gp_est2[IN_FILE];
38 fcplx Temp_est2[IN_FILE];

39 fcplx V1_nrw[IN_FILE];
40 fcplx V2_nrw[IN_FILE];
41 fcplx X_nrw[IN_FILE];
42 fcplx Gma12_1n[IN_FILE];
43 fcplx Gma12_2n[IN_FILE];
44 fcplx Gma12r[IN_FILE];
45 fcplx z_nrw[IN_FILE];
46 fcplx A_nrw[IN_FILE];
47 fcplx C1[IN_FILE];
48 fcplx C2[IN_FILE];
49 fcplx E_NRW[IN_FILE];
50 fcplx U_NRW[IN_FILE];

51 fcplx V1a_nrw[IN_FILE];
52 fcplx V2a_nrw[IN_FILE];
53 fcplx Xa_nrw[IN_FILE];
54 fcplx Gma12a_1n[IN_FILE];
55 fcplx Gma12a_2n[IN_FILE];
56 fcplx Gma12ar[IN_FILE];
57 fcplx za_nrw[IN_FILE];
58 fcplx Aa_nrw[IN_FILE];
59 fcplx C1a[IN_FILE];
60 fcplx C2a[IN_FILE];
61 fcplx Ea_NRW[IN_FILE];
62 fcplx Ua_NRW[IN_FILE];

63 fcplx L_est[IN_FILE];
64 fcplx C_est[IN_FILE];
65 fcplx R_est[IN_FILE];
66 fcplx Rs_est[IN_FILE];
67 fcplx Rsurface[IN_FILE];
68 fcplx G_est[IN_FILE];
69 fcplx Zo_est[IN_FILE];
70 fcplx Zo_cal[IN_FILE];
71 fcplx Cs_est[IN_FILE];

72 fcplx Er_NRW[IN_FILE];
73 fcplx Ei_NRW[IN_FILE];
74 fcplx Ur_NRW[IN_FILE];

```

Appendix C: (Continued)

```

75 fcplx Ui_NRW[IN_FILE];
76 fcplx logz[IN_FILE];
77 fcplx angleS[IN_FILE];
78 fcplx magS[IN_FILE];

79 fcplx Era_NRW[IN_FILE];
80 fcplx Eia_NRW[IN_FILE];
81 fcplx Ura_NRW[IN_FILE];
82 fcplx Uia_NRW[IN_FILE];
83 fcplx logza[IN_FILE];
84 fcplx angleSa[IN_FILE];
85 fcplx magSa[IN_FILE];

86 fcplx Adjust2Er[IN_FILE];
87 fcplx Cd2_manual;

88 fcplx Angle11mNRW[IN_FILE];
89 fcplx Angle21mNRW[IN_FILE];
90 fcplx Angle11eNRW[IN_FILE];
91 fcplx Angle21eNRW[IN_FILE];
92 fcplx Angle11rNRW[IN_FILE];
93 fcplx Angle21rNRW[IN_FILE];

94 #endif // INCLUSION_GUARD_getNRW_H

```



```

95 -----
Source-File
96 -----*/
97 #include "getNRW.h"
98 float n=0;
99 float coax_B = 0.250 * 0.0254;
100 float coax_C = 0.209 * .0254;
101 float coax_A = coax_B;
102 float coax_D = 0.0641 * 0.0254;

103 float rho;

104 float alpha = float(0.5)*(coax_B-
    coax_C)/(float(.5)*(coax_B-coax_D));

105 fcplx
    Cd2=float(Er13/(100*PI))*(((pow(alpha,2)
    +float(1))/alpha)*log((float(1)+alpha)/(float
    (1)-alpha))-float(2)*log(4*alpha)/(float(1)-
    pow(alpha,2)));

106 fcplx Cd =
    float(2*Er13*PI*.5*coax_D)*Cd2;
107 fcplx CdT = Cd/float(2);
108 float getNRW(float Cs)

109 {
110 ofstream fod; // name the output file
111 fod.setf(ios::scientific);
112 fod.setf(ios::showpoint);

113 fod.precision(12);
114 for (int k=0; k<rowNum; k++) {
115 V1a_nrw[k] = S21m[k] + S11m[k];
116 V2a_nrw[k] = S21m[k] - S11m[k];
117 Xa_nrw[k] = (float(1)-
    V1a_nrw[k]*V2a_nrw[k])/(V1a_nrw[k]-
    V2a_nrw[k]);
118 Gma12a_1n[k] = Xa_nrw[k] +
    sqrt(pow(Xa_nrw[k],2) - float(1));
119 Gma12a_2n[k] = Xa_nrw[k] -
    sqrt(pow(Xa_nrw[k],2) - float(1));
120 if (abs(Gma12a_1n[0]) <= 1)
121 Gma12ar[k] = Gma12a_1n[k];
122 else
123 Gma12ar[k] = Gma12a_2n[k];
124 za_nrw[k] = (V1a_nrw[k]-
    Gma12ar[k])/(float(1)-
    V1a_nrw[k]*Gma12ar[k]);
125 logza[k] = log(za_nrw[k]);
126 angleSa[k] =
    atan2(imag(logza[k]),real(logza[k]));
127 magSa[k] = abs(logza[k]);
128 Aa_nrw[k] = magSa[k]*exp(j*angleSa[k] +
    float(2*PI*n));

```

Appendix C: (Continued)

```

129 C1a[k]= -
      pow(((Co/(L2*w[k]))*Aa_nrw[k]),2);
130 C2a[k]=pow((sqrt(Ur13t/Er13t)*((float(1)+Gm
      a12ar[k])/((float(1)-Gma12ar[k]))),2);

131 Ea_NRW[k] = sqrt(C1a[k]/C2a[k]);
132 Ua_NRW[k] = float(1) + j*float(0);
133 Era_NRW[k] = real(Ea_NRW[k]);
134 Ura_NRW[k] = real(Ua_NRW[k]);
135 Eia_NRW[k] = imag(Ea_NRW[k]);
136 Uia_NRW[k] = imag(Ua_NRW[k]);
137 }

138 cout << ZREF_est << '\n';

139 Ea_NRW[0] = Ea_NRW[1];
140 Cd2_manual =
      Calibrate*Era_NRW[1]*float(4.792E-
      12)/float(0.807945);

141 for (int k=0; k<rowNum; k++) {

142 Cp_est[k] =
      (Era_NRW[k]*float(2*PI*Eo))/(log(coax_
      A/coax_D));

143 C_est[k] =
      Cp_est[k]+float(2)*Cd2_manual;

144 R_est[k] = 0;

145 G_est[k] =
      (float(2*PI)*(Eia_NRW[k]*Eo*w[k]+Cdc_
      NRW[k])/float(log(coax_A/coax_D));

146 L_est[k] =
      (Ura_NRW[k]*Uo/float(2*PI))*float(log(c
      oax_A/coax_D));

147 ZWh_est[k]=
      sqrt((R_est[k]+j*w[k]*L_est[k])/(G_est[k]
      +j*w[k]*C_est[k]));

148 Gmah_est[k] =
      sqrt((R_est[k]+j*w[k]*L_est[k])*(G_est[k]
      +j*w[k]*C_est[k]));

149 S11m_est[k] = (pow(ZWh_est[k],2)-
      pow(ZREF_est,2))*tanh(Gmah_est[k]*L2)/
      ((float
      (2)*ZWh_est[k]*ZREF_est)+(tanh(Gmah_
      est[k]*L2)*(pow(ZWh_est[k],2)+pow(ZRE
      F_est,2))));

150 S21m_est[k] = float (2)/(float
      (2)*cosh(Gmah_est[k]*L2) +
      sinh(Gmah_est[k]*L2)*((ZWh_est[k]/ZRE
      F_est)+(ZREF_est/ZWh_est[k])));

151 V1_nrw[k] = S21m_est[k] + S11m_est[k];
152 V2_nrw[k] = S21m_est[k] - S11m_est[k];

153 X_nrw[k] = (float(1)-
      V1_nrw[k]*V2_nrw[k])/(V1_nrw[k]-
      V2_nrw[k]);
154 Gma12_1n[k] = X_nrw[k] +
      sqrt(pow(X_nrw[k],2) - float(1));
155 Gma12_2n[k] = X_nrw[k] -
      sqrt(pow(X_nrw[k],2) - float(1));

156 if (abs(Gma12_1n[1]) <= 1)
157 Gma12r[k] = Gma12_1n[k];
158 else
159 Gma12r[k] = Gma12_2n[k];

160 z_nrw[k] = (V1_nrw[k]-
      Gma12r[k])/((float(1)-
      V1_nrw[k]*Gma12r[k]);
161 logz[k] = log(z_nrw[k]);
162 angleS[k] =
      atan2(imag(logz[k]),real(logz[k]));
163 magS[k] = abs(logz[k]);
164 A_nrw[k] = magS[k]*exp(j*angleS[k] +
      float(2*PI*n));

165 C1[k] = -
      pow(((Co/(L2*w[k]))*A_nrw[k]),2);
166 C2[k] =
      pow((sqrt(Ur13t/Er13t)*((float(1)+Gma12r
      [k])/((float(1)-Gma12r[k]))),2);

167 E_NRW[k] = sqrt(C1[k]/C2[k]);
      U_NRW[k] =
      sqrt(C1[k]*C2[k]);
168 Er_NRW[k]= real(E_NRW[k]);
      Ur_NRW[k] =
      real(U_NRW[k]);

```

Appendix C: (Continued)

```

169 Ei_NRW[k]= imag(E_NRW[k]);
      Ui_NRW[k] =
      imag(U_NRW[k]);
170 U_NRW[k]=float(1);
171 Prop_NRW[k] =
      j*w[k]*sqrt(E_NRW[k]*U_NRW[k])/Co;

172 Alpha_NRW[k]= real(Prop_NRW[k]);
173 Beta_NRW[k] = imag(Prop_NRW[k]);
174 Rsurf_NRW[k]= float(1)/Alpha_NRW[k];

175 Cdc_NRW[k] =
      (float(2)/(w[k]*Uo*Ur_NRW[k]))*pow(float(1)/Rsurf_NRW[k],2);

176 Cprimerw[k] =
      (Er_NRW[k]*float(2*PI*Eo))/(log(coax_A/coax_D));
177 Gprimerw[k] =
      (float(2*PI)*(Ei_NRW[k]*Eo*w[k]+Cs))/(log(coax_A/coax_D));
178 Lprimerw[k] =
      (real(U_NRW[k])*Uo/float(2*PI))*float(log(coax_A/coax_D));

179 Rsurfanrw[k] =
      sqrt(float(1)*Uo*w[k]/(float(2)*float(59.61E6)));
180 Rprimerw[k] =
      (Rsurfanrw[k]/float(2*PI))*float((1/coax_A)+(1/coax_D));

181 ZWhnrw[k] =
      sqrt((Rprimerw[k]+j*w[k]*Lprimerw[k])/
      (Gprimerw[k]+j*w[k]*Cprimerw[k]));
182 Gmahnw[k] =
      sqrt((Rprimerw[k]+j*w[k]*Lprimerw[k])*
      (Gprimerw[k]+j*w[k]*Cprimerw[k]));

183 S11nrw[k] = (pow(ZWhnrw[k],2)-
      pow(ZREF_est,2))*tanh(Gmahnw[k]*L2)/
      ((float(2)*ZWhnrw[k]*ZREF_est)+(tanh(Gmahnw[k]*L2)*
      (pow(ZWhnrw[k],2)+pow(ZREF_est,2))));
184 S21nrw[k] = float(2)/(float(2)*cosh(Gmahnw[k]*L2) +
      sinh(Gmahnw[k]*L2))*((ZWhnrw[k]/ZREF_est)+(ZREF_est/ZWhnrw[k]));

185 Angle11mNRW[k]=atan2(imag(S11m[k]),real(S11m[k]))*float(180/PI);
186 Angle21mNRW[k]=atan2(imag(S21m[k]),real(S21m[k]))*float(180/PI);
187 Angle11eNRW[k]=atan2(imag(S11m_est[k]),real(S11m_est[k]))*float(180/PI);
188 Angle21eNRW[k]=atan2(imag(S21m_est[k]),real(S21m_est[k]))*float(180/PI);
189 Angle11rNRW[k]=atan2(imag(S11nrw[k]),real(S11nrw[k]))*float(180/PI);
190 Angle21rNRW[k]=atan2(imag(S21nrw[k]),real(S21nrw[k]))*float(180/PI);

191 fod.open("Output00.dat");
192 OpenFile(fod);
193 fod << "Capacitance" << " " <<
194 "Conductivity" << " " << "(Gmah_est[i])" <<
      " " <<
195 "(Gma12ar[i])" << " " << "\n" << endl;
196 for (int k=0; k < rowNum; k++){
197 fod << MyFreq[k] << " " <<
198 abs(Cd2_manual) << " " <<
      abs(Cdc_NRW[k]) << " " <<
      Gmah_est[k] << " " <<
199 Gma12ar[k] << " " << " " << endl;
200 }
201 fod.close();

202 fod.open("Output01.dat");
203 OpenFile(fod);
204 fod << "Frequency" << " " <<
205 "abs(S11m[i])all" << " " << "abs(S11e[i])" <<
      " " <<
206 "abs(S21m[i])" << " " << "abs(S21e[i])" <<
      "\n" << endl;
207 for (int i=0; i < rowNum; i++){
208 fod << MyFreq[i] << " " <<
209 float(20)*log10(abs(S11m[i])) << " " <<
      float(20)*log10(abs(S11m_est[i])) << " " <<
      << " " <<
210 float(20)*log10(abs(S21m[i])) << " " <<
      float(20)*log10(abs(S21m_est[i])) << " " <<
      << endl;
211 }
212 fod.close();

213 fod.open("Output02.dat");
214 OpenFile(fod);
215 fod << "Frequency" << " " <<

```


Appendix C: (Continued)

```

216 "abs(S11m[i])all" << " " << "abs(S11r[i]" <<
    " " <<
217 "abs(S21m[i]" << " " << "abs(S21r[i]" <<
    '\n'<< endl;
218 for (int i=0; i < rowNum; i++)
219 {od << MyFreq[i] << " " <<
220 float(20)*log10(abs(S11m[i])) << " " <<
    float(20)*log10(abs(S11nrw[i])) << " "
    << " " <<
221 float(20)*log10(abs(S21m[i])) << " " <<
    float(20)*log10(abs(S21nrw[i])) << " " <<
    endl;}
222 fod.close();

223 fod.open("Output03.dat");
224 OpenFile(fod);
225 fod << "Frequency" << " " <<
226 "Angle11m[i]" << " " << "Angle11e[i]" << " "
227 "Angle21m[i]" << " " << "Angle21e[i]" <<
    '\n'<< endl;
228 for (int i=0; i < rowNum; i++)
229 {fod << MyFreq[i] << " " <<
230 abs(Angle11mNRW[i]) << " " << " " <<
    abs(Angle11eNRW[i]) << " " << " " <<
231 abs(Angle21mNRW[i]) << " " <<
    abs(Angle21eNRW[i]) << " " << endl;}
232 fod.close();

233 fod.open("Output04.dat");
234 OpenFile(fod);
235 fod << "Frequency" << " " <<
236 "Angle11m[i]" << " " << "Angle11r[i]" << " "
237 "Angle21m[i]" << " " << "Angle21r[i]" <<
    '\n'<< endl;
238 for (int i=0; i < rowNum; i++)
239 {od << MyFreq[i] << " " <<
240 abs(Angle11mNRW[i]) << " " <<
    abs(Angle11rNRW[i]) << " " << " " <<
241 abs(Angle21mNRW[i]) << " " <<
    abs(Angle21rNRW[i]) << " " << endl;}
242 fod.close();

243 fod.open("Output05.dat");
244 OpenFile(fod);
245 fod << "NRW Frequency" << " " <<
246 "(Real Er[i]" << " " << "(Imag Er[i]" << " "
    <<
247 "(Loss Const[i]" << " " << '\n'<< endl;
248 for (int k=0; k < rowNum; k++)
249 {fod << MyFreq[k] << " " <<
250 abs(Er_NRW[k]) << " " << abs(Ei_NRW[k])
    << " " << " " <<
251 abs(Ei_NRW[k]/Er_NRW[k]) << " " << " "
    << endl;}
252 fod.close();

253 dcCondT_NRW = Cdc_NRW[1]*float(5);
254 Er_NRW[0] = Er_NRW[1];
255 return 0;
256 }

```

C.6 Parametric determination

The following source code utilizes the metric supplied by the objective function to adjust the genome that consists of the Havrilak-Negami parameters, used for permittivity determination. Based on the goodness of fit as computed in the equations above, the genetic algorithm evolves to minimize the error metric. This GA is configured to evolve over 500 generations.

Appendix C: (Continued)

```

1  #include <stdio.h>
2  #include "extractVNA.C"
3  #include "calMSPParam.C"
4  #include "getNRW.C"
5  #include "calHSPParam.C"
6  #include "compSPParam.C"
7  #include <ga/ga.h>
8  #include <ga/GARealGenome.h>
9  #include <ga/GARealGenome.C>

10 float Objective(GAGenome &);
11 float getVNAdata();
12 float getMSPParam();
13 float getNRW(float Cs);
14 float getHSPParam(float Es, float Ei, float Tne,
15     float Ui, float Us, float Tnu, float Cs, float
16     As, float Bs);
17 float getCompare();

16 float wFactor = float(2*PI*Co*100);
17 int const Loops=10; float Gincr=0;
18 float incr=0; float CondT[IN_FILE];
19 float EiP[IN_FILE]; float EsP[IN_FILE];
20 float TneP[IN_FILE]; float TnuP[IN_FILE];
21 float CsP[IN_FILE]; float GsnP[IN_FILE];
22 float UiP[IN_FILE]; float UsP[IN_FILE];
23 float AsP[IN_FILE]; float BsP[IN_FILE];
24 float InerrP[IN_FILE]; float DsnP[IN_FILE];

25 fcplx EeplxW[IN_FILE];
26 fcplx EeplxHK[IN_FILE];
27 fcplx ErealW[IN_FILE];
28 fcplx EimagW[IN_FILE];
29 fcplx ElossW[IN_FILE];

30 float THigh; float TLow; float value
31 float ErValue;float Ei; float Es;
32 float Tne; float Tnu; float Ui;
33 float Us; float As; float Bs;
34 float AsW;float BsW; float EiW;
35 float EsW;float TneW; float CsW;
36 float UiW;float UsW; float TnuW;
37 float Cs; float ErrorW;

38 float SelectScheme = 0;
39 float ScalingScheme=0;

40 float getDielectric()
41 {
42 ifstream fid;
43 fid.setf(ios::scientific);
44 fid.setf(ios::showpoint);
45 fid.precision(8);

46 system("del Output10.dat");

47 unsigned int seed = 0;
48 getVNAdata();
49 getMSPParam();
50 getNRW(Cs);

51 cout <<"\n _____ ";
52 cout <<"\n _____ ";
53 cout <<"\n Coarse Tuning Algorithm ";
54 cout<<"\n _____ ";
55 cout << "\nNRW-Permittivity:" <<
56     Er_NRW[0]
57     << "NRW-Conductivity(max):" <<
58     dcCondT_NRW<< '\n';

57 Restart:
58 float Gincr2 = 5;
59 THigh = float(1E-7)*pow(10,-Gincr);

60 float m_EiLower= 975;float
61     m_EiUpper=1.025;
62 float m_EsLower= .1; float m_EsUpper = 1.3;
63 float m_TneLower=.1;float m_TneUpper=1;
64 float m_CsLower= .1;float m_CsUpper = .5;
65 float m_UiLower=.1; float m_UiUpper= .2;
66 float m_UsLower= .1;float m_UsUpper = .2;
67 float m_TnuLower= 1;float m_TnuUpper=12;
68 float m_AsLower= 0; float m_AsUpper = 1;
69 float m_BsLower = 0; float m_BsUpper = 1;

69 GARealAlleleSetArray alleles;

70 alleles.add(m_EiLower, m_EiUpper, 1e-3,
71     GAAllele::INCLUSIVE,
72     GAAllele::INCLUSIVE);
73 alleles.add(m_EsLower, m_EsUpper, 1e-2,
74     GAAllele::INCLUSIVE,
75     GAAllele::INCLUSIVE);
76 alleles.add(m_TneLower, m_TneUpper, 1e-4,
77     GAAllele::INCLUSIVE,
78     GAAllele::INCLUSIVE);

```

Appendix C: (Continued)

```

74 alleles.add(m_CsLower, m_CsUpper, 1e-13,
    GAAllele::EXCLUSIVE,
    GAAllele::INCLUSIVE);
75 alleles.add(m_UiLower, m_UiUpper, 1e-4,
    GAAllele::INCLUSIVE,
    GAAllele::INCLUSIVE);
76 alleles.add(m_UsLower, m_UsUpper, 1e-4,
    GAAllele::INCLUSIVE,
    GAAllele::INCLUSIVE);
77 alleles.add(m_TnuLower, m_TnuUpper, 1e-2,
    GAAllele::INCLUSIVE,
    GAAllele::INCLUSIVE);
78 alleles.add(m_AsLower, m_AsUpper, 1e-3,
    GAAllele::INCLUSIVE,
    GAAllele::EXCLUSIVE);
79 alleles.add(m_BsLower, m_BsUpper, 1e-3,
    GAAllele::INCLUSIVE,
    GAAllele::EXCLUSIVE);
80 GARealGenome genome(alleles, Objective);

81 GANoScaling scaling;
82 GARankSelector selector;

83 GAParameterList params;
84 GASteadyStateGA::registerDefaultParameters
    (params);
85 params.set(gaNminimaxi,
    GASteadyStateGA::MINIMIZE);
86 params.set(gaNnGenerations, 500);
    // Number of Generations
87 params.set(gaNpopulationSize, 500);
    //Population Size
88 params.set(gaNnPopulations,64);
    // Number of Populations
89 params.set(gaNscoreFrequency, 2);
90 params.set(gaNnBestGenomes, 2)
    // Number of Best Genome
91 params.set(gaNpMutation,0.5);
    // Mutation probability
92 params.set(gaNpCrossover, 0.9);
    // Crossover probability
93 params.set(gaNflushFrequency, 2);
    // Flush Frequency
94 params.set(gaNpReplacement, .05);
    // Replacement %
95 params.set(gaNselectScores,
    (int)GAStatistics::AllScores);
96 GASteadyStateGA ga(genome);
97 ga.parameters(params);

98 ga.selector(selector);
99 ga.scaling(scaling);
100 ga.set(gaNscoreFilename, "bog1.dat");
101 ga.evolve(seed);
102 genome.initialize();

103 cout <<"-----";
104 cout <<"\n"<<Gincr <<" Ei Es Tne Cs Ui Us
    Tnu As"<<endl;
105 cout << "the ga generated: " <<
    ga.statistics().bestIndividual() <<endl;

106 for(int i=5;i<6;i++)
107 cout << "\nbS11m " << abs(S11m[i])
108 << " bS21m " << abs(S21m[i])
109 << "\nbS11h " << abs(S11h[i])
110 << " bS21h " << abs(S21h[i]) << "\n'
111 << "Err11: " << Avg11_Error
112 << " Err21: " << Avg21_Error
113 << " ErrTot: " << Avg_Error << "\n'
114 << "TotErr11: " << Sum11_Error
115 << " TotErr21: " << Sum21_Error << "\n'
116 << "ErrAng11: " << Avg11a_Error
117 << " ErrAng21: " << Avg21a_Error << "\n'
118 << "AngMis11: " << Sum11m_Error
119 << " AngMis21: " << Sum21m_Error << "\n'
    << endl;

120 ofstream fod; //name the output file

121 fod.setf(ios::scientific);
122 fod.setf(ios::showpoint);
123 fod.precision(12);

124 fod.open("Output10.dat",ios::app);

125 OpenFile(fod);

126 if (Gincr < 1) {
127 fod << "Ei" << "Es" << "Tne" << "Cs"
128 << "Us " << "Ui" << "As" << endl; }

129 cout << ga.statistics().bestIndividual() << " "
130 << ga.statistics().bestIndividual().score() << ""
131 << real(Er_NRW[0]) << " "
132 << THigh << " "
133 << real(dcCondT_NRW) << "\n' << endl;

134 if (ga.statistics().bestIndividual().score() >= 0)

```

Appendix C: (Continued)

```

135 ErValue =
    ga.statistics().bestIndividual().score();
136 else ErValue = 1E9;

137 fod << ga.statistics().bestIndividual() << "
    "
138 << ErValue << "      "
139 << real(Er_NRW[0]) << "      "
140 << THigh << "      "
141 << real(dcCondT_NRW) << "      " << endl;

142 if (Gincr < Loops) {fod.close();Gincr++; goto
    Restart;}
143 else fod.close();

144 fid.open("Output10.dat");
145 OpenFile(fid);
146 fid.seekg (22, ios::beg);
147 for (int i=0; i <= Loops; i++)
148 fid >> EiP[i] >>
149 EsP[i] >> TneP[i] >>
150 CsP[i] >> UiP[i] >>
151 UsP[i] >> TnuP[i] >> Asp[i] >> BsP[i] >>
152 InerrP[i] >> DsnP[i] >>
153 GsnP[i] >> CondT[i];
154 fid.close();

155 for (int i=0; i <= Loops; i++)
156 {
157 if (InerrP[i] <= ErrorW && i > 1){
158 EiW=EiP[i]*DsnP[i];
159 EsW=EsP[i]*float(10);
160 TneW=TneP[i]*GsnP[i];

161 TnuW=TnuP[i]*GsnP[i];
162 CsW=CSP[i]*CondT[i];
163 UiW=UiP[i]*float(10);
164 UsW=UsP[i]*float(10);
165 AsW=AsP[i];
166 BsW=BsP[i];
167 ErrorW=InerrP[i];}
168 else if (i == 0){
169 EiW=EiP[i]*DsnP[i];
170 EsW=EsP[i]*float(10);
171 TneW=TneP[i]*GsnP[i];
172 TnuW=TnuP[i]*GsnP[i];
173 CsW=CSP[i]*CondT[i];
174 UiW=UiP[i]*float(10);
175 UsW=UsP[i]*float(10);
176 AsW=AsP[i];

177 BsW=BsP[i];
178 ErrorW=InerrP[i];}
179 }
180 cout << "\n-----\n"
181 << "\n Einf: " << EiW << "      Ezero: "
    << EsW
182 << "Tne: " << TneW*wFactor << " cm" << '\n'
183 << "\n Uinf: " << UiW << "Uzero: " << UsW
184 << "Tnu: " << TnuW*wFactor << " cm" << '\n'
185 << "\n Conductivity:" << CsW
186 << "AsW: " << AsW
187 << "BsW: " << BsW << '\n'
188 << "\n Error: " << ErrorW << " " << '\n';

189 getHSPParam(EsW,EiW,TneW,UiW,UsW,Tnu
    W,CsW,AsW,BsW);
190 fod.open("Output11.dat");
191 OpenFile(fod);
192 fod << "Frequency" << " " <<
    "S11m[i]" << " " << "S11h[i]" << " " <<
    "S21m[i]" << " " << "S21h[i]" << " " <<
    '\n' << endl;
195 for (int i=0; i < rowNum; i++)
196 {fod << MyFreq[i] << " " <<
    S11m[i] << " " << S11h[i] << " " << " " <<
    S21m[i] << " " << S21h[i] << " " << " " <<
    endl;}
199 fod.close();
200 fod.open("Output12.dat");
201 OpenFile(fod);
202 fod << "Frequency" << " " <<
    "abs(S11m[i])all" << "" << "abs(S11h[i])" <<
    "" <<
204 "abs(S21m[i])" << " " << "abs(S21h[i])" <<
    '\n' << endl;
205 for (int i=0; i < rowNum; i++)
206 {fod << MyFreq[i] << " " <<
    float(20)*log10(abs(S11m[i])) << " " <<
    float(20)*log10(abs(S11h[i])) << " " <<
    " <<
208 float(20)*log10(abs(S21m[i])) << " " <<
    float(20)*log10(abs(S21h[i])) << " " <<
    endl;}
209 fod.close();
210 fod.open("Output13.dat");
211 OpenFile(fod);
212 fod << "Frequency" << " " <<
    "(Angle11m[i])" << " " << "(Angle11h[i])"
    << " " <<

```

Appendix C: (Continued)

```

214 "(Angle21m[i]" << " " << "(Angle21h[i]"
    << '\n' << endl;
215 for (int i=0; i < rowNum; i++)
216 {fod << MyFreq[i] << " " <<
217 Angle11m[i] << "" << Angle11h[i] << "" <<
218 Angle21m[i] << "" << Angle21h[i] << "" <<
    endl;}
219 fod.close();
220 fod.open("Output14.dat");
221 OpenFile(fod);
222 fod << "Frequency" << " " <<
223 "(Real Er[i]" << "" << "(Imag Er[i]" <<
224 "(Loss Const[i]" << " " << '\n' << endl;

225 for (int k=0; k < rowNum; k++){
226 EcplxW[k] = EsW + ((EiW - EsW) / pow((float
    (1) + j*w[k]*TneW), 1 - AsW)) -
    j*(float(1)*CsW / (w[k]*Eo));
227 EcplxHK[k] = (real(EcplxW[k]) -
    j*imag(EcplxW[k]));
228 ErealW[k] = abs(real(EcplxHK[k]));
229 EimagW[k]
    = abs(imag(EcplxHK[k])) + CsW / (w[k]*Eo);
230 ElossW[k] = EimagW[k] / ErealW[k];
231 Fod << MyFreq[k] << " " <<
232 abs(ErealW[k]) << " " << abs(EimagW[k])
    << " " <<
233 abs(ElossW[k]) << " " << " " << endl;

234 }
235 fod.close();
236 return 0;
237 }
238 float
239 Objective(GAGenome& g)
240 {
241 GAREalGenome& genome =
    (GAREalGenome&)g;
242 Ei = genome.gene(0)*real(Er_NRW[0]);
243 Es = genome.gene(1)*float(10);
244 Cs = genome.gene(3)*real(dcCondT_NRW);
245 Tne = genome.gene(2)*THigh;
246 Ui = genome.gene(4)*float(10);
247 Us = genome.gene(5)*float(10);
248 Tnu = genome.gene(6)*THigh;
249 As = genome.gene(7);
250 Bs = genome.gene(8);

251 if (Es <= Ei && Us <= Ui && Avg_Error <=
    1E9 && Es != 0){
252 getHSParam(Es, Ei, Tne, Ui, Us, Tnu, Cs, As, Bs);
253 getCompare();
254 value = Avg_Error;
255 else {value = 1E9;}

256 return value
257 }

```

C.7 Summary

The algorithm setup in section C.6 above is repeated three additional time. In each successive run, the search space boundaries are decreased to provide a fine tuning capability to the genetic algorithm. The GALIB library offered by MIT permits the construction of only a single objective function. As a result, only a single metric is passed to the GA which encompasses a comparison of the phase angle, magnitude, and conductance parameters for the measurement and Havrilak-Negami computation. Adjustments in the limits on the search space may have to be adjusted to fit some data.

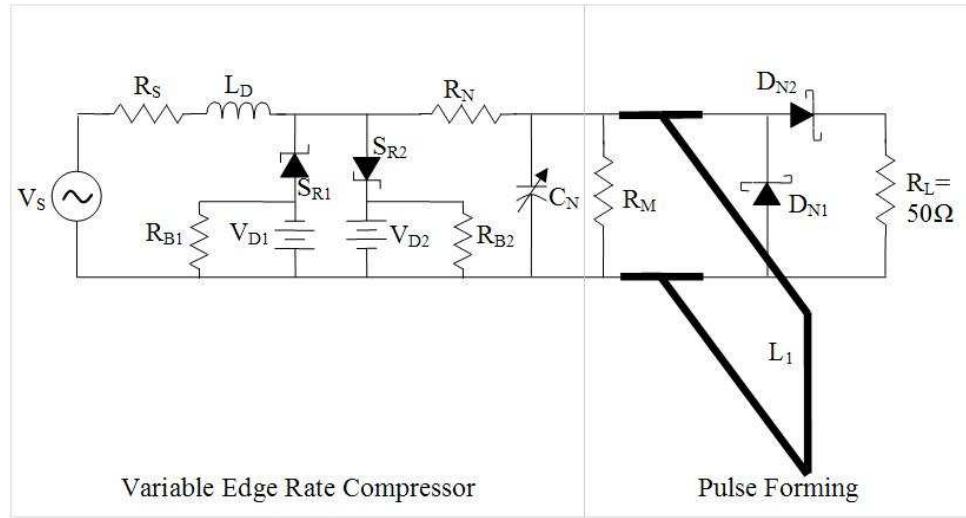
Appendix D: Evolutionary development of the UWB VERC circuits

The circuit presented in Chapter 3, Figure 3.19 is a first generation of UWB VERCs. Parasitics that exist at each of the SMA connector interfaces change the impedance characteristics, which leads to an increase in line reflections. In the following sections, many of the SMA connectors were eliminated to circumvent problems associated with parasitics. The circuits in these sections are described as 2nd and 3rd generation circuits and are presented only to document the efforts in this area. The analysis is consistent with the 1st generation circuit in Chapter 3, therefore a detail evaluation or analysis is not given in this appendix.

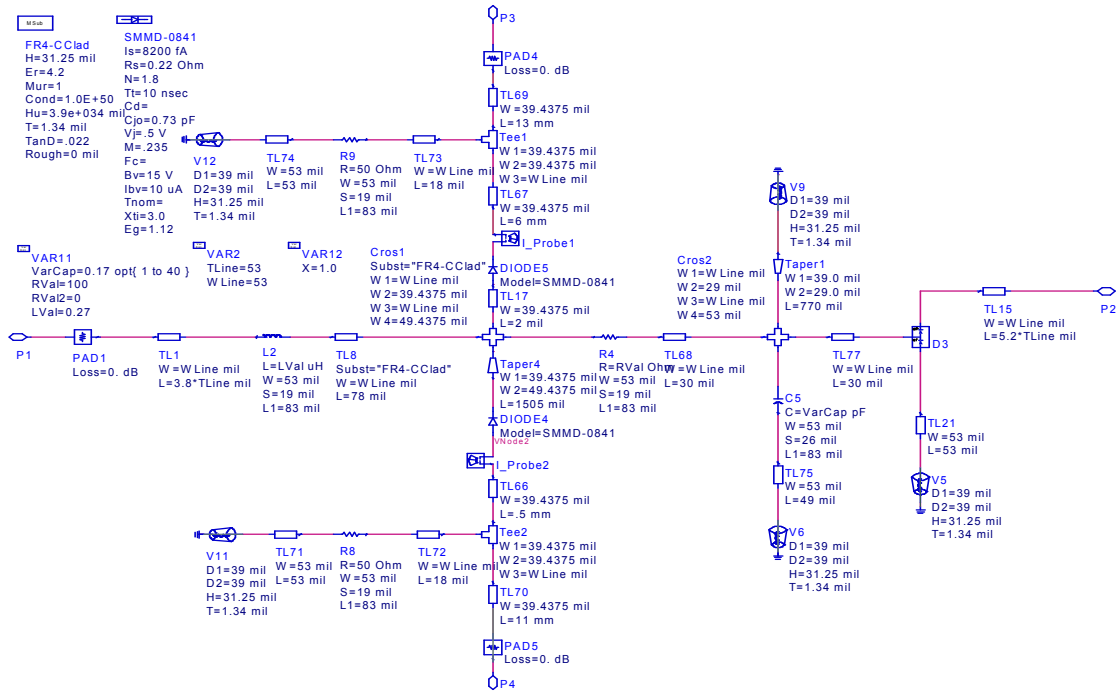
D.1 2nd generation of UWB VERC circuit

The 2nd generation of UWB VERC circuit consisted of all of the components associated with that in Figure 3.19, in addition to DC biasing for the SRDs. The optimization parameter associated with the step-function that is generated by this circuit is slew-rate. The goal of tuning prior to Gaussian pulse formation is established here by varying the (RC) time constant of the circuit, consequently this sub-circuit was constructed using a Metelics SMMD840-SOT23-0S SRD to rapidly charge up and snap back on the rising (S_{R1}) and falling (S_{R2}) edges of the source (see Figure D.1A-B). A bias for S_{R1} was applied using a resistance (R_{B1}) of 50Ω and a voltage (V_{D1}) of $3.8 V$. Likewise, the SRD bias for S_{R2} was achieved using a resistance (R_{B2}) of 50Ω and voltage (V_{B2}) of $0.5 V$. The RC network consisted of a chip resistor R_N of 60Ω and variable

Appendix D: (Continued)



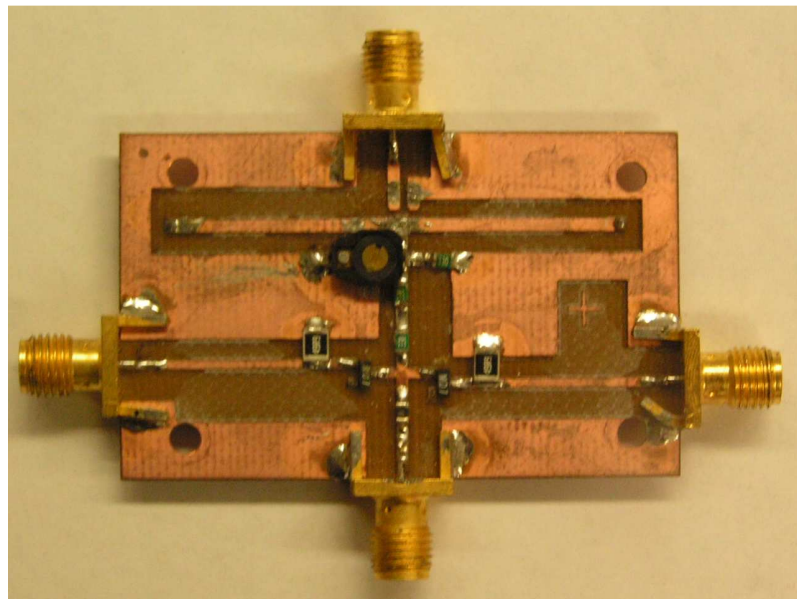
(A)



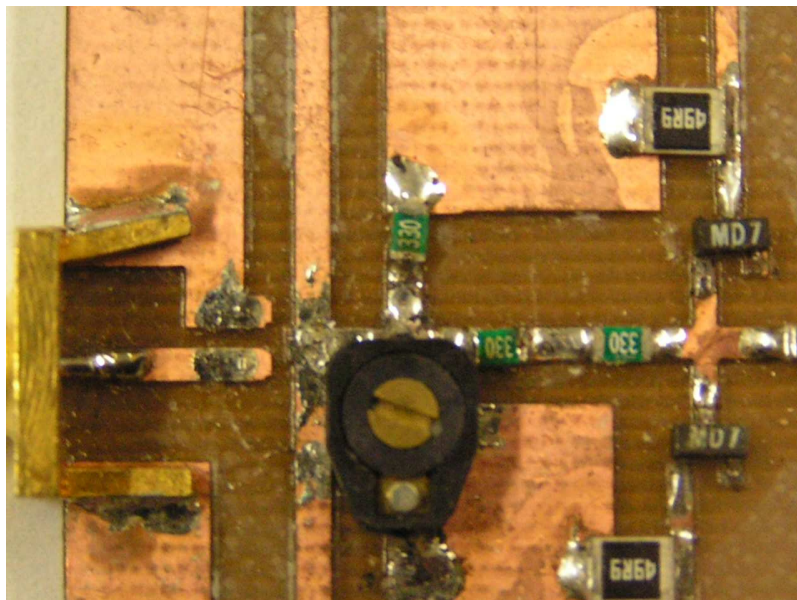
(B)

Figure D.1: A DC biased UWB VERC circuit (A) diagram and (B) ADS schematic.

Appendix D: (Continued)



(A)



(B)

Figure D.2: Fabricated circuit for a DC biased UWB circuit on FR4 at (A) bird's eye view and (B) zoomed view.

Appendix D: (Continued)

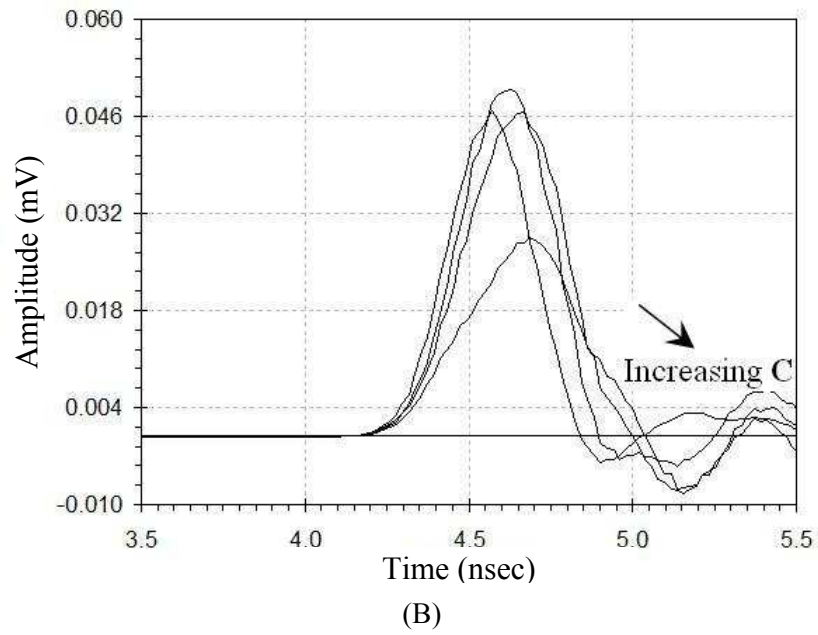
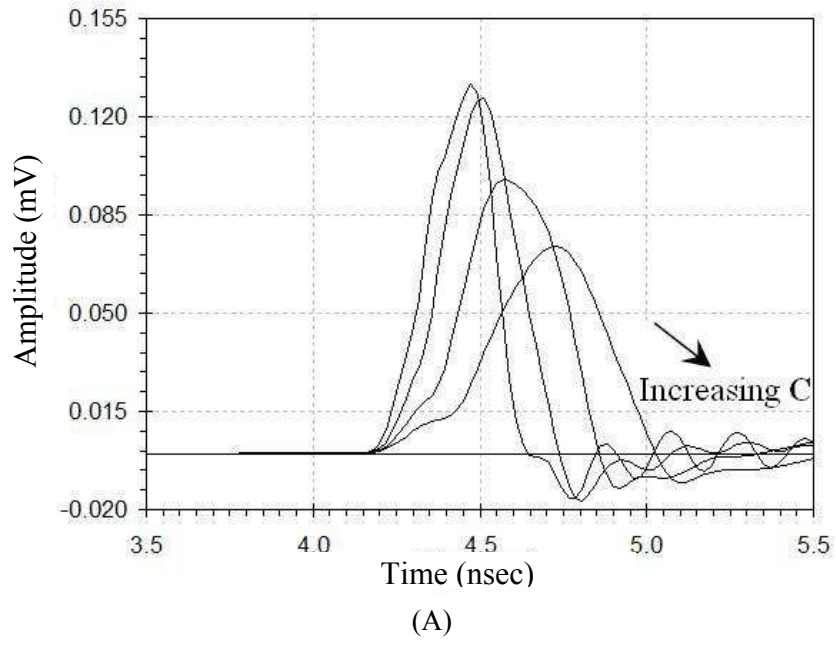


Figure D.3: DC biased UWB VERC circuit (A) simulated and (B) measured results.

Appendix D: (Continued)

capacitor trimmer with a 1-40 pF range (Sprague Goodman SG2020). These circuits were fabricated on a Rogers Corporation RO4003 substrate, where $\epsilon_r = 3.38$, $\tan \delta = 0.022$, and thickness $h = 0.51 \text{ mm}$ (see Figure D.2A-B). Measured and simulated results are shown in Figure D.3A-B below.

D.2 3rd generation of UWB VERC circuit

In the 3rd generation of UWB VERC circuit the capacitor was eliminated in order to produce a compact topology with a fixed pulse-duration (see Figure D.4). This topology consisted of a single SRD in parallel, a series resistor R_D of 34.8Ω , a series tapered transmission line L_1 measuring 335 mils , and a shunt transmission line L_2 of 380 mils . The 3rd generation of UWB VERC circuit was fabricated on a Rogers Corporation RO4003 substrate, where $\epsilon_r = 3.38$, $\tan \delta = 0.022$, and thickness $h = 0.51 \text{ mm}$ (see Figure D.5A-B). Measured and simulated results are shown in Figure D.6A-B below.

D.3 Summary

Tunable and fixed pulse sub-nanosecond pulse generators based on a novel mechanism of applying step recovery diodes towards variable edge-rate compression were developed. The variable edge-rate compression approach promotes more simple UWB generator design by allowing a focus on generating a smooth slope for the step in a rectangular pulse and then developing RF/microwave differentiators. Through this approach novel circuits for pulse generation were developed and demonstrated above.

Appendix D: (Continued)

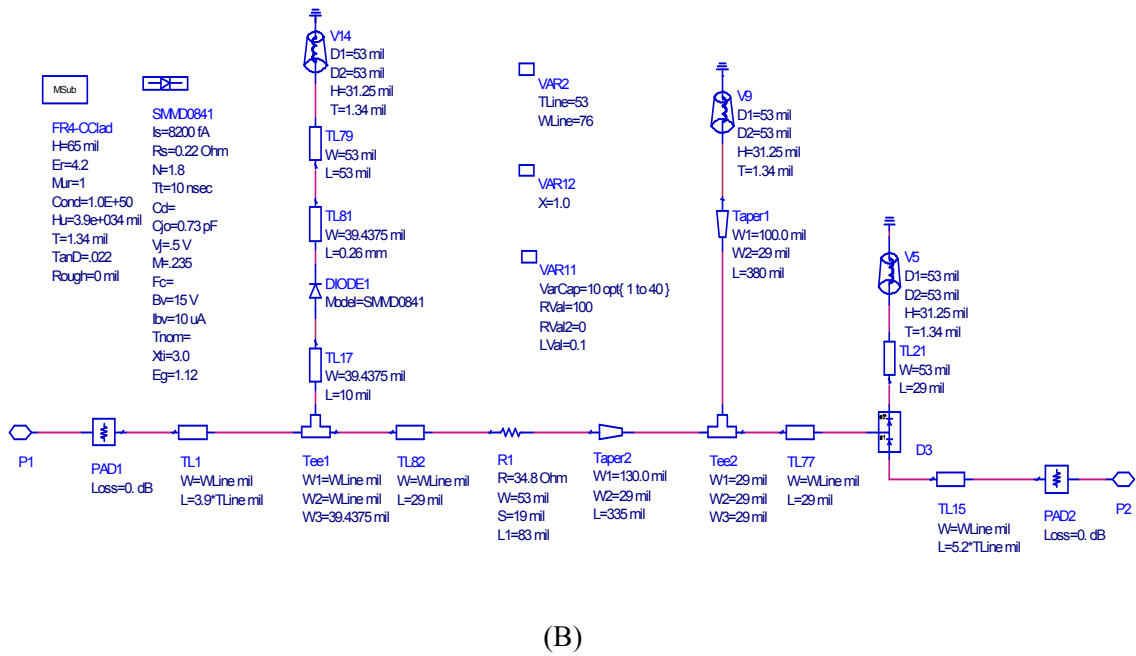
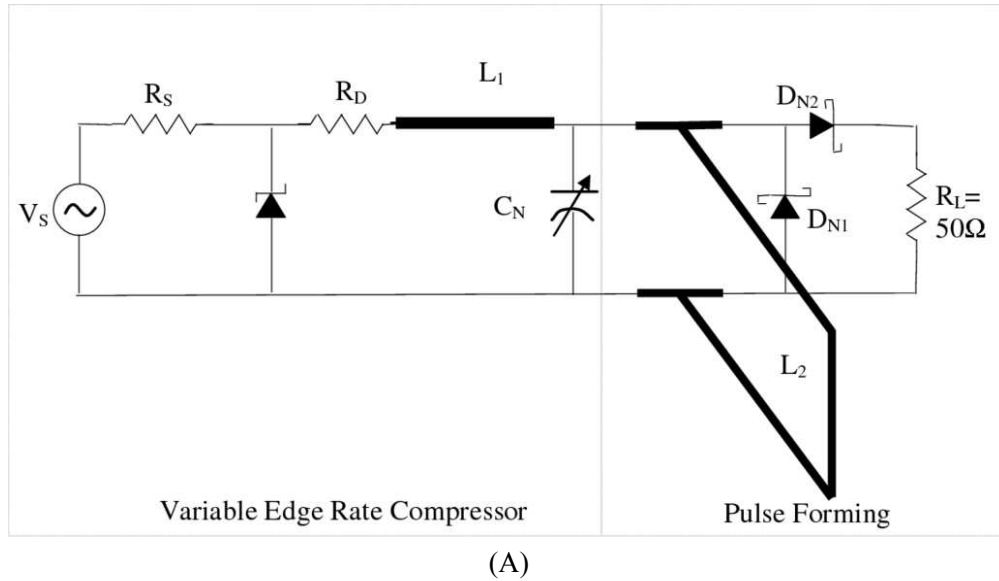
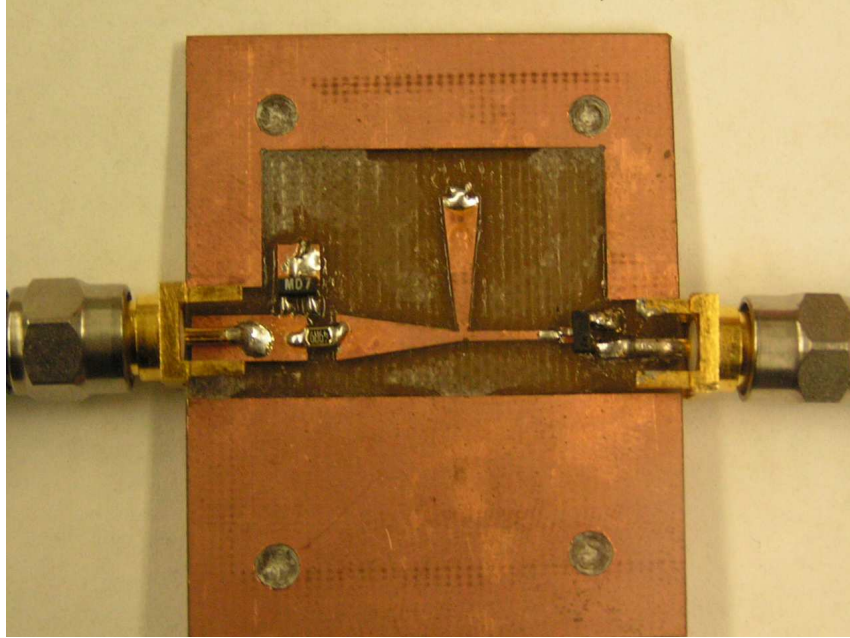
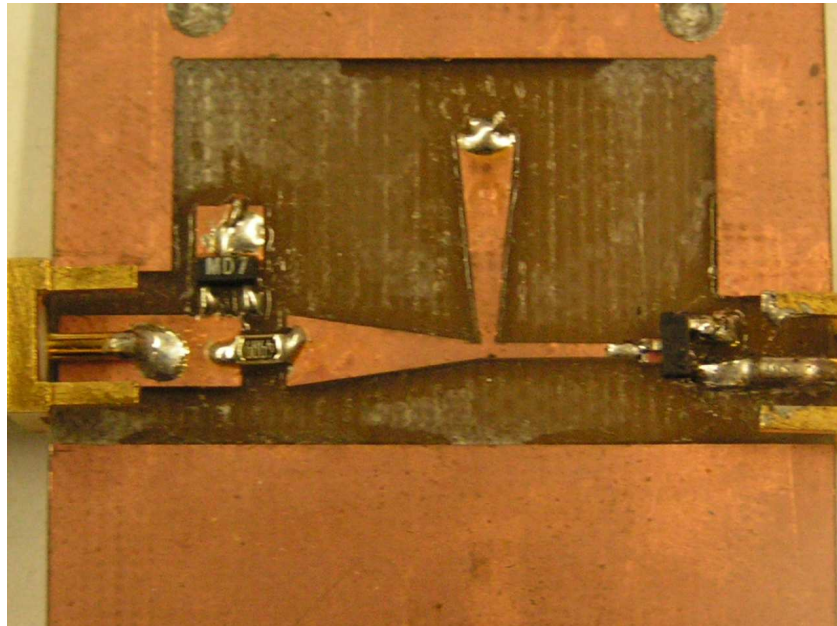


Figure D.4: A fixed pulse UWB VERC circuit (A) diagram and (B) ADS schematic.



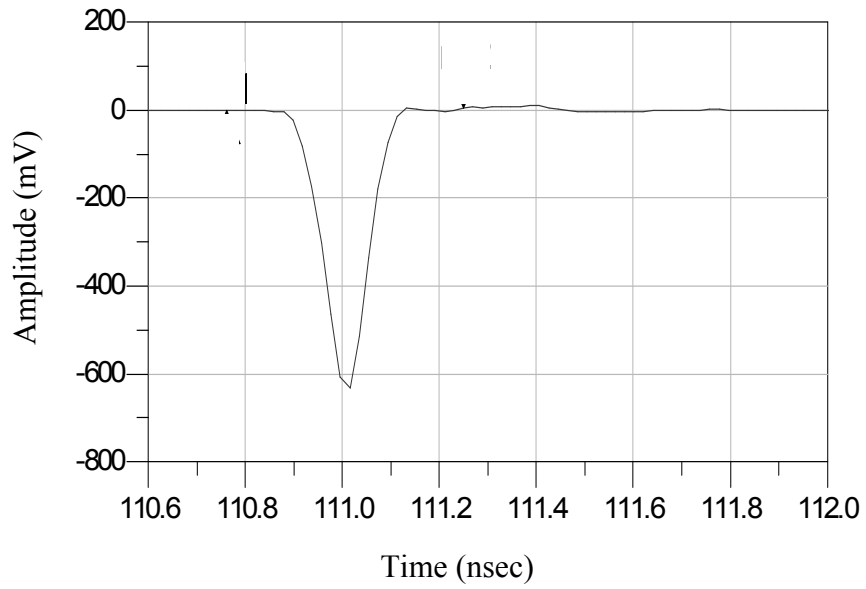
(A)



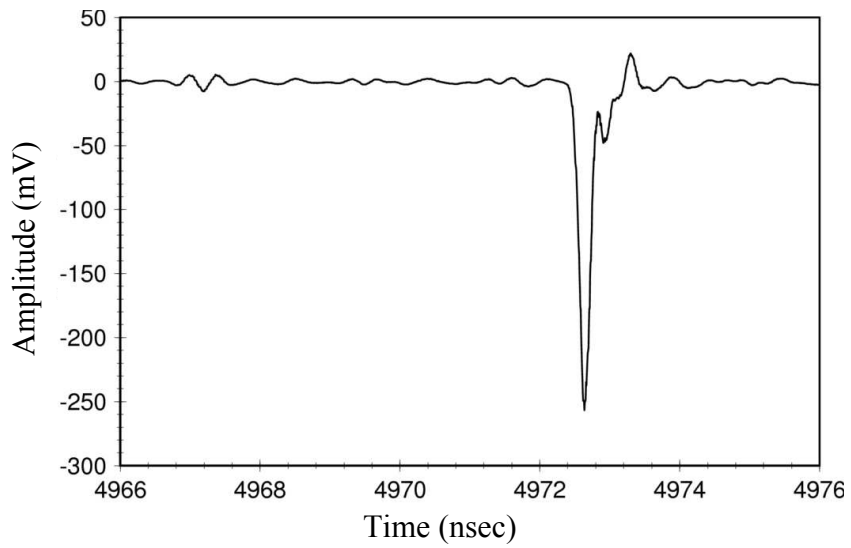
(B)

Figure D.5: Fabricated circuit for a fixed pulse UWB VERC on FR4 at (A) bird's eye view and (B) zoomed view.

Appendix D: (Continued)



(A)



(B)

Figure D.6: Fixed pulse UWB VERC circuit (A) simulated and (B) measured results.

About the Author

Erick Maxwell received the B.S. degree in Electrical Engineering from Southern University A&M, Baton Rouge, La. in 1994; M.S. degree in Electrical Engineering from the University of South Florida (USF) in 2001; M.S. degree in Engineering Management from USF in 2003; and is currently working toward the Ph.D. degree in Electrical Engineering at USF. He is a McKnight Doctoral Fellow, NSF IGERT Fellow, USF Multicultural Research Fellow and Merck Pharmaceuticals/UNCF Dissertation Fellow. From 1993 to 1994, he worked as a design engineer for Delco Electronics where he proposed a \$2.5 million cost improvement to Delco's executives. He has also worked as a digital design and R&D engineer for Harris Corporation in Government Communication Systems since 1995. He is a professionally licensed engineer in Florida and his research interests are in electromagnetic characterization of materials, ultra-wideband and RF/microwave circuits, and non-invasive cancer detection.